Development of a Novel Multi-Dimensional Computational Model of the Teleost Fish Ventricle for the Study of Cardiac Thermal Tolerance

A thesis submitted to The University of Manchester for the degree of
Doctor of Philosophy
in the Faculty of Science and Engineering

2020

Hamsa N. Naser

Department of Physics and Astronomy in the School of Natural Sciences

Contents

Total Word Count = 58632 Words

List of Figures

Lists of Tables

Nomenclature and abbreviations

V	Transmembrane potential
R	Gas constant
T	Absolute temperature
F	Faraday constant
C_m	Membrane capacitance
AP	Action potential
OS	Overshoot of AP
APA	Action potential amplitude
dV/dt_{max}	Maximum upstroke velocity
RMP	Resting membrane potential
APD	Action potential duration
APD_{50}	APD at 50% repolarisation
APD_{90}	APD at 90% repolarisation
I_{Na}	Fast Na^+ current
g_{Na}	Conductance of I_{Na}
I_{CaL}	L-type Ca^{2+} current
g_{CaL}	Conductance of I_{CaL}
I_{Kr}	Rapid delayed rectifier K^+current
g_{Kr}	Conductance of I_{Kr}
I_{K1}	The inward rectifier K^+ current
g_{K1}	Conductance of I_{K1}
I_{Nab}	Sodium background current
g_{Nab}	Conductance of I_{Nab}
I_{Cab}	Calcium background current
g_{Cab}	Conductance of I_{Cab}
I_{Kp}	Plateau K^+ current
g_{Kp}	Conductance of I_{Kp}
I_{pCa}	Calcium pump
g_{pCa}	Conductance of I_{pCa}
$I_{K(ATP)}$	ATP sensitive potassium current
$g_{K(ATP)}$	Conductance of $I_{K(ATP)}$
I_{NaK}	Sodium-potassium pump
g_{NaK}	Conductance of I_{NaK}
I_{NaCa}	Sodium-calcium exchanger current
g_{NaCa}	Conductance of $I_{Na,Ca}$
I_{rel}	Ca^{2+} release from JSR to myoplasm
G_{re}	Rate constant of Ca^{2+} release from JSR
G_{rel}	Maximum rate constant of Ca^{2+} release from JSR
$\Delta[Ca^{2+}]_{i,2}$	Cumulative Ca^{2+} entry into the cell 2 milliseconds after onset of stimulus
I_{leak}	Ca^{2+} leakage from NSR to myoplasm
K_{leak}	Rate constant of Ca^{2+} leakage from NSR
CSQN	Calsequestrin, Ca^{2+} buffer in JSR

TRPN	Troponin, Ca^{2+} buffer in the myoplasm
CMDN	Calmodulin, Ca^{2+} buffer in the myoplasm
m, h	Activation gate and inactivation gate of I_{Na}
y_∞	Steady-state value of activation (inactivation) gate y
α_y, β_y	Opening and closing rate constants of gate y
τ_y	Time constant of gate y
d, f	Activation gate and inactivation gate, of the L-type Ca^{2+} channel
$\tau_{f,fast}$, $\tau_{f,slow}$	Time constant of gate f, fast and slow component
f_{Ca}	Ca^{2+}-dependent inactivation gate of the L-type Ca^{2+}channel
Xr	Activation gate of I_{Kr}
r	Inactivation gate of I_{Kr}
K	Inactivation gate of I_{K1}
$[Na^+]_i$	Intracellular Na^+ concentration
$[Ca^{2+}]_i$	Intracellular Ca^{2+} concentrations
$[K^+]_i$	Intracellular K^+ concentrations
$[Na^+]_o$	Extracellular Na^+ concentrations
$[Ca^{2+}]_o$	Extracellular Ca^{2+} concentrations
$[K^+]_o$	Extracellular K^+concentrations
E_{Na}, E_{Ca}, E_K	Reversal potential of ion Na^+, Ca^{2+} and K^+
I_{up}	Ca^{2+} fluxes from the cytosol to the network sarcoplasmic reticulum (SR)
I_{tr}	Ca^{2+} flux from the network SR (NSR) to junctional SR (JSR)
I_{stim}	Stimulus current
1D	One dimensional
2D	Two dimensional
3D	Three dimensional
CA	Cold acclimation
WA	Warm acclimation
BCL	Basic cycle length
HP	Hypertension (High blood pressure)
CV	Conduction Velocity
ERP	Effective Refractory Period
FDM	Finite Difference Method
FEM	Finite Element Method
HH	Hodgkin and Huxley
IV	Current Voltage (relationship)
ODE	Ordinary Differential Equation
LV	Left Ventricle

Abstract

Cardiac computational modelling has offered an alternative method to experimental cardiology for heart function studies. Although different electrophysiological models in several species have been developed, no such models exist for the fish heart. Fish are vertebrate ectothermic animals, and their body temperature is affected by temperature changes in their aquatic environment. Given the prominence of global warming effects, temperature changes and the rise of water temperature influence different organs in the fish body, including the heart. A better understanding of the process of thermal acclimation of the fish heart at single cell and tissue levels where cardiac ion channels and pumps remodel after prolonged exposure to a different temperature, is of scientific interest. Also, a 3D model based on an accurate anatomy model is a valuable tool for the study of ventricular electrical activities. Furthermore, investigating the effects of heart diseases on cardiac mechanical dynamics and the contracting dynamics of the human ventricular cells is also valuable to study. Thus, the objective of this thesis consists of three parts: In part I, a novel biophysically computer model for the teleost fish ventricular myocyte has been developed at the physiological body temperature of 4°C. First, novel formulations of the major ionic currents including I_{Na}, I_{CaL}, I_{Kr} and I_{K1}, were developed at 4°C and then incorporated into the basal model developed by Luo and Rudy for the guinea-pig ventricle myocytes. The developed model was then used to assess the effects of changing temperatures on ventricle electrical dynamics. The developed models matched experimental findings quantitatively. In Part II, a novel 3D biophysically and anatomically accurate model for the teleost ventricle was developed. First, a 3D geometry of the heart was reconstructed and segmented into the heart's major chambers using a micro-CT scan with sustaining iodine technique. Then, the 3D geometry of the ventricle was incorporated into a 3D computational model to investigate the electrical excitation propagation in the teleost heart. In Part III, a multi-scale electromechanical model of human ventricle cells was modified to assess the impacts of hypertension (HP) on the contractile function of the human left ventricle myocytes. A single cell electromechanical model was modified by integrating experimental data from rat ventricular cells under Sham (control) and HP conditions. Simulations showed that HP prolonged APD_{90} and increased $[\mathrm{Ca}^{2+}]_\mathrm{i}$ with no marked change in the sarcomere length or the contractile force at cellular level, but in 2D tissue simulations, there was an increase in the tissue's vulnerability for initiation and maintenance of re-entrant excitation waves indicating a pro-arrhythmic effect of hypertension.

Declaration

I declare that no portion of the work referred to in the thesis has been submitted in support of an application for another degree or qualification of this or any other university or other institute of learning.

Copyright Statement

I. The author of this thesis (including any appendices and/or schedules to this thesis) owns certain copyright or related rights in it (the “Copyright”) and s/he has given The University of Manchester certain rights to use such Copyright, including for administrative purposes.

II. Copies of this thesis, either in full or in extracts and whether in hard or electronic copy, may be made only in accordance with the Copyright, Designs and Patents Act 1988 (as amended) and regulations issued under it or, where appropriate, in accordance.

III. The ownership of certain Copyright, patents, designs, trademarks and other intellectual property (the “Intellectual Property”) and any reproductions of copyright works in the thesis, for example graphs and tables (“Reproductions”), which may be described in this thesis, may not be owned by the author and may be owned by third parties. Such Intellectual Property and Reproductions cannot and must not be made available for use without the prior written permission of the owner(s) of the relevant Intellectual Property and/or Reproductions.

IV. Further information on the conditions under which disclosure, publication and commercialisation of this thesis, the Copyright and any Intellectual Property and/or Reproductions described in it may take place is available in the University IP Policy (see http://documents.manchester.ac.uk/DocuInfo.aspx?DocID=2442 0), in any relevant Thesis restriction declarations deposited in the University Library, The University Library’s regulations (see http://www.library.manchester.ac.uk/about/regulations/) and in The University’s policy on Presentation of Theses.

Acknowledgements

First and foremost, I would like to thank my supervisor, Prof. Henggui Zhang for his guidance throughout the project and education he has imparted to me in cardiac electrophysiology. His passion for research has been a great source of exceptional inspiration to me.

I would also like to thank Prof. Holly Shiels for all useful discussions, help, support and advice on the project. Iam so grateful for all the time and enthusiasm she has invested in this project.

I would like to express my gratitude and thanks to Prof. Matti Vornanen for all the results and discussions he made to improve the work in this thesis. I would also take this opportunity to thank Prof. Jian Lu for the useful discussion during the examination of this work.

In addition, I would like to thank all Biological Physics group, friends and colleagues, too many to name, who have helped to provide a pleasurable environment. I would also like to thank Dr. Dominic Whittaker for all his help, support and always useful discussions.

I wish to thank my big family; my parents, two sisters and two brothers for their love and support and my small family; my husband and my two kids for their endless love, for enduring with me, understanding and encouragement. They always be my source of positive vibes.

Lastly, I would express my sincere gratitude to the Higher Committee for Education Development in Iraq (HCED) for the financial support and for the HCED staff for their help and support during my PhD journey.

Dedication

To my father, Naji Naser, who passed away during my PhD study in 2018, he used to give me strength when I thought of giving up and always believe in me.

To my mother, Maidah for her love, support and prayers.

To my husband, Nibras for being with me as my big lover, and helper during my whole study journey, without him I would never be able to do it.

To my sons, Ali and Fadhl, the candles of my life.

Supporting work

Naser H, Whittaker D, Shiels H and Boyett M and Zhang H. A Novel Model of Electrical Action Potentials of Teleost Fish Ventricular Myocytes. Computing in Cardiology (CinC), 2018. Maastricht: IEEE; 2018. pp. 1-4. DOI: 10.22489/CinC.2018.032. (Conference proceedings).

Naser H, Zhang Y, Zhang H. Modelling the Effects of Hypertension on Ventricle Cells of Human Heart. Computing in Cardiology (CinC). Singapore: IEEE; 2019. (Conference proceedings).

1. Introduction

1.1 The Heart

The heart is an organ that contracting periodically to pump blood throughout the pulmonary and systemic systems of the network of the body [1–4]. It represents the centre of the circulatory system which is a wide network of vessels in the body. These vessels transport nutrients, hormones, respiratory gases and metabolic waste, and aids in defending the body against disease. During more than 500 million years ago of the heart's evolution, the heart has undergone many alterations and adaptations. It has developed from the early single layered tube such as in the tunicate [5], to the circulatory system of vertebrate that characterized with two-chambered heart (single atrium and single ventricle) such as in teleost fish, to a three-chambered heart system that made up of two atria and one ventricle in amphibian tetrapods [6]. Consequent tetrapods including alligators and crocodiles, birds and mammals evolved a powerful heart with four-chambered (two atria and two ventricles) [4].

As a result, for each individual, the structure and function of the circulatory system of the heart holds a fundamental role that benefits each species particularly [4]. Pathological changes such as cardiac arrhythmia, heart failure, and congenital heart diseases that occur to heart functions can be fatal. Therefore, an imperative understanding to the underlying mechanisms of the heart behaviour in health and pathogenesis is required. Beyond the vital biological and medical problem, the heart is a mechanical pump and electrical conductor, and therefore it requires interdisciplinary methods from physics and mathematics to understand the complicated pathology of heart disorders [3].

In the last few decades, significant development has been made in experimental protocols and methods, which have been applied to make extensive understanding of the heart in both healthy and diseased states [7]. Previous studies [8–10] have been centred mainly on the mechanisms of the intact heart, however, nowadays, they are more focused on the finer details. For example, from segments of cardiac tissue to single cardiac cells and then right down to the levels of protein and

DNA [7], which are partially motivated by enhancements in technology that overcomes the earlier approaches limitations.

At the turn of the new millennium, due to the prominent worldwide problem of global warming, major advances have been taken to further investigate the functions of heart not only in variant pathological conditions but also in variant environment conditions in the ambient eco of some animal species [11–13], specially the ectothermic heart such as fish [11, 14–17]. Rising in water temperature due to changing climate [11, 13, 16, 18] may form a real threat to the heart function of such animal leading to cardiac arrhythmia and sudden death, causing disruption to life-chain and food safety.

Over years, some detailed experimental data have been obtained at the cellular and sub-cellular levels on the temperature effect on fish electrophysiology [15, 17, 19, 20]. Now, it is a challenge to integrate those experimental findings to understand the mechanisms of heart pathologies under different conditions at multi-scales, ranging from subcellular level to functioning cardiac myocytes and then to the tissue level. It is therefore an urgent need to take novel integrative approaches for studying the function of the whole heart.

1.2 Global Warming

Global warming is the phenomenon of the graduate rising in the average temperature of the air near the Earth surface over the past century [21–23], as shown in Figure 1.1. Since the beginning of the industrial revolution, it has been found that the Earth's temperature has risen by 0.75°C than the past century [12, 21]. Moreover, it is expected that in the near future probably by 2100 temperatures could rise by as much as 5°C [12], as shown in Figure 1.1B. The increasing in the production of greenhouse gases has led to more and more heat that trapped in the atmosphere that changes the climate of the Earth , i.e. it is continued to heating up [12].

Human activities have also contributed to greenhouse gases to the Earth's atmosphere. This included mainly carbon dioxide (CO_2) from deforestation and the burning of fossil fuels, nitrous oxides (N_2O) and methane (CH_4) from waste and agriculture, and fluorinated gases from industrial procedures [24]. These additional greenhouse gases have increased their concentrations by 30-50% or even 100% since the beginning of the industrial revolution (around 1750) [12]. The increasing in these gases has resulted in an increase in the amount heat from the sun withheld in the Earth's atmosphere, which is would typically be radiated back into space. This heat increasing has enhanced greenhouse effect, resulting in additional Earth warming and climate change [13]. Therefore, climate change and global warming have become a significant global concern that can lead to more extreme weather events and rising seawater temperature [25, 26]. This may cause a further widespread extinction of many plant and animals, specially, the aquatic ectotherm species [12, 21].

The raised temperature in seawater can affect the ecology, physiology, as well as evolution systems of the animals, particularly ectotherms. It is expected that global warming will be influenced ectothermic animals, strongly [27] with clear latitudinal and altitudinal effects on the distribution of such species [13]. Therefore, for better understandings to the effects of environmental changes on the organisms of lives, it requires detailed knowledge of the thermal limits and the physiological mechanisms underlying the sensitivity of such organism to changing temperature. This will improve predictions of the organism vulnerability to further increases in their habitat temperature and help to predict the potential changes in the ecosystems in the future [18, 21].

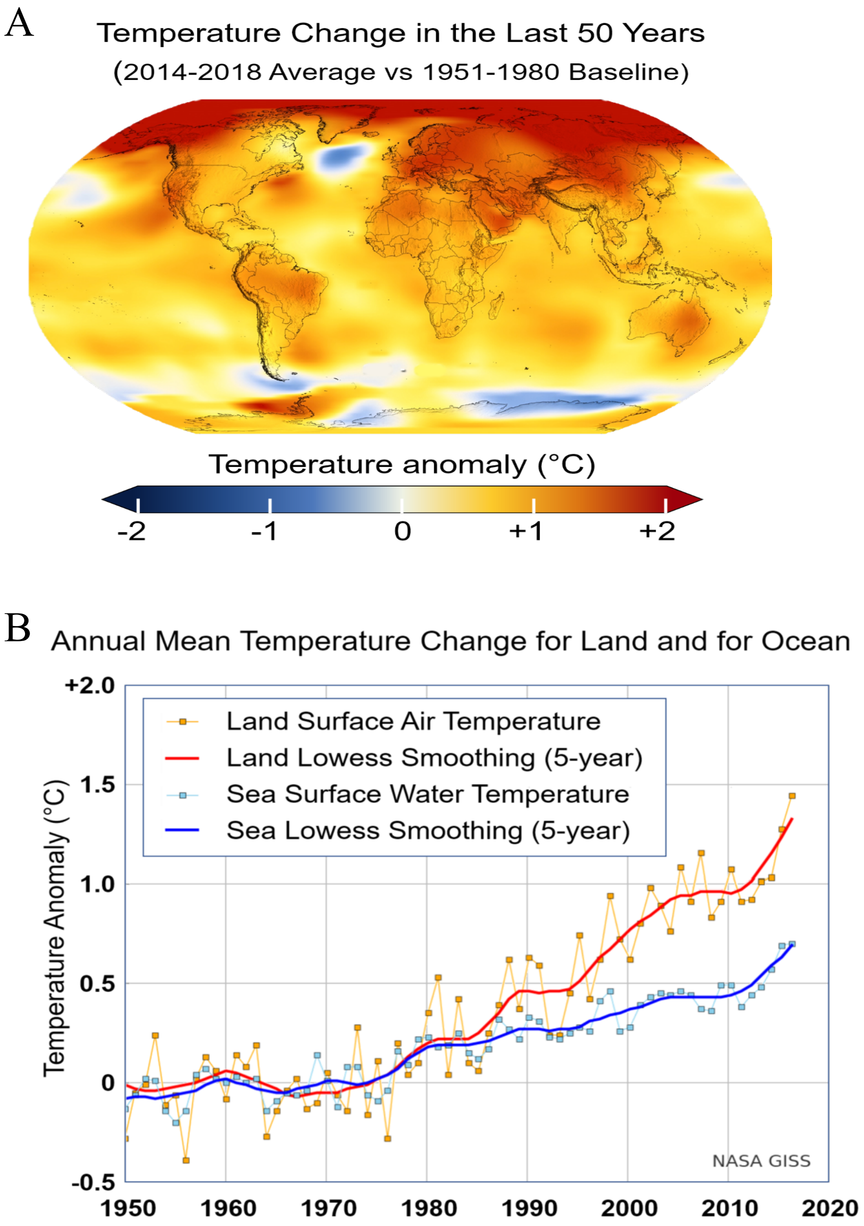

Figure 1.1: Global warming rises the Earth’s atmosphere temperature. A: The average global temperatures between 2014 and 2018 in the comparison to a baseline average between 1951 and 1980. This is according to NASA's Goddard Institute for Space Studies [28]. B: Graph of the illustrated rise in the average annual temperature of Earth's land (red line) and sea water (blue line) surfaces, as shown in the thin lines and five year lowess smooths (represented by thick lines), due to variant climate change consequences that assume different levels of population growth, economic development, and fossil fuel use [29].

1.3 Fish as an aquatic ectotherm

There are more than 33,000 extant fish species. All of which (except approximately 30 species) are ectotherms, meaning that the external thermal environment determines their body temperature and thermoregulation is mostly achieved through behavioural means [30].

Fish are usually categorised into four groups including: Chondrichtyes (cartilaginous fish) (Figure 1.2A), Agnatha (hagfish) (Figure 1.2B), Sarcopterygii (lobe-finned fish) (Figure 1.2C) and Actinopterygii (ray-finned fish) (Figure 1.2D). In this thesis, the work was based on the Teleostei fish species (teleosts or bony fishes) (Figure 1.2E) which belong to the ray-finned fish and represent around 96% of all extant fish species [31].

Fish live in aquatic habitats that thermally varied and the thermal tolerances of most fish vary from cold with −2.5°C to very warm with +44°C temperatures [30, 32]. Based on the extent of temperature tolerance, fishes can be categorised into three groups; stenothermal (with narrow thermal tolerance), mesothermal (with moderate thermal tolerance) and eurythermal (with wide thermal tolerance) [17]. The Southern Ocean fishes are the most remarkable examples of fishes that lives in stenothermal environments. These fishes tolerate only a narrow range of temperatures. Whereas north-temperate fishes usually operate under a wider temperatures range, as they survive at temperatures from close to freezing degree up to ~40°C [17, 33]. Mesothermal fish such as Salmonid fishes typically prefer cool habitats (high oxygen content in cool water) and demonstrate an upper thermal tolerance range of 22–28°C [17]. Furthermore, tropical species, such as the zebrafish (a member of minnow family) have broad thermal tolerances, therefore, they can survive at temperatures close to (+40°C) or even higher [17, 30].

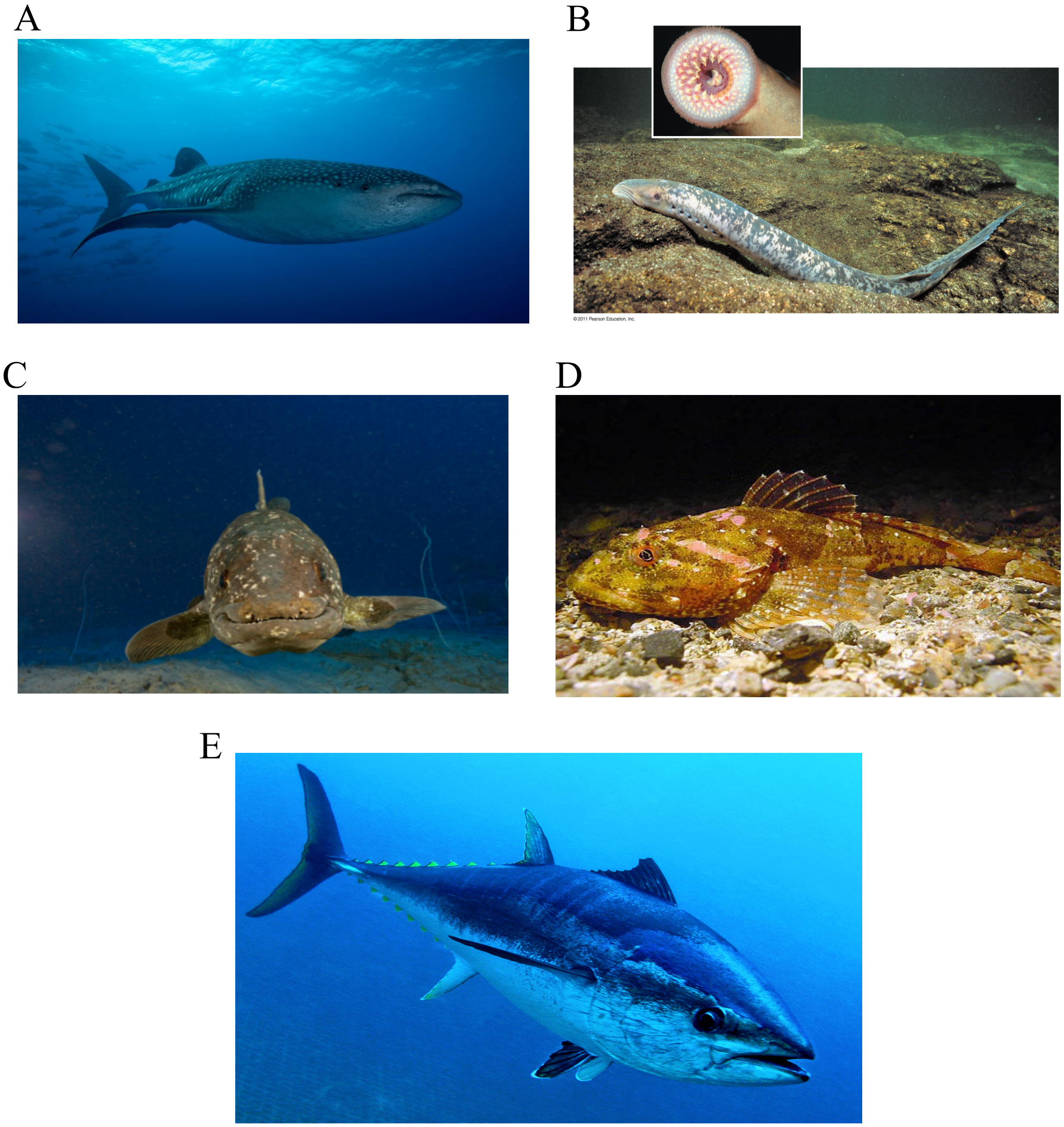

Figure 1.2: Different fish groups. A: the whale shark is one of cartilaginous fishes [34]. B: Lamprey fish one of the jawless vertebrates (Class Agnatha) [35]. C: one of Lobe-Finned Fish (Sarcopterygii) [36]. D: Scorpion fish, one of the Actinopterygii (ray-finned fish) [37]. E: Tuna fish, one of the Teleostei fish species [38].

1.4 Thermal Tolerance of the Fish Heart

Fish as ectothermic species are widely affected by changes in their ambient temperature, which affects their biological functions at different levels, as a result of the universal effect of temperature on molecular interactions that modulates physiological, biomechanical and biochemical functions of a biological system [11, 19, 25, 26, 34]. Therefore, temperature changes become a critical factor in geographical distribution of such animals [16, 40].

Teleost (bony) fish are ectotherm animals which do not maintain body temperature using metabolically generated heat. This means that heart temperature changes with body temperature which can have profound effects on both electrical and mechanical function. Some fish, like the bluefin tuna, are able to warm specific parts of their bodies (regional endothermy) but not their hearts, thus, similar to other ectothermic fishes the tuna heart quickly equilibrate with ambient water temperature [11, 14–17]. This is very different to mammals which are endothermic (use metabolically generated heat to maintain body temperature) with a heart temperature of ~37C, regardless of ambient temperature [40].

Eurythermal fish species live in varied aquatic habitats [30]. Because temperature is a key driver of all biochemical reactions rates, both acute (short term, min to hours) and chronic (long term, day, months, seasons) temperature changes can profoundly impact the function of the fish heart. Experimental studies [15, 17, 41–44] have shown that at cooling the fish heart rate is slow, and can depress cardiac contractility, whereas at warming the fish heart rate is elevated and can improve contractility (up to a point). These changes in whole heart electrical and contractile function with temperature are determined by temperature dependent changes in ionic channel conductance and ionic pumps in membrane of the cardiomyocytes that make up the APs of the fish heart [33, 45]. Thus understanding the effect of temperature change on cellular ionic processes including the cellular action potential provides insight into how such changes influence the whole heart function and hence the well-being of the animal.

Because temperature exerts such a large effect on the function of the heart, eurythermal species are able to adjust the expression and/or the regulation of cardiac ion channels to provide maintained cardiac function during prolong temperature change. This thermal remodelling of ion channel expression is called thermal (or seasonal) acclimatization or thermal acclimation [46]. Thermal remodelling of the heart, thus allows eurythermal animals the ability to maintain cardiac function across a range of temperatures that would be cardiopeliagic to mammals, including humans.

The flexibility of fish ion channel function during chronic temperature changes [15, 42], indicates their involvement in thermal tolerance of cardiac function. Electrical excitability of the fish heart differs between species, due to species-specific differences. These differences might be in channel configuration and subunit assemblies, resulting in different thermal dependencies [15]. The cardiac excitation comprises a range of molecular mechanisms which might be accountable for thermal limitation of the function of the fish heart. Changes in ambient temperature can alter the ectotherms body temperature quite considerably leading to meet special demands of the function of ion channel in order to maintain tolerable excitability of cardiac cells in numerous temperatures [15]. Given the prominent problem of global warming, the global climate studies have predicted the rises in the duration, frequency and severity of temperature extremes in the near future [30]. As a result, cardiac arrhythmias may develop in the fish heart, causing a sudden death and imposing a heavy burden to the society economy. Therefore, a better knowledge of electrical excitation mechanisms of ionic and molecular of the fish cardiac myocytes can provide important information to understand the mechanisms of the heart that limit the performance and survival of ectothermic species, and thus aid to identify potential ‘winners and losers’ of changing climate [32].

1.5 Cardiac Modelling

Cardiac computational modelling has offered an alternative method to experimental cardiology for the heart function studies for more than half century. From early 1950, a mathematical model for simulating neuron membrane action potentials (APs) have been developed [47] forming the basal model of most cardiac cells [48–55]. These models were based on detailed experimental data of kinetics and biophysical properties of the underlying ionic currents. Different complicated possible interactions of intracellular ions and the currents of the transmembrane make computer modelling as the only method accessible to synthesize and clarify these multiple nonlinear interactions. Accordingly, the action potential of the cardiac myocytes can be restructured, based on detailed biophysical formulations of the fundamental ionic channel currents, exchangers and pumps as well as intracellular ionic homeostasis [49, 56, 57].

Recently, cardiac mathematical models have become more complicated and useful at the same time as they can be used to study tissue level behaviour by integrating these models into anatomically-detailed heart geometries with complex microstructure obtained using different techniques such as diffusion tensor imaging [58, 59] and micro computed tomography [60, 61]. This has enabled significant assistances from cardiac modelling for various applications such as investigation of essential mechanisms underlying genesis and maintenance of the cardiac arrhythmias [62, 63], optimisation of surgical interventions [64], and preclinical drug safety testing [65].

In biomedical research, cardiac models offer several advantages over the usage of the traditional experimental methods. For instance, in general, modelling costs less in terms of money and time than experiments. Additionally, it offers unparalleled control to the investigator where all aspects of the model can be recorded and varied simultaneously, in a systematic way. Furthermore, the modelling has a non-invasive nature means it does not require the same ethical considerations like experiments of the cardiac physiology that including animal subjects.

However, computational models of course have some limitations. The heart is a nonlinear biological system as it is highly complicated. The cardiac models development necessitates the system to be simplified and assumptions need to be made in order to do this. While experiments unrevealed more and more complexities of the heart system, computational models can consider only a small amount of the heart's actual complexity [66]. For this reason, the simplifications and assumptions of the cardiac models need to be rigorously validated by comparing them to experimental techniques to obtain models with the ability to provide mechanistic insights and predictive power [66]. In addition, the model functional capabilities must be characterised well, to inform the scope of the model application [67].

Cardiac models are hence most powerful when integrated closely with experimental records and clinical observations [68]. This aids cardiac modelling to offer a valuable involvement to the ongoing interdisciplinary research effort in the investigation of the function of biological systems as complex as the heart.

1.6 Overview of the Thesis

The aim of this thesis can be split into three main areas:

- To develop a novel electrophysiological model for the fish heart based on experimental findings such that it is physiologically and experimentally relevant.
- To use the developed model to investigate the mechanisms underlying the genesis of teleost ventricular arrhythmias under different temperature conditions at single cell, 1D strand and 3D scales.
- To modify an electromechanical model to investigate the functional impacts of another cause of heart failure on heart function, which is relevant but in the mammal heart, arising from the high blood pressure (hypertension) disease at single cell, 1D strand and 2D scales.

The thesis itself is grouped into three parts: Part I consists of two chapters focusing on modelling of teleost fish ventricular myocytes at single cell and 1D strand tissue in different temperature conditions. Part II consists of one chapter focusing on 3D modelling of the teleost ventricle based on anatomically accurate geometry of the ventricle. Part III consists of one chapter focusing on multi-dimensional modelling of the mammal ventricle under hypertension.

In order to understand the work in the thesis, a scientific background first presented and then four results chapters comprising a novel work relating to the above outlined aims, and followed by the final chapter for the general discussion of each chapter findings and summarising the novel contributions of the thesis.

Consequently, the thesis is structured as follows.

The following chapter provide comprehensive introductions to the areas covered in the thesis. Chapter 2 presents the biological, mathematical, and computational background of the basis of the work in this thesis. The teleost fish heart structure and function comparing to the mammal (particularly human) heart are first introduced, then the fish heart electrical and mechanical activities are also presented from the subcellular level to the organ scale.

Chapter 3 presents the mathematical and numerical methods that used to create biophysically-based computational models of both human heart and fish heart which forms much of the work in this thesis.

In Chapter 4, the development of a novel biophysically detailed computer model for the electrical action potential of a teleost fish ventricular myocyte for fish adapted to a chronically cold (cold-acclimated, CA, 4°C) is discussed. Novel formulations for the major ion channel currents I_{Na}, I_{CaL}, I_{Kr}, and I_{K1} based on recent experimental data (from different teleost species) are incorporated into Luo and Rudy model [54] (for guinea-pig ventricular cells) which forms the basal framework of the developed mathematical model of the fish heart. The developed model is then used to simulate the effects of ion channels remodelling on the electrical properties of the ventricular myocytes for fish adapted to a chronically warm (warm-acclimated, WA, 18°C) and for the common experimental data of 11°C, in order to investigate the effects of chronic temperature change condition at cold and warm acclimations.

In Chapter 5, the model developed at the physiological temperatures of 4 and 18°C in Chapter 4 is used to construct a one dimensional (1D) strand tissue model at the same temperatures. Then the single cell models developed in Chapter 4 and the 1D strand tissue models developed in Chapter 5 (at 4 and 18°C), both are used to investigate the mechanisms of teleost ventricular arrhythmogenesis when the acute temperature changes, at a range of temperature from cold to the thermal limit of some teleost species. These models are used to elucidate the functional rolls of changing the chronic or acute temperature in the fish aquatic environment and each of which leads to changes to action potential morphology and dynamic behaviour.

Chapter 6 describes the development of a novel 3D model of the teleost ventricle. First, an accurate teleost ventricle geometry is reconstructed using micro-CT images with iodine staining technique. Second, this geometry is incorporated into the teleost model developed in part I at 18°C. Finally, the electrical excitation wave propagation and the activation time pattern are discussed.

Chapter 7 presents another cardiac arrhythmia but in the mammal heart especially human left ventricular myocytes. A multi-scale electromechanical model is used in the investigations of the hypertension impact on the left ventricle contractile function of the human ventricle cells. The proarrhythmic mechanisms underlying different phenotypes associated with hypertension condition and the re- entrant spiral waves are also investigated.

Chapter 8 summarises the major findings and novelty as well as significance of the work presented in this thesis. Additionally, the key experimental relevance is outlined, and the possible directions of the future work are also suggested.

2. Background

2.1 Introduction

In recent years, the form and structure of the heart have aroused increasing interest due to their probable role as one of the factors that determine the function of the normal heart. Most mammals, such as human, are recognised with a complex heart structure, therefore, numerous cardiac studies have attempted to obtain further details from the hearts of different animal species that share the most common features with the mammals heart but in less complexity in their hearts structure [69]. In this sense, fish, such as teleost species, are a growing model for human cardiac dysfunction [40, 70–73], since they possess the simplest type of heart, with one atrium and one ventricle plus another two chambers: sinus venosus and bulbus arteriosus (Figures 2.1A,B) as compared with the human heart which has four chambers with two separate atrium and two separate ventricles (Figure 2.1C) [19].

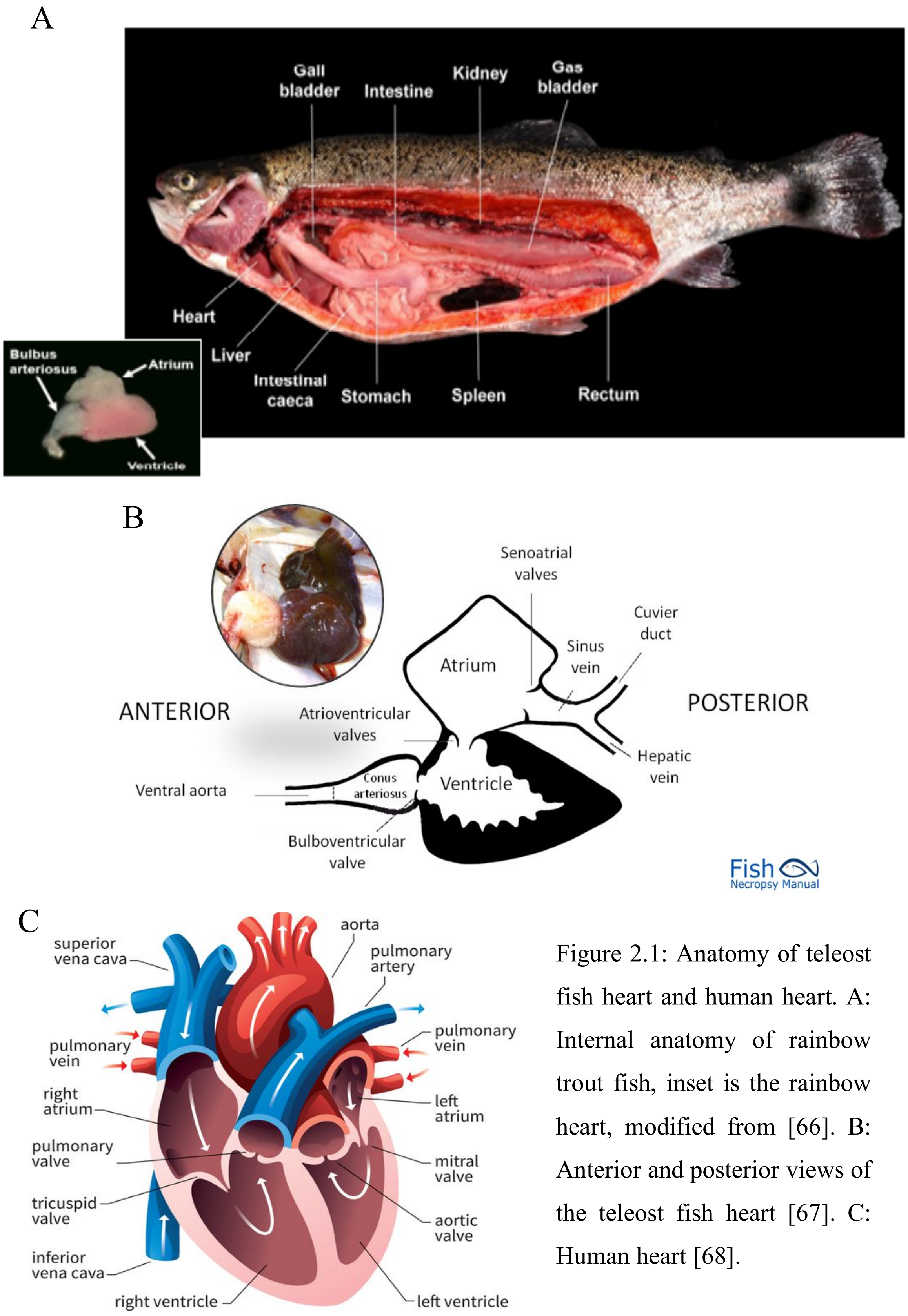

Figure 2.1: Anatomy of teleost fish heart and human heart. A: Internal anatomy of rainbow trout fish, inset is the rainbow heart, modified from [66]. B: Anterior and posterior views of the teleost fish heart [67]. C: Human heart [68].

2.2 Anatomy of the Teleost Fish Heart

The fish heart which is located a little behind and below the gills (see Figure 2.1A) consists of four chambers that arranged into a series [74–76, 76, 77]. These chambers are illustrated as follows:

2.2.1 Sinus Venosus

This chamber represents the most caudal part of the heart, and it has a thin wall. The wall thickness is usually between 60 µm and 90 µm [75, 78]. Its volume differs between species, for example, in teleosts, the sinus venosus volume is similar to that of the atrium while in elasmobranches it is less than the atrium volume [79].

The sinus venosus receives blood from all over the body through various ducts such as the paired cuvier ducts and the hepatic veins which are guarded by the muscular sphincters, while the sinoatrial is guarded by a large valve. The cuvier ducts freely communicate with the major systemic veins [74, 75].

Generally, sinus venosus is described as being formed of connective tissue and muscle, however, the proportions of the two components appear to vary widely. The connective tissue is bounded by the inner endothelial of the sinus wall and lined the outer epicardial of the wall [80]. For example, in zebrafish, the connective tissue mostly makes up the sinus venosus wall while in the Anguilla anguilla species, the wall is formed mostly of myocardium. However, in some species such as Pleuronectes platessa the connective tissue with sparse myocardial bundles forms the sinus venosus wall. Moreover, in species such as goldfish and carp, the myocardium may be replaced by smooth muscle cells [75].

Initiating and controlling the heart beat are the major functions of the sinus venosus. In most teleosts, sinus venosus is the site of a specialized ring of tissue which has been identified as the primary pacemaker region which is densely innervated, and is located between the sinoatrial region and the cuvier ducts [75].

The teleost heart lacks a morphologically defined conduction system; therefore, other components of the cardiac conduction system which are similar to those present in mammals have not as yet been identified in the teleost heart [76].

The preferential spread of electrical excitation is allowed by the geometry of the muscle trabeculae, subsequently being the functional correlate of the His-Purkinje system in mammals. This preferential pathway may be constituted by the trabeculae anchored in the atrioventricular region, (AV muscle ring) [74, 75].

The myogenic activity of the atrium, ventricle or (AV) can also initiate contraction when the specialized pacemaker tissue is absent. However, in this case the contraction rate is likely to be slower and more irregular than the pacemaker rate [80].

2.2.2 The Atrium

The teleost heart has a single atrium chamber. This chamber is irregularly shaped with a thin trabecular wall and shows considerable variability in shape and size between species (Figure 2.2) [74]. Generally, the atrium mass constitutes (0.01-0.03) % of the body mass, and (8-25) % of the ventricular mass, while atrium volume is similar or larger than ventricle volume [74].

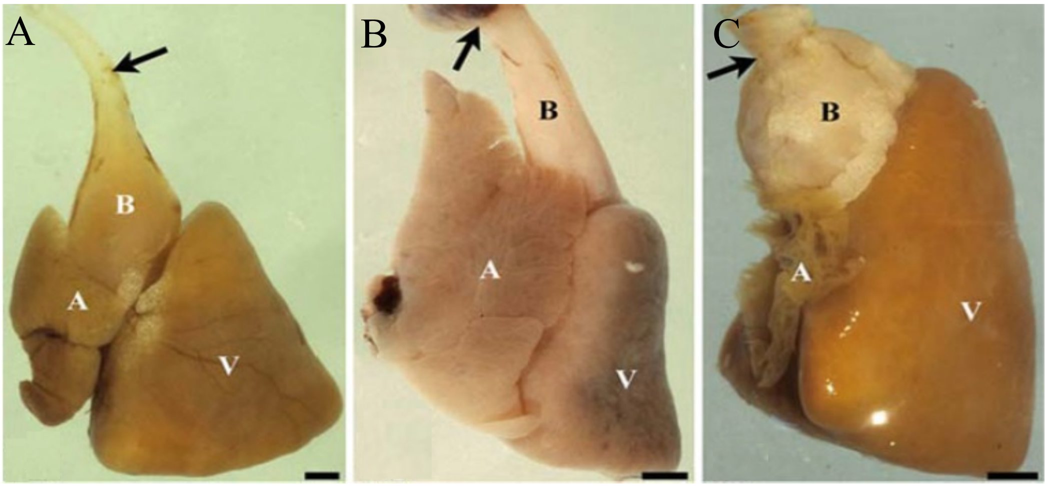

Figure 2.2: Right lateral views of the heart from three types of teleost fish species. A: *Trachurus trachurus*'heart, where the ventricle (V) has a pyramidal shape, with a small atrium (A) and a pear-shaped bulbus (B). B: *Trigla lucerna*'heart, where (V) has a sac-like shape, with a very large (A) and a cylindrical and elongated (B). C: *Sparus pagrus*'heart, where (V) has a pyramidal shape, with a relatively (A) and a short and thick (B). The arrows show the upper insertion of the pericardium and the boundary between the ventral aorta and the bulbus, modified from [75].

An external edge of myocardium and a complex network of thin trabeculae (pectinate muscles) form the atrium [74]. In several teleosts, there are two arcuate fans of muscular trabeculae (19-35 μm in diameter), these arise at the atrioventricular ostium and create a mesh like network, which give the atrium wall the trabecular appearance. A subepicardial, thick layer of collagen surrounds the atrial myocardium, and the atrial trabeculae is encircled by collagen. Trabecular collagen is generally more abundant in the atrium than in the ventricle, and it probably helps to support the atrial architecture. However, in terms of chamber contraction and distension, the significance of this feature is unclear [74, 75].

2.2.3 Atrioventricular Region (AV)

The atrium and ventricle are connected to each other by an area in the heart known as the atrioventricular region (AV) region. In different fish groups, a cardiac tissue ring which supports AV valves, forms the AV region [76]. AV muscle is surrounded by a collagen-rich connective tissue which explains the electrical insulation and the delay in the electrical conduction of the heart [74, 76, 81]. Around 80% of the teleost heart has completely trabeculated ventricle architecture, and a distinct ring of compacted myocardium forms the AV region (Figure 2.3). This compacted myocardium is vascularized in most teleost species, and contains different amounts of elastin and collagen [74, 75]. The amount of collagen and elastin and the AV myocardium thickness vary widely among species [81−83]. As shown in (Figure 2.3A,C,G) the ring of AV muscle can appear very robust, show an intermediate appearance (Figure 2.3F) or it can be a delicate strand of muscle (Figure 2.3B,E) [74].

A ring of connective tissue isolates partially the AV muscles from the ventricular and atrium musculature as shown in (Figure 2.3A–D). The connective tissue appearance also varies widely between species. In most species, it can be thick or compact and apparent regardless of the thickness of the ventricular trabeculae and the thickness of the AV muscle (Figure 2.3A,D) [74] or it can be formed by collagen with loosely arranged strands (Figure 2.3B). Furthermore, in some species such as the Artic species (Arctogadus glacialis), it is practically absent (Figure 2.3E) [81].

Continuity between the pectinate muscle of the atrium and the AV muscle is always present (Figure 2.3A,D) and the continuity between the ventricular trabeculae and the AV muscle is observed in more discrete areas (Figure 2.3A). Moreover, in the Arctic and Antarctic species, the AV region is a rich nerve plexus (Figure 2.3G) [32, 74].

Generally, two leaflets form the AV valves. These leaflets contain large amounts of connective tissue and numerous cells grouped into a dense core [81]. Within the leaflet, there is a wide variation between species in the cell number and morphology and in the extracellular material amount [84].

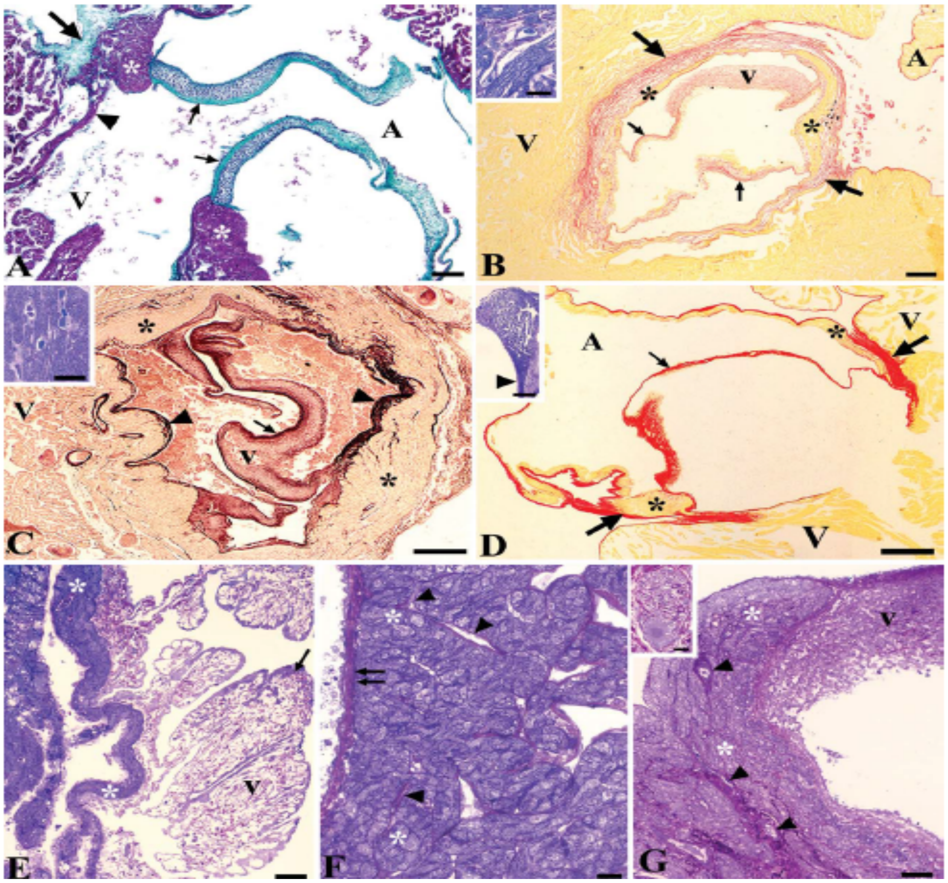

Figure 2.3: The histologic and histochemical characteristics of the atrioventricular (AV) region in the fish hearts with entirely trabeculated ventricles. Note: (A is the atrium, V is the ventricle, v is the AV valve, asterisks refer to the muscle ring of the AV, large arrows refer to connective tissue surrounding the AV, small arrows refer to the valve fibrosa and arrowhead refers to trabecular with the AV muscle connection). A-G are showed the variety structure of the AV muscle ring between different species, where, A: Serranus cabrilla, B: Arctogadus glacialis, inset: Solea vulgaris, C: Diplodus sargus, inset: Sparus pagrus, D: Periophthalmodon schlosseri, inset: Detail of the AV muscle ring, the vascular outlines are clear in the atrial portion but not in the ventricular (arrowhead) portion, which is very thin, E: Chaenocephalus aceratus, F: Mullus surmuletus. Collagen underlines both the subendocardium of the sinus wall (which is indicated by double arrow) and the endocardium prolongations (which is indicated by arrowheads) in the AV muscle. G: Dissostichus mawsoni, inset: A nerve showing a large Schwann cell. Scale bars: 100 µm in A, 200 µm in B, 20 µm in inset B, 250 µm in C, 20 µm in inset C, 250 µm in D, 100 µm in inset D, 50 µm in E, 20 µm in F, 50 µm in G, 20 µm in inset G, adapted from [81].

2.2.4 The Ventricle

The teleost heart ventricle chamber varies widely between species (Figure 2.4) [74]. This assertion can be applied to all fish heart ventricles which show considerable species variability depending on the external shape of the ventricle, the relative mass, the coronary distribution and the histology [78]. There is no typical shape, mass or vascular network to ventricle in fish, therefore, some authors have grouped the ventricle into broad categories [74, 78, 84]. However, these categories reflect functional rather than phylogenetic correlates [84], and also the ventricles very often do not quite fit into any particular category, this is true especially when data between different categories are crossed [74]. However, divisions which are based on the external shape of the ventricle [78], or on the degree of vascularization and muscularization of the ventricular wall, have proven useful [80].

The different external ventricular shapes have been grouped into three main categories: tubular, sac-like, and pyramidal [85] (Figure 2.2 and Figure 2.4).

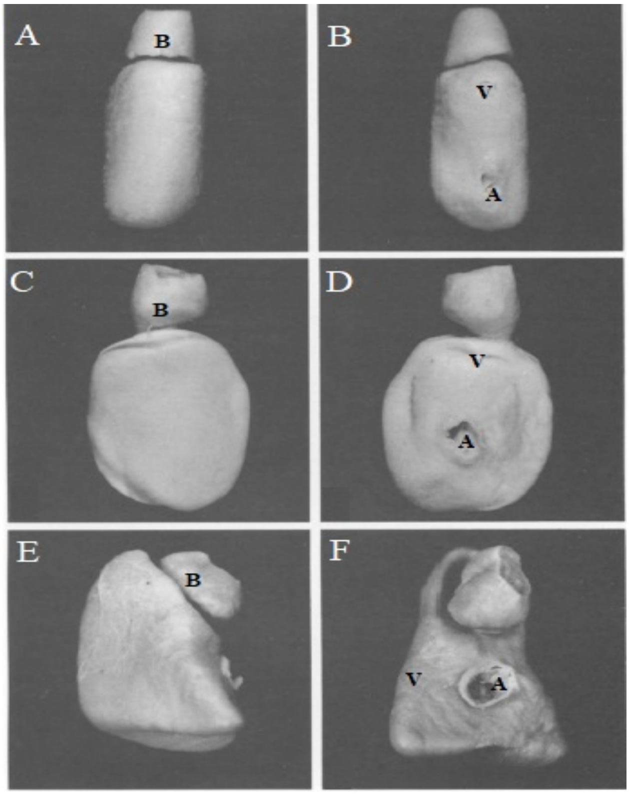

Figure 2.4. Different heart shape from three fish species. It shows hake (A, B), angler fish (C, D) and sea bream (E, F) hearts with a ventral (A, C, E) and dorsal (B, D, F) views of each specie heart. A: Atrioventricular orifice. B: Bulbus arteriosus. V: Ventricle. Note the different ventricle shape between species as tubular, saccular and pyramidal in hake, angler fish and sea bream fish, respectively, adapted from [80].

The saclike ventricle is the most common type of ventricle in fish (Figure 2.2B). It has a rounded shape with an indistinct apex [75, 78], and it is ventral to the bulbus arteriosus in all species. Saclike ventricles are encountered in many species such as *Argentina silus*, *Macrorhamphosus* and *scolopax* (Figure 2.4C,D). The tubular ventricle is found only in fish that have an elongate body; it has an almost cylindrical cross-section and lacks a ventral apex. This ventricle lies in the same longitudinal axis as the bulbus arteriosus. Tubular ventricles are found in just a few species such as *Merluccius merluccius* and *Phycis blennoides* [78] (Figure 2.4A,B).

The shape of the pyramidal ventricle is like an inverted pyramid with a base of triangular which is approximately equilateral proportions. The pyramidal ventricle is orientated so that the caudal aspect of the ventricle is formed by one side of the triangular pyramidal base and therefore the rostral ventricle aspect is angular (Figure 2.2A,C and Figure 2.4E,F) [78]. The pyramidal ventricle lies ventral to both atrium and bulbus arteriosus. Earlier studies (see [78, 86]) have shown that all species that have ventricles with pyramidal shape possess a myocardium in the outer layer [80].

Pyramidal ventricles have several functional implications, such as, an active life style, a high output of work and a robust ventricular wall. This type of ventricle is present in the salmonid, scombrid families and the very active tuna. However, in many species, such as in members of the sparid and serranid families and in the Antarctic teleosts, the presence of a pyramidal ventricle does not correlate with either a very active lifestyle or a robust ventricle [78, 86].

Depending on the extent of myocardial vascularization, on whether the ventricle presents a compact layer and on the relative thickness of the compacta, there is another heart classification [81, 86, 87]. According to this classification, there are four types of heart (Figure 2.5). Type-I hearts lack a compacta layer and have entirely trabeculated ventricles and no capillaries, while in the other heart types, the ventricles present both an external compacta (the epicardium layer which is formed of myocardial cells, that are arranged into bundle layers which appear more complex and thicker in more athletic fish [75]. These bundles are aligned in different directions and form interrelated loops and coils, which provide the structural basis for developing high blood pressures), and an inner spongiosa (the endocardium layer which is formed by crisscrossed arrays of thin muscle bundles that interlace in a complex meshwork, which gives the internal surface of the spongiosa its spongy appearance [75]).

Type-II hearts have vessels in the compacta but not in the spongiosa, while in type-III hearts, vessels reach both the compacta and the spongiosa and in type-IV hearts, the coronary circulation is found in both spongiosa and compacta, which is similar to that of type III. However, the difference between them is that in type IV a large proportion, more than 30% of the ventricular mass is formed by a compacta [87].

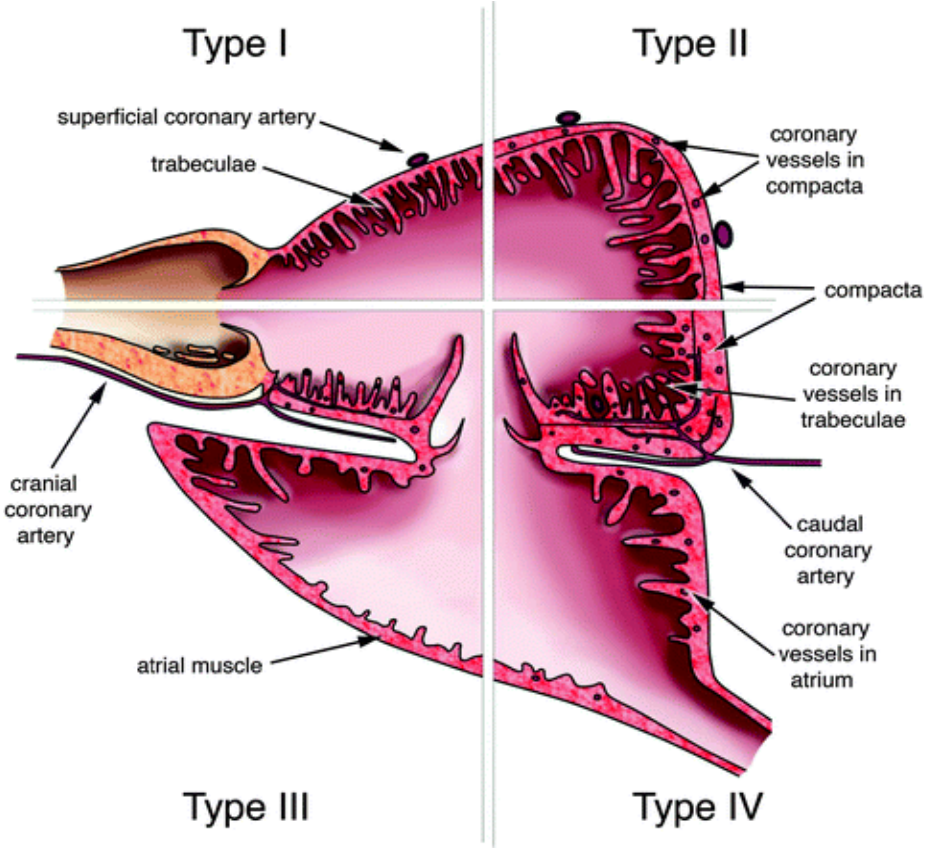

Figure 2.5: Representation of the main characteristics that categorize the four types of ventricle in fish. The fundamental anatomical design of the fish heart has been classified into quadrants. Each quadrant clarifies specific characteristics of a given ventricle type. Type I recognizes with a single myocardial type (spongiosa) with a lack of capillaries in the ventricular muscle. Type II recognizes with two layers of muscle in the ventricle (inner spongiosa and outer compacta), only the outer compacta possess capillaries and a coronary circulation. Type III is analogous to type II except that capillaries are shown in both the spongiosa and compacta. Type IV recognizes with a larger percentage of the ventricle as the outer compacta layer, adapted from [88].

Close to 80% of teleost ventricles belong to Type-I hearts as they are entirely trabeculated [78] (Figure 2.6A). The trabecular network has been described as a highly organised system of trabecular sheets and small lumina which radiate outward from the main ventricular lumen. (Figure 2.6B) [89]. Toward the ventricular periphery, there is a progressive decrease in the size of the lumina. In the spongy component of ventricles that have compacta, a similar pattern is observed [75]; this architectural arrangement has been observed in just a few species. Under this architectural arrangement, the ventricle appears in a multi-chambered segment that is formed of a small number of lumina which are separated by trabecular sheets. The important functional implication of this arrangement is that the highest amount of stress would be supported by the main ventricular lumen; therefore, the stress toward the periphery would be progressively attenuated. Enough contractile force would be produced by the trabecular sheets and the blood squeezing would be facilitated by the communication between the different lumina [74].

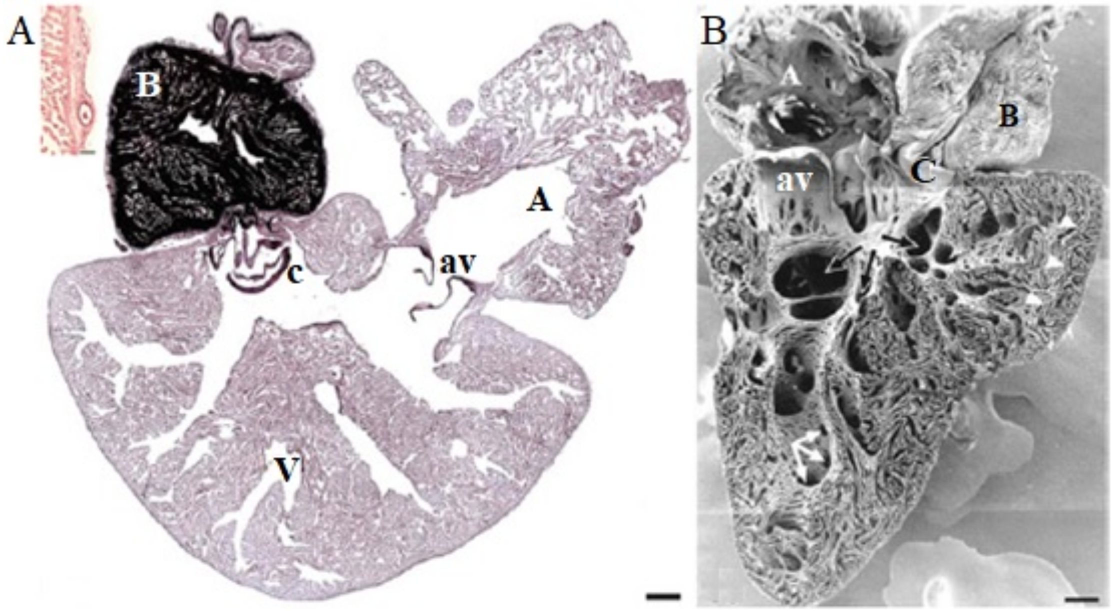

Figure 2.6: Hearts with entirely trabeculated ventricles. A: *Balistes carolinensis*, where the ventricle (V) is totally trabeculated and has saccular shape while the atrium (A) demonstrates thin trabeculae which originates from the AV orifice, inset: Coronary vessels details in the ventricular subepicardium. Note: av, atrioventricular valves; B, bulbus; C, conus and c, conus valves. B: The *Sparus* auratus's heart left side which is presented from the right. The trabecular lumina and sheets (*white* and *black arrows*) radiate outward from the main lumen of the ventricle and become smaller (*white arrows*) near the periphery where a system of single trabeculae is obtained originally from the trabecular sheets and reached the outer myocardial layer. Scale bars: (A) 100 µm; inset*,* 20 µm; (B) 50 µm, adapted from [81]. Many studies have reported that coronary vessels are almost absent in the ventricles of Type-I hearts. They are thought to be present in just a few species of temperate teleosts, while in others, such as stenothermal species, they are mostly absent. However, in most examinations of Type-I hearts vascular profiles are shown in the atrioventricular segment and conus arteriosus [90].

Overall, vessels of the ventricular subepicardial do not appear to form a very rich plexus because they are not very numerous. Thus, their presence may have been underestimated and also the exact role of these vessels in this type of heart is unclear; therefore, it is assumed that the blood flowing through the ventricular chamber supplies myocardial cells in the entirely trabeculated ventricles. Both the compacta and spongiosa that belong to type-II hearts appear in the ventricle of many other teleost species [74] (Figure 2.7).

The thickness of the teleost compacta is quite variable between species; it may range from just a two- to three-cell-thick layer (as in *Echiicthys vipera*) to occupying a large part of the ventricular thickness (as in tuna), and it might vary from apex to base [91]. Moreover, the compacta proportion varies with growth and changing seasons, but not with the exercise (physical activity) [74]. The different morphological arrangements depend on the specifics of the heart design, not on the distinct characteristics of the myocardial cells [74].

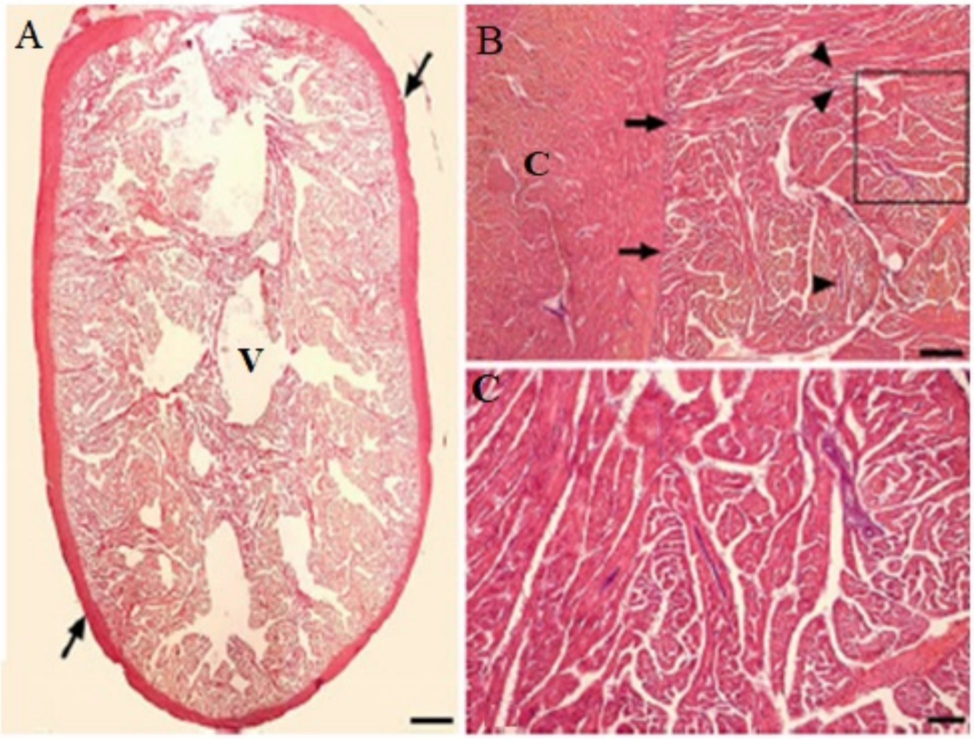

Figure 2.7: Ventricular organization in hearts with its two layers, spongiosa and compacta. A: The ventricular chamber (V) from Oncorhynchus mikiss fish. The outer compacta that limits the ventricle is indicated by arrows. B: The ventricular structure of Thunnus alaunga. The compacta (C) is organized into bundles presenting different orientation. The compacta-spongiosa boundary are indicated by arrows. Arrowheads shows the numerous vascular profiles of the spongiose. C: Detail of the boxed area in (b) and coronaries of different sizes are obvious. Scale bars:(A) 1mm: (B) 300µm: (C) 100 µm, adapted from [74].

2.2.5 The Outflow Tract: the Bulbus, the Conus, and the Conus valves

The outflow tract (OFT), which is located between the ventricle and the beginning of the dorsal aorta, represents the morphological division of the heart. Two segments, a proximal (muscular conus arteriosus) and a distal (arterial bulbus arteriosus), form the OFT in most primitive fish [92, 93]. In several other ancient fish, such as lampreys and hagfishes, the OFT anatomical composition is not clear, but most uncertainties appear to derive from partial observations [92].

Different studies have revealed that the OFT of all primitive fish follows the same general rule, for instance, ancient teleosts show a conus and a bulbus which is similar to that of primitive fish. The conus varies in length and contains up to two valve rows, with a total of four to six valves which regulate the ventricular flow dynamics [78, 92].

In addition to the conus, a distal outflow segment called the bulbus arteriosus is present in the hearts of ancient teleosts. This contains connective tissue and elastic fibers and it opens in the ventral aorta. By contrast, the modern teleosts OFT has classically been described as being formed solely by the elastic bulbus arteriosus. Thus, valves of the OFT were named bulboventricular valves [74].

The prominent bulbus arteriosus in modern teleosts dominates the morphology of the heart outflow (Figure 2.2). As the bulbus is an elastic chamber, it can expand during ventricular ejection in order to store a large part of the cardiac stroke volume. A steady flow of blood toward the gills is achieved by the gradual elastic recovery, which helps to prevent damage to the delicate gill vasculature [94].

In most bulbus, the external shape varies from pear-shaped, to elongated, to thick and robust (Figure 2.2). The wall of the bulbus contains large amounts of elastin material and an external (subepicardial) collagen layer and it is organized into layers. These layers are the endocardium, the endocardial ridges, the middle layer, the subepicardium, and the epicardium [75, 94] (Figure 2.8A,B).

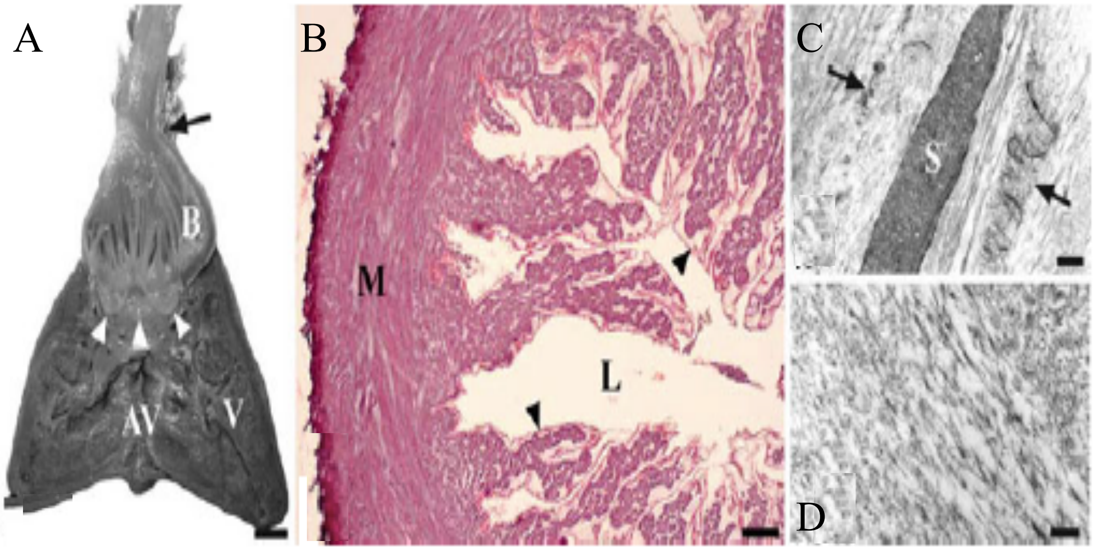

Figure 2.8: Conus and bulbus in different teleost species. A: Internal structure of *Thunnus alalunga* heart, the regions of the outflow tract, the ventricle (V), and the atrioventricular tissue (AV) can be showed and the bulbus (B) shows longitudinal ridges. Arrow shows the boundary of the cranial bulbus that relates to the pericardial insertion. Arrowheads illustrate the conus aids three semilunar valves of approximately equal size. The AV valves guard the AV orifice. B: Cross-section of the bulbus of *Trigla lucerna* species. Arrowheads show the ridges jut into the lumen (L) and are covered by endocardium. M is the middle layer includes large amounts of extracellular material. C: Transmission electron microscopy (TEM) micrograph of the bulbus middle layer of the *Anguilla Anguilla* species. S is the smooth muscle cell which is surrounded by fibrillar and elastin material interspersed with collagen fibers (indicated by arrows). d: TEM micrograph of the bulbus middle layer of *Trematomus bernacchii* species. A filamentous network forms the extracellular matrix collagen and elastin are absent. Scale bars: (a) 0.5 µm; (b) 100 µm; (c) 1 µm; (d) 0.5 µm; (c) [74].

The presence of ridges characterises the inner surface of the bulbus (Figure 2.8A,B). The ridges are longitudinal columns which occupy the entire bulbus length (Figure 2.8A). The ridges vary between species; they may be very prominent (Figure 2.8A,B) or much more discrete [95].

Smooth muscle cells and variable amounts of elastin can be found in the middle layer of the bulbus. In some species, such as eel, there are a few collagen layers interspersed with the elastin material [81], and blood vessels, nerves and collagen bundles are also observed in other species such as tuna, however, in species, like Antarctic teleosts, the elastin material is replaced by a fibrillar network (Figure 2.8D) [74, 93, 95].

A general description of the subepicardium is a thin layer rich in elastin and collagen, vessels, nerves and fibroblasts [81]. However, the bulbus subepicardium layer can be more complex in some species where it contains plasma cells, lymphocytes, and dendrite-like cells and has been thought to be involved in the development of the humoral immune response [96].

The “windkessel” function of the bulbus can be affected by a number of factors which may have specifically adapted the fine bulbus structure to comply with. These factors are lifestyle, cardiovascular dynamics, range of diversification and ecophysiology [74].

As stated above the conus arteriosus, present in ancient teleosts, was believed to have disappeared in modern teleosts, and the loss of conus was considered to be a direct consequence of heart evolution [78]. However, in the last decade, evidence raised indicates that the conus has not disappeared at all in the heart of modern teleosts [74].

The conus arteriosus is a distinct anatomical segment that is interposed between the ventricle and the bulbus arteriosus. It is easily recognised in hearts whose ventricles lack a compact layer while it is difficult to discern in hearts possessing a compacta. A compact myocardium forms the conus and it contains more laminin, collagen and elastin than the ventricular muscle. In some cases, vessels can be found in the conus even when the neighbouring myocardium is not vascularized [81]. The outflow valves, which are known as conus valves, are supported by the teleost conus arteriosus [92].

Different numbers of conus valves have been discovered in different teleost species. For instance, most teleosts possess a single row of two (left and right) pocket-like leaflets while only a few species, those pertaining to the order of the Elopiformes, show two valve rows, and in modern teleosts, a third valve may appear on the ventral or the dorsal side of the conus, however, this valve is mostly rudimentary [97].

2.3 Fish Cardiac Circulatory Blood System

In the physiological machinery, one of the most important components is the cardiovascular system which maintains homeostasis of the animal body. The role of the cardiovascular system is various and ranges from the form of circulating hormones as a carrier of information, to being involved in the hydromineral balance and temperature regulation. However, supplying O_2 and nutrients and removing CO_2 and metabolic waste products (as the processes of the cellular metabolic) from the body is the most fundamental role of the cardiovascular system [98]. The common features between the fish and mammals' cardiovascular systems are a chambered heart with a myogenic pacemaker, that supplies blood into a closed arteries system, and a venous system which returns blood to the heart (Figure 2.9A). However, there are many differences between them relate to their respective respiration modes [98]. A typical teleost fish is characterised by a single circulatory system (Figure 2.9B) that supplies the branchial vasculature from the heart directly with an arterio-arterial respiratory route supplying blood to the systemic circuit directly from the gills, whereas a divided blood system is found in the heart of mammals and birds (Figure 2.9C). This means the circulatory blood system in mammals heart has separate systemic circuits and pulmonary, whilst in fish, the branchial circulation is drained by a subsidiary arteriovenus route [77].

In teleost fish heart, venous blood enters the sinus venosus from the periphery of different parts of the body through the paired ducts of cuvier before entering the atrium. When atrial contraction, blood is pushed to fill the ventricle which can also be filled directly by the inflowing of blood from the central veins during diastole [99]. There are no valves between the sinus venosus and the ducts of cuvier, while large valves guard both the sino-atrial and atrio-ventricular junctions [81]. The ventricle pumps blood into the ventral aorta via the highly compliant bulbus arteriosus. The four pairs of afferent branchial arteries are formed by the split of the ventral aorta and these pairs perfuse the gills where gas exchange occurs.

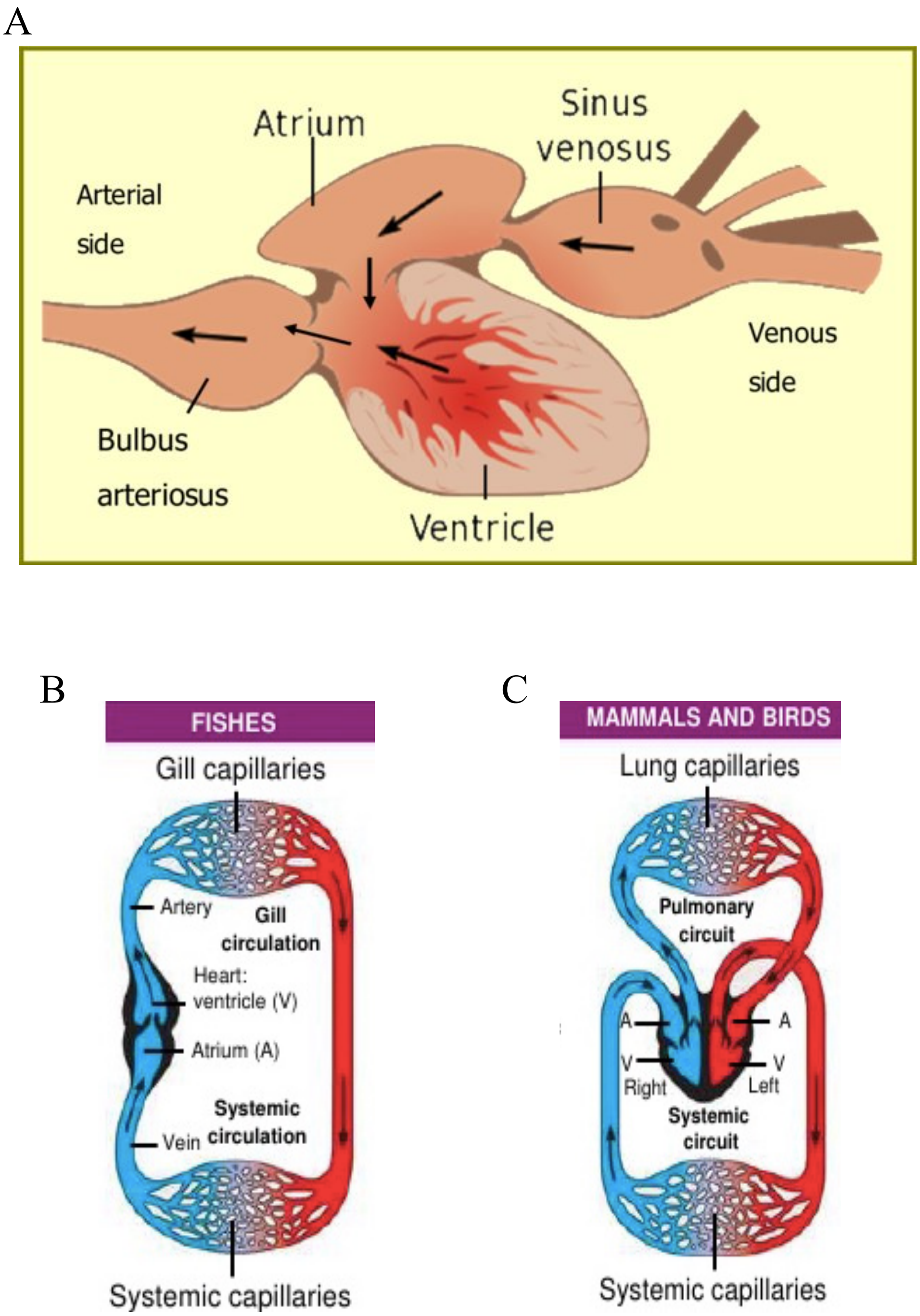

Figure 2.9: The cardiovascular system of the teleosts fish heart and mammals heart. A: Teleost fish heart [100], B and C: The blood circulatory system in fish and mammals (and birds), respectively, adapted from [100].

In the gills, the arterio-venous and arterio-arterial pathways are the major pathways. Blood directly flows over to the compartment of the central venous and provides the tissues of the gills with oxygen and nutrients in the arterio-venous pathway, while in the arterio-arterial pathway, oxygenated blood leaves the gills to the other parts of the body via four pairs of efferent branchial arteries [84, 101] (Figure 2.10).

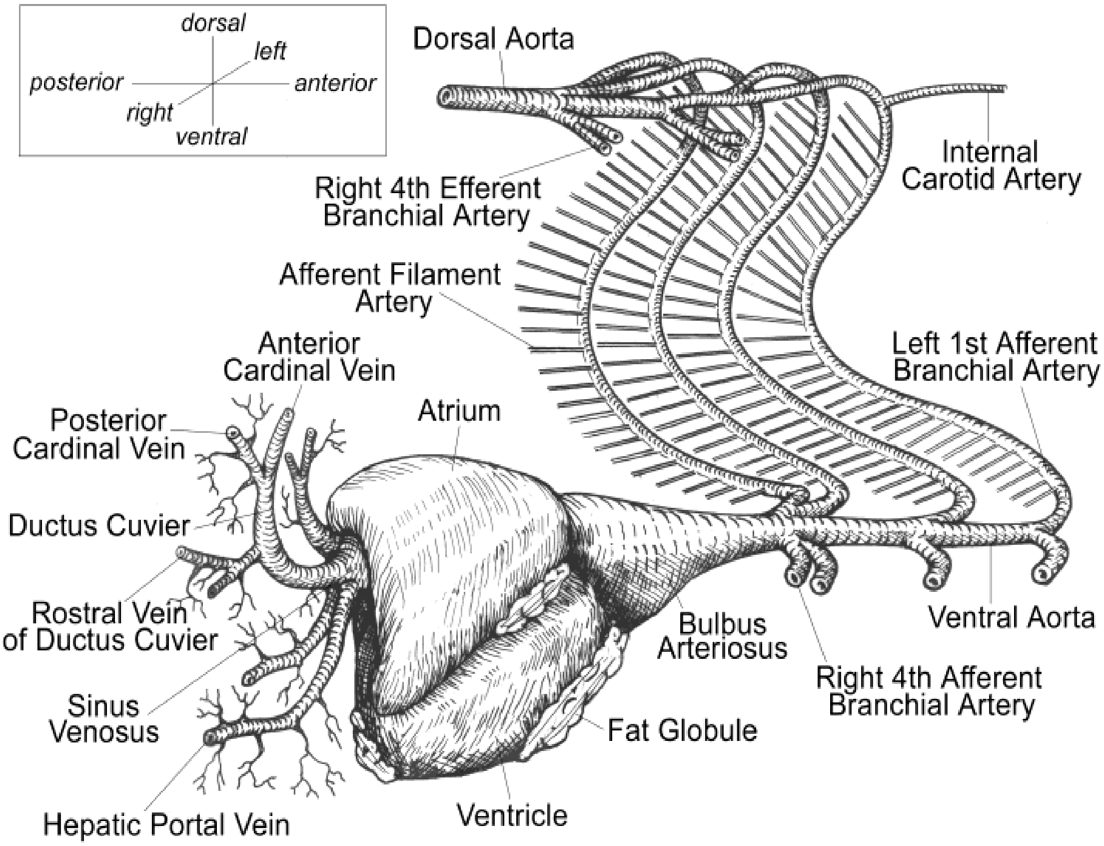

Figure 2.10: A posteroanterior view of a zebrafish heart illustrates the main vasculature in the cardiac region. The venous return from the sinus venosus is received by atrium which is connected to the hepatic portal veins and ductus Cuvier. The heart pumps the blood to the bulbus arteriosus alongside the definite chambers of atria and ventricle. Then the ventricle forces the blood into the ventral aorta which gives off paired vessels (afferent branchials) that curve upward between the consecutive gills to rejoin (efferent branchials), forming the dorsal aorta. The boxed zone signifies the coordinates presenting the orientation of the heart [84].

2.4 Initiation of the Heart Beat

The heart beat is initiated automatically by an electrical excitation pulse or action potential. This excitation begins in a group of active pacemaker cells which further spread to the atrial and ventricular muscles in order to evoke a systematic contraction of the cardiac muscular chambers. In fish heart, the pacemaker cells are located in the sinoatrial junction or sinus venosus, while in the mammals heart, the pacemaker reign is known as sinoatrial node and located in the wall of the right atrium [20].

The spontaneous diastolic depolarization is responsible for the rhythmic activity of the cardiac pacemaker cells. A complex interaction between several ion transporters and ion channels generates a net inward current through the sarcolemma of the pacemaker cells which evokes the pacemaker AP [20, 77, 102, 103].This net inward current results due to the activation of inwards currents channels which include Na^+-dependent current (I_{Na}), L- and T-type Ca^{2+} currents (I_{CaL}, I_{CaT}), a hyperpolarization activated pacemaker current (I_h or I_f), and the activation of the outward current channels, such as the delayed rectifier K^+ currents (I_{Ks} and I_{Kr}) [40, 77, 103, 103, 104].

Additionally, other cell membrane mechanisms including intracellular Ca^{2+} stores of the sarcoplasmic reticulum (SR), sodium-calcium exchanger (NCX) and sodium pump also appear to be involved in cardiac pacemaking process [105−107].

It has been found that large number of ion channels and transporters are involved in pacemaker function of the vertebrate heart. However, there is no consensus about the underlying mechanism of the pacemaker function.

This is because in some fish species the diastolic depolarization can be driven by deactivation of the delayed rectifier current(s) [46, 77, 106, 107], whilst in others, a dominant roles are played by the spontaneous release of $Ca^{2+}$from the SR and subsequent activation of the sarcolemmal NCX [108], and in another the hyperpolarization-activated "pacemaker" current is in the main position [20]. Earlier studies [91, 109, 109]have mentioned that thermal acclimation strongly modifies the heart rate in fish, which seems to be mediated fundamentally by temperature-dependent variations in the autonomic nervous system activity [14, 77].

2.5 Morphology of Teleost Cardiac Myocytes

Cardiac myocytes, also known cardiac working cells, are the muscle cells occupying most of the myocardial mass. Cardiomyocytes vary in shape and size between species and also depending on the heart region from which they are taken [110]. For example, the morphometric characteristics of fish cardiac myocytes vary between species, and the myocytes in the same chamber of the heart are different in size, as seen in some teleosts where the compacta have larger diameters than the spongiosa [111].

Trout fish cardiomyocytes are narrow and long in shape and mainly mono-nuclear. The spindle shape of the trout cardiac cells is thought to be beneficial in heart physiology. In the fish cardiac cell, the narrow myocyte makes the ion diffusion in a shorter distance, which facilitates adequate contraction in the lack of T tubules. However, a smaller diameter probably means a slower conduction velocity because of the higher electrical resistance. In rainbow trout fish with a 300g in mass, ventricular cardiac cells dimensions are 180 and 8µm in length and width, respectively. While the Atrial cardiac cells have similar length to the ventricle with a width of ~6µm. The surface area is 3000 – 4000µm2 in ventricle and a relatively smaller with 2500 – 3000µm2 in atria [80].

In mammals such as human, cardiac myocytes normally have a cylindrical shape and 50-100 µm in length [112], however, both of human and trout cardiomyocytes have almost the same structure and similar function. Intercalated discs connect the cardiomyocytes making adjacent cells strongly connected mechanically and electrically. Some cardiac cells are noncontractile, while most are the primary source of the heart's contractility. The contractile cells (or working myocardium) have main purpose to contract and usually found in the atria and ventricles walls, and they have far more contractile elements than those of the specialised CCS [81] whose main function is not contraction but for rapid conduction of the heart electrical impulses, and are normally smaller than working myocardium cells [113]. Each myocyte is surrounded by the sarcolemma, or the plasma membrane which is impervious to ions except through specific configurations (discussed in details in the next Sections). Within the cardiac cell, there is another important membrane structure is the sarcoplasmic reticulum (SR) which has a specific function in regulating the concentration of the cytosolic Ca2+ and as important implications for Ca^{2+} dynamics and contraction [114]. The SR is sparse in fish hearts and the sarcolemma (SL) lacks the T- tubule system (which is an extension of the surface membrane into the cell allowing the AP to spread into the cell and the interaction of the intracellular Ca^{2+} regulation system and the L-type Ca^{2+}channel) [78] (Figure 2.11). Couplings between peripheral SR with the SL can be observed that are likely to be ryanodine receptors (RyR) [111].

In some fish species, the myofibrils are positioned in the peripheral part of the cell near the SL, with mitochondria being more centrally positioned [86]. This facilitates the calcium diffusion from the extracellular when the T-tubule system is absent. Myofibrils are found in ventricular myocytes in larger amounts than in atrial myocytes [86].

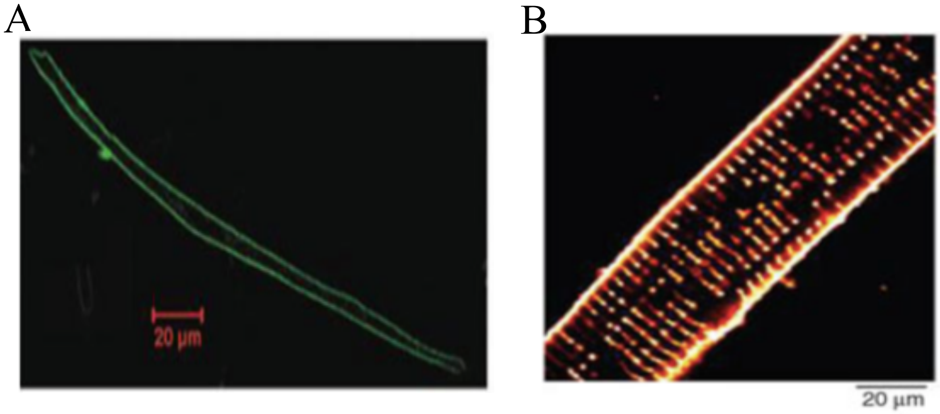

Figure 2.11: Ventricular myocytes isolated from teleost fish (adult rainbow trout (*Oncorhynchus mykiss*)) in (A) and mammal (adult dogs) in (B). Note the T-tubular structure lack in the teleost ventricular cells (A) and can only be seen in adult dog cells as a transverse membrane network (B). Modified from [87].

2.6 Cardiac Electrophysiology

2.6.1 The Cell Membrane

The cardiac cells are bounded by the cell membrane or the sarcolemma which is a thin phospholipid bilayer acts as a barrier for diffusion by allowing the interaction between the intracellular and extracellular space (Figure 2.12). The sarcolemma is composed of different proteins which comprise a hydrophilic head that interacts with the fluids on each side of the cell membrane, and a hydrophobic tail. Difference in charge between the intracellular and extracellular spaces generates a potential difference across the membrane of the cell. This is signified as the membrane potential and indicated V_m which is described as the difference between the internal and external potentials, as such $V_m = ui - ue$, where u, i, e are the potential, intracellular and extracellular, respectively. [114].

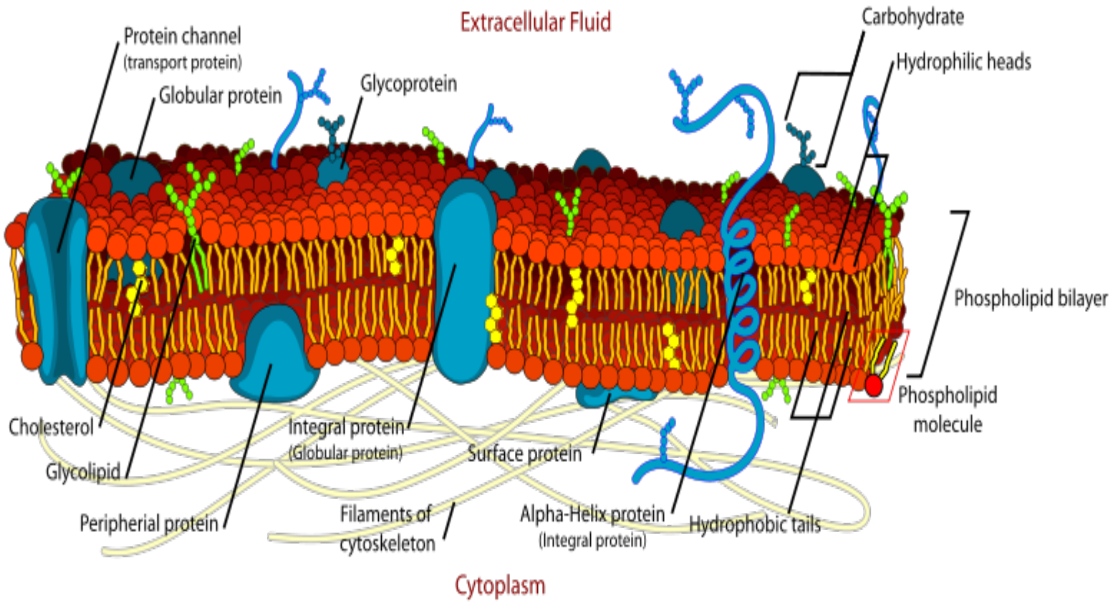

Figure 2.12: Representation of the cell membrane, or sarcolemma (Plasma membrane). Demonstrated the phospholipid bilayer and some of the existing proteins. Adapted from [115].

Various proteins are found within the phospholipid bilayer structure. Integral and peripheral proteins interact with the fluids in the extracellular and intracellular spaces. Charged ions can only flow into the cell or out of the cell through specialised integral proteins structure which are mainly in three different types; ion channels, ion exchanger and ion pumps. Excitability of the cardiomyocytes is the responsibility of the ion channels. All ion channels have ion selectivity which means they are permeable to merely one types of ions as in the ion channels or two types of ions as in the ion exchangers and are distributed heterogeneously across the membrane of the cell [114].

2.6.2 Ionic Channels

In the cardiac myocytes, the ion channels are the most abundant. They permit passive processes of certain types of ions without exerting force on or supplying energy to the ions themselves. The ions flow down their electrochemical gradient resulting from the ionic concentrations differences between the extracellular and intracellular spaces. Ion channels have the ability to function as allosteric proteins, they can be in open, closed, or inactive states as a result of the conformational changes of the proteins of the channel (Figure 2.13). Ion channels may have both activation and inactivation procedures, indicated as two gates which their states determine whether a current can flow through the channel or not [62, 63]. The ion flux can flow through the channel only on the condition when the activation gate is open whereas the inactivation gate is still not inactivated, and thus the channel itself is open [63].

Different stimuli can affect different channels by contributing to the opening and closing states of the gates. These stimuli include the transmembrane potential, stress, stretch and neurotransmitters. The majority of ion channels respond to changes in the transmembrane voltage and are hence said to be voltage-dependent channels or to changes in response to binding to chemical messengers and are hence said to be ligand-dependent channels and in response to changes in the membrane mechanical states and are hence said to be stretch-activated channels [62, 63].

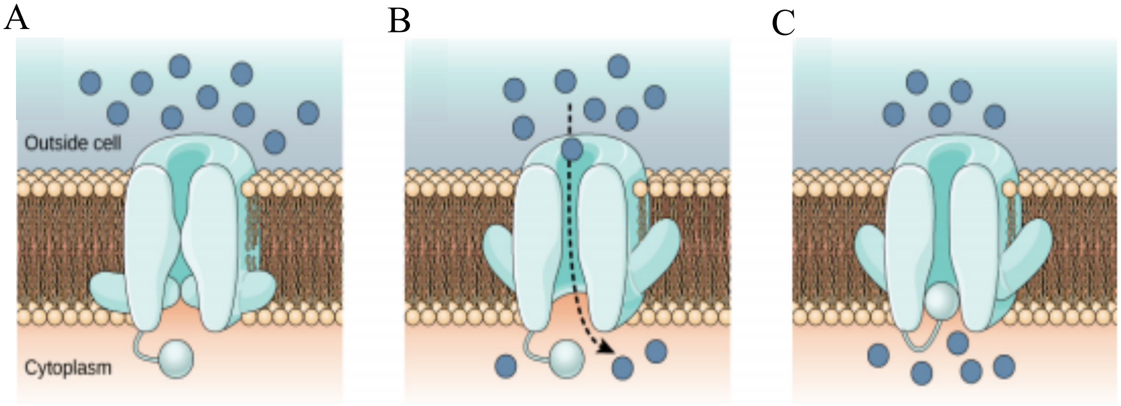

Figure 2.13: Idealised scheme illustrates a voltage-gated Na^+ ion channel. A: The channel is closed at the resting potential. B: The channel opens when electrically stimulated, allowing an influx of Na^+ ions. C: Following activation the channel briefly inactivates, no longer responding to electrical excitation. Hydrophilic portions of the lipid bilayer structure protrude into the outside cell and the cytoplasm [116].

Figure (2.13) shows three different configurations of a voltage-gated Na^+ channel. The channel is closed, at the resting membrane potential (RMP) (Figure 2.13A). During the rising phase of electrical excitation, the channel opens (both activation and inactivation gates are open), and Na^+ ions flow from outside the cell to the cytoplasm which causes the action potential upstroke (Figure 2.13B), then the channel inactivates temporarily and no longer responds to electrical stimuli (Figure 2.13C) [116].

Ionic pumps as opposed to ion channels permit active processes as they can move ions up their electrochemical gradient by an energy consuming from ATP. On the other hand, Ion exchangers can be classified as co-transporters (they are not passive or active), as they use the energy of one ion flowing down its electrochemical gradient to trigger another ion to move against it. Pumps and exchangers are both important, particularly to prevent ion concentration from building up or depletion within the cell. Thus they play a vital role in the cell cyclic ability to be repeatedly excited [116].

2.6.2.1 Ion Channel Currents

In cardiac myocytes, the main ions involved in the ion channels, pumps and exchangers are sodium, calcium and potassium (as shown in Table 2.1) and a lesser extent of chloride ions. When positive ions flow into the cell, this can be defined as an inward current. The inward currents raise the transmembrane potential to more positive values (depolarisation). While the positive ions that flow out of the cell can be defined as an outward current. The outwards currents lower the transmembrane potential to more negative values (repolarisation) [116].

Through the physiological voltage range of membrane potentials for cardiomyocytes, ion channels permeable to sodium and calcium carry inward currents, while outward currents are carried by ion channels permeable to potassium ions. Many different ion channels are permeable to ions of the comparable type and they are categorised by different kinetics and properties.

As there are many of each channel type in the cell membrane, hence the currents are determined by the net flow of ions through all of that channel type. The way of interaction of each current is discussed in the next Section [62, 63].

Table 2.1: Summarises the main currents in cardiomyocytes.

Symbol	Name	Permeability	Type
I_{Na}	Fast sodium current	Ion channel	Na^{+}
$I_{Na,L}$	Late acting sodium current	Ion channel	Na^{+}
$I_{Ca,L}$	L-type calcium current	Ion channel	Ca^{2+}
$I_{Ca,T}$	T-type calcium current	Ion channel	Ca^{2+}
I_{to}	Transient outward current	Ion channel	K^{+}
I_{Kur}	Ultra-rapid potassium current	Ion channel	K^{+}
I_{Kr}	Rapid delayed rectifying K^{+} current	Ion channel	K^{+}
I_{Ks}	Slow delayed rectifying K^{+} current	Ion channel	K^{+}
I_{K1}	Inwardly rectifying K^{+} current	Ion channel	K^{+}
I_{KACh}	Acetylcholine activated K^{+} current	Ion channel	K^{+}
I_{f}	Hyperpolarisation activated Funny current	Ion channel	Na^{+}/K^{+}
I_{NaCa}	Sodium-calcium exchanger current	Ion exchanger	Na^{+}/Ca^{2+}
I_{NaK}	Sodium potassium pump	Ion pump	Na^{+}/K^{+}
I_{Cap}	Calcium pump	Ion pump	Ca^{2+}

2.6.3 Cardiac Action Potential

The cyclically change of the transmembrane voltage results from the action of the sarcolemmal ion currents, which is known as the action potential (AP). AP can be defined as a fast rise and fall of the transmembrane voltage of working myocardial cells as a result of the ions movement through ion channels, exchangers and pumps. Myocytes from pacemaker cells like those located in the SAN in human or sinus venosus in fish are autorhythmic as they spontaneously generate ‘oscillatory’ APs. While the excitable myocytes from the working atrial and ventricular myocardium generate APs merely when stimulated electrically under normal conditions [62]. When the membrane potential in excitable cells of atrial and ventricular myocytes reaches a certain threshold value, the AP is generated and then propagates between the electrically-coupled cells like a wave [62]. The AP morphology has a large degree of heterogeneity in different heart regions and species as shown in Figure 2.14, however, the AP can be described within the same framework. In general, the AP consists of five distinct phases and each phase represents the action of one or more of the ion currents of the cell membrane.

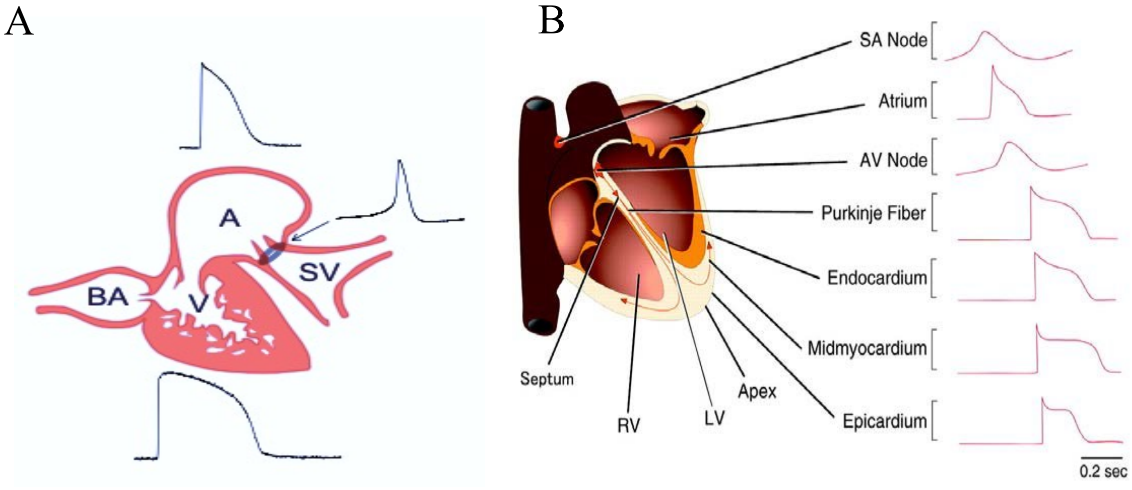

Figure 2.14: Electrical excitation of the teleost fish heart and human heart. A: Schematic diagram of teleost heart illustrates the typical action potential (AP) waveforms recorded at different reigns, where, A is atrium; BA is bulbus arteriosus; SV is sinus venosus, and V is ventricle, while the grey circle at the junction between the sinus venosus and the atrium represents the sinoatrial pacemaker, modified from [30]. B: Schematic picture of a human heart shows the visualization of normal AP waveforms recorded at different regions of the heart [117].

In spite of numerous differences between fish heart and mammals heart, the cardiac AP shares the main features between them, with the regarding of some differences aspects as will show later in this thesis.

In general, the ventricular APs are generated by spontaneous electrical activity which initiates in the atrium [69](Figure 2.14). The normal electrical excitability of the cardiac myocyte occurs as a result of the elaborate balance between the inward currents (depolarisation) and the outward currents (repolarization) (Figure 2.15). When the channels or transporters allow the positive charges such as sodium (Na^{+}) or calcium (Ca^{2+}) ions to enter the cell or enable the negative charges such as Chlorine (Cl^{-}) to exit, this causes the depolarization case, while the repolarisation case can be reached when the efflux of potassium ions (K^{+}) exceeds the sum of the influx of the Na^{+} and Ca^{2+} ions [104].

The opening and closing of Na^{+}, Ca^{2+}, K^{+} and Cl^{-} ion channels produce the cardiac AP which consists of five phases (0-4) [30, 47, 69, 118, 119], these phases are:

Phase 0

This phase is known as the rapid phase depolarization that occurs as a result of the increasing of opening sodium channels thereby increasing the concentration of sodium ions into the cell.

Phase 1

This is a rare development phase in the AP of the heart of fish and occurs as a result of the movement in opposite directions of potassium $K^{+}$and chlorine Cl^{-} ions.

Phase 2

This phase which is known as plateau phase which can be reached by achieving a balance between the Ca^{2+} ions that entering the cell (inward movement) through L-type Ca^{2+} channels (I_{CaL}) and the K^{+} ions that moving out of the cell (outward movement) through K^{+} channels (I_{Ks}, I_{Kr}, I_{K1}).

Phase 3

In this phase, the cell is in the repolarisation case due to the closing of L-type Ca^{2+} channels while the potassium channels are still open, and I_{K1} remains conducting throughout phase 4, while I_{Ks} and I_{Kr} are disappeared when the membrane potential value is restored to a voltage value from -80 mV to -85 mV.

Phase 4

Until the next stimulus which occurs by AP that propagates from the pacemaker of the cardiac myocytes, the cell remains in the resting membrane potential (RMP)[47, 120].

The cardiac AP phases (0-4) are presented in both mammals (such as human) and teleost hearts, expect phase-1 of the rapid repolarization is poorly developed or it is absent in the teleost ventricle due to the lack of the transient outward current (I_{to}) or because the completely absent of I_{to} [69], a comparison between the ventricular currents in both teleost heart and human heart is shown in Figure 2.15.

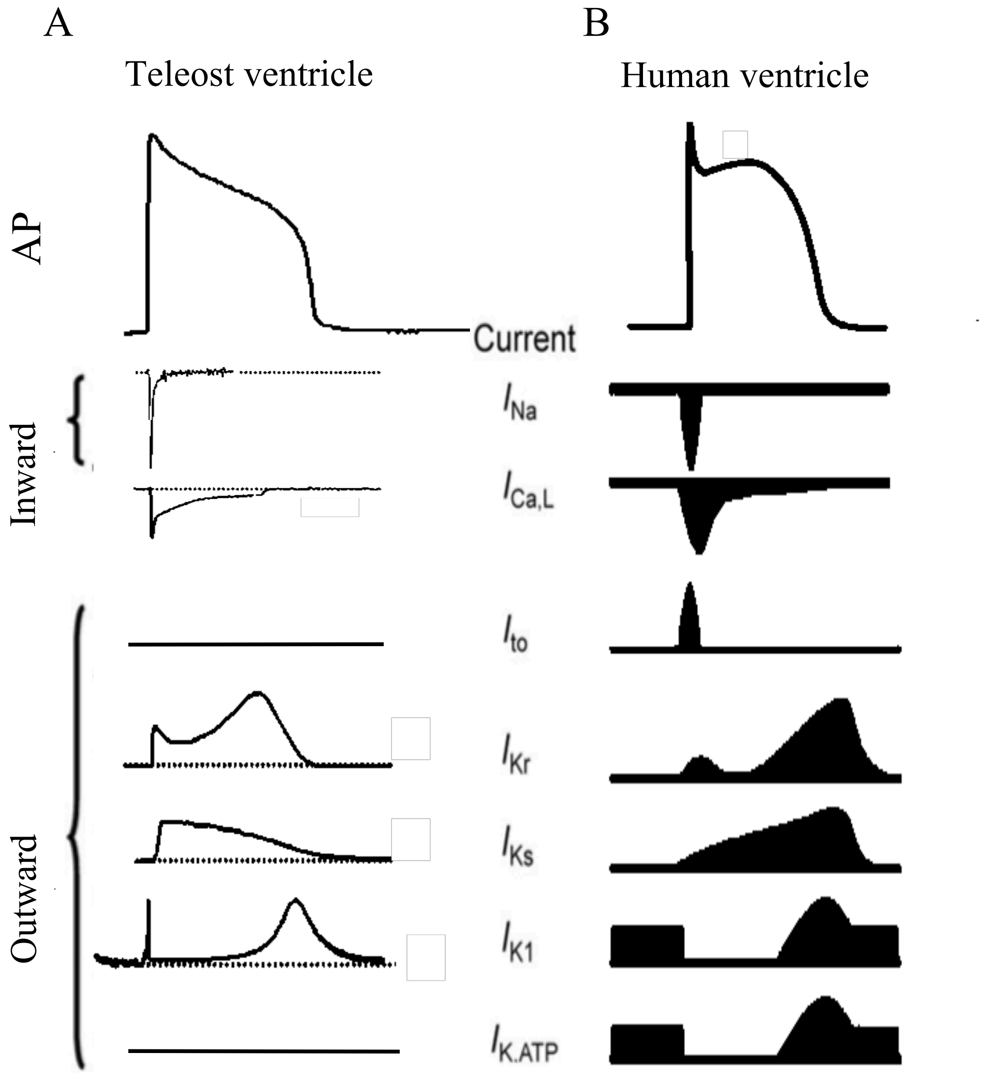

Figure 2.15: A comparison of inward and outward currents underlying the AP in the ventricular myocytes of teleost fish (A) and human (B). It should also be noted that sodium-calcium exchanger current, I_{NaCa} (not shown) plays an important role in shaping the AP as well as Ca^{2+} homeostasis. A adapted from [77] and B adapted from [121]

As illustrated previously in Chapter 1 fish is an ectothermic animal, means their body temperature altered with changing in their environment temperature. Moreover, altered the body temperature affects all the animal body organs, specifically the heart. As a result, temperature plays an important in setting the heart function in all aspects (including electrical and mechanical properties). Therefore, the electrical excitation duration of the heart varies with body temperature, which the main object of this thesis and will explained in more detail later in the next Chapters.

2.6.4 Characteristics of Action Potentials

In electrophysiology, it is essential to characterise different aspects of the cardiac APs in a consistent manner. This allows a direct comparison between the APs of different species, regions or disease states within a consistent framework. Therefore, multiple key parameters, or biomarkers that describing an AP have been proposed and widely used in this field. The most generally used biomarkers of the AP in cardiac myocytes are presented here and shown in (Figure 2.16).

Resting membrane potential (RMP): the resting diastolic membrane potential at which an excitable cell will rest if there is no stimulus, and relates to the most negative potential.

Maximum upstroke velocity (MUV): the maximum rate of change in voltage per time during the fast depolarisation (phase 0) of the AP. MUV or dV/dt_{max} is used as the start of an AP and also a measurement of cell excitability as well as I_{Na} and has significant insinuations on the conduction velocity of the action potential in tissue.

Overshoot (OS): the maximum membrane potential achieved during the upstroke of the AP.

Action potential amplitude (APA): the amplitude of the membrane potential of the AP, resulting from the sum of the absolute values of the OS and RMP.

Action potential duration (APD): a measure of the AP width in time, which is defined as the temporal interval between the upstroke until an identified percentage of total repolarisation of the membrane potential (simply, it is the time interval between the initiate of the depolarisation (by the Na^+ ions influx (phase 0)) and the end of repolarisation (mainly mediated by the efflux of K^+ ion).), i.e. at 50% (APD_{50}) and 90% (APD_{90}) are the most commonly used, as APD_{50} often to evaluate the plateau width while the APD_{90} is widely used to assess the full width of the AP and as an indication of the AP reached the terminal phase of repolarisation.

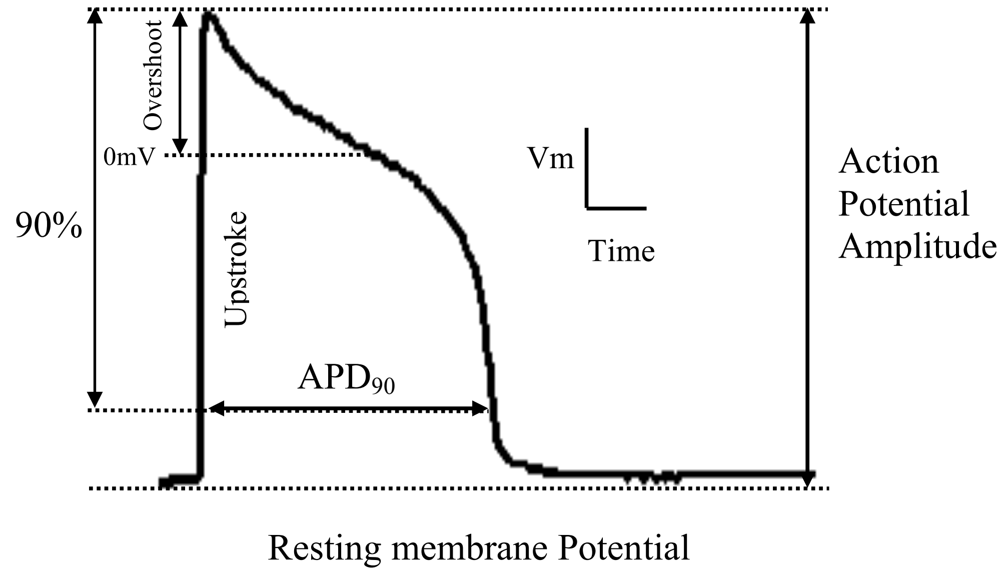

Figure 2.16: Schematic diagram demonstrates the key characteristics of the AP of the fish heart.

2.6.5 Action Potential Restitution, S1-S2 Protocol and Re-entry

The time interval between the end of repolarisation and the following membrane depolarisation is known as the diastolic interval (DI). While the total duration of APD and ID is identified as the basic cycle length (BCL) which is duration of one heartbeat and involves all events occurring from the initiation of one heartbeat to the following one (Figure 2.17A). The APD steady state restitution curves can be constructed by plotting the steady state of APD_{90} versus BCLs.

The S1-S2 simulation protocol is a widely used procedure for characterising the dynamic possessions of cardiac myocytes. A simulation protocol S1 involves repeated stimulation of a cardiac cell or tissue at fixed rates which is the BCL. The external stimulus (S1) is required to apply to the cell or tissue in the S1-S2 protocol at a selected BCL till a steady state is attained. Following this and after a certain time delay, a second (premature) stimulus (S2) is applied, as shown in Figure 2.17B.

When a prematurely stimulus (S2) applied while the cell membrane potential has not recovered yet from a previous depolarisation (S1) could generate either a slowly rising AP, or no activity at all. The period of depressed excitability is known as the effective refractory period (ERP). There are two phases of the refractory period (Figure 2.17C). The first is where no magnitude of S2 stimulus can produce an AP, this is recognized as absolute refractory period. The second is where only S2 stimuli exceeds the normal threshold and can produce an AP, this is recognized as the relative refractory period.

ERP at varying BCLs is calculated as the smallest DI for which the OS of the AP that successfully elicited by the S2 is 80% of the AP elicited by the S1 at each BCL. Restitution curve of Effective Refractory Period (ERP-R) was produced by plotting the calculated ERP against the BCLs [62]. In the heart, the ERP provides a protective role against premature stimuli at fast stimulation [63].

Moreover, restitution has significant implications on re-entry, which is the term referred to a propagating wave which self sustains through a fast circular movement. Re-entry may occur in different forms including leading circle re-entry, spiral or scroll waves (Figure 2.18). High pacing rates might be obtained from such propagation that exceed the natural pacing from the pacemaker cells. The ERP is intimately linked to re-entry by its ability to generate a unidirectional conduction block (where propagation is blocked in only one direction) which may lead to the re-entrant initiation and breaking up the regular propagation wave. Figure 2.19 illustrates a patch of cardiac tissue, where S1-S2 simulation protocol can be used. In Figure 2.19A, a planar excitation wave can be initiated when an S1 stimulus applied at one edge of the tissue, this excitation propagates across the tissue patch, and creates a gradient in the ERP which can be parallel to the electrical activation direction. Figure 2.19B shows that if an S2 stimulus is delivered to a localised region of the tissue when the upper half of the tissue is still refractory (as the ERP acts as a functional barrier to additional excitation), this produces a conduction block that in the parallel direction to planar wave propagation. Thus, the permitted propagation can be only in the perpendicular direction. Figure 2.19C illustrates the upper half of the tissue patch is excited by the outwards spreading of the initiated excitation wave once it has repolarised. Figure 2.19D shows that as the tissue area that has been applied the S2 stimulus recuperates the wave loops back to itself, forming a self-sustaining circuit ‘spiral wave’ re-entry [63].

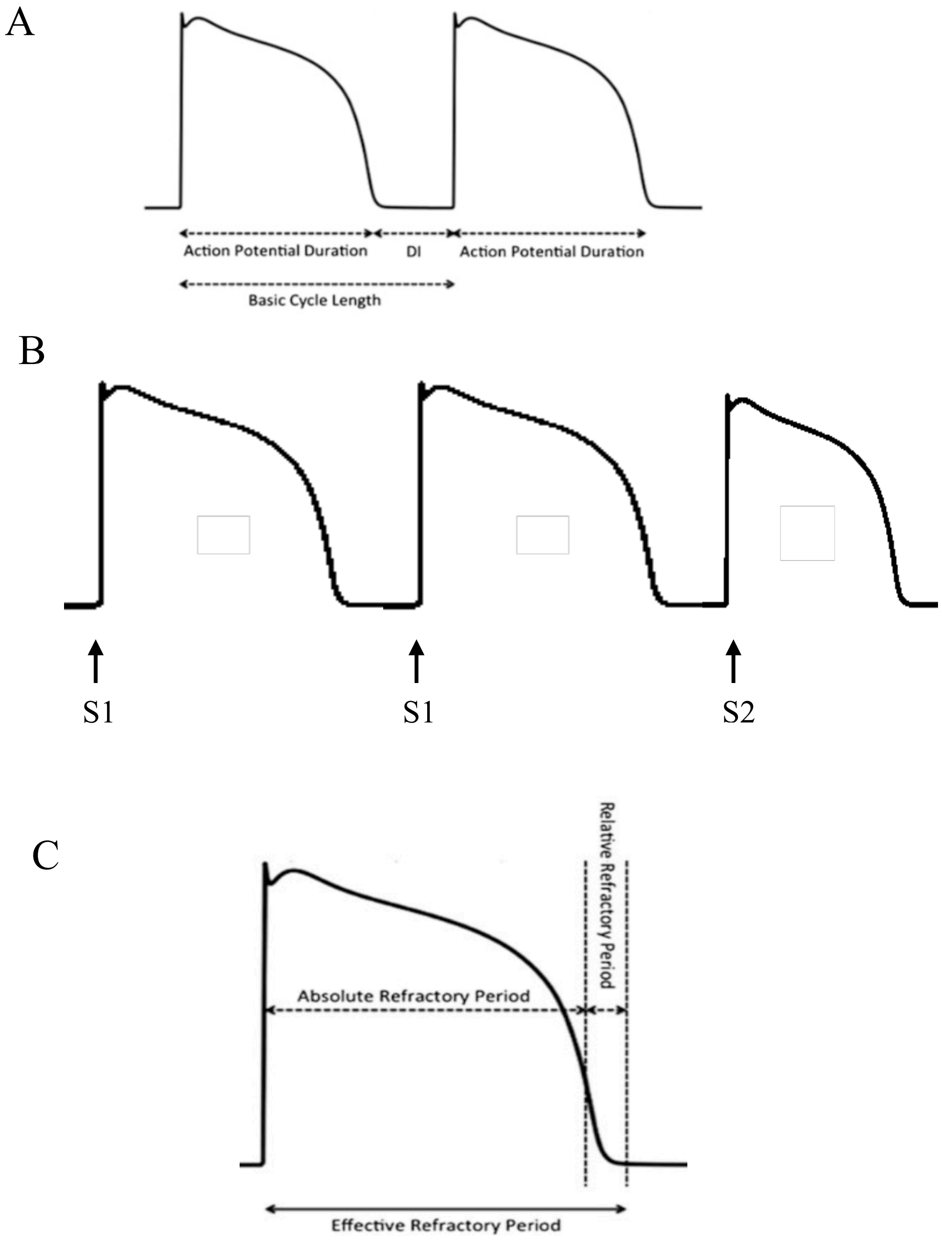

Figure 2.17: The action potential properties. A: The action potential duration, basic cycle length and diastolic interval shown for an action potential. B: A sequence of S1 stimuli that induce action potentials and an S2 stimulus applied after a particular number of S1 stimulus. C: The effective refractory period encompasses the absolute refractory period (where an action potential cannot be initiated in spite of the applied stimulus strength) and relative refractory period (where an action potential can be evoked and arising slowly) [62].

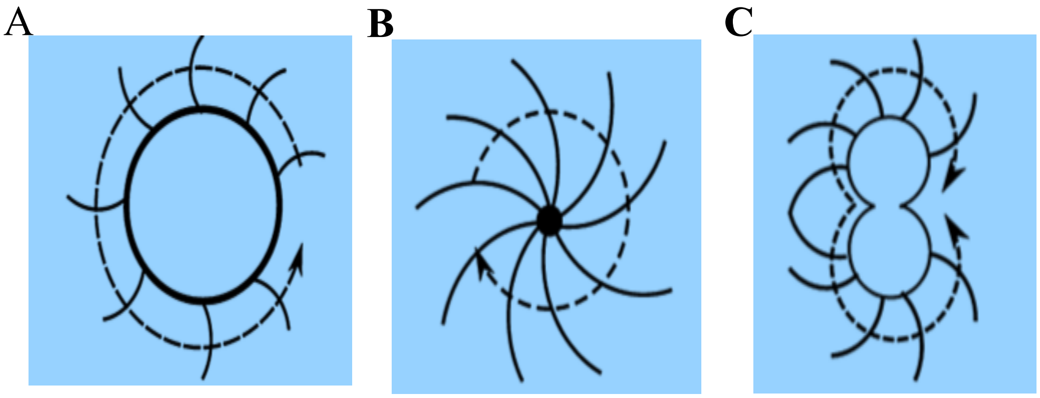

Figure 2.18: Schematic diagram of three different example of re- entry types. The direction of wavefront propagation is indicated by the dotted arrows. A: Leading circle re-entry. B: Single spiral wave re-entry. C: A figure 8 formed from two waves rotate in opposite directions, modified from [63].

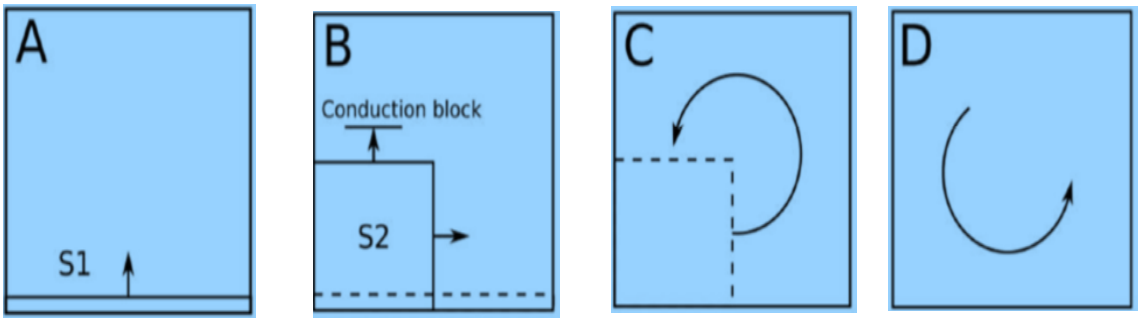

Figure 2.19: A schematic diagram illustrates the mechanism of re-entry initiation in a cardiac tissue patch using an S1-S2 protocol. A: An external stimulus (S1) applied to one edge of the tissue to initiate a planar excitation wave that propagates across the tissue. B: A second stimulus (S2) stimulus applied to a quadrant of the tissue to evoke a uni-directional conduction block, as across the tissue, the gradient in ERP causes a functional conduction barrier. C: The excitation wave stimulates the tissue upper half part as it recovers. D: As the tissue quadrant which was excited by the S2 stimulus recovers, the wave loops return on itself and form a self-sustaining circuit. Modified from [112]

2.6.6 The Calcium Cycle

2.6.6.1 Mammals Cardiomyocytes

The ions movement through sarcolemmal ion channels not only act to change the transmembrane voltage, it also alters the concentrations of corresponding ions in the intracellular space. The Ca^{2+} ions in the intracellular space mediate the contraction of the cardiac myocytes [46]. The sarcoplasmic reticulum (SR) surrounds the mitochondria and myofilaments. It also regulates the Ca^{2+}ions inside the cardiomyocytes as it acts as a store and pump for the Ca^{2+}ions. The SR membrane has similar structures to those of the ion channels and pumps found in the sarcolemma [46].

The ryanodine receptors (RyR) are analogous to voltage-gated ion channels, but depend on the calcium concentration in the intracellular space, $[Ca^{2+}]_i$, rather than the membrane potential. RyRs are located proximately close to the L-type Ca^{2+}channels and they bind with the intracellular Ca^{2+} ions cause more Ca^{2+} release from the SR into the intracellular space. The Ca^{2+} release results from the Ca^{2+} ions influx through I_{CaL} during the phase 2 (plateau phase) of the action potential. This process is known as Calcium-Induced-Calcium-Release (CICR) [112].

The Ca^{2+} released from the SR facilitates binding of Ca^{2+} to the contractile (myofilament) proteins involved in contraction. Then the Ca^{2+} is released from its binding sites on these contractile proteins into the intracellular space [122]. The Ca^{2+} ions within the SR is then pumped back into the SR by SR Ca^{2+}-ATPase (SERCA) which restores the concentration of Ca^{2+} ions within it. The remaining Ca^{2+} ions are extruded from inside the cell via the Ca^{2+}-ATPase calcium pump, ICaP and the sodium-calcium exchanger, I_{NaCa}. The change in the intracellular Ca^{2+}concentration which associates with an AP is known as the Ca^{2+} transient. The calcium cycle features, in addition to more detailed components discussed in [122], the relationship between the time course of the AP, the typical Ca^{2+} transient, and the resulting developed tension (contraction), are shown in Figure (2.20A).

In mammalian ventricular myocytes, transverse (T) tubules penetrate deep within cardiac cells. A close coupling of I_{CaL} to RyRs can be allowed by L type calcium channels along the regular T tubular network. This coupling results in a rapid and near-synchronous rise in intracellular

Ca^{2+}following electrical excitation, which initiates the CICR process and consequent contraction [63].

2.6.6.2 Fish Cardiomyocytes

The sarcoplasmic reticulum (SR) is present in all vertebrate classes studied so far including fish, amphibians and reptiles, however, the contribution of Ca^{2+} ions within the SR release to cardiac contraction varies significantly between species [46]. The cycling of SR $Ca^{2+}$is more prevailing in ventricular vs. atrium tissue, adults vs. neonates and endothermic species vs. ectothermic species [46].

In the majority of ectothermic species including fish, the contraction of ventricular and atrial myocytes do not require Ca^{2+}release from the SR but it is maintained exclusively by transsarcolemmal Ca^{2+}flux through L-type Ca^{2+}channels, LTCCs [107] and with contribution from reverse-mode NCX in some cases [123]. As mentioned in the previous Section, in mammals the sarcolemmal Ca^{2+}ions enter to the cardiac myocytes is lower and alone is insufficient for activate typical physiological contractions [63]. Nevertheless, some ectotherms rely more strongly on SR Ca^{2+}during E-C coupling such as blue fin tunas which are apex oceanic predators that have the highest heart rates and cardiac power output among other fish species [106]. Consequently, the SR Ca^{2+}cycling importance of the hearts of active species seems to be a typical principle that can be applied to all vertebrates including stenothermal fish like burbot [106], which live in cold environments, in eurythermal fish like salmonids [44] and tuna [124], which undergo seasonal cold acclimation. In the cold ectotherm heart, the increased SR function is thought to enhance sarcolemmal $Ca^{2+}$to overcome cold-related decreases in the sarcolemmal Ca^{2+}influx and Ca^{2+}sensitivity of myofilaments. Analogous strategies have been explained in cold-hibernating mammals [46].

The Ectothermic vertebrate animals are often faced the challenging of an unstable environment that can change body temperature, pH and oxygen levels. Specifically, an increasing in the intracellular $Ca^{2+}$is a significant feature of environmental stress in the cardiomyocyte of mammals, which can lead to Ca^{2+}overload and the motivation of cell death pathways [46]. While in ectothermic cardiomyocytes, interestingly, the major mechanism leading to Ca^{2+}overload is the SR Ca^{2+}release suggesting that ectothermic cardiomyocytes may possess an SR whose Ca^{2+}stores are harder to release in order to protect the cell from Ca^{2+}overload. During environmental perturbation and when intracellular Ca^{2+}levels increase to unusual levels in ectothermic myocytes, the sarcoplasmic reticulum could act as a Ca^{2+}buffer with a vast storage capacity. Although these concepts are attractive, more experimental evidence need to support them [46]. In ectotherms, transverse (T) tubules is lack, however it is thought that the inner myocytes of fish ventricle help to increase the sarcolemmal Ca^{2+}flux efficacy in the absence of a t-tubular system. The calcium cycle features in the fish cardiac cells is shown in Figure (2.20B).

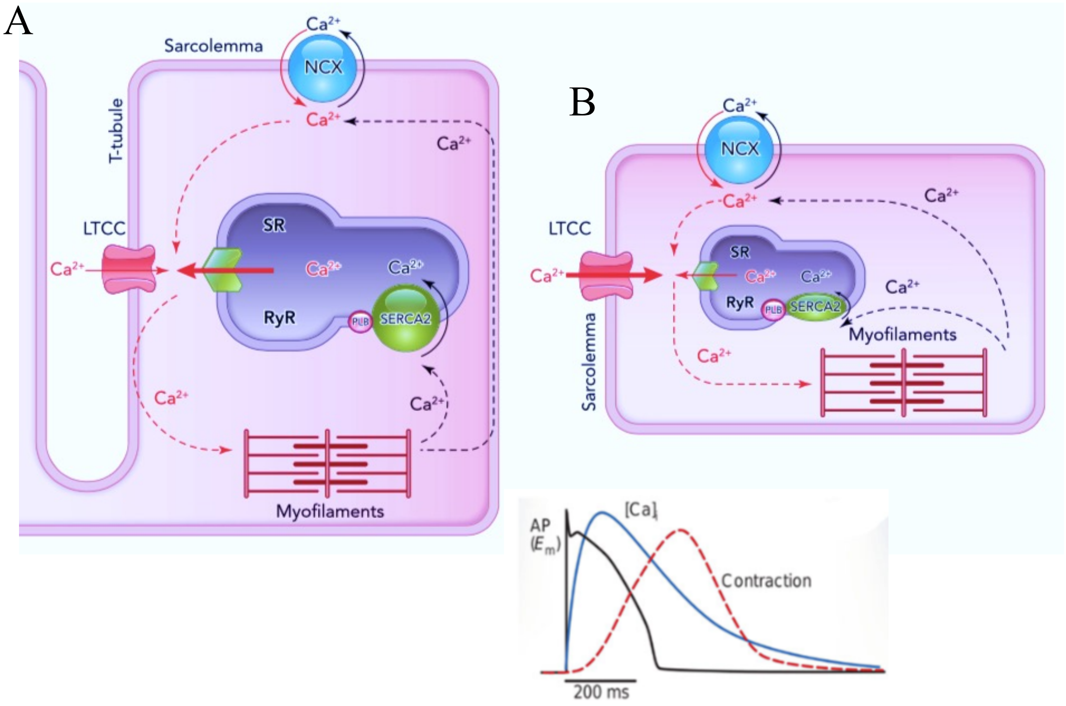

Figure 2.20: Schematic illustration the excitation-contraction (E-C) coupling in mammals (A) and fish (B) cardiac cells. The solid red and black arrows refers to the direction of Ca^{2+} movement during contraction and relaxation, respectively. The dotted red and black arrows refers to cytosolic Ca^{2+} flux during contraction and relaxation, respectively. The insert is time courses of intracellular Ca^{2+} concentration and contraction elicited by an AP. Adapted from [46].

In a brief lines, $Ca^{2+}i$s moved across the myocyte membrane (T-tubules or sarcolemma) through L- type Ca^{2+}channels (LTCC). LTCC releases a larger amount of $Ca^{2+}$from the sarcoplasmic reticulum (SR) through the ryanodine receptor (RyR). Moreover, Ca^{2+}can also enter the cell through the Na^{+}/Ca^{2+}exchanger (NCX). These Ca^{2+}fluxes increase the cytosolic Ca^{2+}, causing cell contraction of the myofilaments. The cardiomyocyte relaxation happens when Ca^{2+}dissociates from the myofilaments and is either sequestered into the SR through the SR Ca^{2+}ATPase (SERCA2) or across the membrane by the NCX [46].

2.7 Experimental Techniques

This Section explains different experimental techniques utilized to either characterise action potentials and currents or cardiac organ constructions.

2.7.1 Voltage Clamp

Voltage clamps techniques, which is also known as patch clamping techniques offer a characterising way to the different ionic currents by measuring currents through a series of 'step' voltages. The current measurement can be done by placing electrodes in both intracellular and extracellular spaces, providing a difference in the potential across the cell membrane and measuring the resulting currents. Firstly, the membrane potential is held at a holding voltage then instantly stepped up to different test voltage (usually in increments in 5,10 or 20mV, somewhere in the range -140 to 60 mV) for a specified time amount which is known as clamping time, then stepped back down to the holding voltage (Figure 2.21A-i). The exact voltage range or clamping time is determined by which current being measured. In the voltage clamp techniques, during the test voltage either the current at the end of the test potential which is known as the peak current, or the end pulse current (also referred as tail current) which is just after the potential is stepped back to the holding voltage) is returned (showed in Figure 2.21A-ii). By using these data, a current–voltage (I–V) relationship can be created where the current (each value is used) is plotted versus the test potential (Figure 2.21B) indicating ranges of voltage in which the current is most active. However, it is not a direct implication of the current value at different voltages during an action potential, because most currents are time dependent [63].

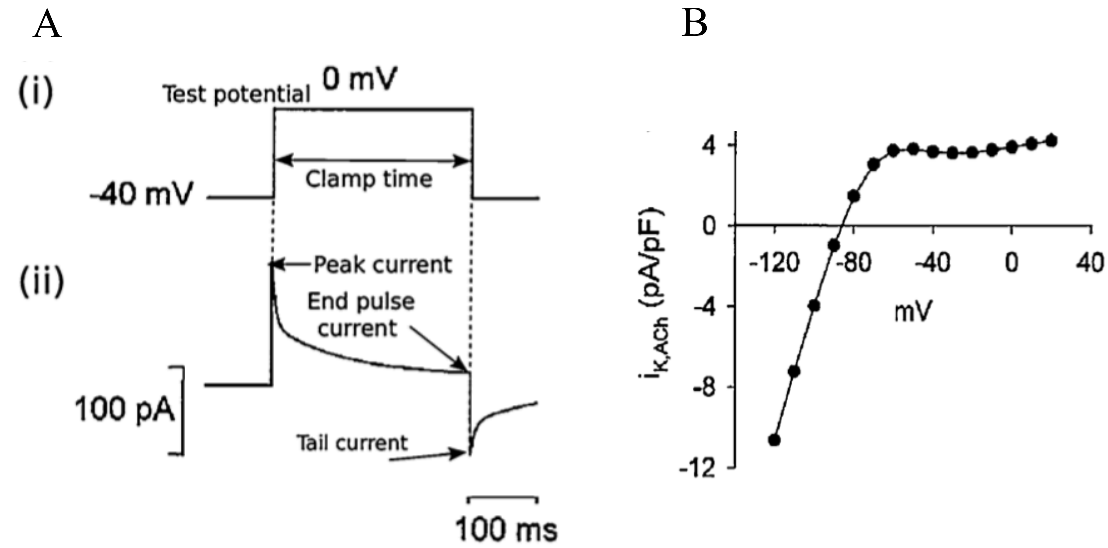

Figure 2.21: Example of a voltage clamp technique. A: Single voltage clamp step function example in (i) and trace of the resulting current is shown in (ii). All the currents that may be returned are labelled. B: Example of the I–V relationship. The y-axis represents the current and is plotted against the x-axis which is the test potential. Adapted from [125].

2.7.2 Micro-CT Scan

Recently, extensive effort has been made to improve the investigating techniques of the biological samples morphology in a non-destructive manner. The most imperative technique is microcomputed tomography (micro CT). It represents a non-destructive imaging tool that includes the recording of two- dimensional (2D) (or ‘slices’) x-ray images from different angles around a target specimen, followed by a digital three-dimensional (3D) reconstruction [126] (Figure 2.22). Although the consequent 3D-rendered volume permits for the multidirectional examination of the interested area such as an organ, it also allows volumetric, dimensional, or even for more advanced measurements that need to be made [127]. In biological sciences, micro CT in the recent years, has gained popularity due to its application in evolutionary and ecological biology [128], paleobiology [129] and taxonomy [130].

Micro CT equipment is contained of numerous major components as seen in (Figure 2.21A). These components include x-ray source with a radiation filter, collimator (to focus the beam geometry to either a fan- or cone-beam projection), sample stand, and phosphor-detector and charge-coupled device (CCD) camera [131]. The 3D image reconstruction can be achieved by rotating (rotates the examine sample through a specific angle, usually 180° or 360°) either the emitter and detector (for live animal imaging) or the sample (for desktop systems) in order to generate a series of 2D projections (Figure 2.22B),then it will be transformed to a 3D data set by the use of a digital process named back-projection algorithms [131, 132].

It is worth to mention that the micro CT scan has a superior resolution in comparison with other techniques such as magnetic resonance imaging (MRI) and ultrasound, as the non-destructive imaging modality has the ability to produce 3D images and 2D maps with volumetric pixel (or voxel) reaching 1 μm [132]. The micro CT principle is based on the x-rays attenuation which is passing through the sample or object being imaged. When the x-ray passes through tissue sample, the incident x-ray beam intensity is diminished according to the formulation of $I_x = I_0 e^{-\mu x}$, where I_0 represents the incident beam intensity, μ represents the linear attenuation coefficient, while x represents the distance from the source and I_x represents the beam intensity at distance x from the source [132]. As a result, the attenuation depends on both the source energy and sample material. It also can be used to calculate the tissues density being imaged when the reduced intensity beams are assembled by a detector array [127].

Essentially, every voxel is imaged (by 2D projections) from various angles, and the summation of its view from every angle creates a demonstration of the actual density of the x-ray and thus brightness of that voxel [131]. After reconstruction, several software tools can be utilized for visualization and analysis of the resultant data [127].

A

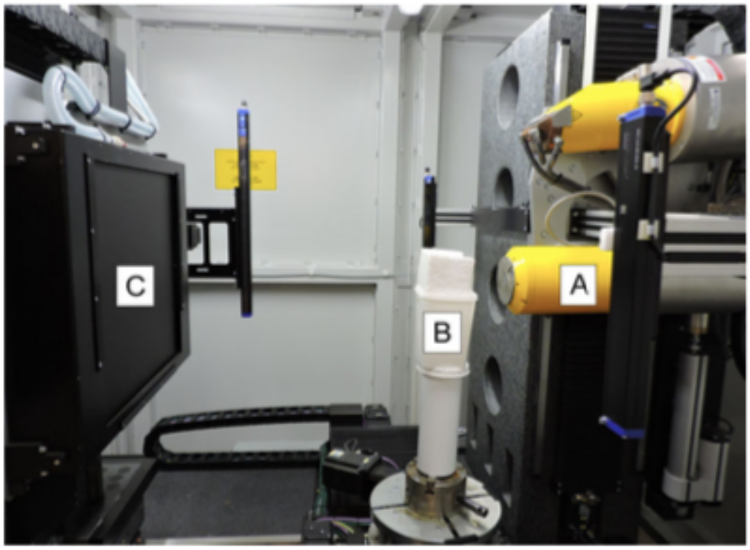

B

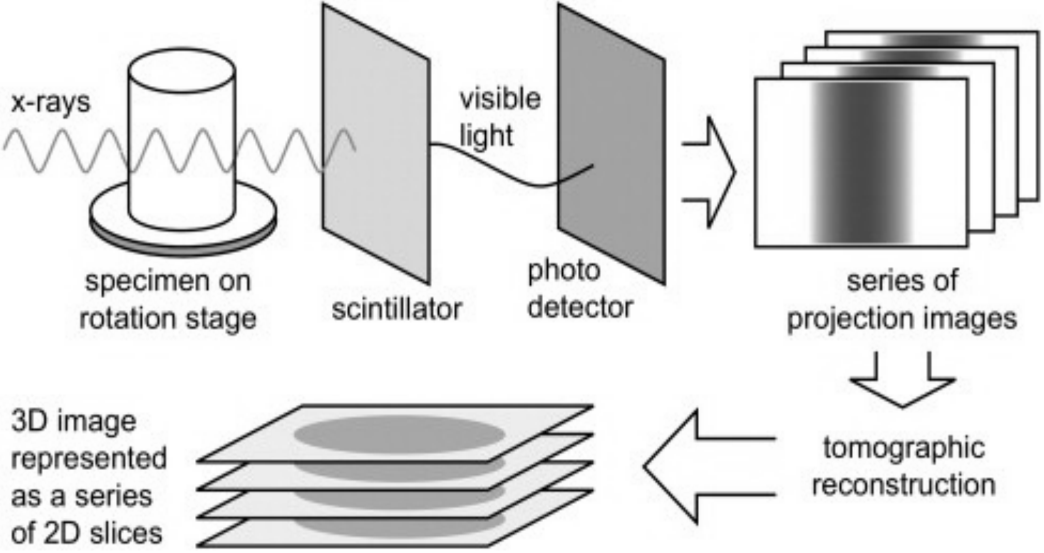

Figure 2.22: A typical micro computed tomography scanner. A: Photograph of the fundamental component of micro CT, consists of an x-ray tube (A) which emits x-rays that pass through a sample (B), then recorded by an x-ray detector (C). B: Graphic illustration of micro CT attainment and reconstruction processes. A 3D version of the sample is achieved by scanning at different rotation angles and then mathematically reconstructed through transformation of two-dimensional projections (2D slice images). A adapted from [127] and B adapted from [126].

2.8 Mechanical Contraction of the Heart

2.8.1 Cardiac Excitation-Contraction Coupling

Cardiac excitation–contraction coupling is identified as the process from electrical excitation of the cardiac cell to contraction of the heart [122].

The ubiquitous second messenger Ca^{2+} is required in cardiac electrical activity and as a direct trigger of the myofilaments causing contraction in all muscle types. The myocytes muscle contains muscle fibres each of which surrounding by the cell membrane known as the sarcolemma. A cluster of thousands of myofibrils is found in each muscle fibre which contain thousands of myosin (thick) filaments and actin (thin) filaments. These filaments are lying in a parallel way and adjacent to each other within the A-band. The myofibril section that bound the ends of the actin filaments is known as Z line (or Z disk) while the myofibril segment lying between two neighbouring Z-lines is called the sarcomere. The sarcomere is the functional unit of the muscle as it represents a fundamental contraction unit in cardiac cell. With thousands of thousands functioning sarcomeres, the contraction of the heart can be achieved. The relaxed and contracting states of the sarcomere are shown in Figure (2.23Ai,Aii). The striated appearance of the myofibrils is due to the Z lines. The myosin filaments which protrude from the M-line and the actin filaments which are embedded in the Z-line represent the major protein complexes that contribute to the sarcomere contraction [133].

The thick filaments are composed of multiple myosin molecules. The myosin heads protrude from the thick filament through rope-like arms and these arms with the protruding heads together known as cross-bridges [133]. The arms flexibility permits the heads to be either extended far away from the myosin filament or drawn closer to it. Moreover, the attaching point of the arms to the head gives the head movement facilitating it to contribute in the contraction process [62].

The thin actin filaments are composed of actin, tropomyosin and troponin protein complexes. A giant protein complex called titin which acts as a molecular spring [134, 135], connects the M line and Z line in the sarcomere (Figure 2.23B). The passive relaxation and recovery of the sarcomere subsequent a contraction are mainly titin accountability [136].

In early 1950s, two outstanding papers have been published by Huxley A. F. et al. [8] and Huxley H. E. et al. [10] revealed that the sliding between the thick and thin filaments shortens the muscle. When the muscle contracts the actin filaments that protrude from the consecutive Z-lines are pulled towards the sarcomere centre, sliding along the myosin filaments resulting in a short distance between the corresponding Z-lines and thus the muscle contracts by the sliding filament mechanism. The force which causes the pivotal, active sliding can be clarified by using the cross-bridge cycling.

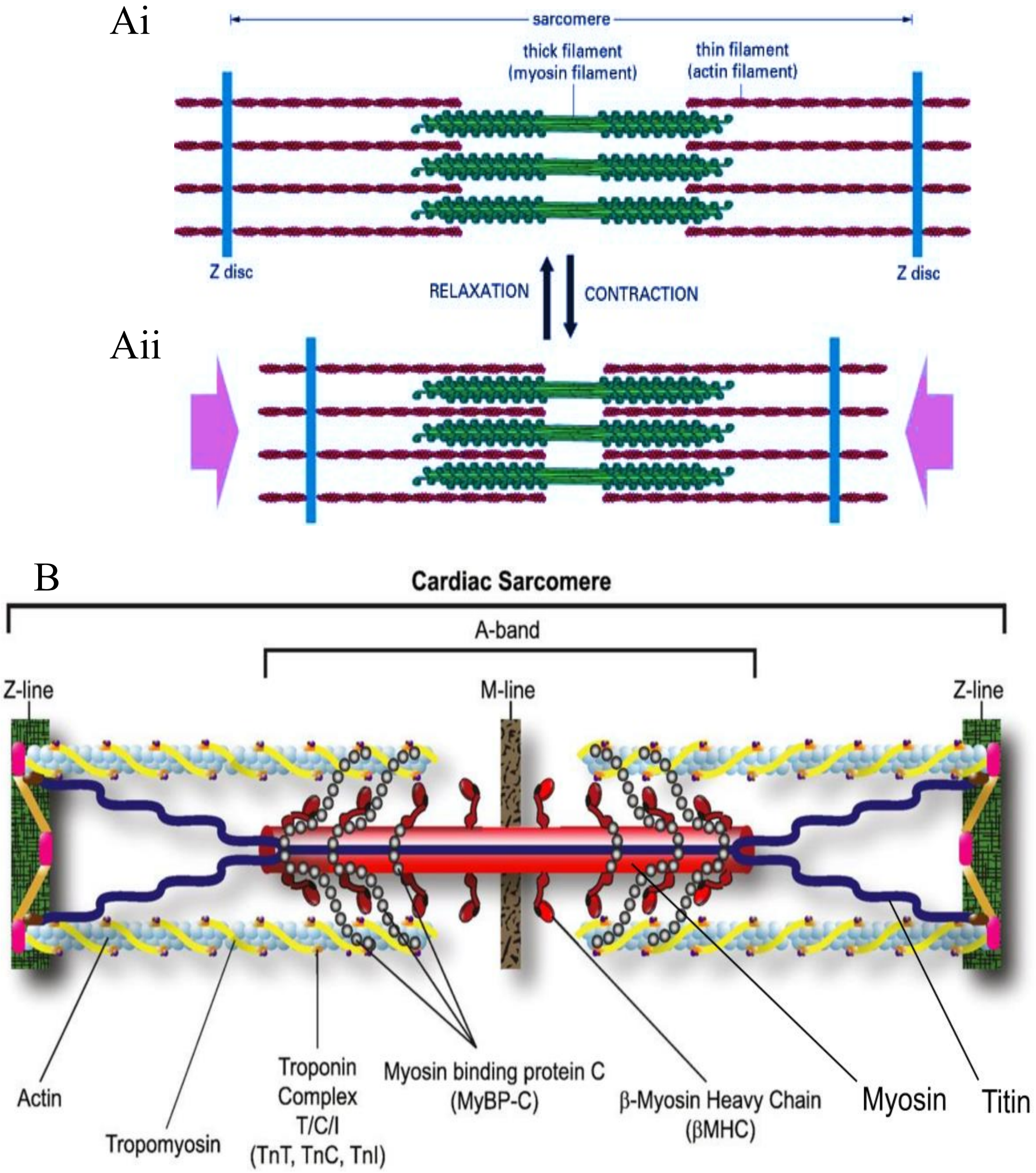

Figure 2.23: Schematic diagram of the interaction of actin (thin) and myosin (thick) filaments in cardiac muscle contraction. The sarcomere, which represents the cardiac muscle functional unit, is presented in a relaxed (Ai) and contracting (Aii) state. B: Diagrammatic representation of the microstructure of a cardiac sarcomere. Adapted from [136].

2.8.2 Cross-Bridge Cycle

As mentioned in previous Section, there are three protein complexes of the thin actin filaments: actin, tropomyosin, and troponin (Figure 2.23B). The tropomyosin (Tm) complex wraps around the actin, which obscures binding sites in the relaxed state with which myosin heads can interact. While the troponin complex itself consists of three complex protein subunits (Figure 2.24A,B). These proteins subunits include troponin I (TnI) which strongly binds to the actin in order to protect the actin-tropomyosin complex in place, troponin T (TnT) which has a high affinity for tropomyosin as it binds with it and forming the troponin- tropomyosin complex, and troponin C (TnC) which can bind strongly with Ca^{2+}[136]. The Ca^{2+} ions released from the SR upon electrical stimulation bind with troponin C, and this binding initiates the contraction process. The myosin filament head is not attached to the binding sites on the actin at the beginning of the cross-bridge cycle, since tropomyosin covers these sites. As shown in Figure (2.24 C), when the Ca^{2+} is absent, the troponin attaches to actins via troponin I (TnI) while the attaching to the tropomyosin (Tm) is through troponin T (TnT). When Ca^{2+} binds to the TnC, this will strengthen the binding of TnC- TnI and weakening the binding of TnI-actin, permitting TnI to detach from the actin. This permits the tropomyosin to relocate to the actin filament surface leading to uncover the binding site on the actin, through which the myosin head is permitted to bind the actin.

The eight steps that involved in a cross-bridge cycle are illustrated in Figure 2.24D. During the cross-bridge cycle, the source of energy has served by ATP [133, 136]. Myosin heads are attached with the actin at the end of contraction. When the ATP concentrations reached a physiological value of (3-5 mM), ATP rapidly and irreversibly binds to myosin (step 1), which leads to actin detachment from the actin-myosin and ATP complex (step 2). Then the tension drops, and the myocytes be in a relaxing period. In step 3, the binding of ATP to myosin head is cleaved although products still bind with the head. When there is a lack in a high-level of Ca^{2+}, the myosin head and actin bindings are weak (step 4). After the electrical excitation of the cells, the Ca^{2+} concentrations increased and as a result of the binding between Ca^{2+} to the TnC, the myosin head binds strongly with actin (step 5). A conformational change in the head can be resulting from the strong binding and thus prompts it to tilt towards the rod-like arm of the cross-bridge, leading to produce the power stroke. Consequently, the cross-bridge undergoes isomerisation, in step 7, the rate of which is limited. The

ADP and phosphate ion detach from the myosin head in step 8 in order to make way to new ATP to bind, that leads to a new cycle.

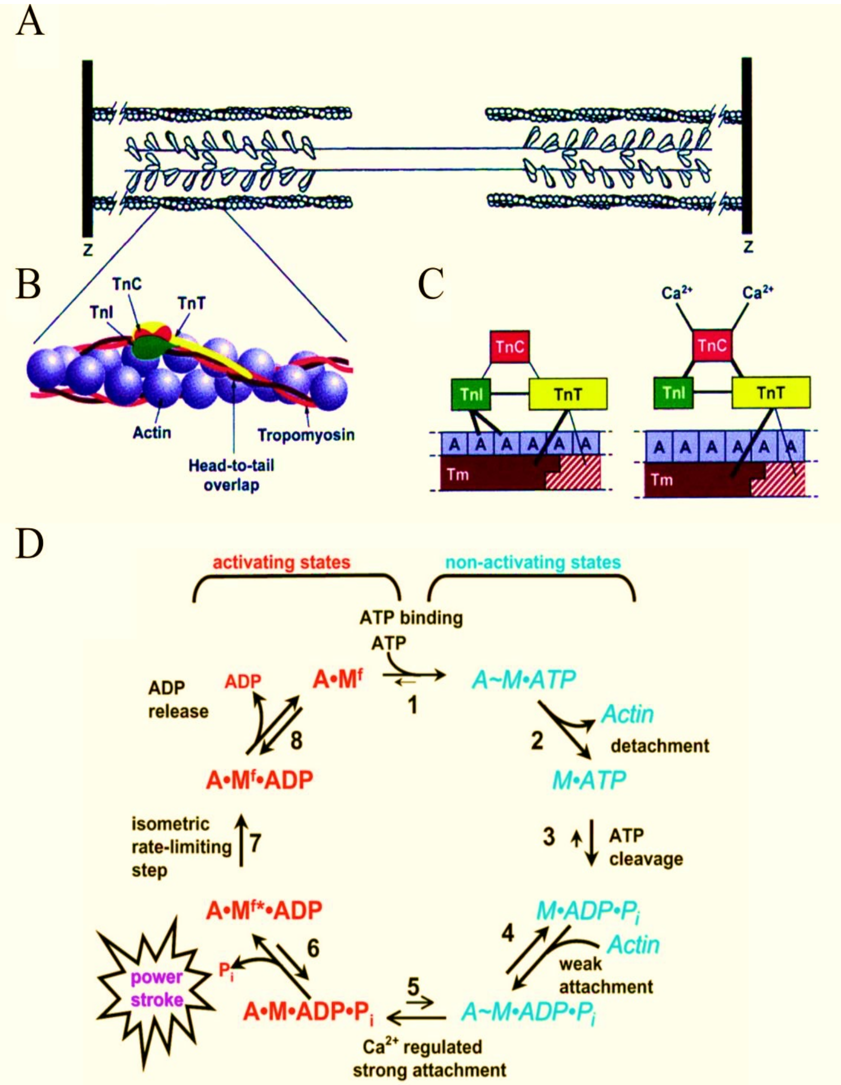

Figure 2.24: Schematic diagram showing the detailed structure of actin filament. A: Overlapping thin and thick filaments and the cross-bridges in the sarcomere. B: Detailed view of the thin filament showing the molecular arrangement of troponin and the overlapping tropomyosins (Tm) along the helical actin. C: Changes in troponin interactions due to Ca binding to TnC, and unbinding of TnI from the actin (labelled as "A"). D: A schematic diagram of the cross-bridge cycle. The abbreviations are actin (A), myosin (M), inorganic phosphate (Pi), adenosine triphosphate (ATP), adenosine diphosphate (ADP). Figure adapted from [133]

2.9 The Electrocardiogram

The electrocardiogram (ECG) is an extremely important tool in the clinical cardiology field as ECG features can indicate heart problems either in clinical diagnosis of the heart diseases or in response to pharmacological therapies [137]. ECG provides aspects on the electrical activity of the heart by assessing alterations in the potential distribution on the body surface. A typical ECG waveform is composed of various different waves [62], that correspond to the depolarisation and repolarisation of different parts of the heart as illustrated in Figure 2.25A.

Although there are many differences in structure and functional characteristics between fish heart and mammals heart, the ECG morphology of both of them is quite similar [138]. Fish heart and human heart show on ECG recording; a distinct P-wave represents depolarisation of the atria in respond to the SAN triggering, while the repolarisation is masked by the triphasic QRS complex, QRS-complex corresponds to activation of the single ventricle in fish heart or the left and right ventricles in human heart (As the ventricles mass are much larger than atria, usually the QRS complex is an order of magnitude larger than the P-wave) and the subsequent T-wave refers to repolarisation of the ventricles as shown in Figure (2.25B,C). Moreover, the activity of the SAN and AVN (sinoatrial and atrioventricular nodes, respectively) does not give any visible deflections on the ECG waveform [69].

2.9.1 ECG Features

The electrocardioum features in both human and teleost hearts (Figure 2.25) are the PR interval is the time interval between the beginning of the P-wave and the first deflection of the QRS complex, and hence signifies entire conduction time of excitation waves from the SAN and through the AVN to the ventricles. The P-wave width can signify the atrial conduction while the PR interval represents an indication of AVN function. Therefore, a prolonged PR interval can be suggestive of AVN dysfunction. The number of QRS complexes linked to each P-wave is known as the PR ratio [17, 63]. This ratio in a healthy heart is 1:1 means each atria activation leads to an activation of the ventricle/s. However, AVN dysfunction can cause larger ratios than this, where each atria activation does not cause an activation of the ventricle/s. Moreover, as the total activation time of the ventricle/s is represented by the QRS complex which its width can give information about the conduction time of the intra-ventricular and origin of possible conduction arrhythmias or defects [63].

Another interval which is widely used as a direct measure of the heart rate in the trout fish is the RR interval which represents the time between successive R waves. RR interval in the healthy heart will also be equal to the PP interval [17, 118]. An important biomarker of the ECG is the QT interval for risk of sudden cardiac death. The QT interval is the time period between the QRS complex starting time and the T wave termination, can be explained as the time interval between electrical depolarisation and repolarisation of the ventricles. Both abbreviated and prolonged QT intervals which is seen in the short QT and long QT syndromes, respectively, are related to increased incidence of malignant ventricular arrhythmias [62].

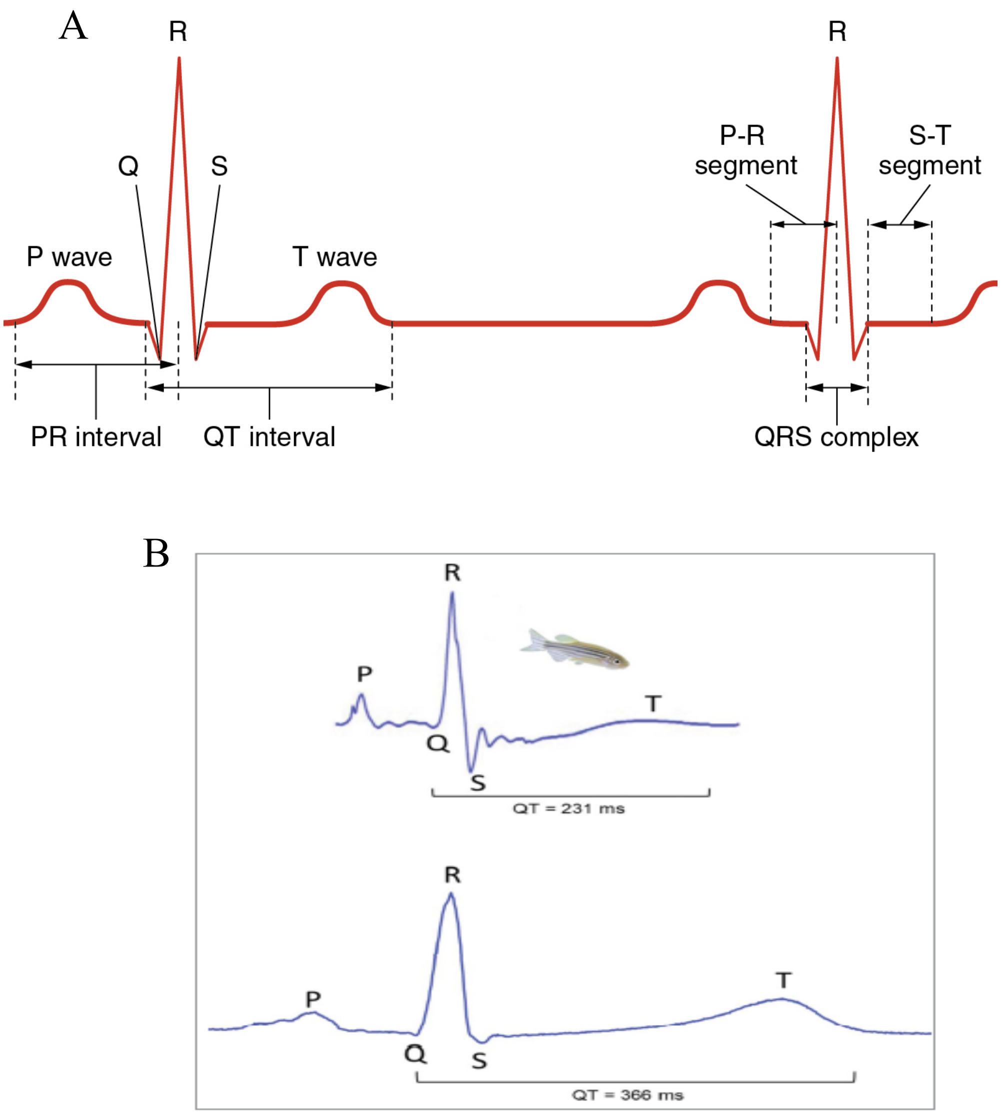

Figure 2.25: The electrocardiogram (ECG) of normal heart. A: ECG features of a typical heart. B: Comparison between ECGs of human and zebrafish heart. An adult zebrafish ECG at 23°C showed on (top). A healthy 43-year old human male ECG showed on (bottom). Note ECGs of both zebrafish and human recorded at the same scale for direct comparison and analogous to the ECG of human, P, QRS and T waves are obviously distinguishable in the ECG of the zebrafish heart. A adapted from [139] and B adapted from [69].

Furthermore, the ECG profile of the fish heart possess some differences based on specific fish species. For example, the ECG of elasmobranches fish such as Shark and Hagfish appeared with additional waves compared with teleosts ECG [74]. These additional waves are B-wave during the S-T interval in elasmobranches when conus cardiac muscle contracts and V-wave during the P-T interval is prominent in hagfish, as shown in Figure 2.26.

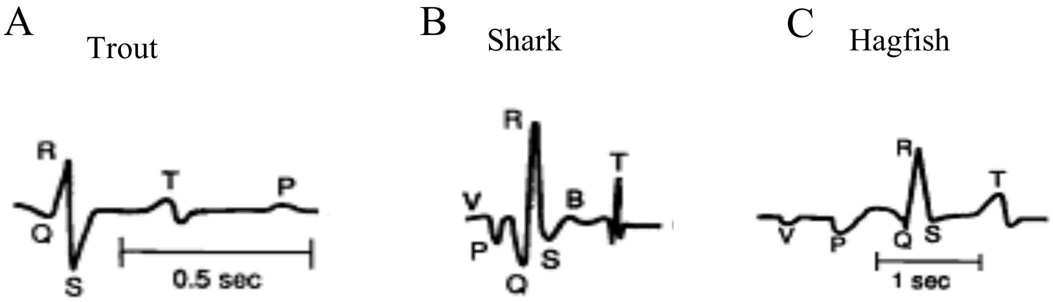

Figure 2.26: Comparison of electrocardiograms of different fish species. A: Trout ECG, B: Shark ECG and C: Hagfish ECG. Modified from [74].

3. Mathematical Modelling of the Heart

3.1 Introduction

The processes of developing a computational cardiac model of cells and organs should be formalised mathematically. The earliest mathematical model of an action potential was published in 1952 by Alan Hodgkin and Andrew Huxley (Hodgkin-Huxley, or HH model) for the squid giant axon [47]. The Hodgkin-Huxley approach revolutionises our understanding of the ion channels function. HH model still used today as a base notion for most mathematical models of action potentials of the cardiac and neural modelling studies.

Their discovery has shown the possibility of represent the cell membrane and ionic currents by different electrical components within a simple electric circuit. In early 1960s, Denis Noble [9] used the HH model and proposed the first biophysically detailed computational model for the canine Purkinje fibre (a specialised part of the ventricular conduction system) action potentials. Shortly thereafter, further experimental data became available, therefore, various refinements were published.

3.2 Electrical Representation of a Cardiac Cell

In general, a simplified electrical representation of the cardiac myocyte [140] can be illustrated as in Figure 3.1. In this schematic Figure, the arrows represent the ion channels, each labelled with the specific ion current carried by the channel while the direction of transport is indicated by the arrowhead. Channels with a solid rectangle represent the passive ion transport while active ion pumps and exchangers are indicated by those with a crossed circle. In addition to transmembrane currents there are some of internal currents which are generated by the ionic transport within the cell itself. These internal currents do not directly influence the ionic concentrations in the intracellular and extracellular, however, they contribute to the overall dynamic of the entire cardiac cell system [140].

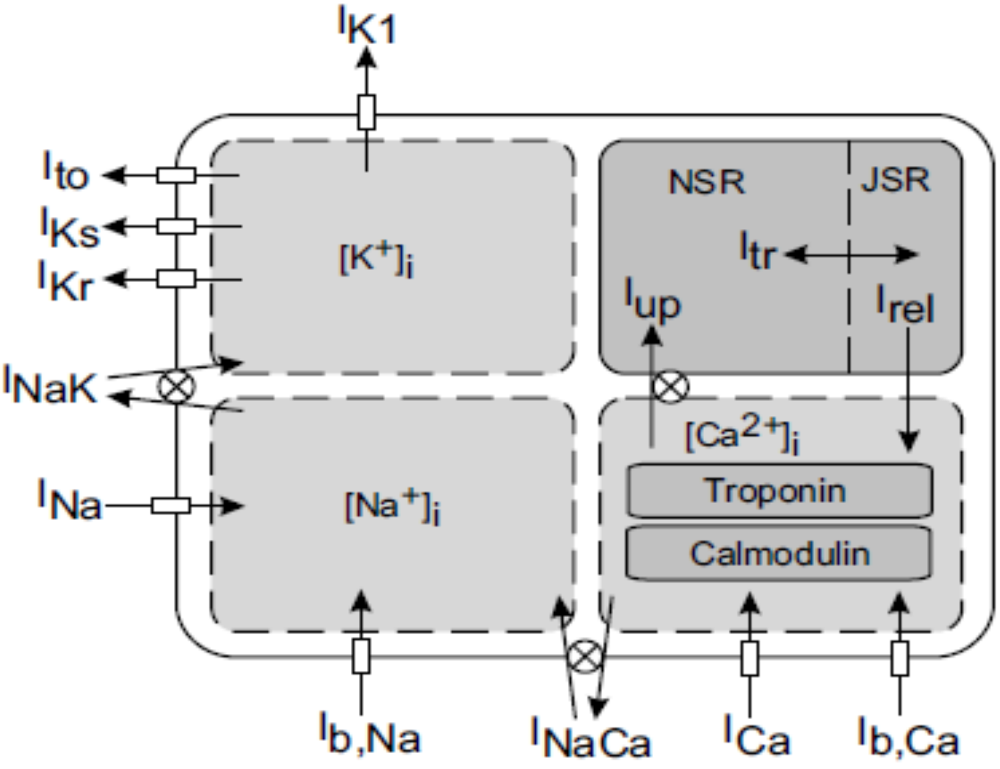

Figure 3.1: A simplified electrical representation of a mammalian heart as illustrated by Popp et al. [140].

3.3 Electric Circuit Model

The experiments of voltage clamp on single cell and multi-cellular tissue samples show that the relationships between ion channel current and cell membrane potential are nonlinear. Therefore, constructing an electrical circuit model whose behaviour is defined by established mathematical models such as Hodgkin and Huxley (HH) model [47], will describe the system clearly.

The former Hodgkin and Huxley mathematical model [47] consisted of a family of nonlinear ordinary differential equations (ODEs) which treated the cell membrane as an electrical circuit, and described the initiation and propagation of APs. The electric circuit of HH model based on experiments performed on the squid giant axon, however, this model forms the basis of modern cardiac electrophysiology and is widely used in cardiac AP models, due to the similarity in the underlying electrophysiology [141]. Figure (3.2) shows the basic framework for all electric circuit models of cardiac myocytes. Each component of an electrically-excitable cell is considered as an electrical element. The cell lipid bilayer separates charges and hence is represented as a capacitor, with a constant capacitance (C_m). Further current is carried into the cell by the ions movement through the cell membrane, which adding extra charge to the capacitor. Variable resistors which are aligned in parallel and have an associated conductance (g_i) represent the voltage-gated ion channels (theses variable resistors are assumed to be independent of each other). Ion pumps and exchangers are represented as current sources [141, 142].

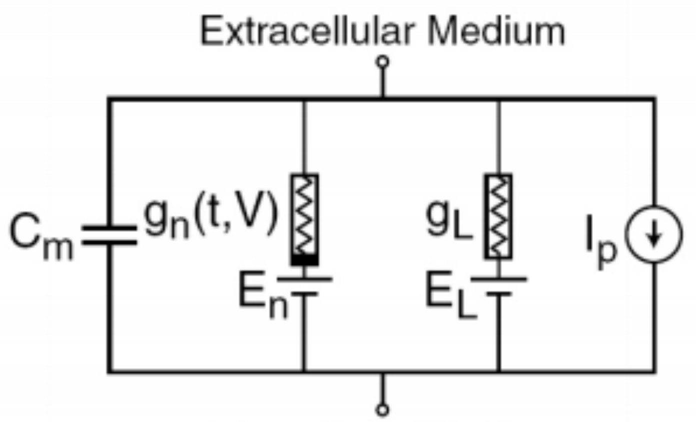

Figure 3.2: The basic constituents of a Hodgkin-Huxley type electric circuit model. The lipid bilayer has capacitance C_m, sarcolemmal ion channels are modelled with either voltage- and time-dependent nonlinear (g_n (t,V)) conductance, or voltage- and time-independent linear (g_L) conductances. The flow of ions is driven by electrochemical gradients represented by Nernst potentials (E), and ion pumps and exchangers are analogous to current sources (I_p) [142].

When a stimulus current (I_{stim}) is absent, the sum of the total ionic current (I_{ion}), and the capacitive current (I_C) must equal zero according to Kirchhoff's current law [141], which gives

$$I_{ion} = -I_C \tag{3.1}$$

According to the capacitor relation, $\mathrm{Q} = \mathrm{C_m V_m}$, the capacitive current can be written as

$$I_C = C_m \frac{dV_m}{dt} \tag{3.2}$$

and thus the change in the membrane potential with time is given by

$$\frac{dV_m}{dt} = \frac{-I_{ion}}{C_m} \tag{3.3}$$

In the original Hodgkin-Huxley axon model (Figure 3.3) I_{ion} was assumed to consist of a depolarising sodium current (I_{Na}), a repolarising potassium current (I_K), and a time- and voltage independent leakage current (I_L) [47], such that the total ionic current was written as

$$I_{ion} = I_{Na} + I_K + I_L \tag{3.4}$$

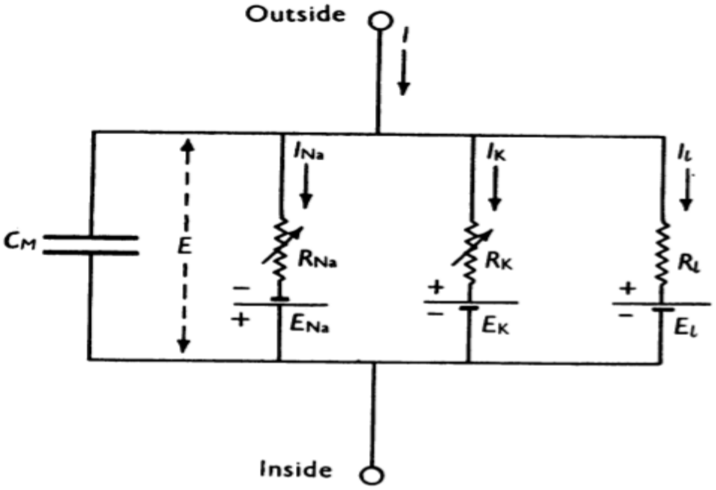

Figure 3.3: Electrical circuit representation of a cell membrane, in the original Hodgkin-Huxley axon model [47].

Equation (3.3) then, can be integrated in order to establish the AP. Now, Ohm's law (Equation 3.5) is used to derive a formulation for the ionic currents. The using of conductance (g) is more conventional than the resistance as shown in Equation (3.6).

$$V = IR \tag{3.5}$$

$$g = 1/R \tag{3.6}$$

$$I = gV \tag{3.7}$$

It is worth to mention that (V) here refers to a driving force to the ionic currents (not the membrane potential), which is formulated in a well- known way and is correlated to the Nernst equilibrium potential (next Section). While the conductance of the channel (g) can be formulated by diverse approaches and the most popular one is the HH formulations (see Section 3.5), which was used in this thesis.

3.4 Nernst Equilibrium Potential

Two forces can affect the ions that located at each side of the cell membrane; the electrical force and the chemical force, due to the charge gradient and the concentration gradient, respectively, through the cell membrane. Nernst equilibrium potential (Er), or the reversal potential, can be defined as the potential at which the electrical force balances the chemical force.

At this potential, the equilibrium is reached as the electrochemical force is zero on an ion and thus no net charge flow throughout the passive ion channels. This means the currents for this channel is also zero.

The Nernst equilibrium potential is given by:

$$Er_{ion} = \frac{RT}{zF} ln\left(\frac{[ion]_e}{[ion]_i}\right) \tag{3.8}$$

where Er_{ion} refers to the Nernst equilibrium potential, F represents Faraday's constant, T represents the absolute temperature (in Kelvin), R represents the universal gas constant, z represents the valence number of the ion, and $[ion]_e$ and $[ion]_i$ represents the ion concentrations in the extracellular and the intracellular spaces, respectively.

The difference between the membrane potential and the reversal potential induces an electromotive force on the ion, providing a form for the driving force (V) in Equation (3.7). Consequently, the ionic current can be calculated from the equation bellow:

$$I_{ion} = g(V_m - Er_{ion}) \tag{3.9}$$

3.5 Hodgkin-Huxley (HH) Model

Hodgkin and Huxley model describes mathematically the electrophysiological behavior of the ion-channels as described previously (see Section 3.3). The ion channel kinetics are modelled by using the activation and inactivation variables. These variables are correlated to the activation and inactivation gates, with the assuming of their independence of each other. The channels fraction in the activated state determines the activation variable value, thus, a value of 0 signifies no one of channel being activated while a value of 1 signifies all of the channels are activated. Moreover, the channels fraction that are not in the inactivated state determines the inactivation variable, thus, a value of 0 signifies all of the channels are in the inactivated state while a value of 1 signifies no one of the channels are. Hence, the channels fraction in the open state (activated and not inactivated) as well as the maximum proportion of the flowing current is described by multiplying these two variables together. Thus, a typical formulation for an ionic current can be described by:

$$I_{ion} = m^a h^b g_{max} \, (V_m - Er_{ion}) \tag{3.10}$$

where m and h represent the gating variables that control the flow of ions (allow or block) and they are known as activation and inactivation gates, respectively, g_{max} is the maximum channel conductance. While a and b represent the powers of the gating variables, which are showed here to empirically fit the gates form that experimentally observed (i.e. they refer to the number of independent activation or inactivation gates)[47]. The HH model allows to incorporate both voltage and time dependence.

If y is an activation gating variable. The y value denotes the activation gates proportion which are open (or equivalently, the channels proportion in the activated state). Thus, the activation gates proportion that are closed (or the channels proportion not in the activated state) must be (1-y).

α_y and β_y are the rate coefficients, corresponding to the transitions between these two states. The rate of change of opening when α_y is related to the gate opening and can be described by $\alpha_y(1-y)$. In a same way, the change of closing rate can be described by $\beta_y y$. The transitions between open and closed states of a gating variable has an equation form as:

$$(1-y) \rightleftharpoons y \tag{3.11}$$

And the change rate of y is given by the differential equation (3.12).

$$\frac{dy}{dt} = \alpha_y(1-y) - \beta_y y \tag{3.12}$$

The gate state will be voltage dependent in addition to time dependent if the values of either α_y or β_y depend on V_m.

The gate steady-state (y_∞) refers to the gate variable value (y) when $\frac{dy}{dt} = 0$; hence, is given by:

$$y_\infty = \frac{\alpha_y}{\alpha_y+\beta_y} \tag{3.13}$$

When there is an instant change in the voltage, the time constant (τ_y) can describe the rate at which steady state value of the gate will approach for the new voltage, as shown bellow:

$$\tau_y = \frac{1}{\alpha_y+\beta_y} \tag{3.14}$$

These offer a better indication to measure the channel ability in responding to changes in potential as well as the channel activity at a certain voltage.

As a result, the differential equation that describes the gating kinetics is:

$$\frac{dy}{dt} = \frac{y_\infty - y}{\tau_y} \tag{3.15}$$

The steady state values and time constants, in both experimentally and modelling studies, are measured and fitted directly. A simple sigmoidal function is the general formula of the steady state values, as illustrated bellow:

$$y_\infty = \frac{1}{1+exp\left((V_m - V_{0.5)}/k\right)} \tag{3.16}$$

where $V_{0.5}$ represents the voltage of half activation, and k represents the gradient of activation. The values of $V_{0.5}$ and k may have positive or negative values, and are determined empirically.

Figure 3.4 shows two examples of this type functions. It can be noticed that both have a $V_{0.5}$ of -20 mV, with 0.5 steady state gate value (dotted line). The sign effect and magnitude of the gradient (k) are also illustrated.

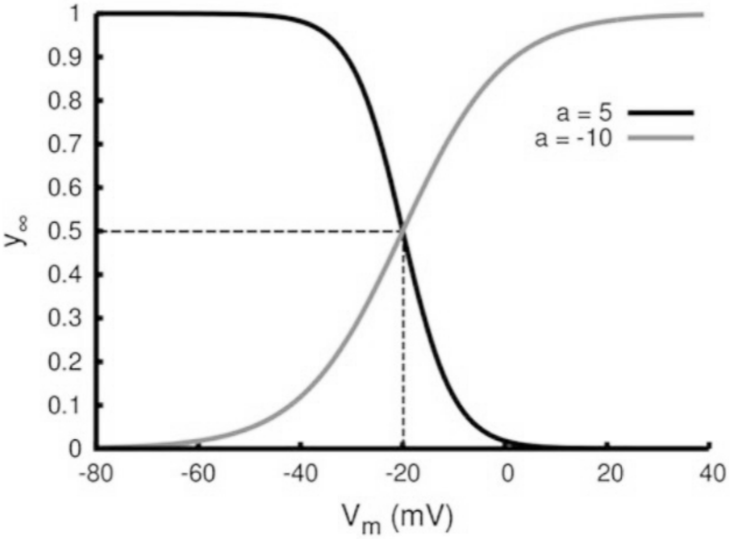

Figure 3.4: An example of steady state gating variable. The relationship example between the membrane potential and the steady state gating variable value. Two examples are shown and both of them have a $V_{0.5}$ of -20 mV (the dotted line). Direction of the variable is determined by the sign of the gradient (k) [63].

From y_∞ (the steady state value) and τ_y, α_y and β_y can be obtained using the equations bellow:

$$\alpha_y = \frac{y_\infty}{\tau_y} \tag{3.17}$$

$$\beta_y = \frac{(1-y_\infty)}{\tau_y} \tag{3.18}$$

As a result, the time course of the gating variable can be given by:

$$y = y_\infty - (y_\infty - y_0)exp\left(\frac{-t}{\tau_y}\right) \tag{3.19}$$

3.6 Cardiac Tissue Models

Electrical waves propagate through adjacent cells in the heart; therefore, the interaction between these cells is also considered in the tissue level modeling of cardiac electrophysiology. The cardiac cells communicate with neighbouring cells electrically through gap junction coupling. The junctions provide a direct electrical connection between the intracellular spaces of two neighbouring cells, where an action potential can be performed from one cell and stimulate the neighbouring cells by providing them with the necessary superthreshold stimulation. The next-neighbour coupling scheme leads to a diffusive interaction; therefore, the cardiac muscle turns into an excitable medium. Therefore, in order to modelling the excitation propagation in tissue, a continuum approach has been used in simulating the electrical activities of the heart in tissue. This is regardless the fact of the gap junctions and myocytes are intrinsically discreet [143, 144]. Two generic cardiac models at tissue level are used in tissue modelling; the bidomain model and the monodomain model.

This bidomain model takes into consideration that the extracellular and intracellular spaces are two separate and overlapping domains and the membrane potential can be calculated through finding the difference between the potential of these two spaces.

If it is assumed that the extracellular and intracellular conductivities are proportional, the bidomain model is the simplified to the monodomain model. And the AP propagation can be described using the monodomain equation as bellow [66, 145]:

$$\frac{\partial \mathrm{V}}{\partial \mathrm{t}} = \nabla . \mathrm{D}(\nabla \mathrm{V}) - \frac{\mathrm{I_{ion}}}{\mathrm{C_m}} \qquad (3.20)$$

where V refers to the membrane potential, C_m is the membrane capacitance, D is the diffusion coefficient tensor (which describing the spread rate of the electrical activity) and I_{ion} is the total ionic current.

The excitation propagation is faster along the fibrous structure of the cardiac tissue than transverse to it. Therefore, the D components (denoted as $\widetilde{\mathrm{D}}$) in a local coordinate system will be heterogeneous. These components can be represented by the diagonal matrix:

$$\widetilde{\mathrm{D}} = \begin{pmatrix} \mathrm{D_f} & 0 & 0 \\ 0 & \mathrm{D_x} & 0 \\ 0 & 0 & \mathrm{D_n} \end{pmatrix} \qquad (3.21)$$

where $\mathrm{D_f}$, $\mathrm{D_x}$ and $\mathrm{D_n}$ represent the diffusion coefficients parallel the fibre axis, trans- verse to it and across the sheet, respectively. By incorporating the cell into the tissue model, $\widetilde{\mathrm{D}}$ should transform to a global Cartesian coordinate system. This can be achieved by:

$$\mathrm{D} = \mathrm{A}\widetilde{\mathrm{D}}\mathrm{A^T} \qquad (3.22)$$

Where A is the matrix indicating the local fibre orientations, T is the transpose matrix of A, which can be represent by:

$$\mathrm{A} = \begin{pmatrix} \mathrm{f} & 0 & 0 \\ 0 & \mathrm{x} & 0 \\ 0 & 0 & \mathrm{n} \end{pmatrix} \qquad (3.23)$$

where f, x and n represent the vectors parallel to the fibre, transverse to the fibre or orthogonal to the sheet, respectively.

3.7 Computation of the Pseudo ECG

The pseudo-ECG was computed following the Gima and Rudy work [186]. At the extracellular space, a unipolar potential ($\emptyset_e$) placed at (x′, y′, z′) position can be calculated at (x, y, z) position on the strand as a spatial gradient integral of the transmembrane potential (∇V_m), as given bellow:

$$\emptyset_e(x',y',z') = \frac{a^2\,\sigma_i}{4\sigma_e} \int (-\nabla V_m) \cdot \left[\nabla \frac{1}{r}\right] dx \tag{3.24}$$

$$r = \sqrt{(x-x')^2 + (y-y')^2 + (z-z')^2} \tag{3.25}$$

Where extra- and intracellular conductivities are represented by σ_e and σ_i, respectively, a is the strand radius while r represents the distance between the source point (x, y, z) and the field point (x', y', z').

3.8 Numerical Methods

Cardiac electrophysiology mathematical models are comprised of two types of equations; the nonlinear ordinary differential equations (ODEs) or the partial differential equations (PDEs). These equations are analytically intractable; therefore, the use of numerical methods will be useful to achieve approximate solutions. Usually, a balance should be found between accuracy and computational time. In this Section, the method used in the models implementation, including the different numerical methods will be discussed.

3.8.1 Numerical Methods for Solving ODEs

3.8.1.1 The Euler Method

The forward Euler method considers as the most basic and prevalent solvers in cardiac modelling. It is used to solve differential equations given an initial value. For accurate solutions and reducing errors, this method typically requires very small time steps (h).

For a simple initial value problem

$$\frac{dy}{dt} = f\big(t, y(t)\big) \tag{3.26}$$

$$y(t_0) = y_0 \tag{3.27}$$

One step of the Euler method is given

$$y_{n+1} = y_n + hf(t_n, y_n) \tag{3.28}$$

where h represents the time between successive integration steps ($t_n + 1 = t_n + 1$). The global error of this method is $O(h^1)$. A time step (h) should be chosen sufficiently small to give stable solutions but not excessively small, as this will increase computation time.

The Rush-Larsen method is a common improvement to the Euler method [146], which solves a gating equation of the form given in equation (3.12) using

$$y_{n+1} = y_\infty + (y_n - y_\infty)\, exp\frac{-\Delta t}{\tau_y} \tag{3.30}$$

3.8.1.2 The Runge-Kutta 4th Order Method (RK4)

The Runge-Kutta fourth order method is reasonably simple, robust and more accurate compared to Euler method in the mathematical models to solve the ODEs. It is a multi-step ODE solver, therefore, instead of taking just one evaluation at each time step (h), the RK4 treats every step identically in a sequence of steps and in each step this method makes four estimations and then averages them: once at both the initial point and trial endpoint while the derivative is evaluated twice at trial midpoints. For the initial value problem (Equation 3.26) (the same as Euler method mentioned before)

The next step is found by the following equations:

$$y_{n+1} = y_n + hf\left(\frac{1}{6}(k_1 + 2k_2 + 2k_3 + k_4)\right) \tag{3.31}$$

$$k_1 = f(t_n, y_n) \tag{3.32}$$

$$k_2 = f(t_n + \frac{1}{2}h, y_n + \frac{1}{2}hk_1) \tag{3.33}$$

$$k_3 = f(t_n + \frac{1}{2}h, y_n + \frac{1}{2}hk_2) \tag{3.34}$$

$$k_4 = f(t_n + \frac{1}{2}h, y_n + \frac{1}{2}hk_3) \tag{3.35}$$

The weighted average of $k_1 - k_4$ can be utilized to evaluate y_{n+1} with more weight given to the mid step (k_2 and $k_3$calculations).

The classical 4th order Runge-Kutta method has global error $O(h^4)$. It should be noted that taking more estimations between time steps, allowing to use larger time steps with a high accuracy [147].

The explicit schemes introduced above may not be favourable for a system with stiff ODEs as these schemes may require extremely small integration steps. Therefore, some robust, usually implicit schemes should be considered for such systems. Many open source ODEs solvers are available to use, including LSODE [148] and CVODE [149].

3.8.2 Numerical Methods for Solving PDEs

Mathematical modelling at tissue level can be generalised using PDEs. In cardiac modelling, PDEs have been solved using either the finite difference method (FDM) or the finite element method (FEM). The FDM method is the simple and most popular method that used for discretising the monodomain equation (Equation 3.20) in updating the cardiac cell voltage within a geometry.

The FDM can be explained simply in 1D problem. Assuming that the myocytes or nodes in a 1D strand are aligned with equivalent spacing step Δx and time step Δt, then the voltage in (Equation 3.20) is solved using the FDM as bellow:

$$V_x^{t+\Delta t} = V_x^t + \frac{D\Delta t}{(\Delta x)^2}(V_{x-\Delta x}^t + V_{x+\Delta x}^t - 2V_x^t) \quad (3.36)$$

The forward Euler method can be used here for the discretisation over time. In cardiac tissue, when using the FDM, the space steps are commonly equivalent in all three dimensions.

The term $\frac{D\Delta t}{(\Delta x)^2}$ is related to the numerical stability, and must be satisfied (usually smaller than 0.5) in order to achieve convergences [66, 150].

The finite element method (FEM) is another method that can be used in cardiac simulations in solving the spatial diffusion of the action potential. Although the implementation of the FEM is non-trivial as it can be more difficult to interpret, FEM is more robust and has advantages over the FDM in terms of assessing boundary conditions and achieving solutions to problems with complex geometries [143].

Furthermore, there are some alternatives methods involving; the finite volume method, the boundary element method and the discrete element method, which are considered as less commonly used methods [143].

4. Development of a Novel Model for Simulating the Electrical Action Potentials of Teleost Fish Ventricular Cells

Cardiac electrophysiological models become an alternative method to experimental cardiology for the studies of the heart function. From early 1950, mathematical models for simulating cardiac membrane action potentials (APs) have been developed [47], these models were based on detailed experimental data of kinetics and biophysical properties of the underlying ion channels. Different complex potential interactions of intracellular ions and transmembrane currents make computer modelling as the only method accessible to synthesize and understand these multiple nonlinear interactions. Accordingly, the action potential of the cardiac myocytes can be restructured, based on detailed biophysical formulations of the fundamental ionic currents, pumps, and exchangers as well as intracellular ionic homeostasis [49, 56, 57].

The range of normal heart rates, sets of ionic currents (where density and kinetics vary among species), shapes and durations of the cardiac myocytes of AP are special features for each animal heart. These differences reflect corresponding variations in the molecular basis of repolarization and thus pharmacological responses. Different electrophysiological models in several species such as human [55], rat [48], mouse [53] and guinea pig [151] and have been developed and have proven useful in the study of mechanisms underlying healthy and diseased cardiac electro- physiology [53]. However, no such models exist for the fish heart, which is unusual as they are a growing model for human cardiac dysfunction [40, 70–73] and an important species to for human food consumption and environmental health. As discussed in Chapter 1, teleost fish as ectotherms do not maintain body temperature using metabolically generated heat, which means that heart temperature changes with body temperature which can have intense effects on both electrical and mechanical function [40]. Therefore, in this Chapter, electrophysiological models will be developed in order to study the ion channels remodelling in the teleost fish ventricular myocytes at thermal acclimation. The thermal adaption may experience by such ectothermic animal to acclimate temperature change in long term such as season temperature or in diving at different water depths.

4.1 Introduction and Aims

Eurythermal fish are species that live in variable thermal environments. For these animals water temperature, and thus heart temperature, may change by more than 30°C seasonally or when diving vertically across thermoclines in the oceans (i.e. acute changes) [30, 152]. Because temperature is a fundamental driver of all reactions rates, both acute or chronic temperature changes can severely impact the fish heart function. Changes in the electrical and contractile function of the whole heart with temperature are determined by temperature dependent changes in ionic conductance through the ion channels and ionic pumps in membrane of the cardiomyocytes that form the fish heart. This indicates that the body temperature of ectotherms can change quite significantly when the ambient temperature changes, leading to set special demands on the ion channels function to maintain tolerable excitability of cardiac cells in different temperatures [15]. Therefore, a well understanding to the temperature change effects on individual ion channels, and their culmination in the cellular action potential, provides insight into how such changes impact the myocyte, the whole heart and possibly the well-being of the animal in a changing thermal environment.

From the late 1980s, many studies [15, 17, 41–44, 80, 109] have made a big effort to investigate the temperature dependence of the properties of ion channels and Ca^{2+} handling in the fish heart. Many articles have been published to date; however, it is still insufficient to give the whole picture of the temperature dependence of the heart function of the fish. This is mainly because different fish species have shown a different response to changing temperature as well as different thermal limitations [41–44, 107, 153].

The global climate studies [12, 21, 23, 26] have predicted that in the near future, rises in the severity, frequency and duration of extremes temperature will occur [30], which may induce cardiac arrhythemais or even a fish sudden death. Therefore, the ionic and molecular mechanisms of electrical excitation of the fish cardiac myocytes can be studied through the mathematical models which can provide essential information to understand the heart mechanisms that limit the performance and survival of ectothermic animals under climate change [32].

It has been found that due to the large impacts of changing acute temperature on the heart function, eurythermal species are able to adjust the expression and/or the regulation of cardiac ion channels to maintain cardiac function during prolong temperature change [30]. This induces a thermal remodelling of ion channel expression, known as thermal (or seasonal) acclimatization when it occurs in nature, or thermal acclimation when animals are subjected to temperatures changes in the laboratory.

Therefore, the first aim of this Chapter was to develop a novel biophysically detailed mathematical model for the electrical action potentials for a teleost fish ventricular myocyte and then used this model to understand the effects of changing temperature acutely and chronically on the teleost heart excitation. The electrophysiological model was first developed for fish living in chronic cold (cold-acclimated) at the physiological temperature of 4°C environment, then this model was developed for fish living in chronic warm (warm-acclimated) at the physiological temperature of 18°C environment, and at the common experimental temperature of 11°C (for cold acclimation (CA) and warm acclimation (WA)). All these models based on the extensive work of Vornanen and colleagues [15, 17, 43, 43, 107, 154]. The equations of the models were based on biophysically derived descriptors of experimentally recorded major ionic currents in isolated ventricular myocytes. A set of novel Hodgkin-Huxley (HH) formulations for the major ion current including (fast Na^+ current (I_{Na}), L-type Ca^{2+} current (I_{CaL}), rapid delayed rectifier K^+ current (I_{Kr}) and inward rectifier current (I_{K1}) have been developed. Although there are species-specific differences in the electrical excitation of fish hearts, most experimental findings demonstrate consistency in ventricular AP shape and its ionic current basis [41, 42, 153]. Nevertheless, the mathematical models used here were based, whenever possible, on published and unpublished experimental data from salmonid species such as rainbow trout [15, 42, 43, 107], but in places also include data from lamprey [155] and bluefin tuna [154].

The developed single cell models were used for simulating the electrical action potentials (APs), and their changes were induced by chronic temperature changes in single cell level to validate the models for CA and WA. Simulation results were compared quantitatively to experimental data. Details of the development models are documented in the following Sections.

4.2 Methods

The teleost ventricular model at cold acclimated, 4°C (or chronic cold, when fish maintained at specific temperature, such as the physiological body temperature of 4°C, for several weeks and all the ion channels properties were assessed experimently at this temperature [43]) consists of a family of mathematical equations for the membrane ion channel currents responsible for generating the electrical APs of teleost ventricular cells. The developed model is based on a set of Hodgkin and Huxley formulations that are inherited from some existing mathematical models of mammalian hearts including Luo and Rudy's model for human ventricular myocytes [54], Pandit and colleagues model for rat ventricular myocytes [48] and Courtemanche and colleagues model for human atrial myocytes [156].

4.2.1 Voltage Clamp Protocols

In this thesis, to produce the current-voltage relationship, voltage clamps were simulated (where needed) for the main ion channels currents using different voltage clamp protocols. This depends on the experimental measurements for each specific ion channel at a particular temperature, as described previously in Section 2.7.1. In the model, the voltage membrane (V_m) is set to the holding voltages and clamp voltages steps for the correct of time periods, and current returned.

4.2.2 Cell Model

Figure 4.1 illustrates the schematic for the cell model developed in the current chapter. The model describes 11 membrane ion currents: one is an ion exchanger, two are ionic pumps, and eight are passive ion channels [157]. Therefore, the total ionic current is given by the following Equation:

$$I_{ion,tot} = I_{Na} + I_{CaL} + I_{Kr} + I_{K1} + I_{Cab} + I_{Nab} + I_{Kp} + I_{pCa} + I_{K(ATP)} + I_{NaCa} + I_{NaK} \quad (4.1)$$

while the dynamical course of membrane potential (V) with over time (t) in the fish models was described by the following differential equation:

$$-C_m \frac{dV}{dt} = I_{Na} + I_{CaL} + I_{Kr} + I_{K1} + I_{Cab} + I_{Nab} + I_{Kp} + I_{pCa} + I_{K(ATP)} + I_{NaCa} + I_{NaK} + I_{stim} \quad (4.2)$$

where C_m is the membrane capacitance and I_{stim} is the stimulus (external) current. The notation for ion channel currents and their permeability type are shown in Table 4.1.

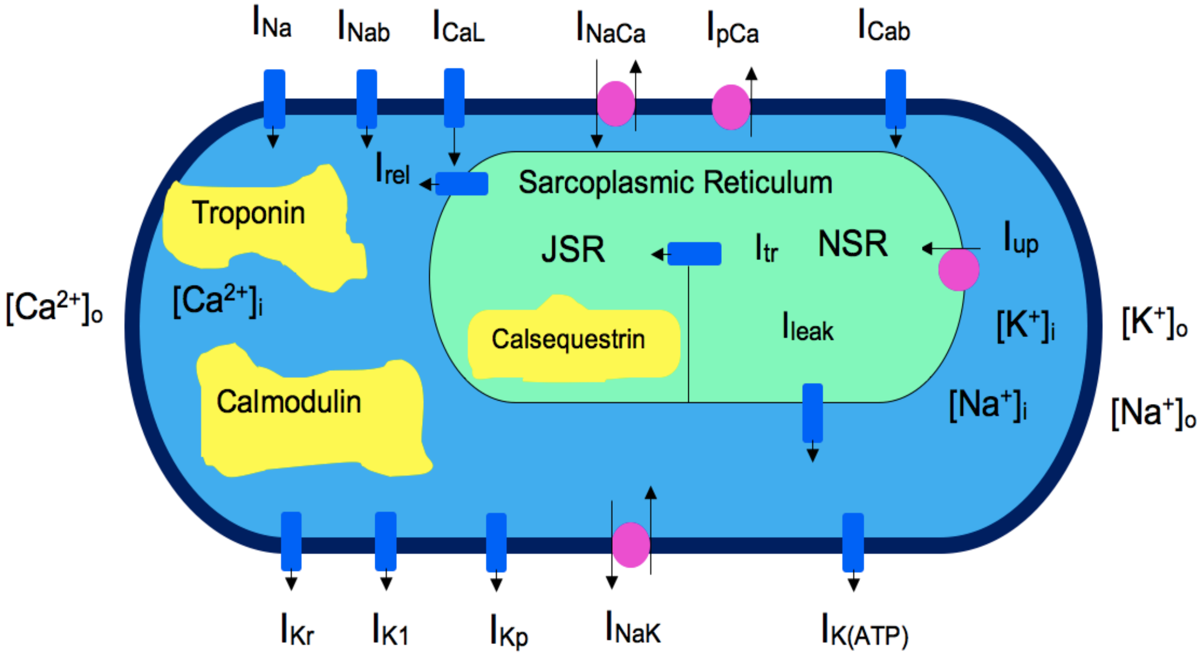

Figure 4.1. Schematic diagram of the teleost fish ventricular model with different ionic currents and Ca^{2+} fluxes that generate APs. The fluxes within the cell are uptake of Ca^{2+} from the cytosol to the network sarcoplasmic reticulum (SR) (I_{up}), Ca^{2+} leak from the SR to the cytosol (I_{leak}), Ca^{2+} flux from the network SR (NSR) to junctional SR (JSR) (I_{tr}), Ca^{2+} release from the junctional SR (I_{rel}). This was published in [157].

Table 4.1: The currents names in the developed fish ventricular model and their permeability type.

Symbol	Name	Permeability	Type
$\boldsymbol{I_{Na}}$	Fast sodium current	Ion channel	Na^+
$\boldsymbol{I_{Nab}}$	background sodium current	Ion channel	Na^+
$\boldsymbol{I_{CaL}}$	L-type calcium current	Ion channel	Ca^{2+}
$\boldsymbol{I_{Cab}}$	background calcium current	Ion channel	Ca^{2+}
$\boldsymbol{I_{Kr}}$	Rapid delayed rectifying K^+ current	Ion channel	K^+
$\boldsymbol{I_{K1}}$	Inwardly rectifying K^+ current	Ion channel	K^+
$\boldsymbol{I_{NaCa}}$	Sodium calcium exchanger current	Ion exchanger	Na^+/Ca^{2+}
$\boldsymbol{I_{NaK}}$	Sodium potassium pump	Ion pump	Na^+/K^+
$\boldsymbol{I_{pCa}}$	Calcium pump	Ion pump	Ca^{2+}
$\boldsymbol{I_{Kp}}$	Plateau potassium current	Ion channel	K^+
$\boldsymbol{I_{K(ATP)}}$	ATP sensitive potassium current	Ion channel	K^+

4.2.3 Inclusion of the Formulations for the Major Ionic Currents

New formulations of the major ionic currents including I_{Na}, I_{CaL}, I_{Kr} and I_{K1} have been developed using the available experimental records from different teleost species at cold-acclimated, 4°C (except for the I_{Kr} kinetics which were calculated at 5°C). Then these formulations have been incorporated into Luo and Rudy's model [54], which forms the basal framework of our computer model for the teleost ventricular cells. In addition, the teleost ventricular cell model also includes formulations for the other currents including I_{Nab}, I_{Cab}, I_{pCa}, I_{Kp}, $I_{K(ATP)}$, I_{NaCa} and I_{NaK}, however, these formulations are similar to those previously developed by Luo and Rudy in 1994 [54] as there are no studies published yet about these currents in the fish heart. The full description of the main currents will be discussed in the next Sections.

4.2.3.1 Fast Sodium Current, $\mathbf{I_{Na}}$

Voltage-gated sodium (Na^+) channels allow fast Na^+ influx, which is essential for the heart excitability [43]. The fast Na^+ current (I_{Na}) is the first current to be activated in the ventricular myocytes and it is responsible for providing the necessary charge to depolarise the cell membrane (initial depolarisation of the AP) and activate other ion channels [158, 159].

The sodium current (I_{Na}) determines the amplitude and slope of the AP upstroke to regulate the excitability threshold and to control conduction velocity impulse [160]. Moreover, I_{Na} plays an important role in the excitation–contraction coupling of cardiac cells [104, 161, 162]. Generally, in the trout fish heart, the I_{Na} current is produced by the Nav1.4a subunits [163].

The I_{Na} equations are obtained by modifying the Hodgkin-Huxley formulations of Luo and Rudy's model [54] for ventricular myocytes and are based on Haverinen and colleagues experimental data for isolated rainbow trout ventricular myocytes at a physiological temperature of 4°C of the fish heart [43].

The I_{Na} mathematical model consists of a fast activation variable (m) and a fast inactivation variable (h) with an absence of the slow inactivation variable (j) as this gate has not shown in the experimental findings of the teleost ventricular cells [43].

The basic kinetic characteristics of I_{Na} utilised in the model are based on voltage-clamp experiments in the ventricular cells of rainbow trout fish at 4°C [43]. These kinetics include the steady-state and their time constants for the activation and inactivation curves. To validate the model equations, the simulated I_{Na} current- voltage (I–V) relationship are compared to the experimental data [43] as shown in Figure 4.2.

The steady-state availability (inactivation gate) of I_{Na} indicates that the rate transfer of the Na^+ channels from resting closed state to the inactivated closed state was calculated when the membrane potential was clamped from -120 to -80 mV for different durations and then recording the I_{Na} at -20 mV was made [43, 104]. Therefore, the availability of Na^+ channel for voltages above -20 mV, was primarily determined by the non-inactivation fraction of Na^+ the channel (see Section 3.5). The kinetics of the inactivation was assessed from -40 to +10mV voltage range, where at 0 and +10 mV all Na^+ channels are activated [104]. As a result, the opening of Na^+ channels generates the inward Na^+ current (I_{Na}), density of which represents a major factor in modulating the rate of AP propagation over ventricular (as well as atrial) myocardia when the amplitude of I_{Na} exceeds those of simultaneously activated outward currents [30, 104].

Additionally, in fish ventricular myocytes, two opposing currents, I_{Na} and I_{K1}, are functionally closely linked and are key factors in the initiation of ventricular APs, where I_{Na} provides depolarizing current for the fast upstroke of the AP and I_{K1} maintains the negative RMP (see Section 4.2.3.4). Cardiac APs are provoked when the membrane is depolarized to the threshold potential, or to the level at which the magnitude of the inward I_{Na} (as numerous Na^+ channels are open) exceeds that of outward I_{K1} [30]. The electrochemical driving force favors Na^+ influx at the resting membrane potential (RMP), while the RMP depolarization restores the driving force for K^+ efflux through the inward rectifier channels. Therefore, a small depolarization of the RMP creates an inward surge of current which is the I_{Na} current by inducing a fast and transient opening of Na^+ channels and an outward surge of current which is the I_{K1} current by an immediate K^+ efflux through constitutively open inward rectifier K^+ channels. The intracellular inactivation gate closes the Na^+ channels quickly while the intracellular Mg^{2+} ions and polyamines temporarily prevents the K^+ efflux, as they enter the K^+ channel pore in a voltage-dependent manner and block it [30].

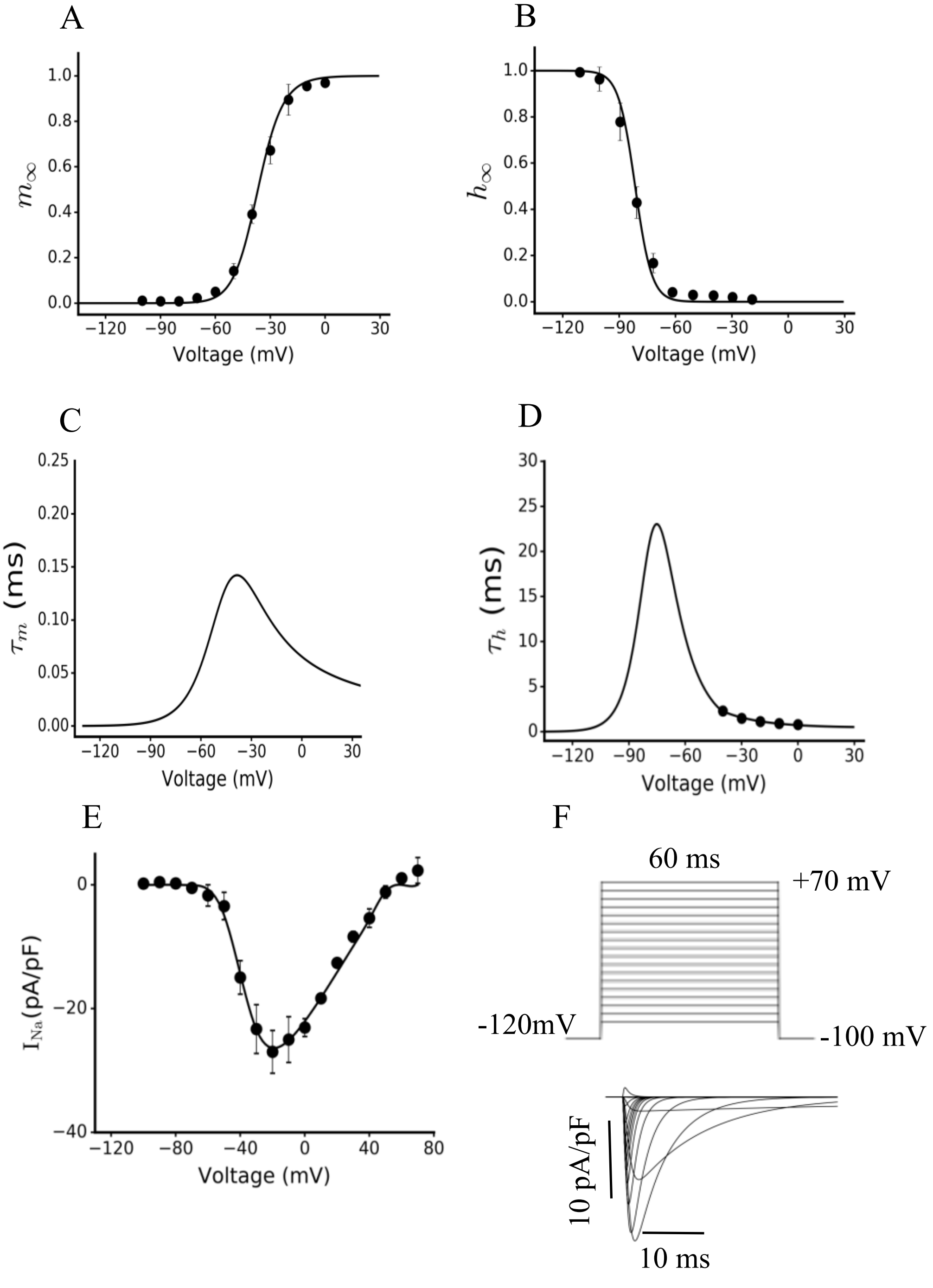

Figure 4.2. Parameters for the I_{Na} current model of the teleost fish ventricular myocytes at cold-acclimated, 4°C. A and B: Steady-state activation (m_∞) and inactivation (h_∞) variables, respectively. C, D: Activation (τ_m) and inactivation (τ_h) time constant. E: Simulated current-voltage (I-V) relationship of I_{Na}. F: Simulated I_{Na} during 60 ms voltage-clamp pulses to -100 to

+70 mV (in 10-mV increments) from a holding potential of -120 mV (top, voltage-clamp protocol; bottom, current trace). Model (lines) and experimental data (points) from [43].

The formulation for I_{Na} in the fish ventricular model is therefore as follows:

$$g_{Na} = 4.0\ (\mathrm{nS/pF})$$

$$I_{Na} = g_{Na} . m^3 . h . (V_m - E_{Na}) \tag{4.3}$$

$$\alpha_m = \frac{0.32(V_m+57.13)}{1-exp\left(-0.1(V_m+57.13)\right)} \tag{4.4}$$

$$\beta_m = 0.08 \exp((V_m + 8)/-11) \tag{4.5}$$

$$\tau_m = \frac{1}{(\alpha_m+\beta_m)} \tag{4.6}$$

$For\ \ V_m$ >= -40

$$\alpha_h = 0.0$$

$$\beta_h = \frac{0.8}{0.12(1+\exp((V_m+30.66)/-11))} \tag{4.7}$$

$For\ \ V_m$ < -40

$$\alpha_h = 0.135\ exp\left((V_m + 90)/-6.8\right) \tag{4.8}$$

$$\beta_h = 3.56 \exp(0.08V_m) + 3.1\times10^5 \exp(0.35V_m) \tag{4.9}$$

$$\tau_h = \frac{1}{(\alpha_h+\beta_h)} \tag{4.10}$$

Where V_m is the membrane potential, g_{Na} is the maximal channel conductance and E_{Na} is the reversal potential for sodium channels. E_{Na} is calculated from Nernst equation (see Section 3.4) and have the formulation of $E_{Na} = \left(\frac{\mathrm{RT}}{\mathrm{F}}\right) . \log\frac{[\mathrm{Na}^+]_\mathrm{i}}{[\mathrm{Na}^+]_\mathrm{o}}$.

The new formulation of I_{Na} closely reproduces the kinetics of the current in experimental conditions (Figure 4.2), which validated the model development. In the integral model, the maximum (g_{Na}) was corrected to produce a proper value for the action potential amplitude (APA) and the (dV/dt_{max}).

4.2.3.2 L-type Calcium Current, I_{CaL}

The L-type calcium (Ca^{2+}) current (I_{CaL}) is one of the major inward currents in vertebrate cardiac myocytes. In ectothermic vertebrates including fish, I_{CaL} is assumed to provide a substantial trans-sarcolemmal entry of Ca^{2+} during the relatively long plateau phase of the action potential, while in mammalian and avian hearts myocytes, it acts mainly as a trigger for Ca^{2+}-induced Ca^{2+} release from the SR [164, 165]. In teleost fish myocytes, the I_{CaL} current represents an essential component for excitation–contraction coupling [166] and for the long plateau phase (phase 2) of the AP of ventricular myocytes [167].

The mathematical model formulations for I_{CaL} were developed by modifying Pandit and colleagues' model [48] for rat ventricular cells based on experimental records from isolated rainbow trout ventricular cells at 4°C [107]. These formulations include voltage- and time-dependent activation and inactivation, in addition to Ca^{2+} dependent inactivation. In a teleost heart, I_{CaL} influences the plateau phase and thus the AP morphology, therefore, the value of the I_{CaL} maximum conductance (g_{Cal}) was corrected to ensure that the Ca^{2+} ion influx via I_{CaL} during the simulated AP was comparable to those measured experimentally [107].

Figure 4.3 shows the basic kinetic characteristics of I_{CaL} including the simulated steady-state activation and inactivation curves, the time constants for activation, fast and slow components of inactivation and also the peak (I–V) relationship with the experimental data [107].

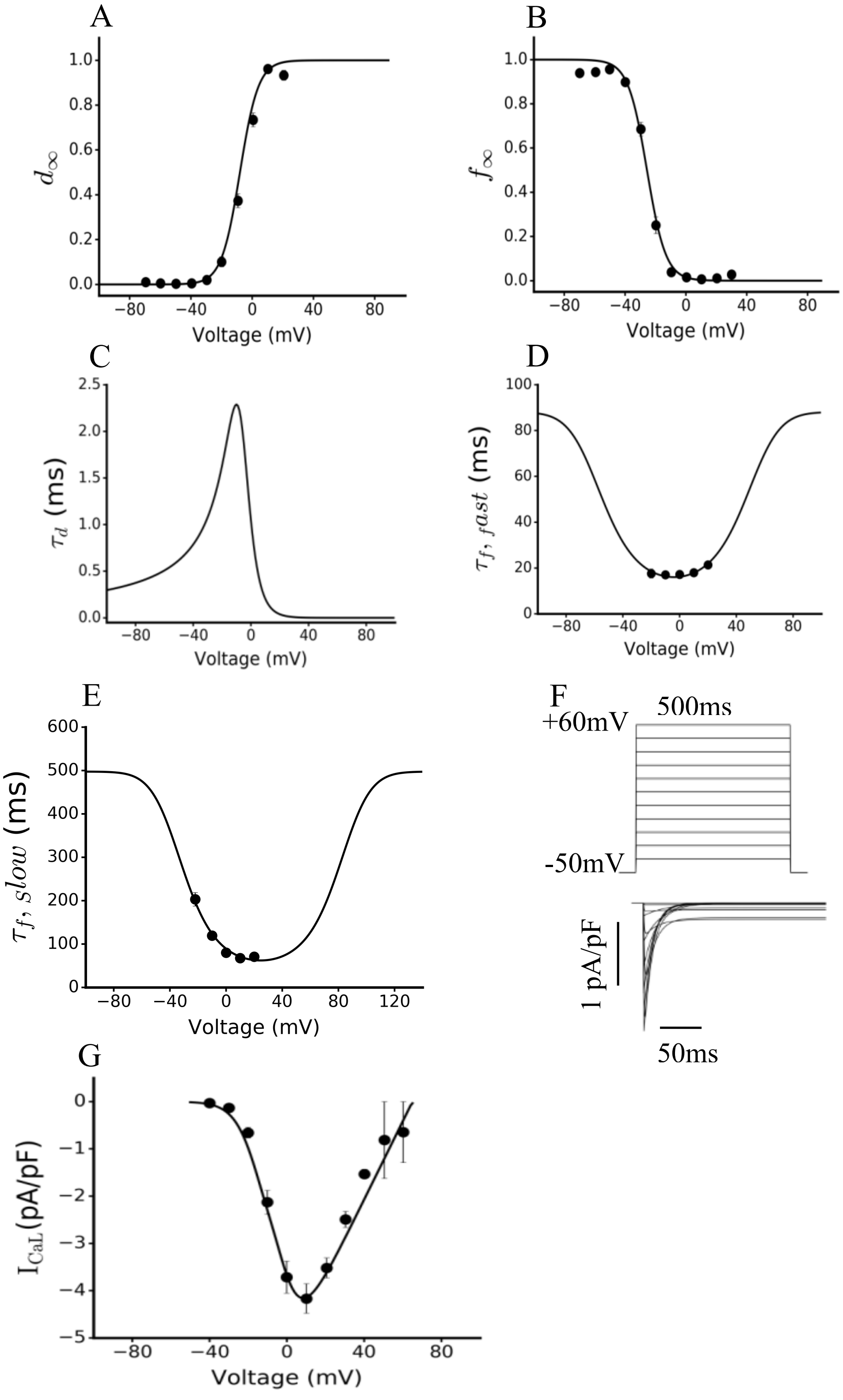
A
d_∞
1.0
0.8
0.6
0.4
0.2
0.0
−80
−40
0
40
80
Voltage (mV)
B
f_∞
1.0
0.8
0.6
0.4
0.2
0.0
−80
−40
0
40
80
Voltage (mV)
C
τ_d (ms)
2.5
2.0
1.5
1.0
0.5
0.0
−80
−40
0
40
80
Voltage (mV)
D
$\tau_{f,\,fast}$ (ms)
100
80
60
40
20
0
−80
−40
0
40
80
Voltage (mV)
E
$\tau_{f,\,slow}$ (ms)
600
500
400
300
200
100
0
−80
−40
0
40
80
120
Voltage (mV)
F
500ms
+60mV
-50mV
1 pA/pF
50ms
G
I_{CaL} (pA/pF)
0
−1
−2
−3
−4
−5
−80
−40
0
40
80
Voltage (mV)

Figure 4.3. Parameters for the I_{CaL} current model of the teleost fish ventricular myocytes at cold-acclimated, 4°C. A and B: Steady- state activation (d_∞) and inactivation (f_∞) variables, respectively. C, D, E: Activation (τ_d), fast inactivation ($\tau_{f,fast}$)and slow inactivation ($\tau_{f,slow}$) time constant, respectively. F: Simulated I_{CaL} during 500 ms voltage-clamp pulses to -50 to +60 mV (in 10-mV increments) from a holding potential of -50 mV (top, voltage-clamp protocol; bottom, current trace). G: Simulated current-voltage (I-V) relationship of I_{CaL}. Model (lines) and experimental data (points) from [107].

The formulation for I_{CaL} in the fish ventricular model is therefore as follows:

$$g_{CaL} = 0.05 \text{ (nS/pF)}$$

$$E_{Ca} = 65 \text{ mV}$$

$$I_{CaL} = g_{CaL}.d.f.f_{Ca}.(V_m - 65) \tag{4.11}$$

$$d_\infty = \frac{1}{1+\exp\left(\frac{V_m+10}{-6}\right)} \tag{4.12}$$

$$\tau_d = \frac{1 - 0.16\,exp\ ((V_m+10)/-6.24)}{0.035(V_m+10)[(0.16\exp((V_m+10)/-6.24))+(1+\exp\ (V_m+10)/-6.24)]} \tag{4.13}$$

$$f_\infty = \frac{1}{1+\exp((V_m+20.6)/6.2)} \tag{4.14}$$

$$\tau_{f,slow} = 600\{1 + 0.1.exp[-0.0007(V_m - 9)^2]\}^{-1} \tag{4.15}$$

$$\tau_{f,fast} = 300\{1 + 0.1.exp[-0.0007(V_m - 4)^2]\}^{-1} \tag{4.16}$$

$$f_{ca} = 0.29 + 0.8\left[1 + exp\left(\frac{[Ca^{2+}]_i - 0.12}{0.6}\right)\right]^{-1} \tag{4.17}$$

where g_{CaL} is the maximum conductance, E_{Ca} is the reversal potential and V_m is the transmembrane potential.

The new formulation of I_{CaL} satisfactorily replicates the kinetics of the current as seen in experimental conditions (Figure 4.3), which validated the model development.

4.2.3.3 Rapid Delayed Rectifying Potassium Current, $\boldsymbol{I_{Kr}}$

The delayed rectifier K^+ current with its two major components, fast (I_{Kr}) and slow (I_{Ks}), produces the final rapid repolarisation of the AP of the cardiac myocytes [51, 156, 158]. This is true in the fish heart; however, most fish cardiac studies to date have shown that the delayed rectifier slow component current (I_{Ks}) is absent in the teleost ventricular myocytes [15, 155]. In early AP plateau, I_{Kr} activates and it has a strong modulate to the AP duration (APD) with a slight, if any, effect on resting membrane potential (RMP) [42].

Therefore, in this model, we incorporated the rapid current only (I_{Kr}). I_{Kr} equations were constructed by modifying the model by Courtemanche et al. [156] for human atrium cells and using the experimental findings measured by Haverinen et al. [155]. Haverinen et al. found experimentally that with a small E-4031 sensitive (2μM), the ventricular myocytes of lamprey fish demonstrated an I_{Kr} tail current with a peak density of 1.3 ±0.32 pA/pF at 5°C [155]. I_{Kr} conductance was set to a value that matched tail current recordings in lamprey ventricular myocytes [155].

At the potassium (K^+) equilibrium potential (E_K), I_{Kr} has been observed to reverse direction consistently, thus, only K^+ is supposed to carry I_{Kr}, and the reversal potential is equivalent to E_K [103]. The new formulation of I_{Kr} closely reproduces the kinetics of the current in experimental conditions (Figure 4.4).

Figure 4.4 shows the I_{Kr} activation curve which was fitted to the simulated activation curve of Courtemanche and colleagues' [156] model (as no experimental fish data was found) and the (I-V) relationship curve. I_{Kr} was measured at the end of the pulse from the model, which is reasonably close to the experimental data [155].

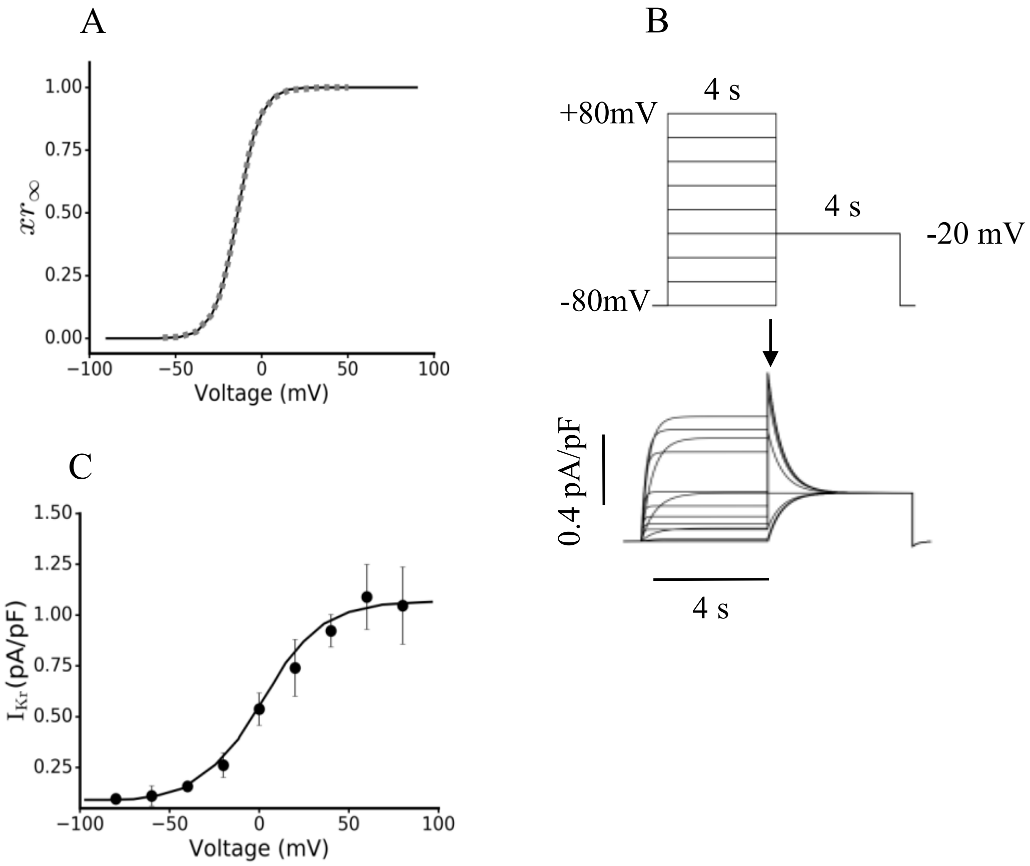

Figure 4.4. Parameters for the I_{Kr} current model of the teleost fish ventricular myocytes at 5°C. A: Steady- state activation (xr$_\infty$) variable. B: Simulated I_{Kr} during 4s pulses applied to potentials between -70 to +80 mV (in 10-mV increments) from a holding potential of -80 mV (top, voltage-clamp protocol; bottom, current trace). I_{Kr} was measured at the end of the voltage-clamp pulses (I_{Kr}, measured as the peak 2μM E-4031-insensitive tail current after a 4s pulse to -20 mV from a holding potential of -80 mV). C: Simulated current-voltage (I-V) relationship of I_{Kr}. Model (lines), dashed line represents the steady- state activation from [156] while experimental data (points) from [155].

The formulation for I_{Kr} in the fish ventricular model is therefore as follows:

$$g_{Kr} = 0.08 \text{ (nS/pF)}$$

$$I_{Kr} = g_{Kr}.xr.r.(V_m - E_K) \tag{4.18}$$

$$r = \frac{1}{1+exp((V_m+15)/22.4)} \tag{4.19}$$

$$xr_\infty = \frac{1}{1+exp((V_m+16.1)/-9.5)} \tag{4.20}$$

$$\alpha_r = \frac{0.3\times10^{-5}(V_m+13.1)}{1-exp((V_m+5.0)/-3.3)} \tag{4.21}$$

$$\beta_r = \frac{7.4\times10^{-5}(V_m-328)}{exp((V_m-328)/5.1)-1} \tag{4.22}$$

$$\tau_{xr} = \frac{1}{\alpha_r+\beta_r} \tag{4.23}$$

where g_{Kr} is the maximum conductance, E_K is the reversal potential for potassium channels and V_m is the transmembrane potential. The new formulation of I_{Kr} reasonably reproduces the kinetics of the current as seen in experimental conditions (Figure 4.4), which validated the model development.

4.2.3.4 Inwardly Rectifying Potassium Current, I_{K1}

K_{ir} channels are robust inward rectifier potassium channels, conducting inward currents at transmembrane potentials negative to (E_K), with a merely permit to a limit K^+ efflux at more positive voltages. This is based on the voltage-dependent block of the channels [15]. In physiological system, the small amount of the outward current is important to control excitability, set RMP, and contribute in different body functions in numerous organs [15].

The inward rectifier current (I_{K1}) in the fish heart participates in the regulation of AP duration as it contributes to the late phase 3 repolarisation of AP. It also clamps the resting membrane potential (RMP) close to K^+ equilibrium potential to maintain the negative RMP (phase 4).

The formulations of I_{K1} modified from Luo and Rudy model [54] for ventricular cells and based on experimental data from isolated rainbow trout ventricular myocytes at 4°C measured by Hassinen et al. [168]. The new formulation of I_{K1} fairly reproduces the current kinetics in experimental conditions (Figure 4.5). The I_{K1} maximum conductance (g_{K1}) when $[K^+]_o$=5.4 mmol at 4°C was set to obtain a good fit to the experimental data [168], as shown in Figure 4.5.

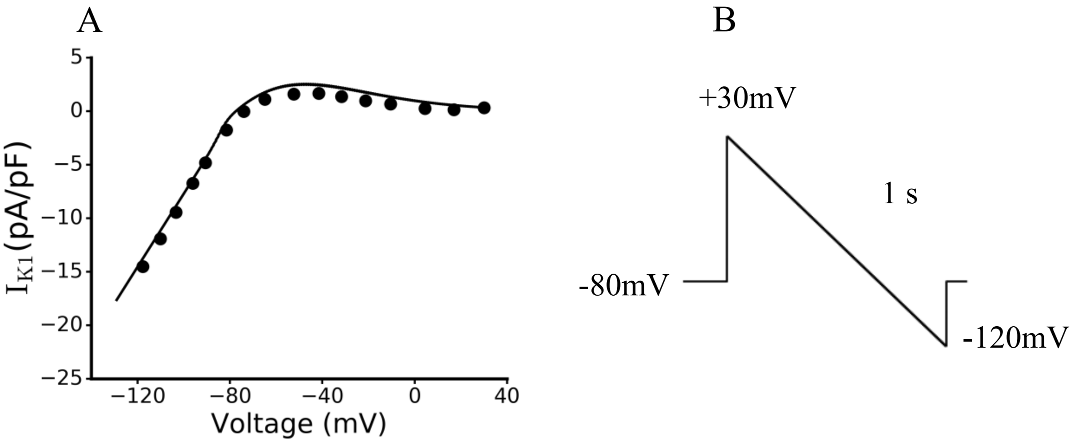

Figure 4.5. Parameters for the I_{K1} current model of the teleost fish ventricular myocytes at cold-acclimation, 4°C. A: The current-voltage relationship for I_{K1} from simulations. B: Simulated I_{K1} during 1s voltage-clamp pulse to -120 to +30 mV (in 10-mV increments) from a holding potential of -80 mV. Model (lines) and experimental data (points) from [15]

The formulation for I_{K1} in the fish ventricular model is therefore as follows:

$$I_{K1} = g_{K1}.K.(V_m - E_K) \tag{4.24}$$

$$\alpha_K = \frac{1}{1+exp\left(0.014(V_m - E_K + 7.21)\right)} \tag{4.25}$$

$$\beta_K = \frac{0.4\,exp\left(0.07(V_m - E_K + 0.57)\right) + exp\left(0.06(V_m - E_K + 584.31)\right)}{1+exp\left(-0.5(V_m - E_K + 4.35)\right)} \tag{4.26}$$

where g_{K1} is the maximum conductance, E_K is the reversal potential for potassium channels and V_m is the transmembrane potential. The new formulation of I_{K1} reproduces well the current kinetics as presented in the experimental data (Figure 4.5), which validated the model development.

4.2.4 Modelling Effects of Thermal Acclimation on the Major Ionic Currents

It has been found that ion channels of the fish cardiac myocytes respond strongly to chronic temperature changes [15, 43, 153], indicating that they are intimately involved in thermal tolerance and temperature acclimation of cardiac function. The species-specific differences in the electrical excitability reflected in different thermal dependencies of the fish heart, which might result from different channel structures and subunit assemblies. This Section centres on developing novel mathematical formulations of the kinetics of the major ion channels in the plasma membrane (contributing to the AP including I_{Na}, I_{CaL}, I_{Kr} and I_{K1}) of the teleost cardiac myocytes at cold and warm acclimation. The mathematical models (formulations) for each current were based on modifying the formulations that early developed in this Chapter at cold acclimation (or chronic cold), 4°C (see Section 4.2) in the regard of the related experimental findings from different teleost species. These models were developed at warm acclimation, 18°C (or chronic warm, when fish kept at warm of 18°C (which is a physiological body temperature) for several weeks and all the ion channels features were evaluated experimently at such temperature [43]) and at the common experimental 'test' temperature of 11°C when changing the ambinet temeprature of the examined fish; 1) acutely warmed from 4°C to 11°C (which are reffered to 11°C CA in the whole thesis), 2) acutely cooled from 18°C to 11°C (which are reffered to 11°C WA in the whole thesis). The kinetics of the major currents include steady- state activation and inactivation, time constants and the current voltage relationship (I-V), all of which were fitted (wherever possible) to the respective experimental data, and the effects of changing chronic acclimation (when 11°C WA and 11°C CA are compared) as well as changing temperature acutly (warmed from 4°C to 11°C CA or cooled from 18°C to 11°C WA) on these kinetics will discuss in details in the next subsections.

4.2.4.1 Temperature Effects on I_{Na}

The effects of thermal acclimation on I_{Na} are distinctive for teleost species and between cold-active and cold-dormant fish [43]. The mathematical model of I_{Na} at cold- acclimated, 4°C (see Section 4.2.3.1) has been modified according to the experimental data of rainbow trout from [43] to produce mathematical models of I_{Na} at 11°C (in CA and WA) (Figure 4.6 I, II) and at warm- acclimated, 18°C (Figure 4.6 III).

In rainbow ventricular cells, acclimation to cold (in the comparison of 11°C WA to 11°C CA) slightly shifted the steady-state activation curve of the I_{Na} current to the left for more negative values, by 6 mV, as shown in Figure 4.6 IA, IIA and Table 4.2. However, there was no difference noticed in the half voltage ($V_{0.5}$) of the steady-state inactivation curve (Figure 4.6 IB, IIB and Table 4.2), suggesting that the left shifting was specific for the steady-state activation curve [43, 104]. In addition, when the temperature acutely changed from the chronic acclimation temperature (4°C and 18°C) to the common experimental of 11°C (11°C CA and 11°C WA), it did not show any substantial effect on the $V_{0.5}$ of either steady-state activation or steady- state inactivation curves (see Table 4.2) [43]. Furthermore, when an acute increase in experimental temperature, the slope factor (k) of the steady-state activation curve in CA and WA rainbow trout and also the slope factor of the steady-state inactivation curve in WA trout were slightly increased (see Table 4.2). All of these changes in the kinetics of the channel, as seen from Haverinen and Vornanen [43], were considered in our simulations, as illustrated in Table 4.2.

On the other hand, cold acclimation increased the I_{Na} density of the ventricular myocytes of rainbow fish more than its value at warm acclimation as shown when compared the I_{Na} density at the common experimental temperature of 11°C (at CA and WA), (see Table 4.2). The trout I_{Na} density increase by cold is in line with the compensatory changes in function and size of the heart of trout fish, which counteract the effects of direct decelerating of low temperature on circulation [14, 169]. However, this thermal compensation was only partial [104], which can be seen when compare the density of I_{Na} at cold acclimated, 4°C (Figure 4.2) and warm acclimated, 18°C as the I_{Na} density at 4°C was approximately 58% of the density at 18°C [104] as shown in Table 4.2. This suggested that thermal compensation was only three-fifths of the amplitude of the I_{Na} current of the WA summer fish is required in the maintaining of the cardiac excitability in CA winter fish. Briefly, changes in the I_{Na} density as acclimation effects would mean that the upstroke rate and conduction velocity of APs are abstemiously depressed in rainbow trout while in other teleost fish species, such as carp, it can become harshly depressed [43].

In this study for model development, the basic kinetic characteristics of I_{Na} including the steady-state and the time constants for activation and inactivation curves used in the models are based on voltage-clamp experiments records of rainbow trout ventricular myocytes at 11°C CA, 11°C WA and 18°C, as shown below in Figure 4.6.

I

11°C (CA)

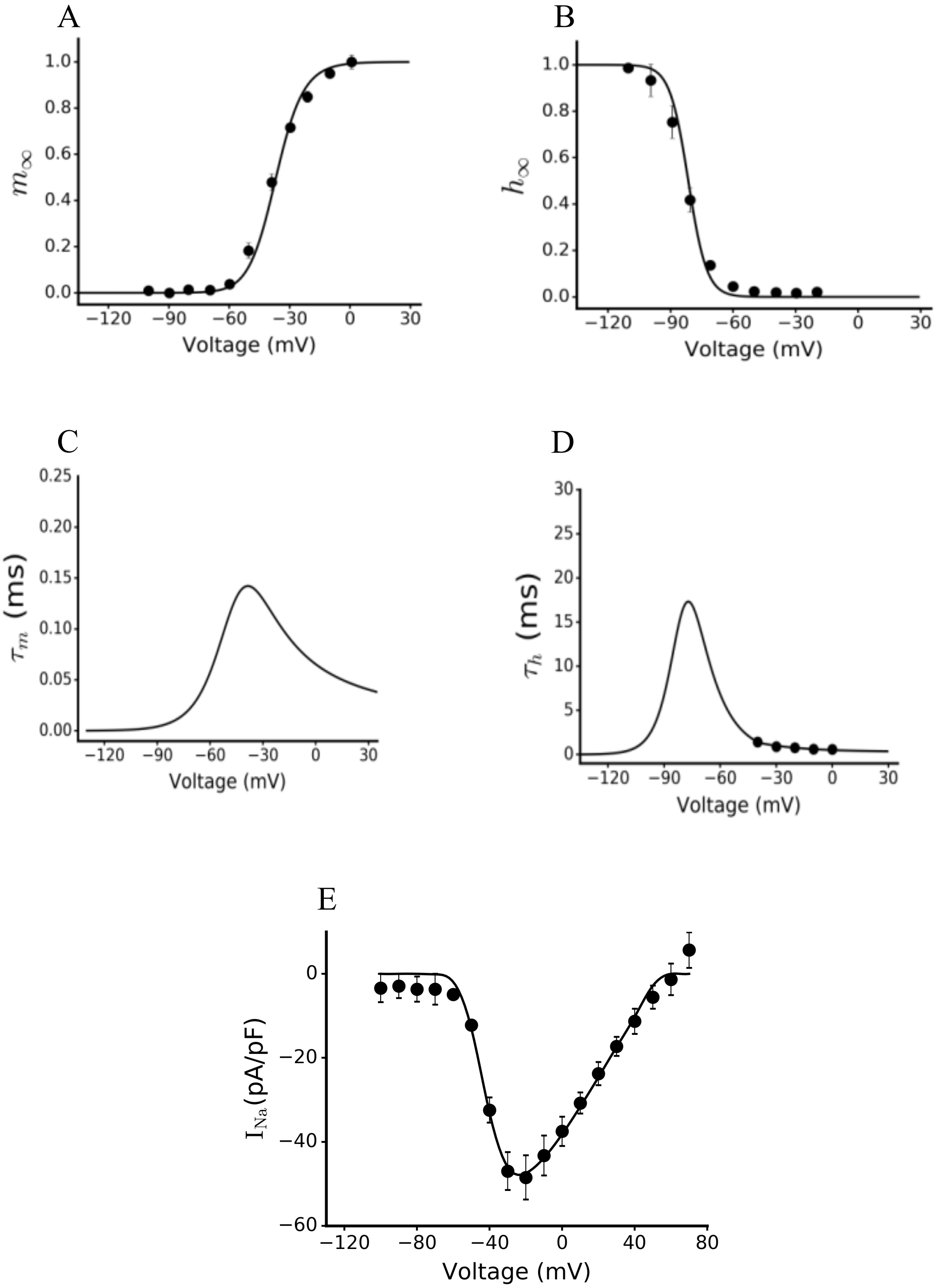

A
m_∞
1.0
0.8
0.6
0.4
0.2
0.0
−120
−90
−60
−30
0
30
Voltage (mV)
B
h_∞
1.0
0.8
0.6
0.4
0.2
0.0
−120
−90
−60
−30
0
30
Voltage (mV)
C
τ_m (ms)
0.25
0.20
0.15
0.10
0.05
0.00
−120
−90
−60
−30
0
30
Voltage (mV)
D
τ_h (ms)
30
25
20
15
10
5
0
−120
−90
−60
−30
0
30
Voltage (mV)
E
I_{Na}(pA/pF)
0
−20
−40
−60
−120
−80
−40
0
40
80
Voltage (mV)

II 11°C (WA)

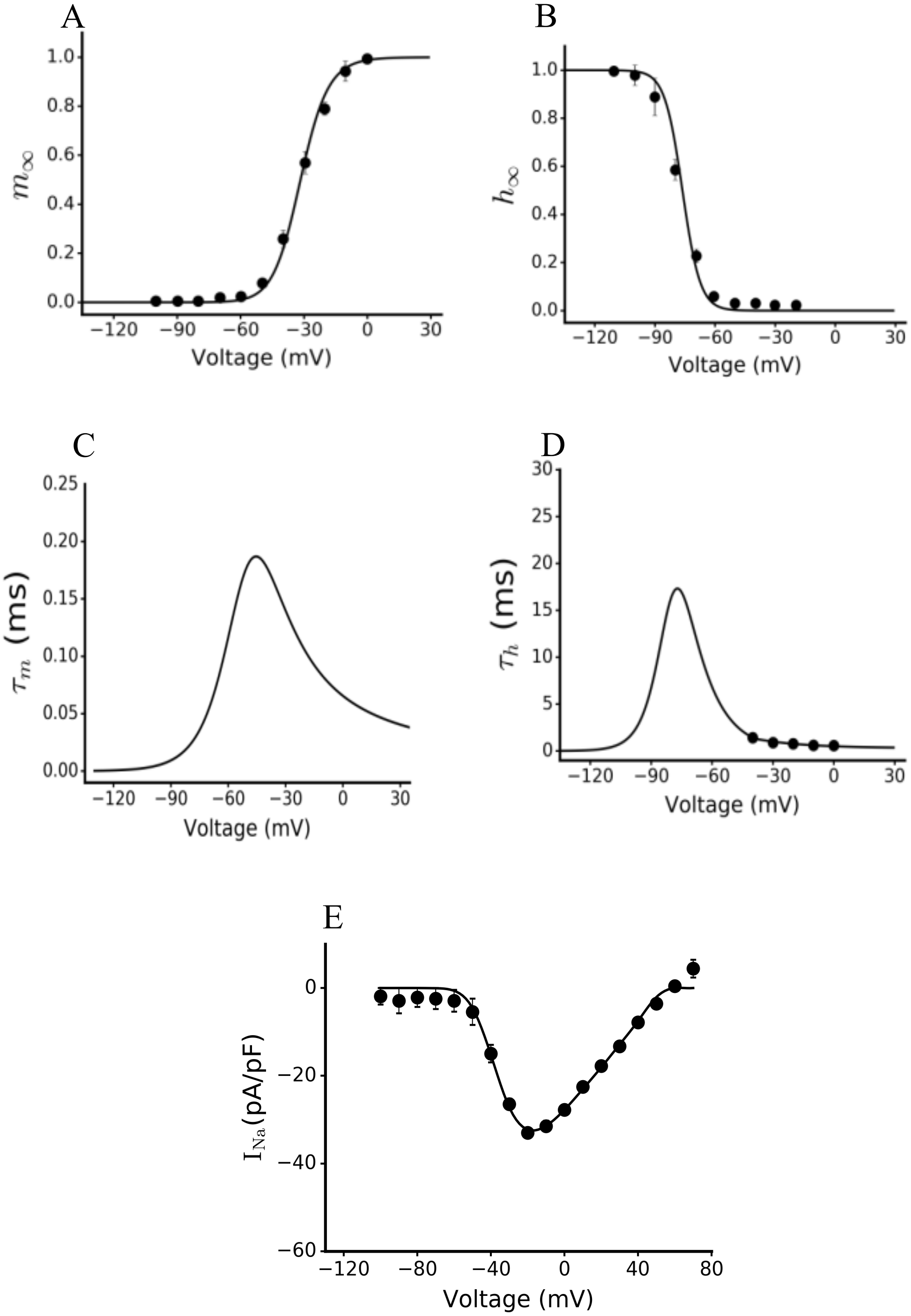
A
m_∞
1.0
0.8
0.6
0.4
0.2
0.0
−120
−90
−60
−30
0
30
Voltage (mV)
B
h_∞
1.0
0.8
0.6
0.4
0.2
0.0
−120
−90
−60
−30
0
30
Voltage (mV)
C
τ_m (ms)
0.25
0.20
0.15
0.10
0.05
0.00
−120
−90
−60
−30
0
30
Voltage (mV)
D
τ_h (ms)
30
25
20
15
10
5
0
−120
−90
−60
−30
0
30
Voltage (mV)
E
I_{Na}(pA/pF)
0
−20
−40
−60
−120
−80
−40
0
40
80
Voltage (mV)

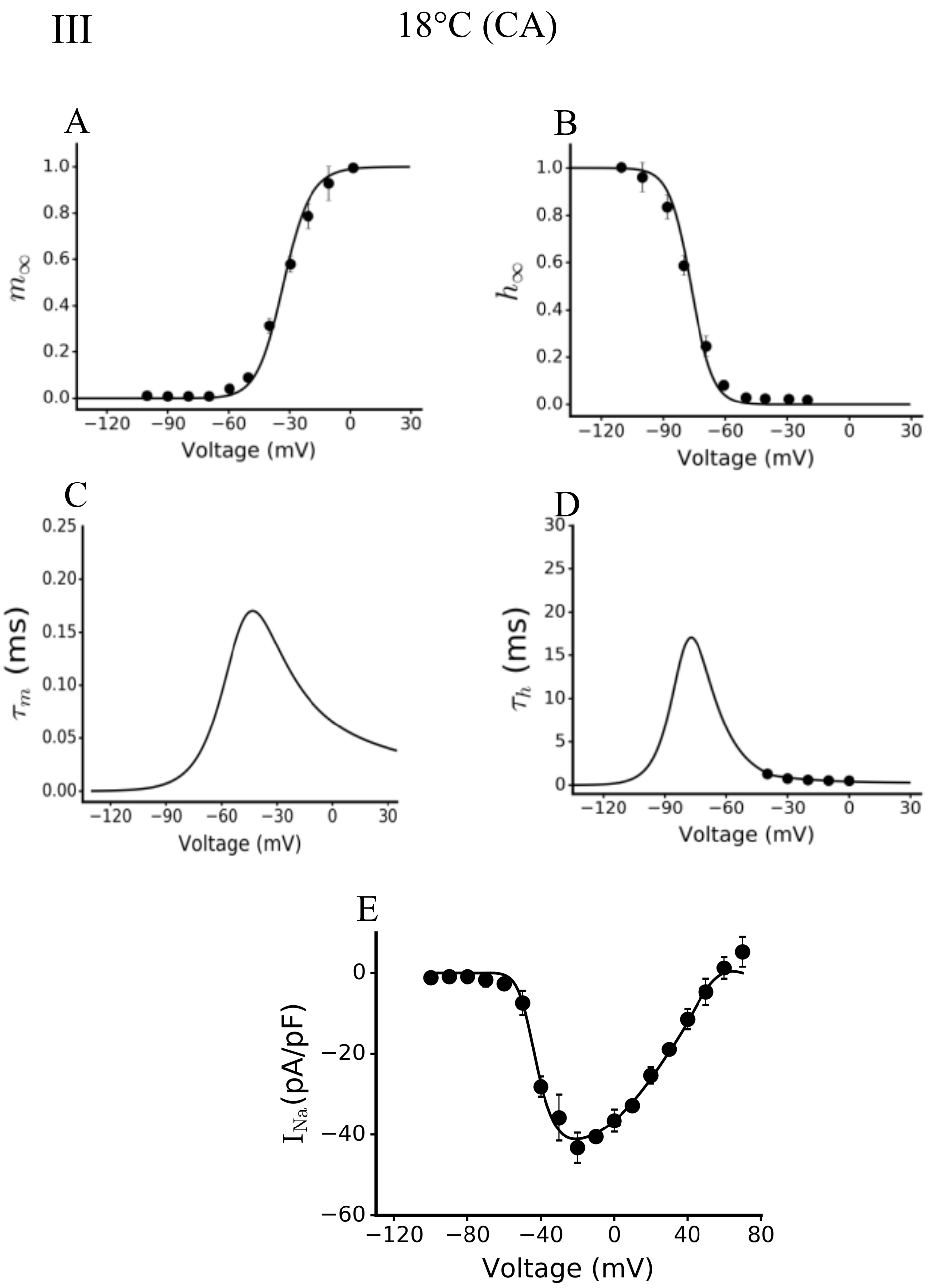

Figure 4.6. Parameters for the I_{Na} current model of the teleost fish ventricular myocytes at cold and warm acclimation. I, II and III, parameters for the I_{Na} current models at 11°C CA, 11°C WA and warm- acclimated, 18°C, respectively. From all the three Figures; A and B: Steady- state activation (m_∞) and inactivation (h_∞) variables, respectively. C, D: Activation (τ_m)and inactivation (τ_h) time constant. E: Simulated current-voltage (I-V) relationship of I_{Na}, Simulated current-voltage (I-V) relationship of I_{Na}. Model (lines) and experimental data (points) from [43].

Table 4.2: Temperature dependence of I_{Na} in ventricular myocytes of the rainbow trout heart as seen experimentally [43] and simulated in models, where T is the temperature in (°C), $V_{0.5}$ is the half voltage in (mV), k is the slope and CA and WA are the cold acclimation and warm acclimation, respectively. Note: blue refers to the cold temperatures while red refers to the warm temperatures.

T °C	**$V_{0.5}$ Steady-state activation (mV)**		**Slope(k)**		**$V_{0.5}$ Steady-state inactivation (mV)**		**Slope(k)**	
	Exp.	**Sim.**	**Exp.**	**Sim.**	**Exp.**	**Sim.**	**Exp.**	**Sim.**
4	-36.51±1.8	-36.31	7.32±0.3	7.63	-81.91±2.21	-82.22	6.42±0.23	6.66
11CA	-37.78±1.16	-38.56	8.5±0.39	8.44	-82.81±1.7	-82.63	6.6±0.29	6.58
11WA	-31.45±1.25	-31.50	7.32±0.2	8.02	-79.58±1.28	-78.12	6.05±0.12	5.93
18	-31.72±1.02	-32.23	9.05±0.39	8.80	-79.39±1.59	-78.21	6.64±0.25	7.02

4.2.4.2 Temperature Effects on I_{CaL}

Numerous physiological factors can modulate L-type Ca^{2+} channels of the vertebrate hearts such as nerve stimulation, circulating hormones, cellular pH and ATP supply [170]. Vornanen [107] discussed that in the fish heart, the physiological regulation of I_{CaL} significantly occurs through β-adrenergic receptors by circulating catecholamine or by releasing the local transmitter from autonomic nervous endings [107]. β-Adrenergic regulation of the fish heart is a dominant mechanism to maintain normal heart functions and to adjust the heart muscle to changing physiological and ecological conditions [107]. The trout heart sensitivity to β-adrenergic is increased when the temperature changes [171], indicating that cold-active species, such as rainbow trout fish, may need a tonic β-adrenergic stimulation to maintain sufficient cardiac function in the cold and during acute temperature changes [109]. Although thermal acclimation did not alter the density of I_{CaL} [107], the probability remains that extrinsic control of Ca^{2+} channel function, for example, by circulating hormones or neurotransmitters, is modified by the animal's previous thermal history [106].

In order to investigate the thermal acclimation impact on the I_{CaL} kinetics, mathematical models have been developed at cold and warm acclimation (similar to those of I_{Na}, that discussed in the previous Section). These kinetics have been computed using the formulations of I_{CaL} developed at cold- acclimated, 4°C (Section 4.2.3.2) after adjusting them with experimental data measured by Vornanen (unpublished data) at the common experimental temperature of 11°C (in CA and WA) (Figure 4.7 I, II) and at warm acclimated, 17°C (Figure 4.7 III) that measured by Vornanen [107]. There was a fairly close match between simulations and the experimental records, as shown in Table 4.3 and Figure 4.7.

It has been seen that acclimated to warm (11°C CA- 11°C WA) (Vornanen, unpublished data) did not show any noticeable change in the steady-state activation, but warm reduced the steady-state inactivation by around 6.5 mV, as shown in Figure 4.7 IA and Figure 4.7 IIA, respectively. Whereas at warm-acclimation, 17°C, the steady-state activation curve (Figure 4.7 IIIA) of trout ventricular myocytes was shifted slightly, but notably to more negative voltages, by 4 mV, compared with that of trout ventricular cells at cold-acclimation (Figure 4.2 A), with no obvious change in the steady-state inactivation curve [107] as shown in Table 4.3. This agrees with the leftward shift of the I-V curve in the myocytes of warm-acclimated trout [107]. Furthermore, when the fish body was acutely warmed from 4°C to 11°C CA, there was a 6 mV left shift in the $V_{0.5}$ of the steady-state activation (see Figure 4.2 A and Figure 4.7 IA) while the $V_{0.5}$ of the steady-state inactivation shifted significantly for more negative values, by 13 mV (see Figure 4.2 B and Figure 4.7 IB). Moreover, at warm acclimation (were acutely cooled from 17°C to 11°C), no substantial effect showed on $V_{0.5}$ of the steady-state activation (see Figure 4.7 IIIA and Figure 4.7 IIA), whilst a 6 mV shifting towards the negative was shown in the value of $V_{0.5}$ of the steady-state inactivation (see Figure 4.7 IIIB and Figure 4.7 IIB)). Additionally, at CA and WA trout, there was no major change in the slope factor (k) of the steady-state activation, however, the slope factor (k) of the steady-state inactivation slightly increased, as shown in Table 4.3. Furthermore, thermal acclimation unaltered the fast time constant of I_{CaL}, while there is a substantial long in the time constant of the slow component indicating that the decay of I_{CaL} was accelerated in the ventricular myocytes of warm-acclimated than in cold-acclimated trout [107] (Figure 4.7).

While thermal acclimation was unchanged the I_{CaL} density (Table 4.3), the inactivation kinetics difference between cold- and warm-acclimated trout, cannot be attributable to the influx of Ca^{2+}

through the channels themselves. The cold-induced increase in the Ca^{2+}- handling capacity of the SR suggesting more extensive Ca^{2+} release from the SR, which could be the reason for the faster inactivation of I_{CaL} in cold-acclimated trout [172]. Accordingly, in 1998, Vornanen [107] assumed that isoform changes in the components of the Ca^{2+} channel complex may be induced or that the diffusion-restricted microdomain structures that regulate Ca^{2+}-mediated inactivation of I_{CaL} alter by thermal acclimation [107].

Such temperature-dependent kinetics have been simulated at the common experimental temperature of 11°C CA and 11°C WA that measured by Vornanen (unpublished data) and at warm acclimated, 17°C [107]. These kinetics include steady-state activation and inactivation curves, the time constants for activation, the fast and slow components of inactivation used in the models, and the (I-V) curve with the respective experimental data, all of which are based on voltage-clamp experiments of rainbow trout ventricular myocytes from Vornanen (unpublished data) and from [107], as shown in Table 4.3 and Figure 4.7.

11°C (CA)

I

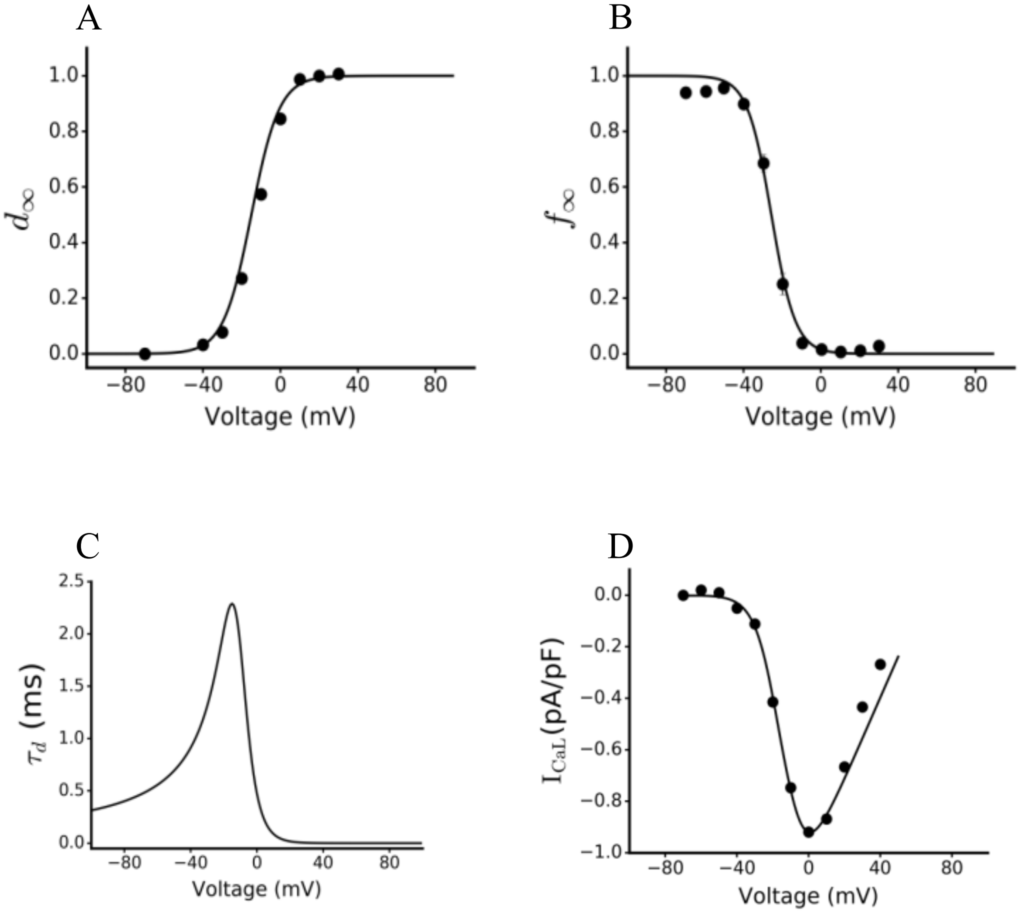
A
B
C
D
d_∞
f_∞
τ_d (ms)
I_{CaL} (pA/pF)
Voltage (mV)
1.0
0.8
0.6
0.4
0.2
0.0
2.5
2.0
1.5
1.0
0.5
0.0
−0.2
−0.4
−0.6
−0.8
−1.0
−80
−40
0
40
80

11°C (WA)

II

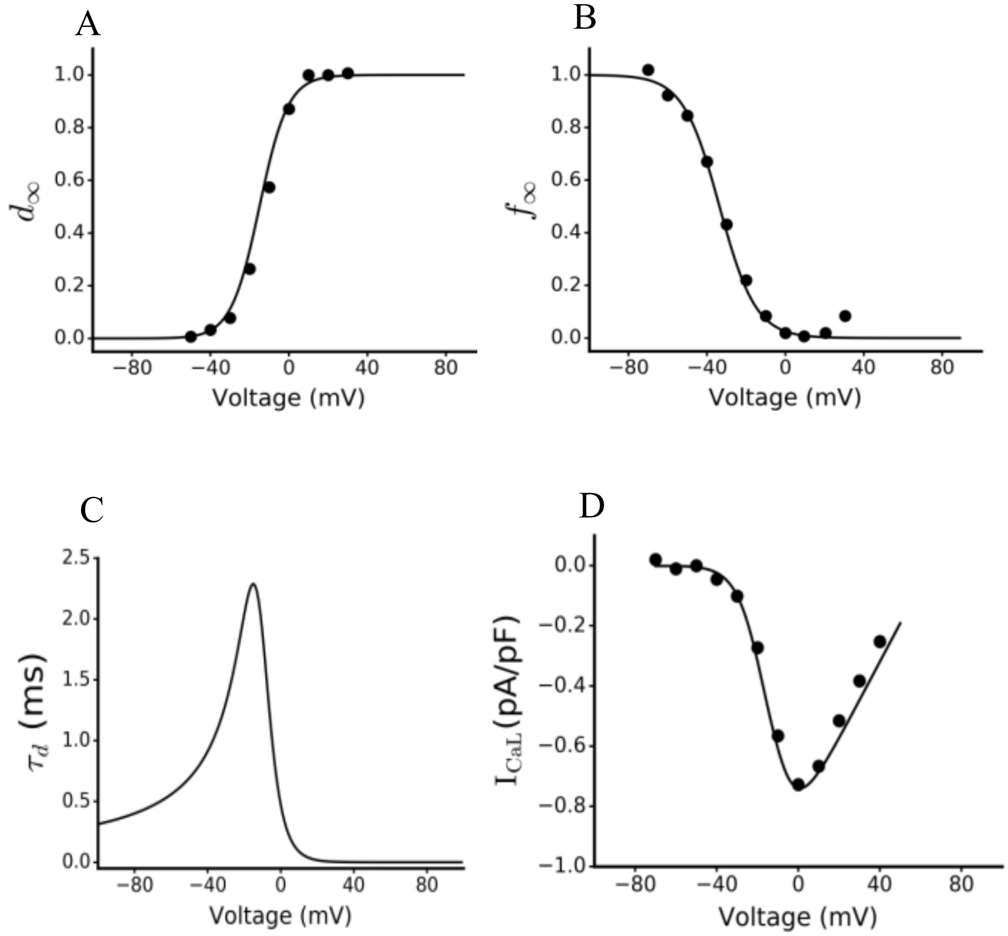
A
B
C
D
d_∞
f_∞
τ_d (ms)
I_{CaL} (pA/pF)
1.0
0.8
0.6
0.4
0.2
0.0
2.5
2.0
1.5
1.0
0.5
0.0
0.0
−0.2
−0.4
−0.6
−0.8
−1.0
−80
−40
0
40
80
Voltage (mV)

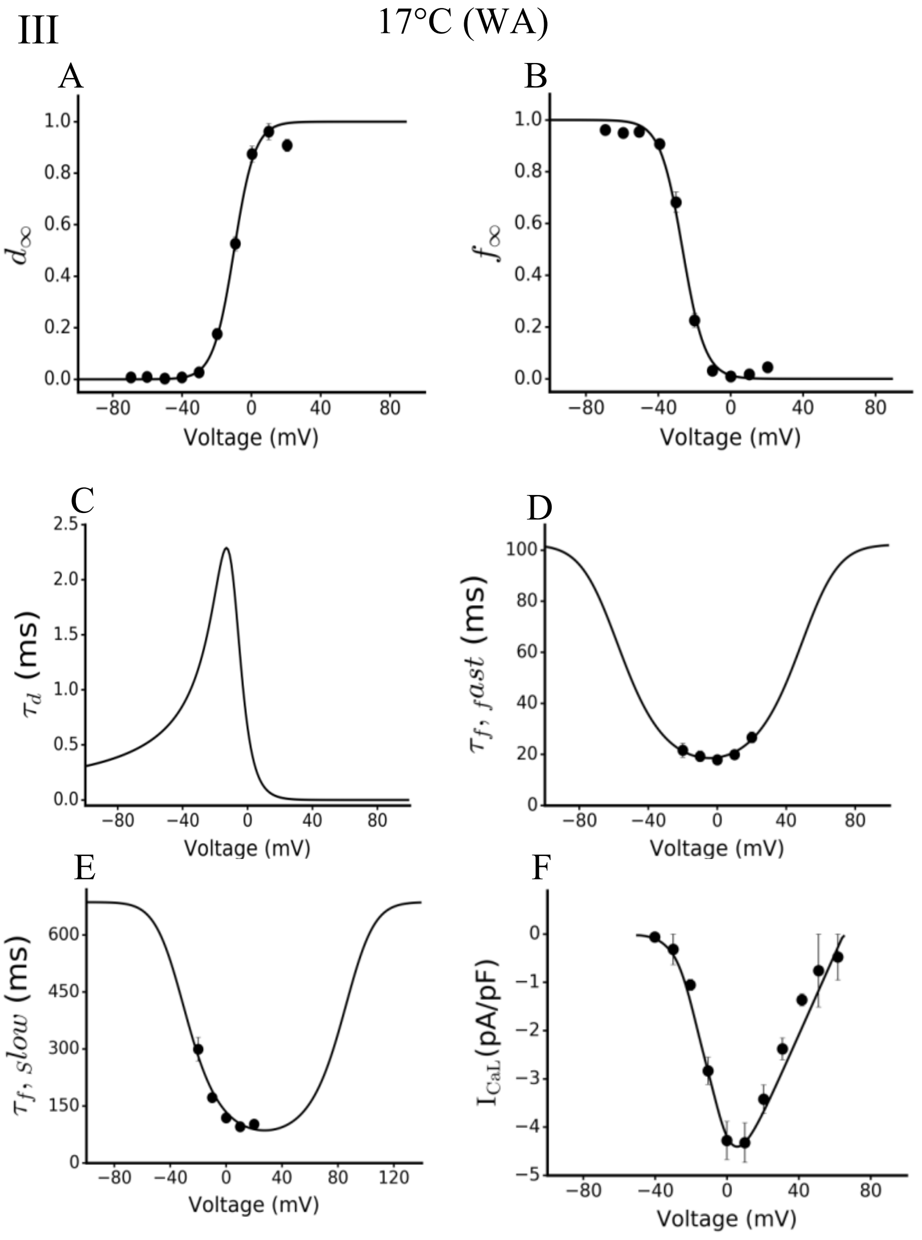

Figure 4.7: Parameters for the I_{CaL} current model of the teleost fish ventricular myocytes at cold and warm acclimation. I, II and III, parameters for the I_{CaL} current models at 11°C CA, 11°C WA and 17°C, respectively. From I and II Figures; A and B: Steady- state activation (d_∞) and inactivation (f_∞) variables, respectively, C: Activation (τ_d) time constant, D: Simulated (I-V) relationship of I_{CaL}. While for III Figure; A and B: Steady- state activation (d_∞) and inactivation (f_∞) variables, respectively, C, D and E: Activation (τ_d), fast inactivation ($\tau_{f,fast}$)and slow inactivation ($\tau_{f,slow}$) time constant, respectively. F: Simulated (I-V) relationship of I_{CaL}. Model

(lines) and experimental data (points), for 11°C CA and 11°C WA from [unpublished data] while at 17°C from [107].

Table 4.3: Temperature dependence of I_{CaL} in ventricular myocytes of the rainbow trout heart as seen experimentally [107] and implemented in simulations, where T is the temperature in (°C), $V_{0.5}$ is the half voltage in (mV), k is the slope and CA and WA are the cold acclimation and warm acclimation, respectively. Note: blue refers to the cold temperatures while red refers to the warm temperatures, (Exp. is experimental and Sim. is simulation).

T °C	**$V_{0.5}$ Steady-state activation (mV)**		**Slope(k)**		**$V_{0.5}$ Steady-state inactivation (mV)**		**Slope(k)**	
	Exp.	**Sim.**	**Exp.**	**Sim.**	**Exp.**	**Sim.**	**Exp.**	**Sim.**
4	-6.44±0.9	-7.11	5.81±0.2	5.78	-26.01±1	-25.73	5.04±0.31	4.60
11CA	-12.45	-13.80	7.12	7.24	-39.4	-38.02	9.44	9.23
11WA	-12.19	-13.82	6.67	7.24	-32.77	-33.63	10.29	9.52
17	-10.55±0.8	-11.47	5.74±0.4	5.14	-26.37±0.6	-27.34	4.98±0.27	3.63

4.2.4.3 Temperature Effects on I_{Kr}

Potassium currents have the plasticity to adapt the electrical activity of the teleost heart in chronic thermal stress and other different physiological conditions [15]. In the trout cardiac myocytes, including salmonid species, the rapid component of the delayed rectifier current (I_{Kr}) density was affected by changing temperature, in the absence of the slow component (I_{Ks}) in most trout species [15, 155, 173]. The outward I_{Kr} current plays a vital role in regulating the APD of the cardiac myocytes as the long plateau phase of the cardiac AP is maintained by the balance between inward and outward currents. This balance is affected by changes in the chronic temperature and therefore, APD will be modified by thermal acclimation [42, 174].

The mathematical model of I_{Kr} at 5°C (see Section 4.2.3.3) has been modified, based on available experimental data to produce mathematical models of I_{Kr} at 11°C [42] and 19°C [154].

Due to the lack of experimental data for the I_{Kr} kinetics at CA and WA, the I_{Kr} developed model at 11°C was used to investigate the effects of CA and WA on the I_{Kr} density according to the experimental records of Haverinen and Vornanen [42]. This was achieved by modifying the g_{Kr} in corresponding to those changes (in the I_{Kr} density) then implemented these modifications in the teleost fish computational models of CA and WA.

It is worth to mentioned that the current-voltage (I_{Kr}-V) relationships for the trout ventricular myocytes at 4 and 18°C are lacking from literatures so far, therefore, this thesis have used (in the mathematical models of the I_{Kr} at 4 and 18°C) experimental findings from other species and in close temperatures assuming that the sarcolemmal K^+channels in the ventricular myocyte that generate I_{Kr} behaves similar to those of trout fish ventricular cells. Although there may be species-specific differences in the electrical excitation of fish hearts, most experimental findings demonstrate consistency in ventricular AP shape and its ionic current basis [41, 42]. These species include the lamprey ventricular cells at cold of 5°C [155] as shown in Figure (4.4B) and Pacific bluefin tuna at warm of 19°C [154] as shown in Figure (4.8B). Both of those currents were used in our simulations, as the (I_{Kr}-V) relationships in Figure (4.4B) was used in the teleost models at 4°C while the (I_{Kr}-V) relationships in Figure (4.8B) was used in the teleost model at 18°C.

The comparison between the density of the delayed-rectifier potassium current, I_{Kr} in lamprey fish at 5°C (Figure 4.4B) and Pacific bluefin tuna at 19°C (Figure 4.8B) shows that there was no significant difference in the I_{Kr} density but they are not the same, as shown in Table 4.4, the I_{Kr} density is slightly higher at 5°C (Figure 4.4B) by ~ 5% comparing to the I_{Kr} density at 19°C (Figure 4.8B). This is quantitatively close to the previously experimental findings of the I_{Kr} density of the rainbow trout at 4 and 18°C that empirically examined by Haverinen and Vornanen [42] (see [42] for more details as Haverinen and Vornanen showed the I_{Kr} density values as isolated data and for the modelling development accuracy, data from a voltage clamp technique need to be used), validating our assumption.

The upregulating and downregulation of the I_{Kr} influence the repolarisation phase of the cardiac APs particularly, in the absence of the slow delayed-rectifier potassium current, I_{Ks} (so far) , as shown later in Table 4.4. In our simulations, the I_{Kr} downregulation prolonged the APD_{90}, while the upregulation shortened it (with taking into account the effects of other currents of the mathematical models on the APs of the ventricular myocytes of trout fish. This will be explained in more details later in Section (4.3).

Figure 4.8 shows the simulated (I-V) relationship curves at 11°C from rainbow trout [42] and 19°C from bluefin tuna [154], as our simulations were fit to the experimental data.

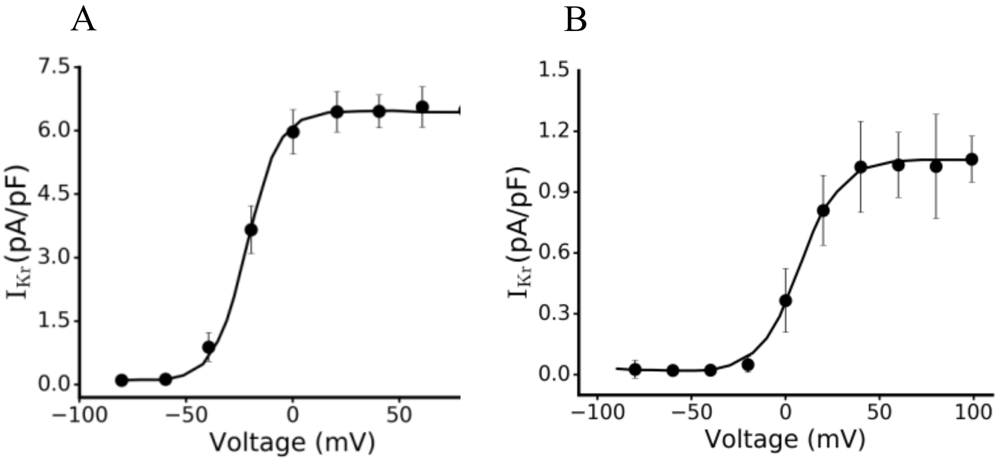

Figure 4.8: Parameters for the I_{Kr} current model of the teleost fish ventricular myocytes at 11°C and 19°C. A and B: Simulated current-voltage (I-V) relationship of I_{Kr} at both temperatures. I_{Kr} was measured at the end of the voltage-clamp pulses as the peak 2μM E-4031-sensitive tail current**.** Model (lines) and experimental data (points) for 11°C from [42] while at 19°C from [154].

4.2.4.4 Temperature Effects on I_{K1}

The inward rectifier potassium current, I_{K1}, activates in the later phase of the AP plateau to regulate the final rate of AP repolarisation and maintain the negative resting membrane potential (RMP) [15, 42, 153, 173].

The mathematical model of I_{K1} at 4°C (see Section 4.2.3.4) has been modified to the corresponding experimental data to create mathematical models of I_{K1} at 11°C in CA and WA and warm acclimated, 18°C. However, the ability to modify the I_{K1} current at thermal acclimation is different between fish species. For example, in *Salmoniformes* fish such as rainbow trout, I_{K1} modification seems to be weakly developed or even absent and shows an exceptional inverse thermal compensation. This can be explained by the fact that in different teleost fish species, I_{K1} is generated by different Kir2 channels [15, 153]. For instance, in trout cardiac myocytes, I_{K1} is formed by Kir2.1 and Kir2.2 channels only, whereas in another species such as crucian carp heart, it is formed by Kir2.2 and Kir2.5 channels. It is clear that the Kir2.5 channels are lacking in trout (such as rainbow and brown species). This is possibly the reason why acclimating to cold decreases I_{K1} in rainbow trout myocytes while inducing an increase in I_{K1} in others such as crucian carp myocytes [153]. Hence, when a rainbow trout heart acclimates to cold, this modifies the two main potassium currents in opposite manners, evidenced by a strong downregulation in the inward rectifier current density, I_{K1} and a simultaneous strong upregulation in the delayed rectifier current density, I_{Kr} [173].

Under chronic cold exposure, the APD of the trout cardiac cells is shortened, enabling larger cardiac output and higher heart rates. This indicates compensatory changes in the function of the cardiac ion channel, however, the reduction in I_{K1} current by cold acclimation prevents it from contributing to the AP shortening. Although the physiological importance of decreasing the I_{K1} density in the cold is not fully understood, this reduction might increase cardiac excitability by reducing the requirement for the depolarising Na^{+} current, I_{Na}, in the trout ventricular myocytes [15].

These results denote the flexibility of the K^{+}channels of trout cardiac myocytes in regulating cardiac excitability and contractility as a temperature function [173]. Figure 4.9 shows the simulated

(I-V) relationship curves at 11°C in CA and WA and at warm acclimated, 18°C, from rainbow trout [15], as our simulations showed a good fitting to the experimental data.

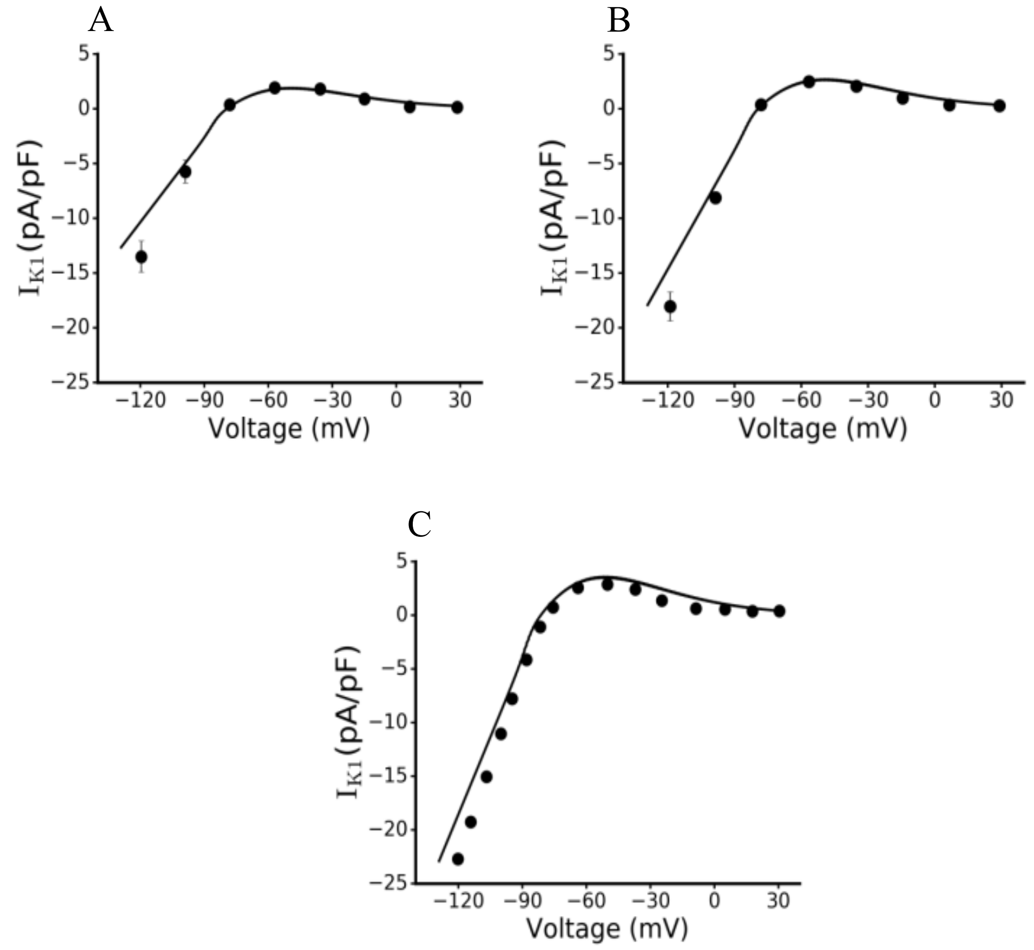

Figure 4.9: Parameters for the I_{K1} current model of the teleost fish ventricular myocytes at cold and warm acclimation. A, B and C: Simulated current-voltage (I-V) relationship of I_{K1} at 11°C CA, 11°C WA and 18°C. Model (lines) and experimental data (points) from [15].

4.2.5 Summary of Temperature Effects on Currents Densities

The thermal acclimation effects on the main ion currents and their kinetics of the teleost ventricular myocytes are illustrated in the above Sections. This Section summarises the simulated changes in the densities of these currents and validated them to those empirically recorded at warm and cold acclimation conditions. The simulated densities showed a reasonable close to the experimental data from different teleost species as shown Table 4.4.

Table 4.4: Major current densities at different temperature conditions [cold (4-11)°C and warm (11-18)°C acclimation], (Exp. is experimental and Sim. is simulation). For I_{Na}, experimental data at all temperature were from [104], I_{CaL} at 4 and 17°C were from [107], while at 11°C in CA and WA from Vornanen (unpublished data), I_{Kr} at 5°C was from [155] and at 11°C from [42] while at 19°C from [154], finally, I_{K1} at all temperature was from [15]. Note: Blue refers to cold acclimation while red refers to warm acclimation.

Peak density (pA/pF)	**Exp.**	**Sim.**	**Exp.**	**Sim.**	**Exp.**	**Sim.**	**Exp.**	**Sim.**
	4-5 °C		**11°C (CA)**		**11°C (WA)**		**17-19°C**	
I_{Na}	-26.9	-26.41	-48.47	-48.37	-32.97	-32.98	-43.23	-43.32
I_{CaL}	-3.5	-3.40	0.91	0.89	0.77	0.76	-3.62	-3.62
I_{Kr}	1.08	1.08	6.55	6.54	6.557	6.55	1.03	1.03
I_{K1}	14.6	14.7	13.4±1.01	12.7	18.3±0.95	17.94	23.87	23.77

4.2.6 Other Ionic Currents, Exchanger and Pumps in the Fish Ventricular Model

Formulations for the resting currents in the model including the background currents, sodium and calcium currents, ATP sensitive potassium current, the sodium-calcium exchanger current, calcium pump current, potassium pump current and sodium-potassium pump current, were based on those from the basal model (Luo and Rudy model) [54]. These currents formulations were not modified as no published studies exist involving such currents in the teleost fish cardiac myocytes, particularly the salmonid species which are the main teleost species of our models.

4.2.7 Computational Methods

The models at cold and warm acclimation were coded in the C programming language and by using the Rush and Larsen numerical integration method [146] to solve the ordinary differential equations (ODEs). To achieve a stable solution for all models' equations and to maintain the accuracy of the computation of membrane current and potential, the time step was set to a value of 0.01 ms in all models at CA and WA, and all of the models equations (formulations) are shown in the Appendix.

With a sequence, supra-threshold stimuli (amplitude; duration and time interval (between two successive APs)), the models can produce a series of action potentials (APs) with characteristics that matched quantitatively to experimental data. Moreover, the induced AP characteristics, such as OS, RMP, APD_{50}, APD_{90} and $\mathrm{dV/dt}_{\mathrm{max}}$, are computed on the last two APs after a 30s simulation in order to ensure consistency between different calculations, allowing appropriate comparisons to be made.

Table 4.5: Models parameters for the developed models at cold ((4-11°C), in blue) and warm ((11-18°C), in red) acclimation.

Model parameters	**Temperature (°C)**			
	4	**11 CA**	**11WA**	**18**
$C_m\ pF$	1.0	1.0	1.0	1.0
$F\ C/mmol$	96.5	96.5	96.5	96.5
$T\ K$	277	284	284	291
$R\ J.mol^{-1}1.K^{-1}$	8.314	8.314	8.314	8.314
$I_{stim}\ pA/pF$	-57	-50	-48	-41
$[Na^{+}]_o\ mM$	132	132	132	132
$[K^{+}]_o\ mM$	5.4	5.4	5.4	5.4
$[Ca^{2+}]_o\ mM$	1.8	1.8	1.8	1.8
$g_{Na}\ nS/pF$	4.0	4.9	4.5	4.7
$g_{CaL}\ nS/pF$	0.05	0.044	0.041	0.061
$g_{Kr}\ nS/pF$	0.08	0.49	0.05	0.06
$g_{K1}\ nS/pF$	0.60	0.62	0.67	0.71
$g_{bNa}\ nS/pF$	0.004	0.004	0.004	0.004
$g_{bCa}\ nS/pF$	0.005	0.005	0.005	0.005
$g_{Kp}\ nS/pF$	0.00001	0.00001	0.00001	0.00001
$g_{K(ATP)}\ nS/pF$	0.00039	0.00039	0.00039	0.00039

Table 4.6: Initial values for the developed models at cold ((4-11°C), in blue) and warm ((11-18°C), in red) acclimation.

Initial value	Temperature (°C)			
	4	**11 CA**	**11WA**	**18**
V, mV	-80	-65	-70	-75
m	0.004	0.004	0.004	0.004
h	0.993771	0.993771	0.993771	0.993771
d	3.210618e-06	3.210618e-06	3.210618e-06	3.210618e-06
f	0.999837	0.999837	0.999837	0.999837
f_{Ca}	0.999837	0.999837	0.999837	0.999837
xr	0.000124042	0.000124042	0.000124042	0.000124042
$[Na^+]_i, mM$	9	9	9	9
$[Ca^{2+}]_i, mM$	0.00006	0.00006	0.00006	0.00006
$[K^+]_i, mM$	131	131	131	131

4.3 Results

Mathematical models were validated against the experimental data for the major ion channel at each acclimation temperature (described previously). They were then used to validate the AP characteristics derived from the model against those derived experimentally, firstly at cold acclimated, 4°C, then at the common experimental temperature of 11°C (in CA and WA), and finally, at warm acclimated, 18°C [42]. Following validation, the two major aims of this Chapter were addressed, namely the effect of (1) chronic and (2) acute temperature change on the electrophysiology and excitability for the teleost fish ventricular model.

4.3.1 Fish Ventricular Action Potential at Cold Acclimated, 4°C

The simulated AP for teleost fish ventricular myocytes at 4°C obtained with a stimulation rate of 0.5 Hz (BCL = 2000 ms) and calculated after 500s continuous simulation until the steady-state solution has been reached. The simulated AP with the experimental AP (inset) from rainbow trout [104] and the time course of intracellular calcium and all currents in the fish ventricular model at 4°C are shown in Figure 4.10.

The APs of vertebrate ventricles were recognised with five different phases (0-4) [30]. In teleost fish ventricular cells, 1) phase 0 is the rapid depolarisation phase of the membrane AP that can be calculated from the resting membrane potential to a few positive voltages, usually from +10 to +40 mV. This phase results from an increase in the opening of sodium channels that generates the I_{Na} current, which represents the main factor that determines the AP propagation rate over ventricular myocardia. 2) phase 1 is lacking in the fish ventricular cells. This might be due to the absence of the I_{to} current, which is mainly carried by K^+ ions, indicating that the channels generating I_{to} are not expressed in the fish ventricular myocytes. 3) phase 2 is the long plateau phase produced from the balance between the inward and the outward currents. The APD is long in the fish ventricular cells, ranging from several hundred milliseconds to several seconds. This is necessary for the sarcolemmal Ca^{2+} influx as well as the cardiac contraction. 4) phase 3 is the repolarisation phase that results from different outward K^+ currents, especially the rapid rectifier K^+ current, I_{Kr} and the inward current, I_{K1}; however, the slow delayed rectifier K^+ current (I_{Ks}) may also be involved in some fish species [41]. 5) phase 4 is the negative resting membrane potential (RMP) (usually from -70 to -90 mV) [42, 104]. It is maintained by a small efflux of K^+ ions from the cell through the inward rectifier K^+ channels that produce the I_{K1} current [30].

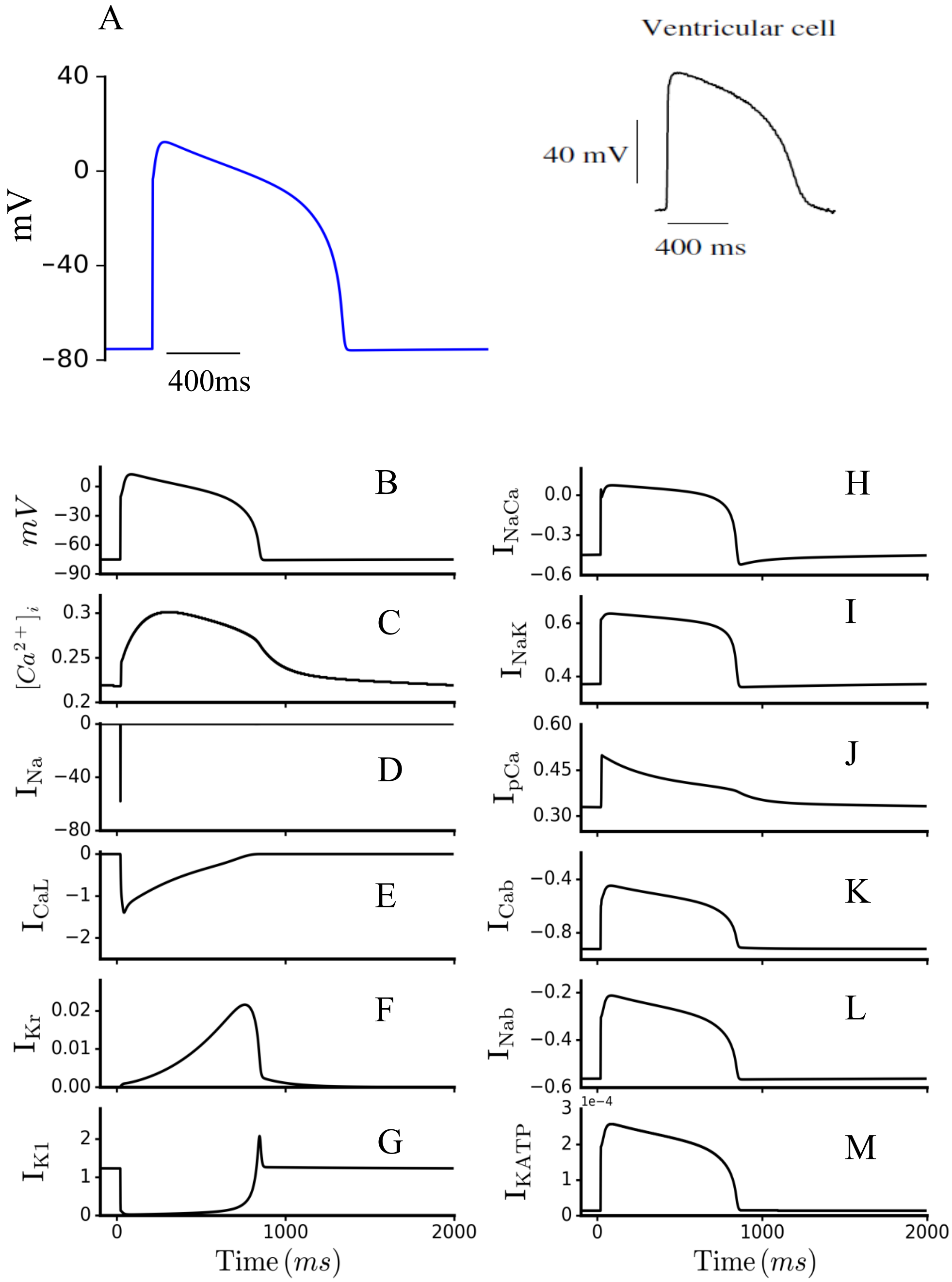

Figure 4.10: Steady-state AP, calcium transient, and major ionic currents simulated at 4°C with physiological 0.5-Hz pacing rate. A: Simulated Action potential (the inset is the AP profile recorded experimentally by [104]). B: Action potential. C: Cytosolic $[Ca^{2+}]_i$ in µM units. D: Fast sodium current. E: L-type calcium current. F: Rapidly activating delayed rectifier potassium current. G:

Time-independent potassium current. H: Sodium-calcium exchange current. I: Sodium-potassium ATPase current. J: Calcium ATPase current. K: Background calcium current. L: Background sodium current. M: Potassium ATP sensitive current. All the currents are in pA/pF units.

4.3.1.1 Model Validation

After the fish ventricular myocytes model was constructed as described earlier in this Chapter, the model was validated by computing and comparing the characteristics of the APs to experimental data from different teleost species at 4°C from [42]. Results are shown in Figure 4.11.

The characteristics include the overshoot (OS) and AP amplitude (APA). In simulations, they were 11.1 and 89.1 mV, respectively, which are in a good agreement with experimental records [42]. In the developed model, the computed resting membrane potential (RMP) is -77.5 mV, which is fairly close to that of experimental recordings [42]. The simulated APD at 50% of AP repolarisation (APD_{50}) of the ventricular cell is 750 ms and the simulated APD at 90% of AP repolarisation (APD_{90}) is 862 ms, all of which match well with experimental findings of different teleost species, including rainbow, lamprey, perch, pike, burbot, roach, and crucian carp from Haverinen and Vornanen [42]. The computed maximum upstroke velocity (dV/dt_{max}) is 56.7 V/s, which compares well to the experimentally observation with a value of 58.5±6.3 V/s [104].

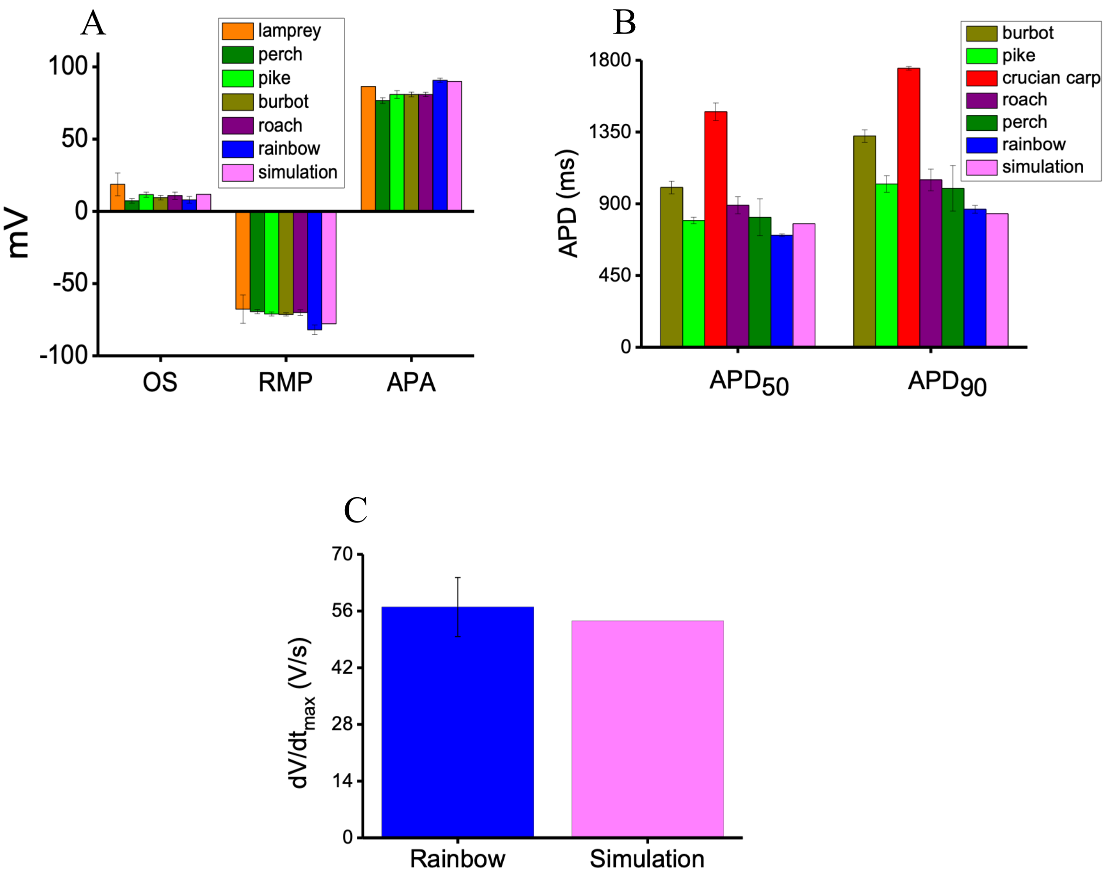

Figure 4.11: Simulated AP properties with available experimental data for teleost fish model. A: The overshoot (OS), resting potential (RP) and AP amplitude (APA) for the ventricular cells. B: Action potential duration at 50% and 90% of repolarization values (APD_{50} and APD_{90}, respectively). C: The AP upstroke velocity from both simulation and experimental records. The source of the experimental data for A and B are from Haverinen and Vornanen [42]while C is from [104].

Furthermore, the effects of changing the steady state inactivation variables of the inward I_{Na} current (including the half voltage, $V_{0.5}$ in (mV) and the slope, k values) on the simulated APs characteristics of the ventricular myocytes, were revealed in this Chapter. Therefore, the ventricular single cell model at 4°C was paced at 0.5 Hz and the $V_{0.5}$ and k values of the wildtype (WT) were shifted to the right for more positive values and to the left for more negative values, for several values. Then, the relative changes in steady-state inactivation variables were incorporated in the developed model at 4°C and at each shifting value, the APs characterises were calculated, which are summarised in Table (4.7) and Figure (4.12).

Table (4.7) demonstrates the right shift and left shift of the I_{Na} inactivation variables ($V_{0.5}$ and k) by 30%, 50%, 70% and 90% and the associated APs characteristics under those changes. Figure (4.12) shows the effects of the changing in the I_{Na} inactivation variables on the simulated AP morphology.

Simulation results demonstrated that both of the right and left shifts to the I_{Na} inactivation variables markedly altered the profile of the teleost ventricular AP in the cold acclimated model at 4C. In comparison to the WT, simulations show that: i) right shift produces: 1) prolongation of the APD_{90}, from 828.91 ms (for WT) to 876.76 ms (for +90%); 2) decreased the OS from 12.32 mV (for WT) to 11.3 mV (for +90%) and APA values from 87.39 mV (for WT) to 86.369 mV (for +90%); 3) no significant change in the RMP and dV/dt_{max}; ii) left shift produces the following: 1) abbreviation of the APD_{90}, from 828.91 (for WT) to 825.34 (for -90%); 2) elevated the OS from 12.32 mV (for WT) to 16.79 mV (for -90%) and APA values from 87.39 mV (for WT) to 91.86 mV (for -90%); 3) no obvious change in the RMP; 4) accelerated the dV/dt_{max}, from 61 V/s (for WT) to 129.84 V/s (for -90%), as shown in Table (4.7) and Figure (4.12).

Collectively, the right shift of $V_{0.5}$ of the I_{Na} inactivation kinetics prolonged APD while the left shift of it abbreviated APD in the teleost fish ventricular myocytes.

Table 4.7: Changes in parameters of steady-state inactivation variables ($V_{0.5}$ is the half voltage in (mV), k is the slope) of I_{Na} relative to WT, and the associated action potential (AP) characteristics of the teleost ventricular myocytes at 4°C. $V_{0.5}$ and k were shifted to the right for +30%, +50%, +70% and +90% and to the left for -30%, -50%, -70% and -90% (from its value at WT) to investigate the effects of changing the I_{Na} inactivation variants on the AP characteristics. These characteristics including overshoot (OS), action potential amplitude (APA), action potential duration at 90% of repolarisation (APD_{90}), resting membrane potential (RMP) and the maximum upstroke velocity (dV/dt_{max}).

			Right shift				Left shift			
Shifting factor		**WT**	**+30%**	**+50%**	**+70%**	**+90%**	**-30%**	**-50%**	**-70%**	**-90%**
Inactivation	$V_{0.5}$	30.66	+349.85	+45.99	+52.12	+58.25	-21.46	-15.33	-9.19	-3.06
	k	11.1	14.43	16.65	18.87	21.09	7.77	5.55	3.3	1.11
AP characteristics	OS	12.32	12.33	12.10	11.78	11.3	12.22	12.59	13.526	16.79
	APA	87.39	87.39	87.16	86.84	86.369	87.28	87.65	88.59	91.86
	APD_{90}	828.9	839.07	846.8	858.08	876.76	827.66	826.36	825.82	825.34
	dV/dt_{max}	61	50.97	50.98	50.982	50.98	76.65	101.114	121.23	129.84
	RMP	-75.06	-75.06	-75.06	-75.06	-75.07	-75.06	-75.065	-75.06	-75.06

Right shift

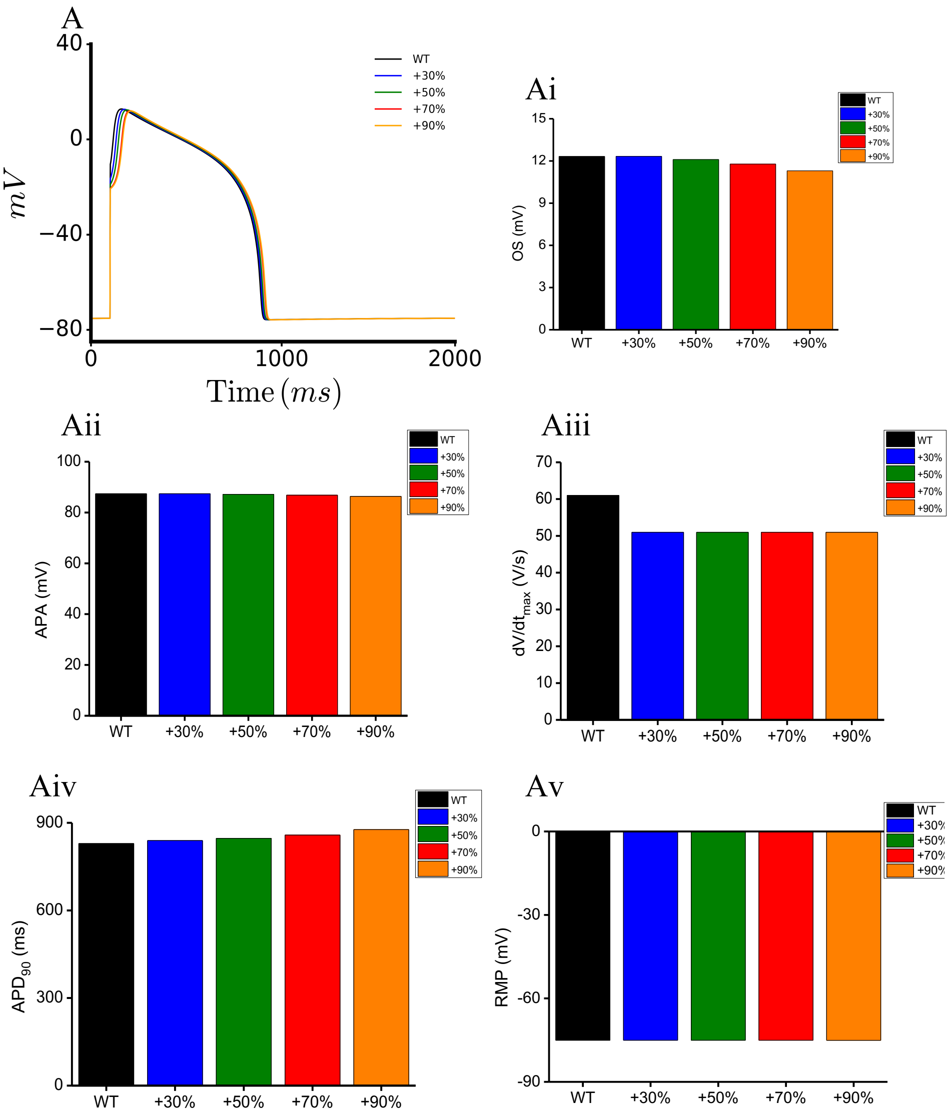
A
40
0
−40
−80
mV
0
1000
2000
Time (ms)
WT
+30%
+50%
+70%
+90%
Ai
OS (mV)
15
12
9
6
3
0
WT
+30%
+50%
+70%
+90%
Aii
APA (mV)
100
80
60
40
20
0
WT
+30%
+50%
+70%
+90%
Aiii
dV/dt$_{max}$ (V/s)
70
60
50
40
30
20
10
0
WT
+30%
+50%
+70%
+90%
Aiv
APD$_{90}$ (ms)
900
600
300
0
WT
+30%
+50%
+70%
+90%
Av
RMP (mV)
0
-30
-60
-90
WT
+30%
+50%
+70%
+90%

Left shift

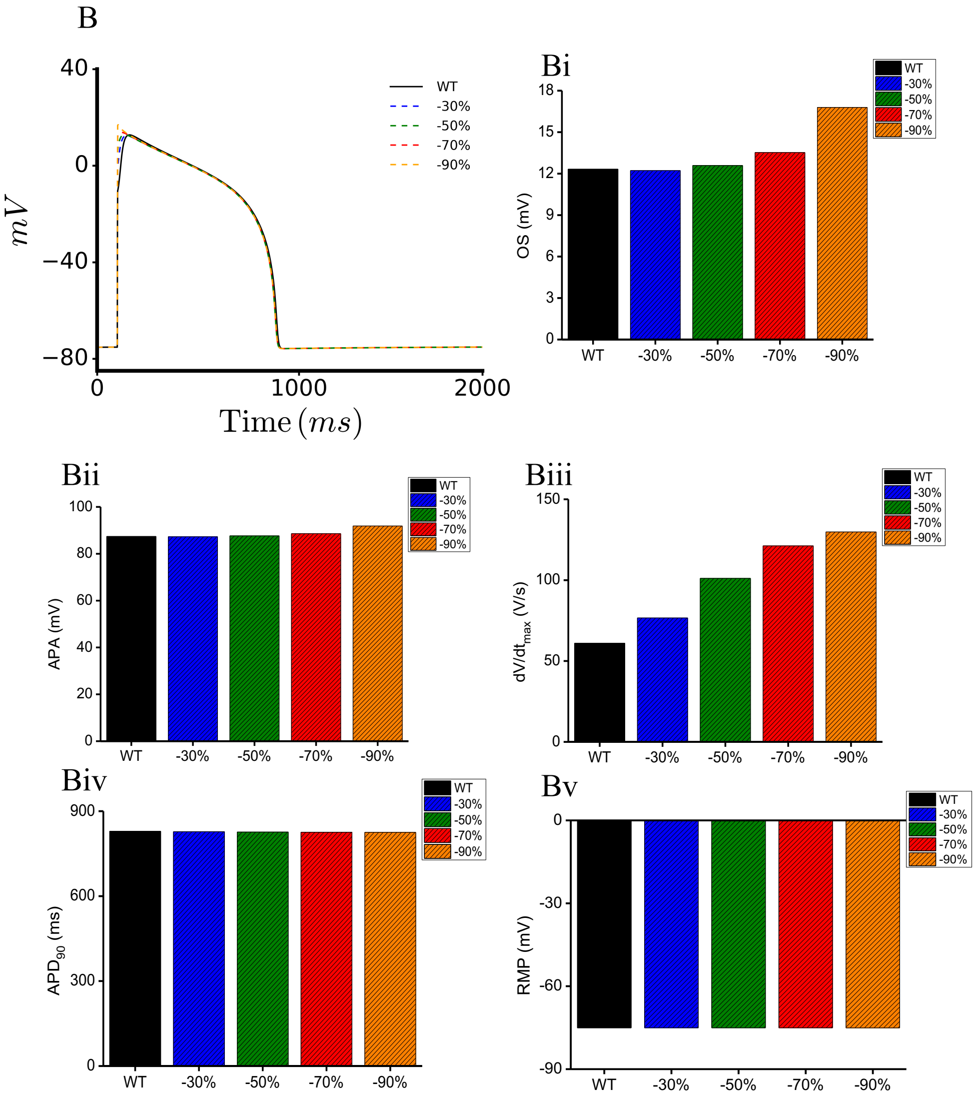

Figure 4.12: Effects of different values of I_{Na} inactivation parameters of the half voltage, $V_{0.5}$ and the slope, k on the simulated action potential (AP) morphology and AP characteristics of the teleost ventricular myocytes at 4°C. A: The simulated AP when $V_{0.5}$ and k were shifted to the right for +30%, +50%, +70% and +90% from its value for WT. B: The simulated AP when $V_{0.5}$ and k were shifted to the left for -30%, -50%, -70% and -90% from its value for WT. The simulated characteristics of the action potential (AP) are shown as follows: Ai, Bi: the action potential overshoot (OS); Aii, Bii: the action potential amplitude; Aiii, Biii: the maximum upstroke velocity($\mathrm{dV/dt_{max}}$); Aiv, Biv: the action potential duration at 90% of repolarisation (APD_{90}); Av, Bv: the resting membrane potential (RMP).

In addition, the teleost single cell model also was used to investigate the effects of changing the I_{K1} conductance (g_{K1}) on the simulated resting membrane potential (RMP) and thus other simulated AP properties. To achieve that g_{K1} was increased by +10%, +20%, +30% and +40% and decreased by -10%, -20% and -30% of its value at wildtype (WT). At each increase or decrease value of the g_{K1}, the AP properties were calculated as shown in Table (4.8) and Figure (4.13).

Simulations reveal that increasing the g_{K1} (and thus the I_{K1} magnitude) will hyperpolarised the RMP from -75.06 mV (for WT) to -76.7 mV (for +40%). Whereas, the g_{K1} reduction will decrease the I_{K1} magnitude and thus the RMP will be decreased, from -75.06 mV (for WT) to -73.5 mV (for -20%), however, in our model we could not reduce g_{K1} further as the AP will be unstable as shown when g_{K1} reduced by 30% in Table (4.8).

Moreover, other AP properties were also influenced by increasing the I_{K1} magnitude in comparison with their values in the WT. From Table (4.8) and Figure (4.13), it can be noticed that the OS was decreased by ~ 3% while the APA was slightly increased by ~ 2% (due to RMP hyperpolarised), from their values for WT; there is also a 20% abbreviation of the APD_{90}, from 828.9 (for WT) to 661.96 (for +40% of g_{K1}); the maximum upstroke velocity, dV/dt_{max} accelerated by 13% when the g_{K1} increased by 40%.

On the other hand, decreasing in the g_{K1} increased slightly the OS by 1.2% with a reduction in the APA by 1.5% (as RMP decreased), from its value for WT; the APD_{90} prolonged by 31%; a slowing down the maximum upstroke velocity by 12%; all of these values were calculated from there values for WT to -20% reduction in the g_{K1} value. As Table (4.8) illustrates, if the g_{K1} reduced further by 30% results in unstable APs with strong reduction in the APA, RMP and dV/dt_{max} from their values for WT by 68%, 89% and 35%, respectively; while there was a moderate increasing in the OS by 37% and prorogation in the APD_{90} by 7.7%, from their values for WT.

Table 4.8: Changes in the conductance of I_{K1} , g_{K1} relatives to its value for wildtype (WT), and the associated action potential (AP) characteristics of the teleost ventricular myocytes at 4°C. G_{K1} was increased by +10%, +20%, +30% and +40% and decreased by -10%, -20% and -30% (from its value for WT) to investigate the effects of changing the g_{K1} on the AP characteristics. These characteristics including overshoot (OS), action potential amplitude (APA), action potential duration at 90% of repolarisation (APD_{90}), resting membrane potential (RMP) and the maximum upstroke velocity (dV/dt_{max}).

			g_{K1} increased				g_{K1} decreased		
Scaling factor		**WT**	**+10%**	**+20%**	**+30%**	**+40%**	**-10%**	**-20%**	**-30%**
	g_{K1}	0.60	0.66	0.72	0.78	0.84	0.54	0.48	0.42
AP characteristics	RMP	-75.06	-75.5	-75.9	-76.29	-76.7	-74.4	-73.5	-8.6
	OS	12.32	12.24	12.17	12.1	12.0	12.4	12.47	19.6
	APA	87.3	87.8	88.1	88.4	88.61	86.82	86.0	28.25
	APD_{90}	828.9	770.6	726.59	691.36	661.96	915.45	1084.73	896.15
	dV/dt_{max}	61	64.71	66.80	68.497	69.88	56.86	53.93	40.98

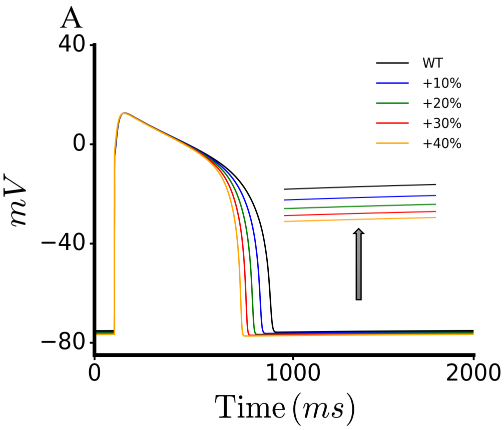
A
40
0
−40
−80
mV
0
1000
2000
Time (ms)
WT
+10%
+20%
+30%
+40%

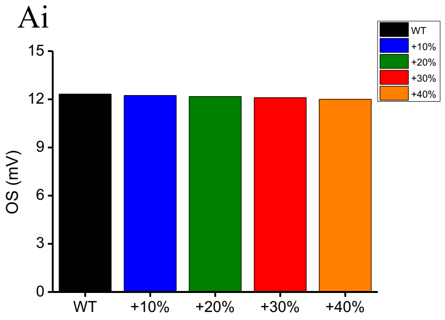
Ai
15
12
9
6
3
0
OS (mV)
WT
+10%
+20%
+30%
+40%
WT
+10%
+20%
+30%
+40%

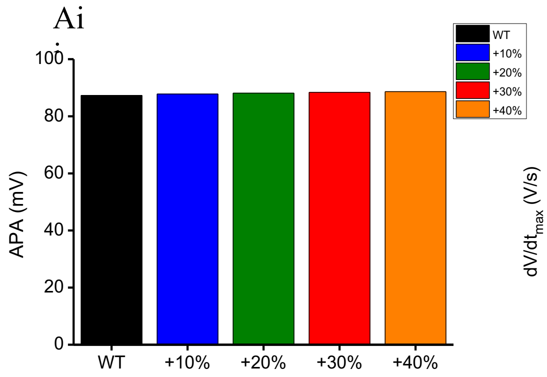
Ai
:
100
80
60
40
20
0
APA (mV)
WT
+10%
+20%
+30%
+40%
WT
+10%
+20%
+30%
+40%

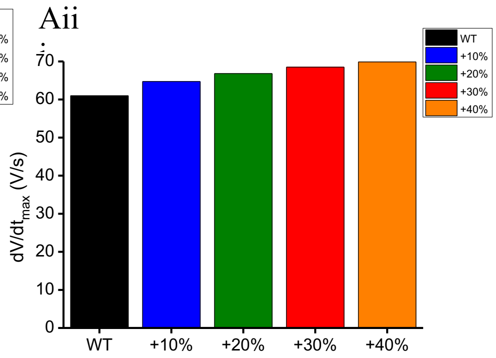
Aii
:
70
60
50
40
30
20
10
0
dV/dtmax (V/s)
WT
+10%
+20%
+30%
+40%
WT
+10%
+20%
+30%
+40%

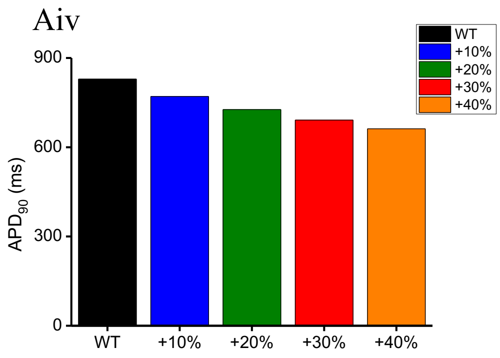
Aiv
900
600
300
0
APD90 (ms)
WT
+10%
+20%
+30%
+40%
WT
+10%
+20%
+30%
+40%

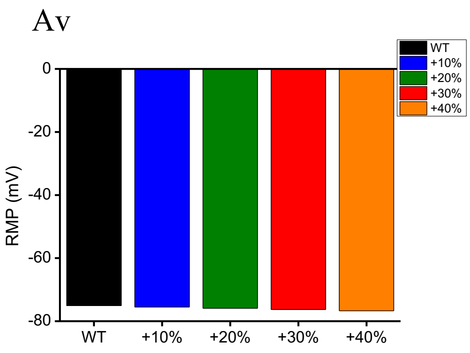
Av
0
-20
-40
-60
-80
RMP (mV)
WT
+10%
+20%
+30%
+40%
WT
+10%
+20%
+30%
+40%

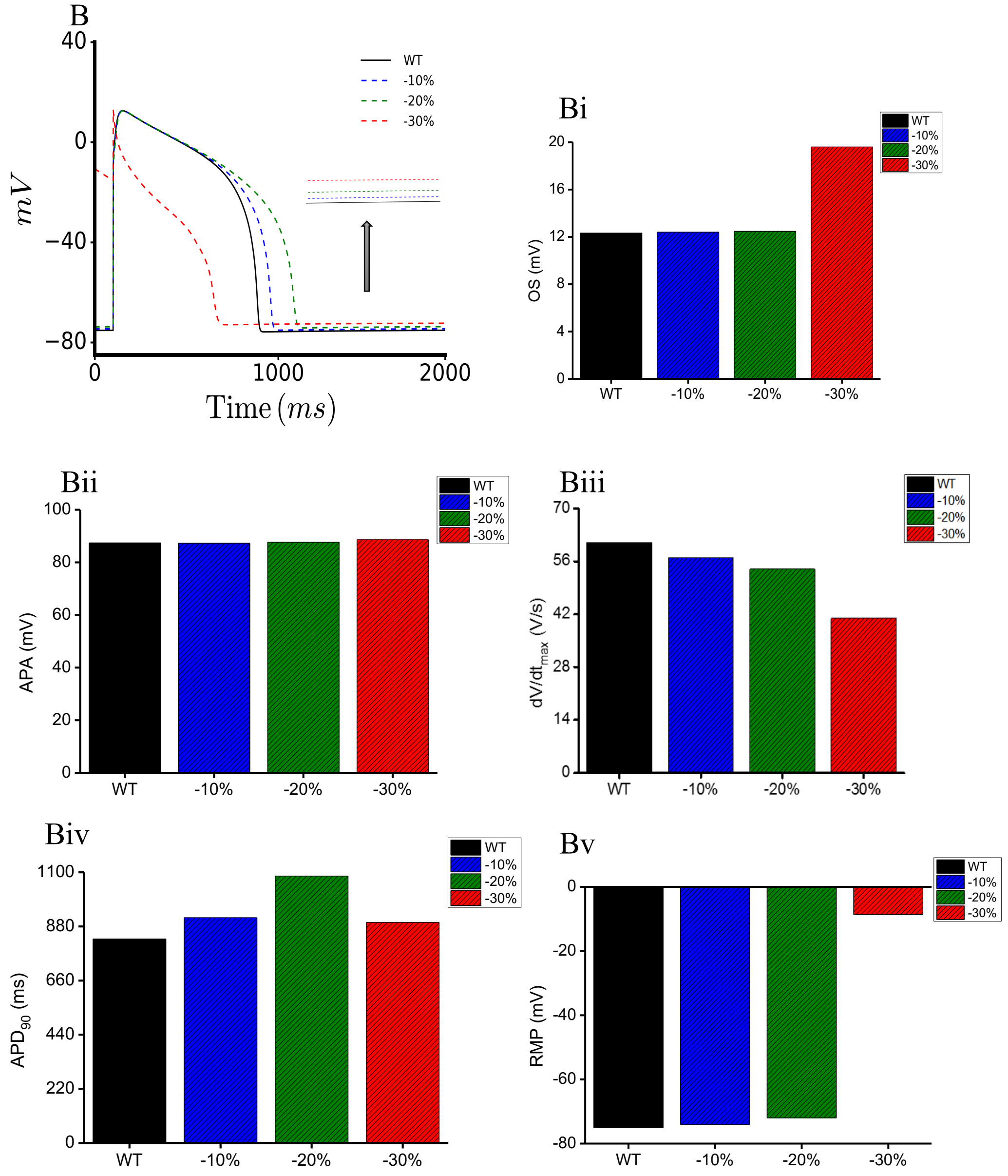

Figure 4.13: Effects of different values of the time-independent potassium current,I_{K1} coundactance, g_{K1}, on the simulated action potential (AP) morphology and AP characteristics of the teleost ventricular myocytes at 4°C. A: The simulated AP when g_{K1} was increased by +10%, +20%, +30% and +40% from its value for WT. B: The simulated AP when g_{K1} was decreased by -10%, -20% and -30% from its value for WT. The simulated characteristics of the action potential (AP) are shown as follows: Ai, Bi: the action potential overshoot (OS); Aii, Bii: the action potential amplitude; Aiii, Biii: the maximum upstroke velocity($\mathrm{dV/dt_{max}}$); Aiv, Biv: the action potential duration at 90% of repolarisation (APD_{90}); Av, Bv: the resting membrane potential (RMP).

4.3.2 Thermal Acclimation Effects on Cardiac APs

As an ectothermic animal, the fish body temperature can vary quite significantly as a result of changes in their ambient temperature. In order to maintain adequate cardiac myocytes excitability in various temperatures, ion channel remodelling will occur owing to gene expression alterations, either at the transcript or protein level [15, 33, 43, 107, 154], resulting in compensatory changes of prolonged APs [30].

In fish hearts, physiological plasticity is required to acclimate to different temperatures; however, the animal physiological response may vary depending on environmental conditions such as aquatic habitat type (lake, ocean or river), water depth, geographical location, and specific species differences [43]. Therefore, at low temperatures, some ectotherms, such as rainbow trout, try to keep active and compensate by several physiological mechanisms [14, 43, 169] while during severe winter conditions, other fish species, such as crucian carp, become inactive as it might be a successful way in harshly hypoxic environments [175–179].

In aquatic habitats, fishes experience varying in the acute temperature over minutes to hours as the temperature can be spatially heterogeneous. This results in remodelling of all aspects of fish cardiac function [30, 33], for example, the opening and closing rate of ion channels as well as the catalytic rates of transporters and pumps. This suggests alterations in the rhythm, rate and the characteristics of the APs [180]. Despite the significant differences in the morphology and duration of the APs of the cardiac myocytes between fish species, numerous studies [46, 154, 155, 173] have showed that the AP duration (APD) in all cardiac compartments decreases when the temperature acutely increases (this will be illustrated later in this thesis). This indicates that at the plateau phase of AP, temperature affects inward I_{CaL} and outward K^+ currents (I_{Kr} and I_{K1}) in a different way. Under acute increases in temperature, the APs shortening suggests that repolarising K^+currents increase more than the depolarising I_{CaL} with an enormous thermal sensitivity to warm temperatures. Moreover, the considerable changes in APD induced by temperature are possibly owning to temperature-dependent alterations in the I_{CaL} rate [44]. The temperature dependence of I_{K1} density in fish cardiac myocytes is weak compared to that of I_{Kr} density [173].

The amplitude and slope of the AP upstroke is regulated by the inward sodium current, I_{Na}, which affects the excitability threshold and controls the conduction velocity impulse [160]. In the cold, the excitability of ventricular myocytes of the teleost heart is reinforced by an acclimation-induced upregulation in the I_{Na} density, and a leftward shift of the steady-state activation curve [43].

Therefore, in order to investigate the possible effects of changing temperatures on AP in cold and warm acclimation, our developed model at 4°C has been used to develop three models at 11°C in (CA) and at 11°C in (WA) and warm acclimated, 18°C. These models are obtained with the physiological stimulation rate of 1, 0.6 and 1Hz at 11°C CA, 11°C WA and 18°C, respectively, and are calculated after at least 500s of continuous simulation to ensure that a steady-state solution has been achieved. The computed action potential and the time course of intracellular calcium and all currents in the developed models are shown in Figure 4.14.

I

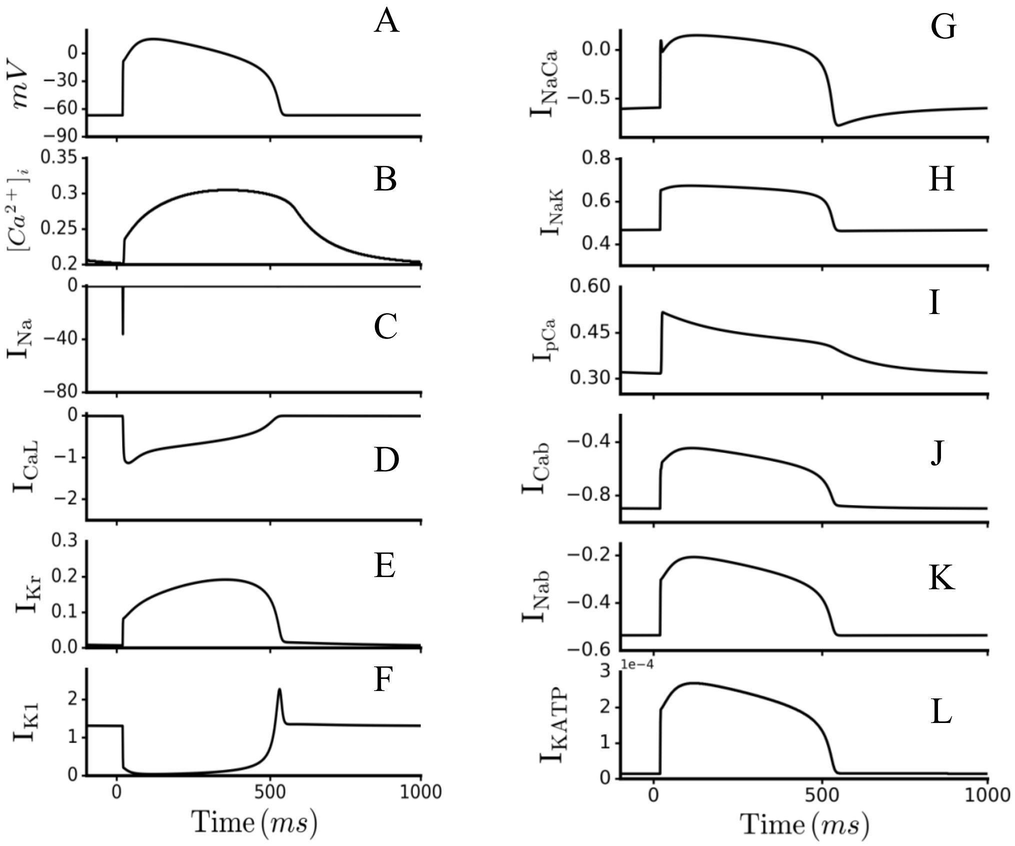

A
mV
0
−30
−60
−90
B
$[Ca^{2+}]_i$
0.35
0.3
0.25
0.2
C
I_{Na}
0
−40
−80
D
I_{CaL}
0
−1
−2
E
I_{Kr}
0.3
0.2
0.1
0.0
F
I_{K1}
2
1
0
0
500
1000
Time (ms)
G
I_{NaCa}
0.0
−0.5
H
I_{NaK}
0.8
0.6
0.4
I
I_{pCa}
0.60
0.45
0.30
J
I_{Cab}
−0.4
−0.8
K
I_{Nab}
−0.2
−0.4
−0.6
L
I_{KATP}
1e−4
3
2
1
0
0
500
1000
Time (ms)

II

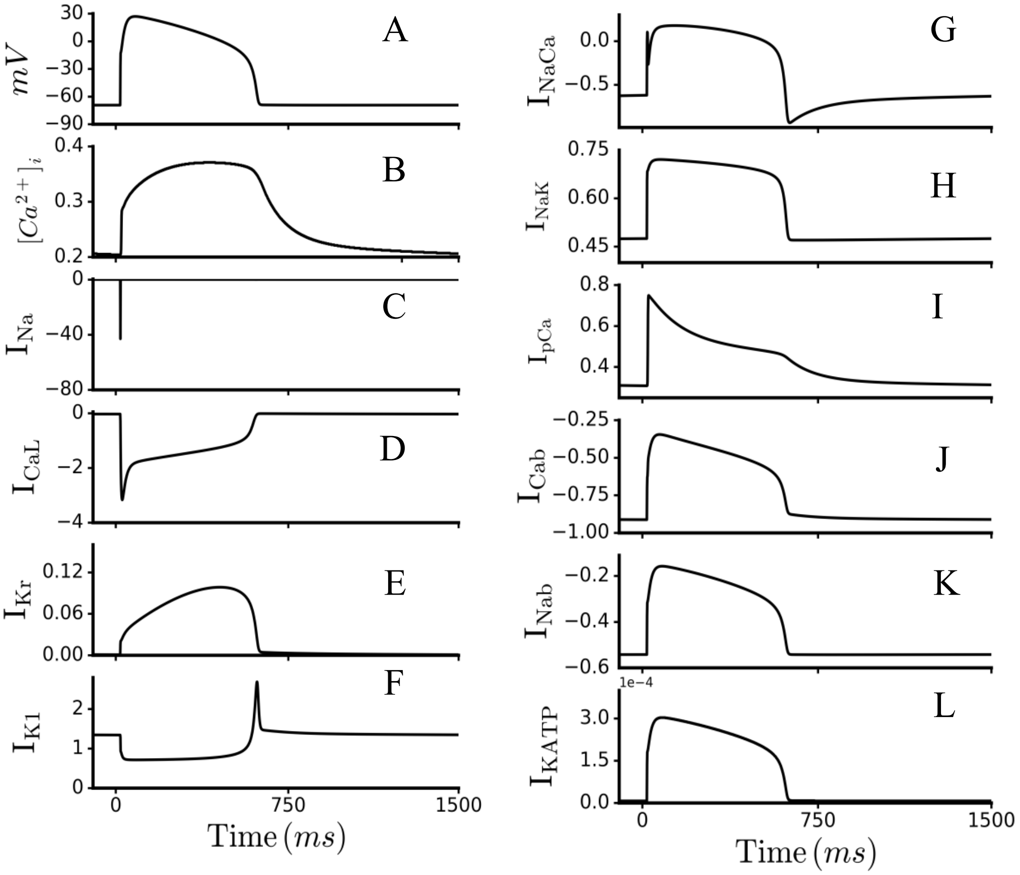
A
B
C
D
E
F
G
H
I
J
K
L
mV
30
0
−30
−60
−90
[Ca2+]i
0.4
0.3
0.2
I_Na
0
−40
−80
I_CaL
0
−2
−4
I_Kr
0.12
0.06
0.00
I_K1
2
1
0
0
750
1500
Time (ms)
I_NaCa
0.0
−0.5
I_NaK
0.75
0.60
0.45
I_pCa
0.8
0.6
0.4
I_Cab
−0.25
−0.50
−0.75
−1.00
I_Nab
−0.2
−0.4
−0.6
1e−4
I_KATP
3.0
1.5
0.0
0
750
1500
Time (ms)

III

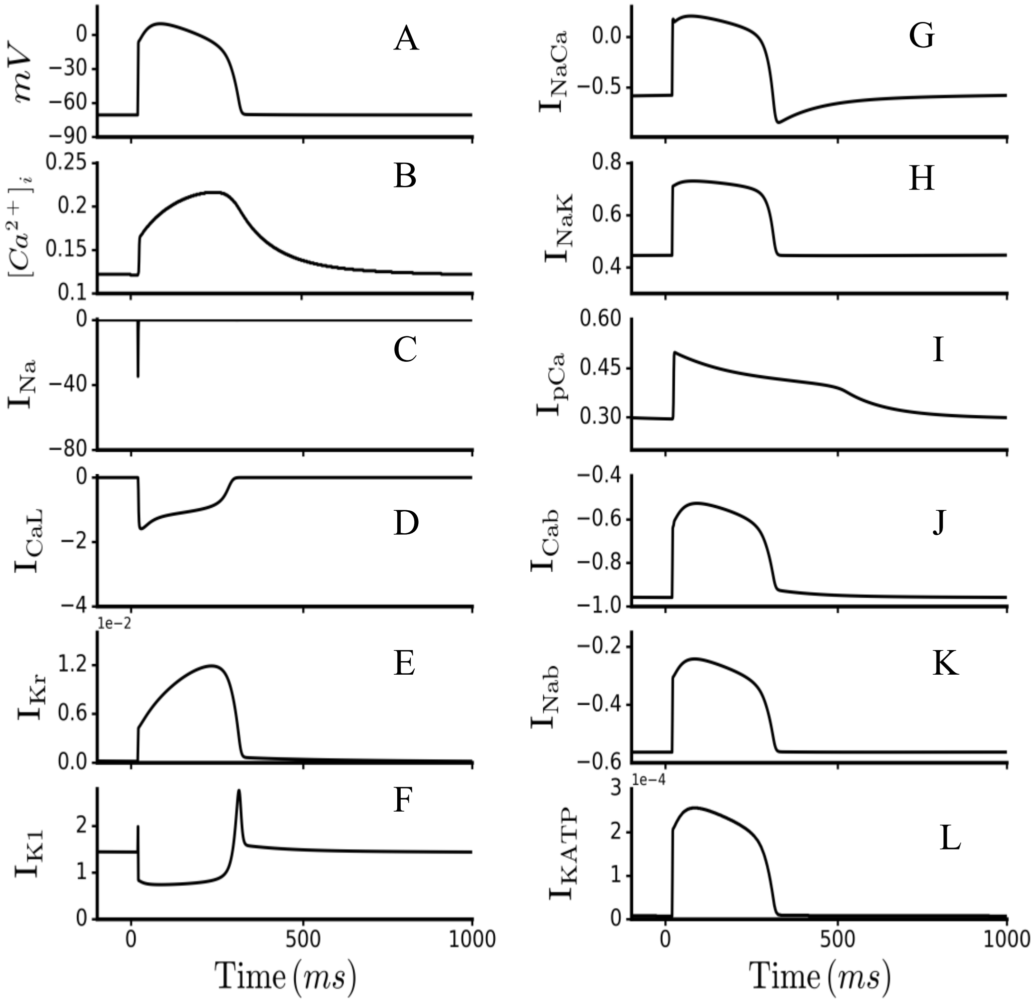

Figure 4.14: Steady-state AP, calcium transient, and major ionic currents simulated at cold and warm acclimation. I, II and III: Fish models at 11°C CA with 1Hz pacing rate, at 11°C WA with 0.6 Hz pacing rate and at 18°C with 1Hz pacing rate, respectively. In all of which A: Action potential. B: Cytosolic $[Ca^{2+}]_i$ in μM units. C: Fast sodium current. D: L-type calcium current. E: Rapidly activating delayed rectifier potassium current. F: Time-independent potassium current. G: Sodium-calcium exchange current. H: Sodium-potassium ATPase current. I: Calcium ATPase current. J: Background calcium current. K: Background sodium current. L: Potassium ATP sensitive current. All the currents are in pA/pF units.

4.3.2.1 Models Validation

After constructing the models, the simulated action potential characteristics were compared to those measured experimentally from ventricular cells of different teleost species at cold (4-11°C) and at warm (11-18°C) acclimation. All the experimental data are from [42]. Results are shown in Figure 4.15. As shown in Section 4.3.1.2, the compared characteristics include OS, APA, RMP, dV/dt_{max}, APD_{50} and APD_{90}.

Simulations at 4°C, 11°C CA, 11°C WA and 18°C, the OS was 11.3, 16.2, 24.8 and 9.0 mV, which match well with experimental data [42]. The APA has values of 91, 80, 96.7 and 76.4 mV, which are reasonably close to experimental findings [42]. In the four models, the computed RMP is -77.5, -64.5, -69.1 and -72 mV, which are within the experimental recordings [42]. The simulated APD_{50} of the ventricular cell is 750, 470, 550 and 292.3 ms and the simulated APD_{90} is 862, 540, 630 and 315.5 ms, all of which are in agreement with experimental findings of different teleost species including rainbow, perch, pike, burbot, roach, crucian carp from Haverinen and Vornanen [42]. The computed $\mathrm{dV/dt_{max}}$ is 61 V/s and matches well with 56.5±6.3 V/s, which was observed experimentally at 4°C [104], while its value at 11°C CA, 11°C WA and 18°C are 50, 52.2 and 56 mV, respectively; however, comparisons cannot be made as there is no experimental data published to date. After the models were validated with the available experimental data from different teleost species, it is clear that most of the simulated results are close to rainbow trout fish recordings, which is expected as most of the ion channel kinetic fitting models are from this species.

After the models were validated, the simulated APs of the four models at a 0.5 Hz pacing rate were plotted to show the effects of thermal acclimation on the teleost cardiac myocytes when chronic and acute temperatures changes, as shown in Figure 4.16.

Simulations showed that increase temperature acutely (warming) from 4°C to 11°C (Figure 4.16A) induced: 1) an increase in the AP overshoot (OS) by approximately 30%; 2) a decrease in the hyperpolarization (less negative) of the resting membrane potential (RMP) by 17%; 3) reduction in the AP amplitude (APA) by 12%; 4) shortening of the action potential duration at 50% repolarization (APD_{50}) and at 90% repolarization (APD_{90}) by approximately 36% and 38%, respectively; 5) a slower maximum upstroke velocity ($\mathrm{dV/dt_{max}}$) of the AP by 18%. While cooling from 18°C to 11°C (Figure 4.16B) produced: 1) the OS value increased by 175%; 2) the RMP was less negative by 4%; 3) the APA raised by approximately, 27%; 4) a prolongation of APD_{50} and APD_{90} by 88% and 99%, respectively; 5) a slower $\mathrm{dV/dt}_{\mathrm{max}}$ by 6%.

Moreover, the comparison between the two acclimated temperatures 4°C and 18°C (Figure 4.16C), showed that the OS decreased by 25%, the RMP decreased by 7%, the APA also decreased by 16%, the APD_{50} and APD_{90} shortened by 61% and 64%, respectively, and slowing the $\mathrm{dV/dt}_{\mathrm{max}}$ by 8%, all of these results when compared temperature from cold acclimated, 4°C to warm acclimated, 18°C.

On the other hand, the remodelling that occurs with thermal acclimation is appreciated when WA at 11°C and CA at 11°C are compared, as shown in Figure 4.16D. Simulations showed that warming (from 11°C CA to 11°C WA) produced: elevated the OS by 53%, increased the hyperpolarisation of the RMP by 7%, increased the APA by approximately 21%, prolonged the APD_{50} and APD_{90} by 17% and accelerated the $\mathrm{dV/dt}_{\mathrm{max}}$ by 4%. All of these simulations in a good matching to the corresponding experimental findings from [42]. These results suggested that electrical excitability of the rainbow heart is reduced by warm temperatures; however, when the activation threshold of an AP is achieved, the action potential progresses rapidly [20, 118].

Figure 4.16E shows a comparison between the simulated APs for ventricular myocytes of the trout fish at three at selected temperatures from our developed models at 4°C, 11°C WA and 18°C. This Figure showed how rising temperature can alter the morphology of the AP, and these alterations represent the acclimation strategy that help fish to cope changes in their ambient temperature, when these changes are in their thermal limits.

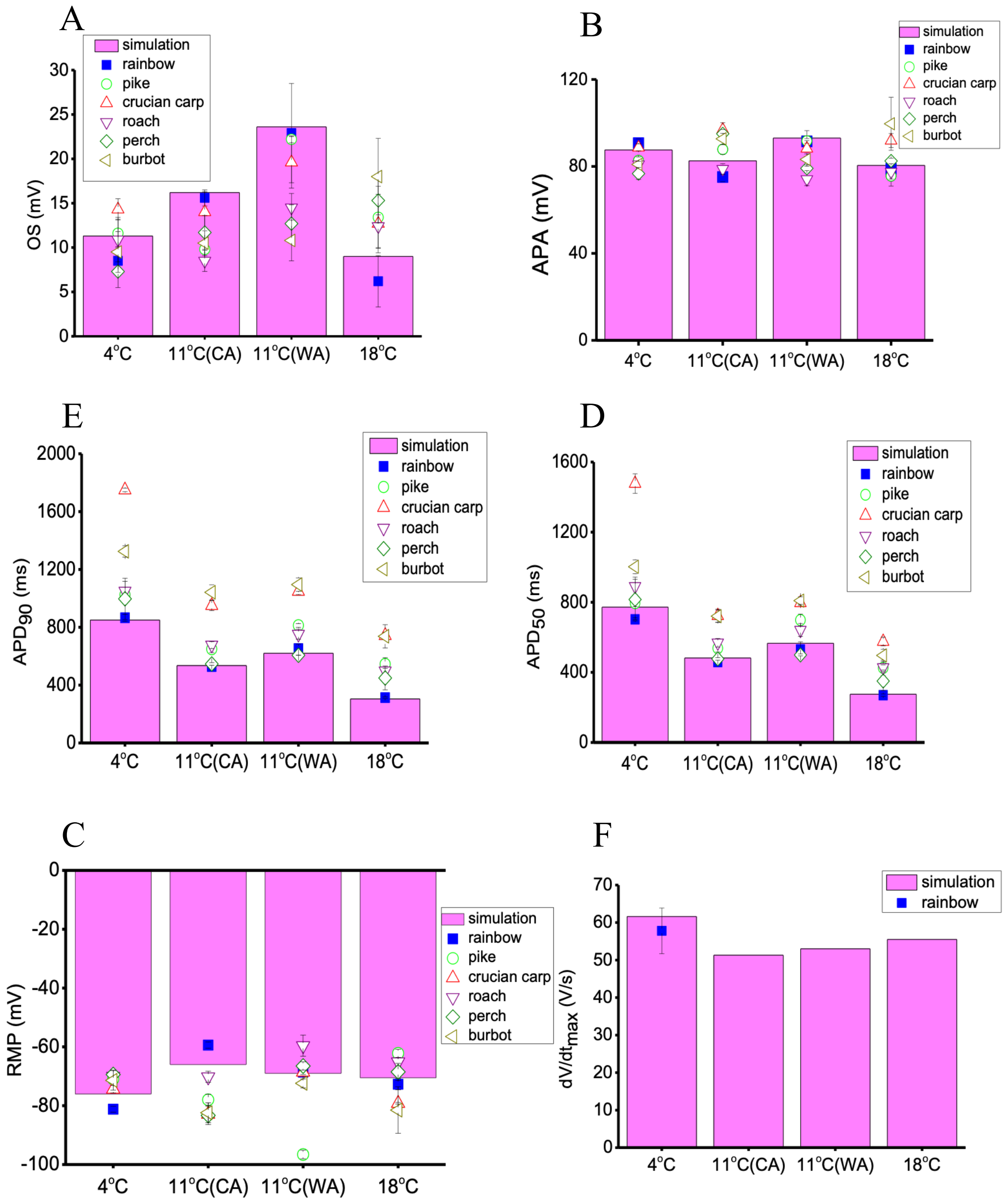

Figure 4.15: Characteristics of simulated APs compared with available experimental data for teleost fish models at cold (4-11CA)°C and warm (11WA-18)°C acclimations. A: The overshoot (OS). B: Action potential amplitude (APA). C: Resting membrane potential (RMP). D: Action potential duration at 50%repolarization (APD_{50}). E: Action potential duration at 90% repolarization (APD_{90}). F: The maximum upstroke velocity (dV/dt_{max}). The source of the experimental data is from Haverinen and Vornanen [42] except for dV/dt_{max}at 4°C is from [104].

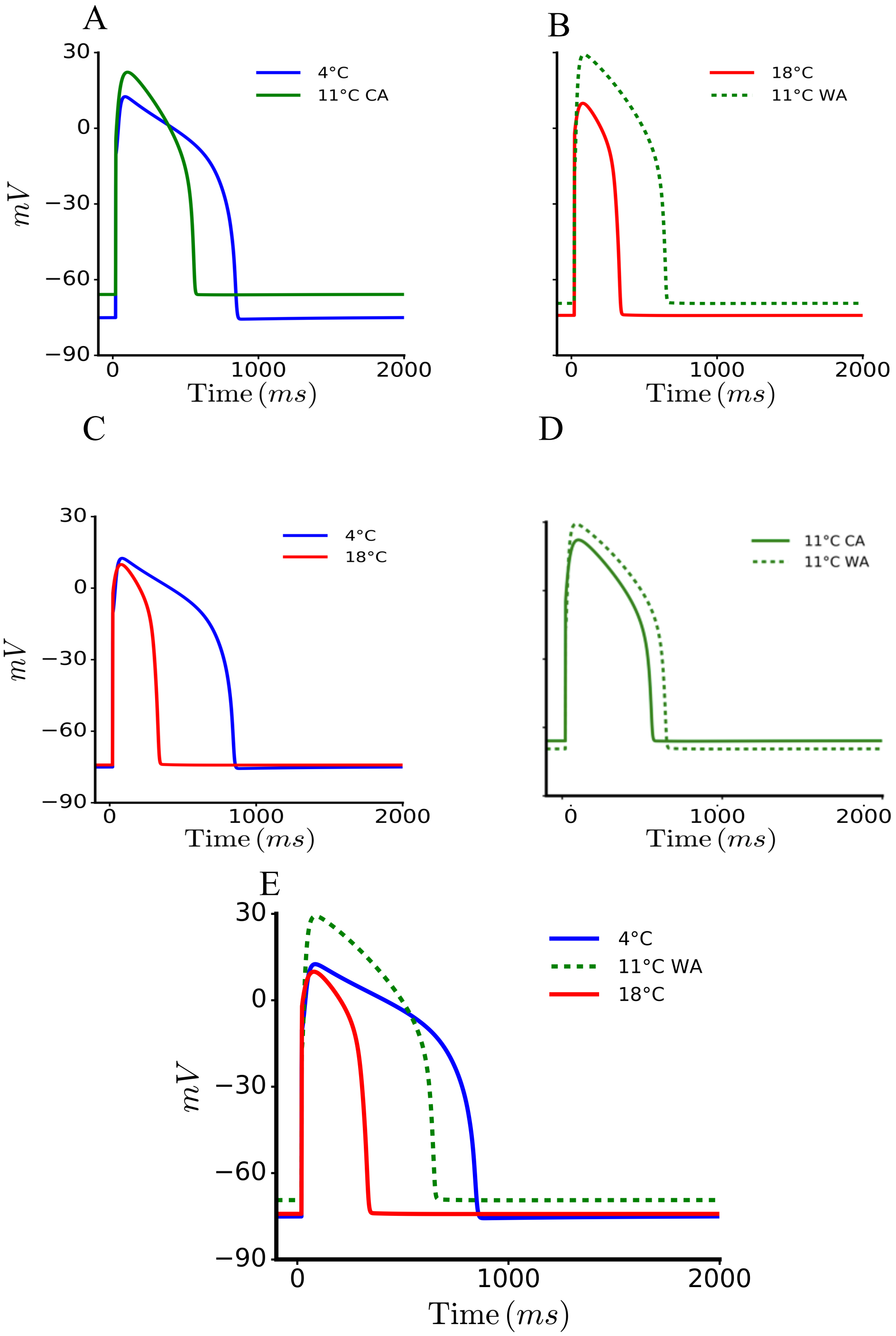

Figure 4.16: Effects of thermal acclimation on ventricular action potential (AP) of the teleost fish. A: AP profile at cold acclimation. B: AP profile at warm acclimation. C: AP profile at the two acclimated temperatures 4°C and 18°C. D: AP profile at WA, 11°C and CA, 11°C. E: AP profile of three selected temperatures from the developed models at 4°C, 11°C WA and 18°C.

4.4 The APD Rate Dependence

The steady state of the action potential duration (APD) rate dependence for the APD_{90} of the fish ventricular models at cold and warm acclimations are shown in Figure 4.17. In all models, the APD_{90} restitution curve illustrates that at BCLs above 1000 ms, the model demonstrates a great rate dependency and it was flat at BCLs from 1500 to 3000ms while there was an increase in the APD_{90} at slow pacing (above 3000 ms); however, 11°C WA and 18°C models show more stability. The simulation results are compared to available experimental data of different teleost species, including rainbow, perch, pike, burbot, roach, crucian carp from Haverinen and Vornanen [42]. Results are shown in Figure 4.17.

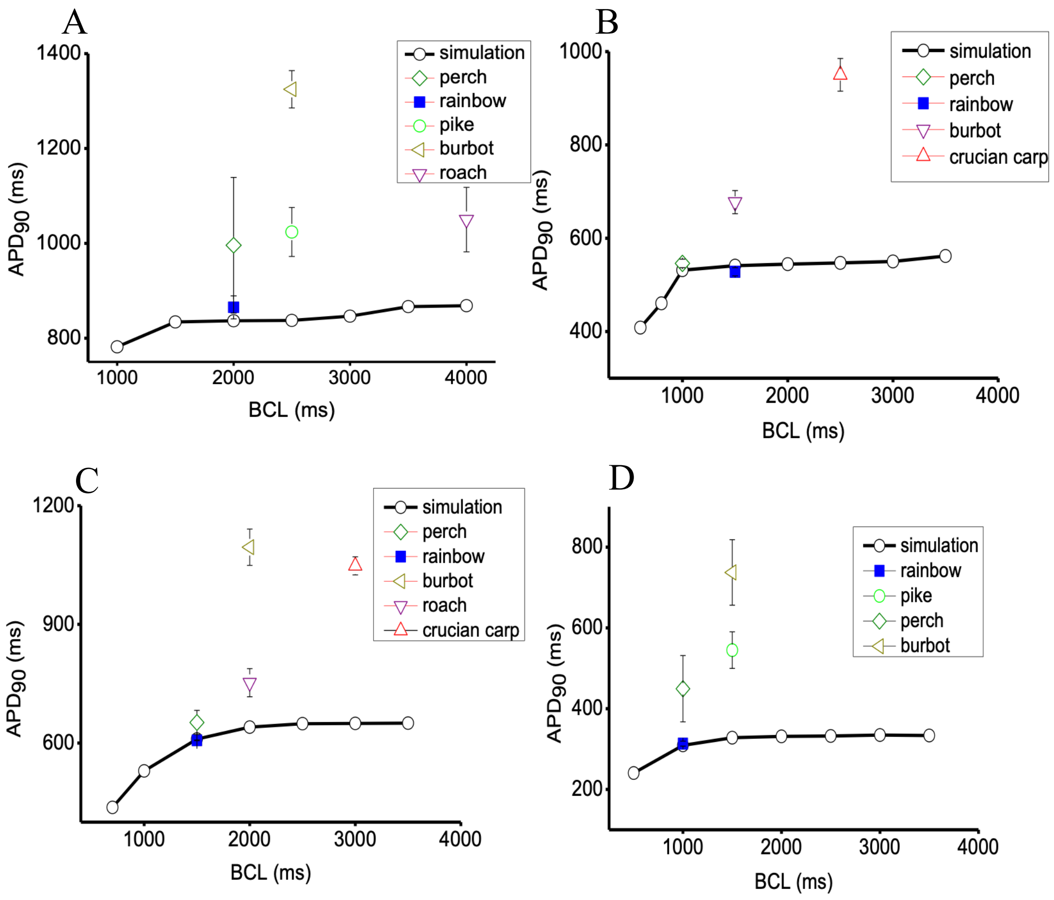

Figure 4.17. Steady state APD rate dependence of the fish ventricular model at different temperature. A: The cycle length dependency of the APD_{90} at 4°C. B: The cycle length dependency of the APD_{90} at 11°C CA. C: The cycle length dependency of the APD_{90} at 11°C WA. D: The cycle length dependency of the APD_{90} at 18°C, experimental data from [42].

4.5 Discussion

The novel models presented here successfully reproduced experimentally recorded teleost fish ventricular APs from two thermal acclimation conditions coupled with acute warming and acute cooling [15, 17, 42, 43, 46, 104, 153]. Specifically, two novel models for the teleost ventricular myocyte were developed for fish living in a chronically cold (4°C) environment (cold acclimated, CA) and a chronically warm (18°C) environment (warm acclimated, WA). The model was then modified to investigate the effects of acute warming from 4 to 11°C and acute cooling from 18 to 11°C, to understand the effects of rapid temperature change on the thermally acclimated fish heart. Finally, by comparing the output WA and CA model at a common 'test' temperature of 11°C, the models could be used to isolate the effects of thermal acclimation on ionic conductance from the direct effects of temperature on ions conductance.

The developed models were validated first by their ability to replicate the effects of thermally induced ionic remodelling on the action potential of the teleost fish heart. Chronic temperature alterations impacts the expression of the major ionic currents and their kinetics including: I_{Na}, I_{CaL}, I_{Kr} and I_{K1}, which remodel to optimise cardiac function in a given thermal environment [30]. Such investigations are essential to obtain information of the molecular mechanisms behind these cardiac thermal acclimation procedures in order to increase our understanding of the impact of global warming on fish life and species distribution [16, 42].

4.5.1 Thermal Acclimation Effects on the Main Currents

As discussed in Section 1.4, fish heart responses to changing in their ambient temperature differently. It shows a variable tolerance and plasticity to temperature; however, the mutability molecular and evolutionary origin are not completely understood [14, 91, 123, 163, 173]. This might be associated with environment conditions, the fish thermal preferences may represent molecular phylogenies which are different by which temperature-related problems have been solved in evolution [166]. A range of molecular mechanisms is involved in the electrical excitation of the heart, which might be responsible for thermal limitation of the heart function [43, 104]. In general, the functions of the ion channels are; controlling heart rhythm, initiating contraction and regulating force production of cardiac myocytes [181]. The developed models provide tools for quantitatively evaluating the functional role of major ion channel currents at cold and warm acclimation. Simulated results showed the following:

1. Acclimation to cold increased the density of I_{Na} in trout fish ventricular myocytes. This is in line with the common compensatory changes in function and size of the heart in most trout species to counteract the decelerating effects of low temperature on circulation [14, 42, 91]. However, thermal compensation in the trout heart was only partial, as the I_{Na} density at 4°C was 58% of the value of the density at 18°C [43]. This suggests that more than half of the current amplitude of the warm acclimation summer fish is required to maintain the excitability of the heart in cold acclimated winter fish. Briefly, the changes in I_{Na} density induced by the acclimation would mean that in winter, there is only a moderate depression in the upstroke and conduction velocity rate of APs of the cold active trout such as rainbow trout. Moreover, in other teleost species such as cold dormant carp, including crucian carp, there is a severe depression in the I_{Na} density. This is due to differences in the response of different fish species to acclimation which could induce changes in the number of functional channels such as protein degradation rate, transcription, translation and trafficking of channels to the sarcolemma [107]. In addition, a negative shift with a value of 6 mV in the steady-state activation curve of the I_{Na} current occurs when acclimated to cold, which may decrease the stimulus threshold needed for provoking an AP. Accordingly, change in voltage-dependence of steady-state activation induced by temperature will further improve on that obtained by partial compensation of the I_{Na} density, and thus maintain the cardiac excitability in the trout heart at cold.

2. The I_{CaL} density was not quite altered by thermal acclimation in the trout heart indicating no temperature-dependent compensation either in the I_{CaL} density or in the L-type Ca^{2+}channel function. However, acclimated to cold will accelerate the inactivation kinetics of I_{CaL}. In the cold, it could be expected that the force production of cardiac cells would be compromised as low temperatures reduce the peak amplitude of the I_{CaL} current and decrease the Ca^{2+}-sensitivity of the myofilaments [107]. At low body temperature, the APD is greatly prolonged; the peak amplitude reduction of the I_{CaL} current could be compensated by slower inactivation of I_{CaL}, maintaining the influx of Ca^{2+} ions through non-inactivating channels (window current) and reopening of individual Ca^{2+} channels during the prolonged plateau phase of the cardiac AP [107, 182].

Consequently, the long APD at cold temperatures permits a prolonged Ca^{2+} ion influx through the same number of Ca^{2+} channels and/or Na^{+}/Ca^{2+} exchanger molecules, therefore, the combined Ca^{2+} ion influx of the sarcolemmal remains comparatively independent of ambient temperature.

3. The potassium (K^{+}) channels have the plasticity to adjust the cardiac electrical activity under different physiological conditions such as chronic thermal stress. They facilitate repolarising currents, mainly the rapid delay rectifier current, I_{Kr}, which regulates the teleost cardiac AP duration (APD) and the inward rectifier current that maintains the negative RMP [15, 74, 153]. The APD thermal compensation indicates a changed balance between depolarising and repolarising currents. As I_{Kr} represents the main repolarisation current of the teleost heart, the APD compensation can generally be attributed to noticeable alterations in the I_{Kr} density. Results showed that cold acclimation upregulated the I_{Kr} [30], which can be an almost ubiquitous response in approximately all teleost fish and hence an essential factor in adapting the electrical activity of the heart to chronic cold. It has been found that in trout fish, the I_{Kr} thermal response was uniform in comparison with other fish species. This could be due to the simpler genetic basis of the I_{Kr} current as vertebrate hearts usually express only one kind of channel that produces I_{Kr}, which is the ERG channel [153].

4. The ability to modify the inward rectifier current, I_{K1}, at thermal acclimation is different between fish species. In Salmoniformes fish such as rainbow trout, modulated I_{K1} is weakly developed or absent, which shows an exceptional inverse thermal compensation, while in other species such as cyprinid species, the ability to modify I_{K1} is vital in thermal adaption. Haverinen and Vornanen [42] and Hassinen et al. [153] have found experimentally that I_{K1} is generated by different Kir2 channels. For example, in trout cardiac myocytes, I_{K1} is formed by Kir2.1 and Kir2.2 channels only, whereas in the cardiac cells of crucian carp, it is generated by Kir2.2 and Kir2.5 channels. The absence of Kir2.5 channels in trout hearts may explain the reduction of I_{K1} (inverse thermal compensation) when trout species (rainbow and brown trout) acclimate to cold, while an obvious increase can be noticed in crucian carp myocytes. Hence, under chronic temperature changes, the ability to modify I_{K1}may have a phylogenetic origin depending on the exciting of different Kir2 channels and/or the possibility of different isoforms of Kir2 being expressed in the heart.

4.5.2 The Role of Changing the Chronic Temperature in Modulating Action Potential Morphology and Duration

The present study shows a non-linear role of changing temperatures on shaping the morphology and duration of ventricular AP at cold acclimation, CA and warm acclimation, WA. Thus, thermal remodelling is import for fish hearts because acute changes in temperature can dramatically affect cardiac function. As discussed in Section 4.3.2.1, the effects of changing chronic temperature can be investigated when a comparison made between the AP characteristics at 11°C CA and 11°C WA. This is due to the ion channels remodelling that occurs with thermal acclimation at this temperature. Simulations showed that acclimation to warm (from 11°C CA to 11°C WA) (Figure 4.16D) elevated the OS and the APA, hyperpolarised the RMP and accelerated slightly the $\mathrm{dV/dt_{max}}$. Moreover, analysis of warm acclimation on the modulation of APD showed a prolongation in the duration of the trout ventricular AP (Figure 4.16D) from 11°C CA to 11°C WA. These simulations match quantitatively well to those experimentally observed by Haverinen and Vornanen [42]. These results suggested that warm temperatures reduces the electrical excitability of most teleost species hearts, particularly the rainbow trout heart; however, when the activation threshold of an AP is achieved, the action potential progresses rapidly [20, 118].

From the above, acute warming accelerated whilst acute cooling slowed ionic process. Importantly, when the CA and WA models were run at a common temperature of 11°C to reveal remodelling responses, the CA models generated action potential has a faster upstroke, more positive peak value, greater amplitude and longer duration than the WA models, in line with experimental data. This Chapter develops and validates novel mathematical models for the electrical action potential at single cell of a CA and WA teleost fish ventricular myocytes. Because aquatic systems across the globe are currently warming, such models will be vital for understanding the possible effects of changing temperatures on fish health and the economies of human populations who rely on fisheries.

4.6 Limitations of the Study

Like all other models for the electrical action potential of cardiac cells, the presented models for teleost fish ventricular myocytes do have intrinsic limitations.

Although the mathematical models for the main ionic currents, including I_{Na}, I_{CaL}, I_{Kr} and I_{K1} at cold and warm acclimation, were based on teleost-specific experimental data, the mathematical models for other currents in the developed models, including I_{NaCa}, I_{Nab}, I_{Cab}, I_{Kp}, I_{pCa}, $I_{K(ATP)}$ and I_{NaK}, were assumed to be the same as in the basal model [54] for the guinea pig and the human, due to the lack of experimental data of such currents for the teleost fish. This might not be the case as there is a possibility of differences in the kinetics of those currents between the teleost fish, guinea pig and human ventricular cells, especially when acclimated to different temperature conditions. Moreover, some other currents may present in the teleost ventricle but not in the guinea pig or human ventricles. However, so far there are no data to indicate that the types of ion channels differ between mammals and fish, and the currents modelled are those present in the ventricle of several other species [48, 53–55], indicating that this is a valid assumption.

The data that used to fit the kinetics of the I_{Na}, I_{CaL}, I_{Kr} and I_{K1} currents at different temperatures were obtained from different teleost fish species of ventricular myocytes, which might vary in their ion channels' isoforms. It is possible that the kinetics of these channels in the fish ventricle are specially altered at different temperatures and that interaction with additional accessory subunits occurs.

In addition, the intracellular and extracellular ion concentrations, including $[Na^{+}]_i$, $[Ca^{2+}]_i$, $[K^{+}]_i$ and $[Na^{+}]_o$, $[Ca^{2+}]_o$, $[K^{+}]_o$, respectively, were used with the same values at a different temperature. The ion concentration might be temperature dependent as well; this needs a deeper look experimentally.

Another limitation of the present fish models is that the description of the Ca^{2+} handling mechanism in the SR is adapted from an existing quantitative model of the mammal ventricular cell [54], which resulted in a higher value for the Ca^{2+} transient of fish ventricular cells than the experimental findings for different types of teleost fish. However, we reduced the rate constant of the Ca^{2+}

release from the JSR by 20% (couldn't decrease more in order to keep the stability of the APs), but the Ca^{2+} transient was still a bit higher. The improvement to the Ca^{2+} handling system and thus the value and shape of the Ca^{2+} transient suggests that this may be a good model for the investigation of fish ventricular myocyte contraction mechanisms.

4.7 Summary

Novel, integrated, single cell models for the teleost fish ventricular myocyte at warm and cold acclimation have been developed. These models have used the model developed by Luo and Rudy in 1994 [54] as a basal framework of these computer models.

These models are based on a set of Hodgkin and Huxley formulations for the major ionic currents, including I_{Na}, I_{CaL}, I_{Kr} and I_{K1}. Those models were inherited from some existing mathematical models of mammal hearts, including Luo and Rudy's model [54], Pandit and colleagues' model [48] and Courtemanche and colleagues' model [156], and based on recent fish data from different teleost species. The models produce well-validated APs, with a morphology reasonably similar to that observed experimentally. Simulations showed that acute cooling prolonged the APD_{90} of the trout ventricular than warming, which shortened it, whereas chronic temperature change from WA 11°C to CA 11°C prolonged the APD_{90}; this finding agrees with the experimental data from Haverinen and Vornanen [42]. Additionally, the simulated AP characteristics at cold and warm acclimation were satisfactory close to those empirically measured from different teleost fish species [15, 104, 107, 173].

5. Investigating the Effects of Increasing Acute Temperature on the APs and ECGs of the Teleost Ventricular Using Single Cell and 1D Strand Tissue Models at Different Temperature.

5.1 Introduction and Aims

The rate of life processes of the ectotherms, such as fish, is influenced pervasively by the environmental temperature, which can be a crucial factor in the geographical distribution of such animal species [17]. Although environmental temperature can affect the fish animal performance, there are restricted thermal limits for all biological functions of the animal body. This includes the cardiac electrical excitation that regulates both the rate and rhythm of the fish heart, which can be a vital factor in the modulation of temperature-dependent cardiac function [30]. The electrical excitability control needs to be sufficiently sensitive to respond to alterations in temperature. However, it should be concurrently robust to protect the fish heart from an arrhythmia that might occur due to altered temperature. Therefore, the fish ability to adjust to climate change may be determined by physiological qualities, including the thermal flexibility and elasticity of the electrical excitation.

Acute temperature changes induce alterations in the heartbeat rate (f_H) as well as the ventricular action potential (AP) duration of the teleost fish heart, which are not entirely different from the chronic temperature changes discussed in Chapter 4.

Remarkably, the thermal tolerance limits develop firstly at the intact animal's level, then in the tissues, cells and molecule functions [183]. For instance, the thermal tolerance of the lipid membrane structure and proteins is higher than the thermal tolerance of the whole organism [32]. It has been found that exposing animals to long term new thermal conditions produces compensatory alterations in the ion channel's expression and function to partially alleviate the direct effects of temperature on the cardiac action potentials [17]. Although the thermal dependence processes of different molecules and cells are well researched, factors that limit the thermal tolerance of ectothermic animals are poorly understood. However, recent findings from vertebrates, including fish, indicate that heart functions could be one of the most obvious factors limiting the upper thermal tolerance of such ectothermic species [11, 184].

In fish cardiac cells, the ion channels are flexible entities that have a strong ability to respond to changes in the chronic temperature [15, 42, 43, 153]. This indicates that ion channels are entirely involved in both temperature acclimation and thermal tolerance of cardiac functions. The channel's configuration and also the subunit assemblies differ from one species to another. These differences may explain the thermal dependency variations of the electrical excitability of different fish species [15, 30, 153].

Numerous studies of the fish heart [15, 42, 43, 153] have indicated that Na^+channels seem to be the most heat-sensitive molecular components contributing to cardiac electrical excitation. Hence, at high temperatures, Na^+ channels may determine the upper thermal limit for the heart excitability by compromising the AP initiation of the cardiac myocytes [30]. In addition, the altered temperature dependencies of the inward Na^+current, I_{Na}, and the outward K^+ current, I_{Kr}, may compromise the electrical excitation in cardiac and other excitable cells at extreme temperature, referred to as the temperature-dependent depression of electrical excitation.

In fish hearts, the electrical excitation comprises a range of molecular mechanisms, which possibly determine the thermal limitation of cardiac functions. The previous chapter investigated the effects of the temperature dependence of ion channels on ventricular APs. It was demonstrated that experimentally observed changes in APs at the cellular level due to changes in ionic channel levels could be accounted for by changes at the ion current levels. However, it is still unclear how such temperature-dependent changes at the cellular level affect excitation wave conduction at the tissue level. Hence, the aim of the current chapter was twofold: the first name was to develop a one-dimensional strand tissue model for the teleost ventricular tissue at the physiological temperature at cold (4°C) and warm (18°C). The second aim was to examine whether temperature-sensitive changes in ion channel properties of the trout heart represent a limiting factor for the electrical excitability of the heart, which might lead to the heat death of the fish. This was done by investigating possible effects of rising the acute temperature on excitation wave conduction in response to altered function of the major ion channels of the trout heart. In this chapter, two ion channels have been studied including sodium ion channels with a fast sodium current (I_{Na}) and potassium ion channels with a rapid delay rectifier potassium current (I_{Kr}). These currents represent the most sensitive currents to high temperatures, particularly for the I_{Na} current, which is the lowest threshold for temperature-dependent deterioration and the I_{Kr} current, which is the next heat-sensitive current. Other currents, such as I_{K1} and I_{Ca}, are known as the most resilient to high temperatures [17]. The I_{Na} and I_{Kr} densities change with increasing temperature from 4°C to 33°C (with some temperature steps) and these changes has been implemented in single cell models and 1D strand tissue models to investigate the effects of changing temperatures on the action potentials (APs) and electrocardiogram (ECG) and hence on the function of the teleost fish heart.

5.2 Methods

5.2.1 Homogeneous 1D Strand Ventricular Tissue Model

One-dimensional (1D) simulations were performed using a homogeneous ventricular model. The 1D tissue strand model used for the simulations has an entire length of 16.5 mm, similar to those used by Zhang and Hancox for human ventricle tissues [185]. The simulated one-dimensional strand used a spatial resolution of 0.15 mm that discretised the tissue strand into 110 nodes. The AP propagation in all tissue simulations was described using the monodomain equation, as shown in (Equation 5.1), previously described in Chapter 3.

$$\frac{\partial V_m}{\partial \mathrm{t}} = -\mathrm{I}_{\mathrm{tot}} + \nabla . (\mathrm{D} \nabla V_m) \tag{5.1}$$

where V_m is the transmembrane potential, I_{tot} represents the summation of all ionic currents in the transmembrane and was modelled by the developed single cell model equations at 4 and 18°C in (Chapter 4). D is the diffusion coefficient that describes the intercellular electrical coupling by gap junctions [185, 186] and was set to 0.00135 $cm^{-2}ms^{-1}$ (constant value), similar to that previously utilized by Zhang and Hancox [185] and Clayton and Holden [187] for human ventricular myocytes.

Single cells at cold (4°C) and warm (18°C) temperatures were paced until a stable solution was achieved, as shown in Chapter 4. Then the 1D strand was paced utilising these initial conditions from one end with five successive conditioning stimuli. A supra-threshold stimulus (amplitude: -57 pA/pF (at 4°C) and -41 pA/pF (at 18°C) tissue models, duration: 10.0 ms and time step: 0.01 ms (for both models)) was applied to evoke a conducting excitation wave (Figure 5.1A,B).

5.2.2 Measurement of Conduction Velocity

The 1D strand model was used to compute the conduction velocity (CV) using the same method as implemented in [185]. The CV was computed from one-quarter and three-quarter nodes of the way alongside the 1D strand. For an individual point, the activation time was defined as the time at which the dV/dt_{max} occurred.

By applying a sequence of five conditioning stimuli at a frequency of 1Hz, the CV was calculated in the 1D tissue strand by measuring the time ΔT for the conducting wave to propagate from $x-\Delta x$ to $x+\Delta x$ and describe $\mathrm{CV} = \frac{\Delta \mathrm{x}}{\Delta \mathrm{T}}$.

5.3 Results

5.3.1 Simulation of the ECG at the Physiological Temperatures 4 and 18°C

A pseudo-electrocardiogram was computed (as discussed in Chapter 3) utilising a one-dimensional strand of cells across the teleost ventricular wall at a stimulation rate of 1 Hz for the physiological temperatures at cold (4°C) and warm (18°C) temperatures, as seen in Figure 5.1 C, D. The 1D strand model of the teleost ventricular tissue at both temperatures was paced at BCL = 1000 ms to make the comparison between the two temperatures conditions much easier. The space-time plots of the action potential propagation in the 1D strand at 4°C and 18°C are shown in Figure 5.1. The transmembrane potential distribution across the 1D transmural strand is presented by the use of a standard rainbow palette that ranges from -80 to +15 mV at 4°C (Figure 5.1, A) and from -75 to +15 mV at 18°C (Figure 5.1, B). Simulations were performed, and a homogeneous ventricular wall was incorporated (Figure 5.1), which gives negative T-waves.

For each temperature model, delivering a sequence of supra-threshold stimuli initiates a propagating excitation wave at one end of the strand (see Section 5.2.1). This produced action potentials, provoking excitation waves that propagate towards the rest of the strand with time, as space runs vertically from the bottom of each panel to the top, while time runs horizontally from left to right on each panel [185]. The propagating excitation wave was calculated by the fifth stimulus in the sequence was tested, and the ECG characteristics, including ORS, RT and QT intervals in the teleost physiological temperature (4°C and 18°C), were also computed. Simulations showed that at warming, there is a slight change in the QRS interval width by 5% from 33.7 to 32.03 ms.

Fish research usually calculates the pseudo-RT interval instead of the QT interval due to the ECG waveform of the fish heart, which prevents a reliable identification of the position of the Q-wave [17]. Results show a linear decreasing in the pseudo-RT interval, which was shortened at warming by 52%, shortening from 524 to 247.5 ms. The pseudo-QT interval also showed a linear change with temperature and was shortened at warming from 4°C to 18°C by 50%, shortening from 554 to 277 ms (Figure 5.1 C, D). This is associated with the shortened APD_{90} in single cell simulations (Chapter 4). In addition, the conduction velocity (CV) was also calculated using the aforementioned protocol (Section 5.2.2). Simulation results showed that at warming, the CV slowed by approximately 4%, from 0.5 to 0.52 m/s, due to the slowing in the upstroke velocity. All the pseudo-ECG features are shown in Table 5.1. The 1D model was constructed at different temperatures in order to simulate the likely effects of changing temperatures on electrocardiogram (ECG) using multicellular simulations, which will be described in the next section.

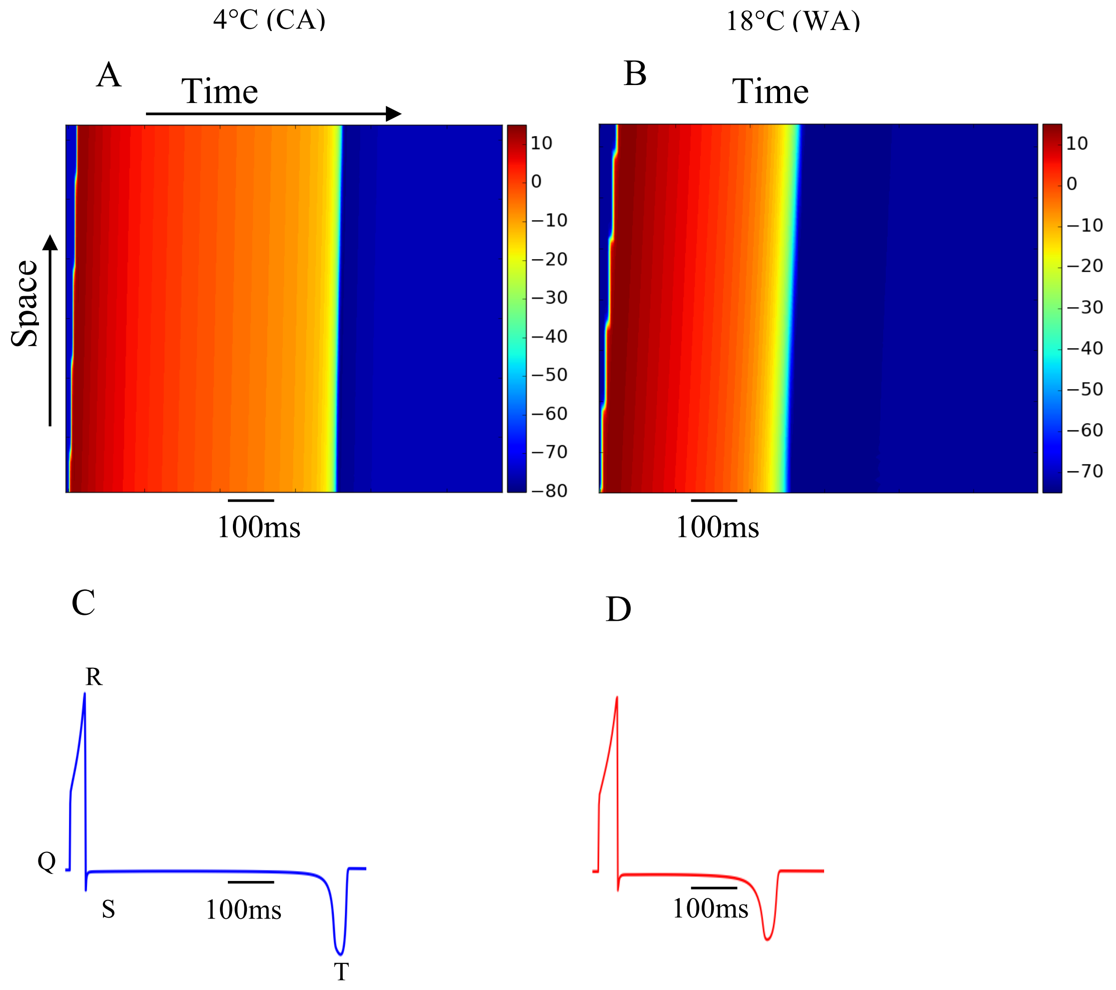

Figure 5.1: The propagation wave and QT interval reconstruction. An excitation wave propagation through the 1D strand model of the teleost fish ventricular is shown at the upper panels. A, B: Space-time color-mapping of membrane potential of fish ventricular wall strand at 4°C (CA) and at 18°C (WA), respectively. By the applying of a supra-threshold stimulus to the one end of the strand, the excitation waves were induced and propagated toward the rest parts of the strand. On each panel, space runs from the bottom of each panel to the top, vertically, while time runs from left to right on each panel, horizontally. The computed pseudo-ECG is shown in the lower panels, at 4°C in C and at 18°C in D. In each case, depolarisation initiated from the one end of the strand, while repolarisation initiated from the other end of it, with an obvious negative T-waves. BCL = 1000ms.

5.3.2 Effects of Rising Aquatic Temperature on AP and ECG

As explained in the previous chapters, the AP and ECG are generated by the combined activity of all transmembrane ion channels of cardiac cells; therefore, heat-related disturbances in APs and ECGs are owed to the imbalance between depolarising or repolarising ion currents. This result is due to different temperature dependencies or even failure in the temperature dependent of one or more ion channels. The failure could occur in any region of the fish heart; it might be in the pacemaker cells (which initiate the heartbeat) or in the conducting pathway between the atrium and the ventricle or in the working cells of the atrial and ventricle [17]. As shown in Chapter 4, the major ion currents in the fish cardiac myocytes (I_{Na}, I_{CaL}, I_{Kr} and I_{K1}) are often highly variable [15, 41, 43, 107, 153] while in mammals, these currents work optimally at 36–39°C (which is the body temperature).

Regarding heat tolerance of most fish hearts, the large variability between various ion channel currents indicates that the thermal features of the bulk lipid membrane are not conclusive; however, the direct involvement of the lipid environment of the ionic channel (the lipid annulus) cannot be discounted [188].

As a result, there are possible effects of rising temperature on the teleost cardiac function in one or more ionic membrane channels. Therefore, we studied the temperature-dependent effects of two ionic channel currents including the sodium channels represented by the inward current (I_{Na}) (which is responsible for the depolarisation phase) and the potassium channels represented by the outward current (I_{Kr}) (which is responsible for the repolarisation phase), as these currents represent the lower resistant currents to changing temperatures [17]. Hence, these currents can be a useful tool in our study of the effects of temperature changes. These effects were then incorporated into the I_{Na} and I_{Kr}, which are either increasing or decreasing for both currents in the previously developed models (in Chapter 4) at the physiological temperature of cold 4°C and warm 18°C, as shown in Table 5.1. The temperature effects on I_{Na} and I_{Kr} are taken from the available experimental findings measured by Vornanen et al. [17] for brown trout teleost fish. Although the thermal sensitivity of the cardiac myocytes of the teleost fish is different between species, the main effects of increasing temperature on the electrical excitation can be similar concerning current density and voltage dependence [43], especially at temperatures above their thermal tolerance. In this sense and according to a lack of experimental data regarding rainbow trout, we compared our simulation results of AP and ECG temperature sensitivities to those of brown trout recorded by Vornanen et al. [17], as shown in Figure 5.2.

Vornanen et al. [17] showed that I_{Na} density increased between 4°C and 17°C while above that (until 33°C), the I_{Na} current strongly decreased, and above that, it is slightly higher than at 4°C [17] (see Table 5.1). It was noticed that the temperature dependence curve of I_{Na} has a V-shape, which is a mirror image to the inverted V-shaped curve of the upstroke velocity of the action potential [17]. However, the density of the tail current, I_{Kr} increased 6.2-fold between 4°C and 29°C and above 30°C I_{Kr} steeply declined [17] (see Table 5.1). Results of simulated AP and ECG characteristics with the relevant experimental data [17] are shown in Table 5.1 and Figure 5.2.

Table 5.1 illustrated the scaling factor of changing densities of I_{Na} and I_{Kr} currents with increasing temperatures from 4°C to 33°C, calculated from the experimental records of Vornanen et al. [17]. Following the application of these factors for both currents in the single cell models (developed in Chapter 4) and 1D strand tissue models (developed in this chapter) at 4°C and 18°C, the new simulated AP and ECG characteristics obtained from those models (both single cell and tissue) have been arranged in Table 5.1 at each temperature. The simulated AP features included OS, APA, dV/dt_{max} and APD_{90}, while the simulated ECG features included QRS, QT, and RT intervals and the conduction velocity (CV). Most of those features have been validated with the available experimental data, as can be seen in Section 5.3.3.

Table 5.1: Simulated features of the action potential (AP) and electrocardiogram (ECG) of teleost ventricular myocytes at different temperature. A: Simulated AP and ECG properties at 4,6,10,12,14 and 16°C. B: Simulated AP and ECG properties at 18,24,26,28,29,31 and 33°C. Abbreviations are as follows: Exp.= experimental, Sim.= simulation, T= temperature, I_{Na}= Fast Na^{+} current, I_{Kr}= Rapid delayed rectifier K^{+}current, OS= overshoot , APA= action potential amplitude, $\mathrm{dV/dt_{max}}$= maximum upstroke velocity, $\mathrm{APD_{90}}$= action potential duration at 90% of repolarisation, QRS= The QRS complex duration, RT= The RT interval, QT= The QT interval, CV= conduction velocity. For the physical meaning of the AP characteristics and the ECG features see Section (2.6.4) and Section (2.9.1), respectively.

A

T °C	4	6		10		12		14		16	
	Scaling factor										
I_{Na} pA/pF		Exp.	Sim.	Exp.	Sim.	Exp.	Sim.	Exp.	Sim.	Exp.	Sim.
		×1.61	×1.61	×2.07	×2.07	×2.36	×2.36	×2.62	×2.62	×2.80	×2.80
I_{Kr} pA/pF		Exp.	Sim.	Exp.	Sim.	Exp.	Sim.	Exp.	Sim.	Exp.	Sim.
		×1.18	×1.18	×1.17	×1.17	×1.76	×1.76	×1.89	×1.89	×2.46	×2.46
AP characteristics											
OS (mV)	7.5	8.02		10.4		14.3		16.4		19.6	
APA(mV)	83.3	83.8		86.2		90.08		91.9		95.36	
dV/dt_{max} (V/s)	61	106		137		159		165		145	
APD_{90} (ms)	845.22	797.37		726.36		659.09		594.45		501.99	
ECG features											
QRS (ms)	33.7	34.02		32.91		32.71		31.9		32.02	
QT (ms)	554	544		538		500		460		313.6	
RT (ms)	524	513		508		473		460		295	
CV (m/s)	0.52	0.6		0.68		0.74		0.72		0.7	

B

T °C	18	24		26		28		29		31		33	
	Scaling factor												
I_{Na} pA/pF		Exp.	Sim.	Exp.	Sim.	Exp.	Sim.	Exp.	Sim.	Exp.	Sim.	Exp.	Sim.
		×0.83	×0.83	×0.78	×0.78	×0.72	×0.72	×0.69	×0.69	×0.62	×0.62	×0.43	×0.43
I_{Kr} pA/pF		Exp.	Sim.	Exp.	Sim.	Exp.	Sim.	Exp.	Sim.	Exp.	Sim.	Exp.	Sim.
		×1.19	×1.19	×1.26	×1.26	×1.27	×1.27	×1.3	×1.3	×1.03	×1.03	×1.11	×1.11
AP characteristics													
OS(mV)	9.7	8.4		7.8		0.7		0		0		0	
APA(mV)	80.3	79		78.3		71.4		70.5		70.8		71.1	
dV/dt_{max}(V/s)	55	42.8		39.4		39.1		38.9		38		37.2	
APD_{90}(ms)	351.41	283.59		267.21		150.82		92.88		54.21		32.69	
ECG characteristics													
QRS(ms)	32.03	33.9		34.3		36.8		37.8		39.2		44.1	
QT(ms)	277	257		252		250.2		248.4		271		266.8	
RT(ms)	247.5	226.3		220.1		216.7		215.8		246		235.7	
CV (m/s)	0.50	0.47		0.45		0.43		0.42		0.40		0.31	

Figure 5.2 shows the simulated AP and ECG for teleost fish ventricular myocytes at different temperatures, from a cold 4°C until the thermal limitation of some teleost fish (specially, the salmonid species such as brown trout and rainbow trout fish), at a warm 31°C. The AP and ECG in all the models at the various temperatures were obtained with a stimulation rate of 1-Hz (BCL=1000 ms in order to compare them easily) and calculated after at least 30s of continuous simulation to ensure the steady-state solution was reached. In Figure 5.2A, the simulated AP at different temperatures were compared to those of the AP of brown trout fish (Figure 5.2B inset) as it is assumed to have the same behaviour at increasing temperatures as most salmonid species. However, for the simulated ECG at different temperatures (see Figure 5.2C), there was no available experimental data for comparison. However, some characteristics of the ECG, such as QRS and RT intervals, have been measured experimentally for the brown trout by Vornanen et al. [17] and have been used in this thesis to compare findings with our simulation results, as can be seen in Section 5.3.3.2.

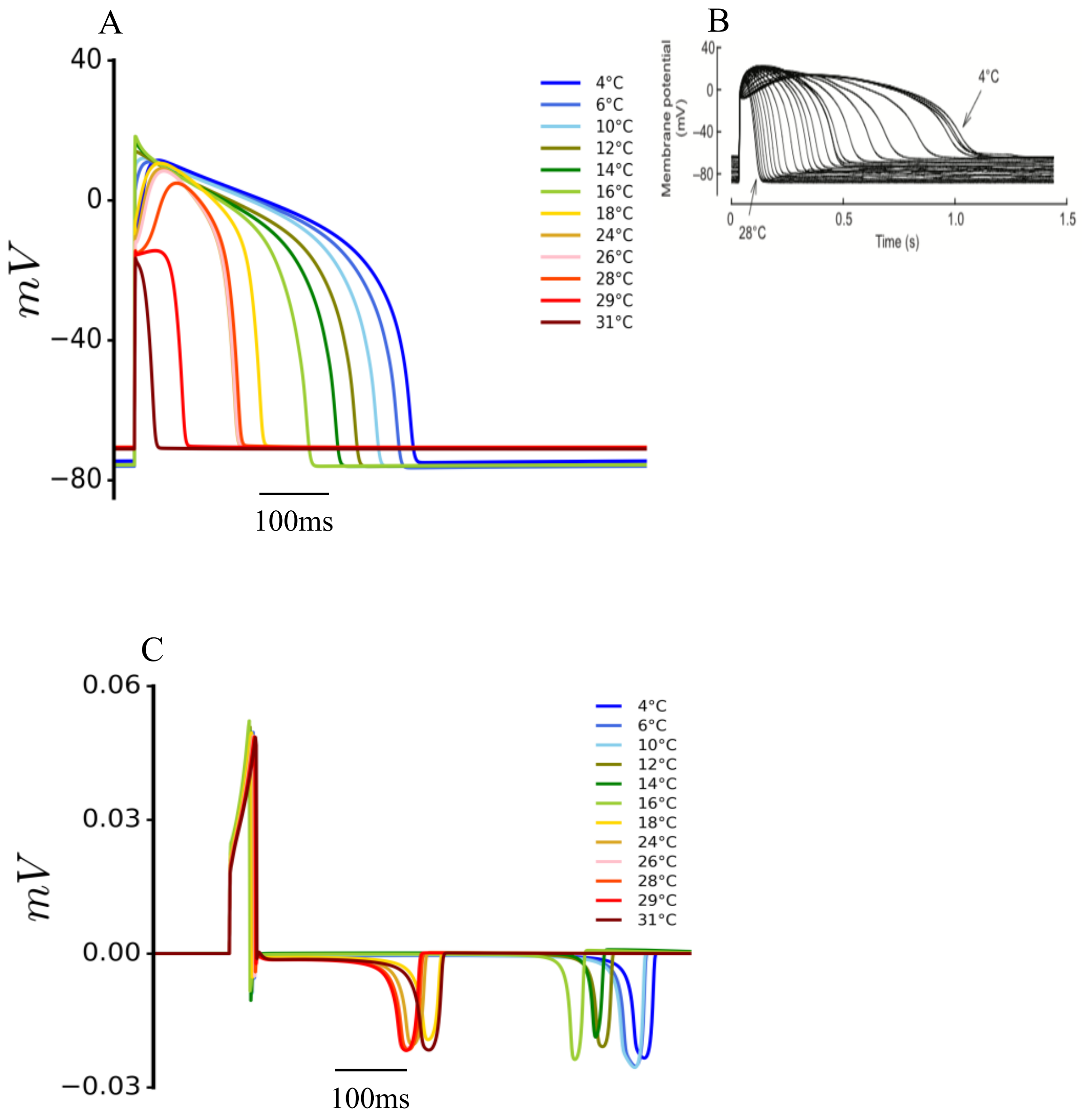

Figure 5.2: The simulated effects of acute temperature increase on both AP and ECG of the teleost ventricle. A: Temperature changes acutely impacts on the simulated AP. B: The inset represents the empirical AP of brown trout fish at different temperature from [17]. C: Temperature changes acutely impacts on the simulated ECG.

5.3.3 Models Validation

5.3.3.1 Single Cell Simulations

It can be noticed that the simulated amplitude of AP (Figure 5.3 A) first increased with the increasing temperature between 4°C and 17°C with a good agreement with experimental data of brown trout [17], and then levelled off between 18°C and 31°C. Moreover, at 4°C and 18°C, the simulated APA was satisfactorily close to the experimental data from rainbow trout [42].

The thermal response of the maximum upstroke velocity (dV/dt_{max}) of the ventricular AP increased between 4°C and 17°C with a peak at 16°C, then decreased at a temperature between 18°C and 26°C. The dV/dt_{max} thermal curve had an inverted V shape with a peak at approximately 16°C and minimum values at 4°C and 33°C [42]. These results showed a close agreement to those experimentally recorded by [42] of brown trout and at 4°C of rainbow trout from [104], as seen in (Figure 5.3B).

Unsurprisingly, rises in temperature were linked with a decrease in the action potential duration (APD). Reduction in APD_{90} becomes shorter at higher temperatures; however, there was no obvious limitation to the AP shortening [17]. The APD shortening with increasing temperature suggests that the balancing between inward (Ca^{2+} and Na^{+}) currents and outward (K^{+}) currents (which determines the AP plateau duration) altered at high temperatures in favour of the repolarising K^{+} currents. Shortening of AP plateau is necessary for cardiac functions to make room for the heart diastolic filling when cardiac cycles are abbreviated [17], leading to fast heart rate which might cause a sudden cardiac failure (Figure 5.3 C).

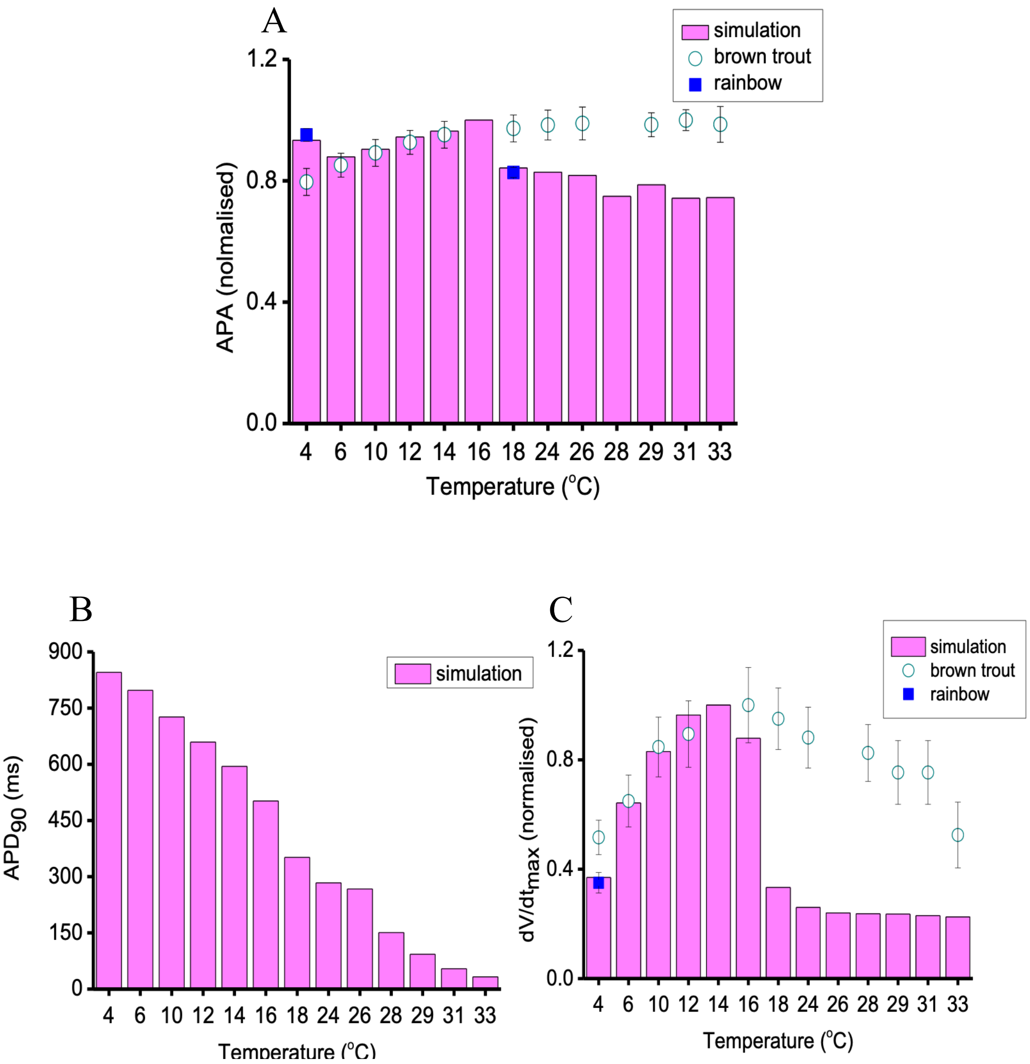

Figure 5.3: The effects of changing the acute temperature on the AP characteristics. A: Acute temperature changing effects on APA. B: Acute temperature changing effects on APD_{90}. C: Acute temperature changing effects on the maximum upstroke velocity (dV/dt_{max}). Note: columns refer to the simulation results while the full blue squares refer to the experimental data from rainbow trout fish [42] and the open circles refer to the experimental data from brown trout fish [17].

5.3.3.2 1D Simulations

Acute temperature changes had an intense effect on the ECG features of the teleost fish heart (Figure 5.4). At rising temperatures, a sudden increase in the QRS complex duration was noticed. First, there was a slight reduction in the QRS duration by around 5% with rising temperature from 33.9 ms at 4°C up to 32.4 ms at 24°C, after which there was a strong increase by approximately 36% with a QRS duration value of 44.1 ms at 33°C (Figure 5.4A). As the QRS duration represents a measure for the velocity transmission impulse over the ventricle, hence, a widening in the QRS duration signifies depression in the AP propagation rate over the heart when temperature increases [17].

Another change was in the simulated RT interval (experimental studies used RT for definitions instead of the QT interval), which decreased linearly with increasing temperature from 4°C to 18°C; above that the RT interval somewhat declined (Figure 5.4 B). These results are relatively close to the experimental data [17]. Temperature dependencies of RT interval suggest that duration of systolic/diastolic of the heart remains fairly constant under acute temperature changes. Moreover, the QT interval also presented a linear change with the rising temperature (Figure 5.4C).

Conduction velocity is also affected by changing temperature, which increased from 4°C to 17°C by 24% and at higher temperatures, it slowed by approximately 60% at 33°C, as seen in Figure 5.4D, following the behaviour of the maximum upstroke velocity changes.

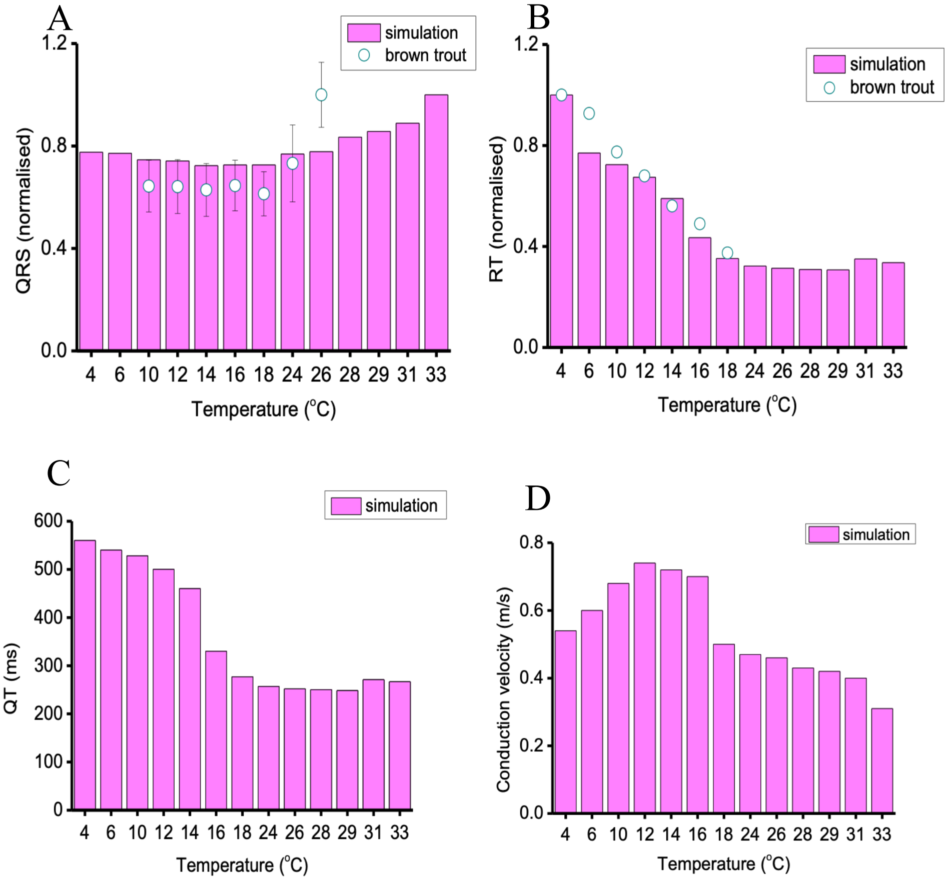

Figure 5.4: The effects of changing the acute temperature on the ECG features. A: Acute temperature changing effects on QRS duration. B: Acute temperature changing effects on RT interval. C: Acute temperature changing effects on QT interval. D: Acute temperature changing effects on conduction velocity. Note: columns represents the simulation result and open circles are the experimental records from brown trout fish [17].

5.4 Discussion

In this Chapter, firstly, a one-dimensional (1D) strand tissue model has been developed for the physiological body temperatures at 4°C (cold) and 18°C (warm). The simulated electrocardiogram (ECG) features from the 1D development models for fish ventricle including QRS, QT, RT and conduction velocity were in agreement with the available experimental data from brown trout fish [17], which validated the models.

Secondly, the developed single cell models at 4°C (CA) and 18°C (WA) (previously developed in Chapter 4) were further used to investigate the fish cardiac thermal tolerance by investigating the effects of acute temperature changes on two main ion channel currents: the depolarisation current I_{Na} and the repolarisation current I_{Kr}, at the single cell and tissue levels. These models have been modified at temperatures ranging from 4°C (cold) to the thermal limits of most teleost fish (salmonid species such as brown trout and rainbow trout fish), 31°C (warm). Here too, the developed model showed excellent agreement with experimental observations from different teleost species [17].

Acute thermal tolerance and thermal remodelling of cardiac ion channels are key factors in setting whole heart and thus whole organism thermal tolerance limits for ectothermic animals [15, 16, 91]. This is because changing temperature to lower or upper limits of thermal tolerance leads to mismatch between the required oxygen and the capacity of oxygen supply to tissues, which possibly makes oxygen delivery systems fail to provide enough oxygen to the tissues. Therefore, temperature-dependent limitation will succumb the animal to hypoxia or anoxia. Close to the animal preferred temperature, a maximum performance of the fish heart is achieved while above or below that heart performance declines [15, 91], however the oxygen demand for the whole-body continues to increase. Therefore, it is important to investigate the molecular mechanisms behind these thermal limitations in order to increase our understanding of the impact of global warming on fish life and species distribution [16, 42]. The developed models thus provide tools for quantitatively evaluating the functional role of major ion channel currents at different temperatures in fish.

5.4.1 Effects of Increasing Acute Temperature on I_{Na} and I_{Kr} Currents

The effects of increasing temperature have been investigated on two of the main ionic currents of the teleost cardiac myocytes: I_{Na} and I_{Kr} currents. These currents have been chosen as they represent the most sensitive current to changing temperatures. Simulation results (Table 5.1) showed the following:

1) At high temperatures, the I_{Na} current function is compromised. This could be one of the factors of the temperature-dependent depression of contractility of the cardiac myocytes in the trout heart [17].
2) It has been found that in addition to cardiac cells, the voltage-gated Na^+ channels exist in different cell types such as muscle and neuron cells [189]. Hence, there is a possibility of showing a thermal sensitivity of I_{Na} similar to that for cardiac myocytes, but in skeletal muscles and the nervous system (also compromise Na^+ channel functions). This suggests possible threatening effects to locomotion, behaviour and other vital functions.
3) The I_{Na} current is mainly generated by the Nav1.4a subunits in the teleost cardiac myocytes [163]. Therefore, more investigations are required to ensure whether other Na^+channel isoforms demonstrate thermal sensitivity analogous to that shown in the cardiac isoform.
4) When the inward I_{Na} current density exceeds the outward K^+ current's total density, this prompts the membrane potential to depolarise and initiate an AP. The voltage at this point is known as a threshold potential. Therefore, large decreases in depolarisation currents (I_{Na}) or increases in repolarising K^+ currents can result in AP failure [17, 119, 190].
5) Under a rising temperature regime in trout cardiac cells (particularly brown trout), the I_{Na} current declines above 21.2°C, while there is a continuous increase in the potassium currents including the I_{Kr} current with temperature. This leads to an imbalance between repolarising and depolarising currents, preventing the threshold potential being reached. This may result in an electrically unexcitable cardiac myocyte, i.e. AP failure.

5.4.2 Effects of Increasing Acute Temperature on AP

The simulated AP characteristics for teleost fish ventricular myocytes at different temperatures (Figure 5.2 A) from 4°C (cold) until the thermal limitation of 31°C (warm) showed the following:

1) An increase in the AP amplitude with the increasing temperature between 4°C and 17°C, with a good agreement with experimental data, which then levelled off between 18°C and 31°C [17] (Figure 5.3 A).

2) The upstroke velocity of ventricular AP increased between 4°C and 17°C with a peak at 16°C, and then it decreased at a temperature between 18°C and 26°C. The thermal response curve of the dV/dt_{max} of the action potential had an inverted V shape, with a peak at 16°C and the lowest values at 4°C and 33°C [42]. These results showed a close agreement to the experimental findings by [42] of brown trout and at 4°C of the rainbow trout from [104], as seen in Figure 5.3 B.
3) Temperature rises were linked with a reduction in the action potential duration. This is due to an imbalance between inward (Ca^{2+} and Na^{+}) currents and outward (K^{+}) currents, in favour of repolarising K^{+} currents. AP plateau shortening is needed for cardiac functions to give enough space for diastolic filling when cardiac cycles are abbreviated [17], as shown in (Figure 5.3 C).

5.4.3 Effects of Increasing Acute Temperature on ECG

The simulated ECG characteristics for teleost fish ventricular myocytes at different temperatures (Figure 5.2 C) from 4°C (cold) until the thermal limitation of 31°C showed the following:

1) The QRS complex duration is slightly decreased with increasing temperature from 4°C to 24°C, after which it abruptly increased (Figure 5.4 A). The QRS duration widening denotes depression in the AP propagation over the heart when the temperature increases [17].
2) The RT interval decreased linearly with increasing temperature from 4°C to 18°C; above this temperature it declined (Figure 5.4 B), suggesting that the duration of systolic/diastolic of the teleost fish heart under acute temperature changes remains constant. These results are in agreement with the experimental data [17].
3) The QT interval also changed linearly with increasing temperatures (Figure 5.4 C).
4) Conduction velocity (CV) is also affected by changing temperature, which increased from 4°C to 17°C by 24%; at higher temperatures (33°C), it decreased by approximately 60%, as seen in (Figure 5.4 D).

5.5 Limitations

In addition to the limitations with developing the single cell models which already discussed in Chapter 4 (Section 4.5), the tissue modelling are also has some limitations.

The lack of experimental data about the tissue structure of the teleost ventricular, whether heterogeneous or homogeneous, causes us to assume the 1D models as isotropic, homogeneous strands. This leads to a negative T-wave in the ECG profile, which needs more experimental investigations. Furthermore, the effects of changing the acute temperature have been studied on only two ion channels (I_{Na} and I_{Kr}). Although these currents have a higher sensitivity to changing temperatures, it is better to conduct more investigations on other currents under acute temperature changes, such as I_{K1} current, which sets the resting membrane potential. This will help for more understanding to stability of the cardiac cell when the temperature changes.

5.6 Summary

The present study suggested that in trout fish hearts, the cardiac Na^+ channel's heat sensitivity may set the upper thermal tolerance of the heart function. This is due to the fact that the I_{Na} currents of the trout cardiac cells are thermally the weakest link in electrical excitation. Simulations showed that above 21.2°C, the function of impaired Na^+ channels depress the I_{Na} current density, and hence, the AP upstroke velocity and conduction that spread over the heart result in cardiac rhythmicity disturbance and heart rate depression. Furthermore, additional increases in temperature may cause a total loss of the electrical excitability. This results from the continuous decrease in the sodium current, and at the same time, the outward potassium currents still increase, making the threshold voltage unable to regenerate the opening of the sodium channels with a consequence of cardiac standstill [17].

The ECG of the teleost heart identified with a high sensitivity to temperature-dependent deterioration in comparison to the ion channel in a single isolated cell [17]. Therefore, the ECG features such as QRS, RT, QT, as well as the conduction velocity, are extensively affected by changes in the animal habitat temperatures. Rising temperatures above the cardiac thermal tolerance widen the ORS interval and decrease the RT and QT intervals linearly, in addition to significantly reducing the conduction velocity with more than 50% of its value at cold, causing a slower AP propagation which might result in cardiac failure. All the simulation results are validated using the available experimental records.

From the above, it is clear that although fish as ectothermic animals can adapt to changes in their ambient temperature, they still have an upper limit thermal tolerance; thus, when the temperature exceeded this, it can cause cardiac arrhythmia or sudden animal death. This can be a curious topic for future research in the molecular mechanism to investigate the specific factors (such as ion channel domains or the different amino acid sequences) involved in the heat sensitivity of ectothermic species. Such information will be increasingly valuable to predict the possible changes in the fish populations under changing climates or global warming.

6. Developing a Three-Dimensional Model of the Teleost Fish Ventricle

Addendum Part of this Chapter has been presented in the form of a conference proceeding [157]: Naser H, Whittaker D, Shiels H and Boyett M and Zhang H. A Novel Model of Electrical Action Potentials of Teleost Fish Ventricular Myocytes. Computing in Cardiology Conference (CinC), Maastricht, Netherland: IEEE; 2018. DOI: 10.22489/CinC.2018.032.

The previous two chapters focused mainly on the development of novel electrophysiological models of the teleost fish heart at the single cell and 1D tissue strand levels. These models were used to investigate how changes in temperature affect the function of the fish heart.

Although single cell and 1D tissue simulations can give some important insights into the functional behaviours and the mechanisms of the heart, 3D-dimensional simulations are quite often required to reveal full mechanisms for cardiac arrhythmogenesis. This is because single cell and 1D tissue simulations are limited in revealing the spread of electrical activation through cardiac tissue due to neglecting the cell-to-cell arrangements and detailed anatomical structures that play an important role for cardiac conduction. Moreover, anatomical properties of the heart and anisotropy also play a significant role in generating cardiac disorder; hence, it is essential to develop an accurate and anatomically detailed model of the heart.

In this regard, in the present Chapter, a biophysically detailed three-dimensional (3D) model of the teleost ventricle with accurate anatomical geometry was developed, into which the single cell model developed in Chapter 4 was integrated. This allowed simulating the conduction pattern in the ventricle of the teleost fish, from which a detailed activation map was reconstructed and compared to experimental data (e.g. activation time).

6.1 Introduction

Numerous studies showed that the structure of the heart forms one of the key factors that determine the heart function [74, 85, 191–194]. Mammalian hearts, such as human hearts, are characterised by complex structures with two atria and two ventricles, while vertebrate hearts, such as fish hearts, possess a simple heart structure with a single atrium and a single ventricle along with another two chambers: sinus venosus and bulbus arteriosus (see Chapter 2). As ectothermic animals, the function of the fish heart is affected widely by changing their ambient temperatures as described in previous chapters. Changes in temperature may lead to heart arrhythmias for the fish animal.

To date, there is no fully detailed three-dimensional model of the whole teleost fish heart and no comprehensive model of the fish heart. Most teleost fish ventricles such as salmonid fish (where brown trout belongs) have a pyramidal-shaped ventricle with a high trabeculated structure (as shown in Chapter 2). This type of ventricle is widely correlated with an active lifestyle, a high output of work and a robust ventricular wall that most salmonid fish have. The highly trabeculated structure of the ventricle makes the experimental understandings of fish cardiac problems more difficult. Hence, 3D computational models based on experimental findings can provide an alternative method in simulating the fish cardiac function at various conditions. Therefore, it is important to build a model for the investigation of fish cardiac phenomena.

In the present Chapter, firstly a 3D anatomical model of the teleost fish heart, particularly a brown trout fish heart, has been reconstructed using a micro CT scan to obtain an accurate anatomical geometry for each heart chamber.

Micro CT allows non-invasive visualisation of the internal structure of the sample. It produces 2D cross-sectional and 3D volumetric images. Moreover, enhancing the contrast enables visualisation of soft cardiovascular tissue (see Chapter 2). The resulting images can then be reconstructed and segmented for the construction of computational cardiac models; this will be shown in the next sections of this Chapter.

The 3D anatomical model work has been done by a collaboration between our group (mainly by Dr Dominic Whittaker used to be one of the Biological Physics group), CTF and HMXIF (Henry Moseley, X-ray imaging facility) from the University of Manchester.

With the 3D reconstruction of anatomical geometry of the brown trout ventricle, single cell models developed in previous chapters at the physiological temperature of 18°C (Chapter 4) are implemented. The 3D model developed in this thesis can be further used to study the electrical excitation and the time mapping at different temperatures, particularly in the investigations of the potential effects of global warming on the fish heart as an organ.

6.2 Methods

6.2.1 3D Anatomical Modelling of the Teleost Fish Heart

In order to simulate the electrical activity of the teleost heart, it is necessary to have a representation of the geometry of the heart that contains detailed tissue structures.

6.2.1.1 Tissue Preparation

Four brown trout hearts were dissected and stained utilising the same method previously used by Aslanidi et al. for mammal hearts, described in [60, 195]. The hearts were cleaned in saline and inundation fixed in around 10% neutral buffered formaldehyde (NBF, Sigma–Aldrich). They were then kept inundated in NBF until the imaging process. In some consecutive experiments, staining was optimised with the same tissue sample and by changing iodine-potassium iodide solution concentrations (3.75%–7.5% I_2KI) and also changing sample incubation duration in the solution (3–5 days), as seen in Figure (6.1A), and the tissue sample was stained, and micro-CT imaged for each time. After which the tissue was placed for one week (at least) in order to leach out the contrast agent. The leached tissue sample was retained and rescanned, and the micro-CT image's optimal contrast was obtained after seven days of incubation with 7.5% I_2KI. After staining, the NBF was used to wash the tissue and then the excess solution was drained. After that, the sample was set onto the rotatory stage of the micro-CT scanner in a plastic container, as shown in Figure (6.1B).

6.2.1.2 Micro-CT Scanning with Iodine Staining

High-resolution contrast-enhanced sample scans were obtained with a Nikon 320 kV bay system at the HMXIF, Manchester University. The sample was rotated during the analysis through 360° (Figure (6.1 B)) and the prognoses were filmed on a 2 K × 2 K Perkin Elmer 1621-16-bit detector, an amorphous silicon flat-panel with a 200-pixel pitch. In order to optimise resolution, the X-ray beam energy was adjusted by a Mo-target, Cu-filter (with 0.5 mm thickness) combination. The scanning time was 60 min with 150 kV voltage, 125 μA current and 16 gain. Consequently, 1000 prognoses per sample were assembled by the use of a frame rate of 1000 ms and a voxel resolution of 11.7 μm.

Although micro-CT has many benefits in tissue imaging, it still has some limitations, thus is frequently disregarded in the imaging of soft tissue. These limitations include the high energies of the X-ray beam, which are dangerous to living organisms and hence, makes in vivo studies practically impossible. Moreover, there is a possibility of poor inter tissue contrast, which results from tissues with analogous X-ray absorption. However, some studies recently have demonstrated that in various soft tissues, X-ray absorption can be significantly enhanced by the use of contrast agents such as iodine. Therefore, in order to image details of smooth muscle tissues, such as cardiac tissues [60], the micro-CT scan was applied with iodine contrast enhancement in the last few years.

Within muscle cells, the iodine diffuses within tissue layers and binds to fat [60, 196]. The resulting accretion of iodine in the muscular fibres relatively increases the absorption of the X-ray in the fibres in comparison to connective tissues. This can be explained by the iodine tissue staining as well as contrast enhancement mechanisms. Therefore, the micro-CT combined iodine staining technique can be useful for the cardiovascular tissues to obtain both high-resolution contrast imaging that can include details of fibre architecture.

6.2.1.3 Tissue Segmentation

In order to post-process the micro-CT raw data, Nikon Metrolasis CT-Pro software (Metris XT 1.6) was used for the reconstruction, and for visualisation, the standard edition of Avizo 6.3.1 was used. The fish heart segmentation of the inter-tissue contrast that was enhanced by iodine and subsequent volume rendering was used in the reconstruction of 3D structures of the fish heart.

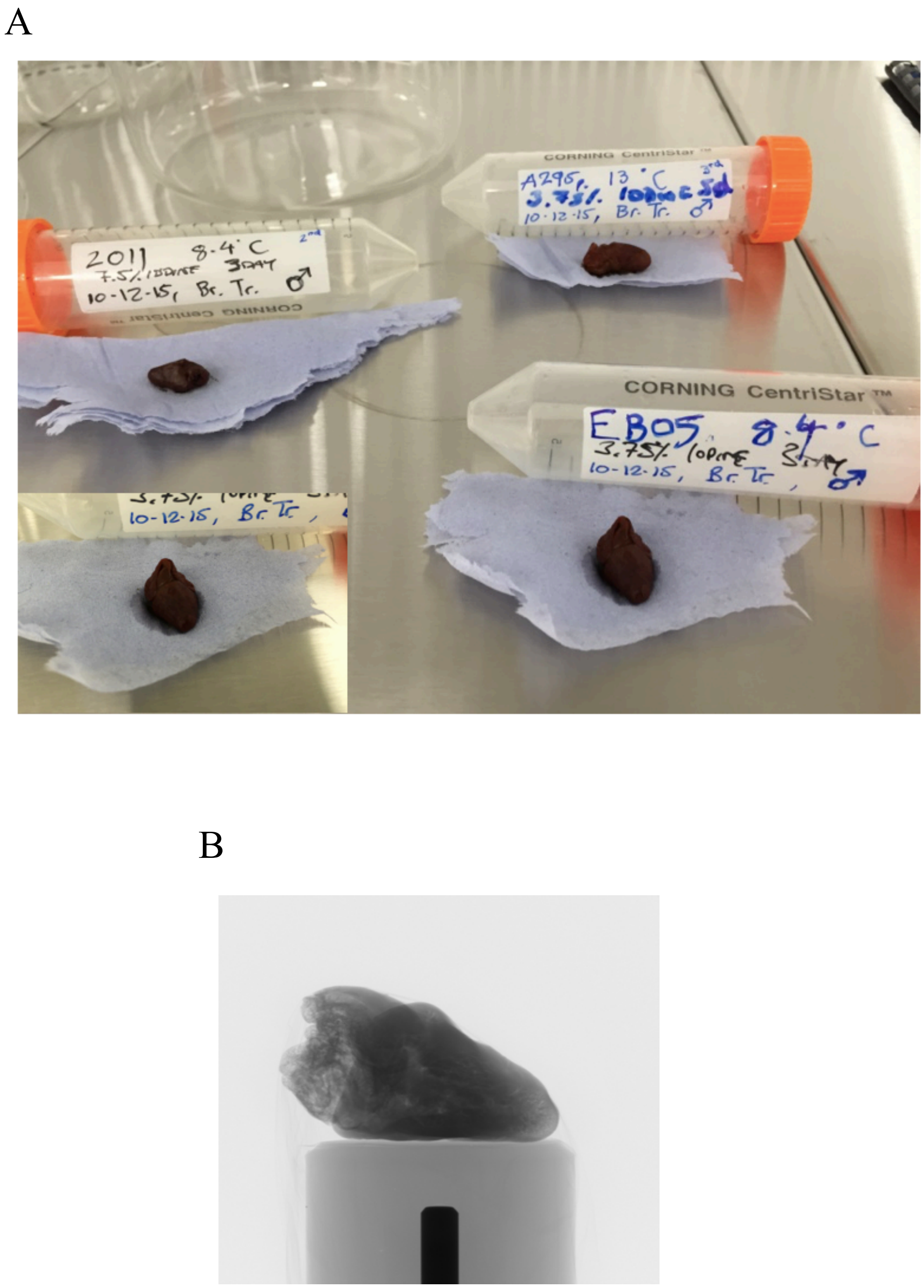

Figure 6.1: Four trout hearts under investigation in the Lab. A: The trout hearts were stained with iodine-based contrast agent (I_2KI) at 3.75-7.5% for 3-5 days, B: High resolution contrast-enhanced scans obtained with Nikon 320kV bay at HMXIF.

6.2.2 Developing a Novel Three-Dimensional Model of Teleost Fish Ventricle

6.2.2.1 Single-Cell Model of Teleost Fish Heart Ventricle Cells at 18°C

As discussed in Chapter 4, a single cell model for a cardiac cell of the ventricular teleost heart at the physiological temperature of 18°C has been developed [157]. The model consists of a family of HH formulations for the main membrane ion channel currents including I_{Na}, I_{CaL}, I_{Kr} and I_{K1} responsible for generating the electrical APs of teleost fish ventricular myocytes, as shown in Figure (6.1).

The simulated kinetics of the major ionic current included current-voltage (I-V) relationships, steady-state activation, inactivation and time constant, which were fitted to the experimental findings obtained from different teleost species; this was previously discussed in Section 4.2.4 and published in [157]. The full details of the model parameters are shown in Chapter 4 (Table 4.5 and Table 4.6).

6.2.2.2 3D Model of Teleost Fish Heart Ventricle

Recently, anatomically detailed 3D geometric computational models have been developed for different mammalian heart regions for different species, but not for the fish heart. Therefore, in this chapter, we developed a computational 3D ventricle model at the physiological temperature of 18°C by incorporating our previously developed single cell model (Section 6.2.2.1) (and published in [157]) into an anatomically detailed 3D geometry of a fish ventricle.

In the 3D model, the electrical activity in the single ventricle was simulated using an anatomically accurate teleost ventricular geometry (particularly, brown trout fish) that was reconstructed from a micro-CT scanned ventricle, as detailed in Section 6.2.1. The spatial resolution was 0.18 mm along all axes, with approximately 1.4 million nodes in total. Fibre orientations were not incorporated into our developed model; therefore, for simulations, we assumed the media was homogeneous and isotropic. The FDM method (Section 3.7.2) is used to solve the monodomain equation (Equation 3.20).

As in several previous models [58, 63, 137, 197], Neumann boundary conditions are applied on the geometry boundary. For the integration method, the space step used corresponding to the spatial resolution of the anatomical model was 0.18 mm in all directions, with a 0.01ms time step. Simulations were implemented under these baseline conditions. The diffusion coefficient that makes up the diffusion tensor, D, was set to 0.005 mm^2/ms throughout the tissue. The D value was chosen to produce an activation time map and conduction velocity of the ventricle match that was measured experimentally by Shiels et al. [unpublished data].

Following previous studies of ventricular modelling from different animal species [58, 62, 198, 199], in the present study, the ventricle was paced at the activation sites (empirically determined) across the endo-surface of ventricular walls (in the absence of the anisotropic fibre orientation). In order to improve the computational efficiency, lookup tables are integrated for different gating variables that are voltage dependent. This helps to give an error with less than 0.1% in the action potentials taken from de-coupled tissue.

In the 3D model, a standard procedure was used to choose the initial conditions: the corresponding single ventricular cells model at 18°C were paced five times at 1000 ms as a baseline cycle length. All the state variable values at the end of such simulations of the single cell model were utilised as initial conditions for the corresponding simulations of the 3D tissue model at 18°C.

6.3 Results

6.3.1 3D Tissue Reconstruction of the Teleost Fish Heart

6.3.1.1 Initial Dataset

In the current study, micro-CT images for the whole heart of the brown trout fish have been made available, and a complete dataset for the heart was obtained and the geometry extracted. Approximately ~1000 of 2D-images obtained from the micro-CT (Figure 6.2 A, B) have been stacked in each plane, and the contrast-enhanced images reconstructed to make a 3D dataset (voxel size: 11.7 µm). The full geometry of the whole teleost fish heart geometries reconstructed from micro-CT images is shown in Figure (6.3).

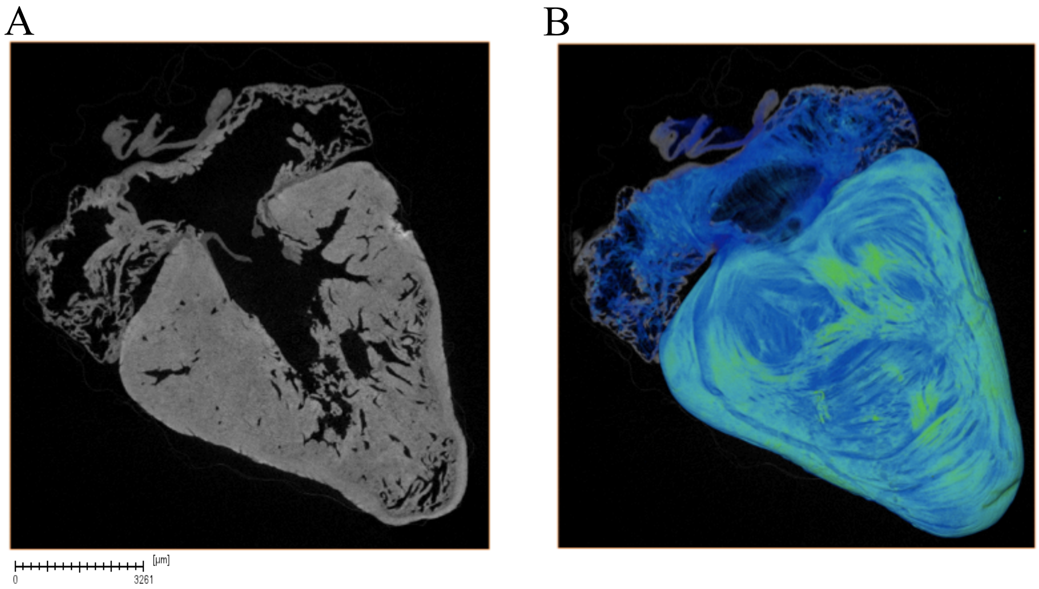

Figure 6.2: Nonsegmented 3D geometry of the brown trout heart. A: 3D volume representation of the dissected heart (a “hot metal” palette is used to color-coded the X-ray intensity), it shows an orthogonal 2D plane (x-y) of the heart. Note the anatomical constructions details are not clear. B: Respective micro-CT images, showing clearly inter-tissue contrast between constructions, enabling 3D geometries segmentation. The brightness of the micro-CT images in A and B are correlated to the X-ray intensity, where brighter colors related to lower intensity/higher X-rays absorption. This is because of the higher iodine accumulation levels in the corresponding tissues.

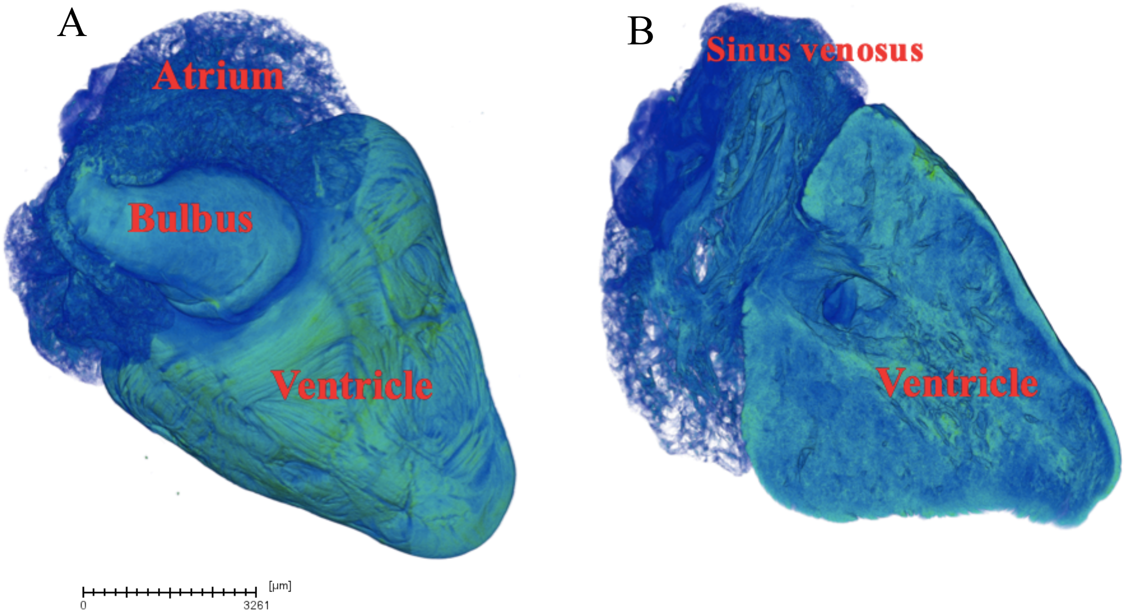

Figure 6.3: 3D geometry of the teleost fish heart reconstructed from micro-CT scan. A and B: Epicardial view and Endocardial view, respectively. The X-ray intensity isosurfaces in micro-CT images are presented, with isovalues chosen such that the heart endocardial and epicardial surfaces can be seen. The trabeculaeted structures of the heart tissue can be determined from the high-resolution images with the voxel size of 11.7 µm. Three heart chambers can be seen in A including: atrium, bulbus and ventricle, while two chambers are in B including: sinus venosus and ventricle.

6.3.1.2 Segmentation of the Fish Heart

As discussed previously, the teleost fish was formally identified with four chambers, including the atrium as the first chamber adjacent to the sinus venosus, which was identified as the second chamber and separated from the atrium by the bulbus, which represented the third chamber. The fourth chamber was the ventricle, which included a sufficient network-like construction of myocardial fibres. The segmented 3D teleost heart geometry in Figure (6.4) agreed qualitatively with anatomical studies of the teleost fish heart [74, 75].

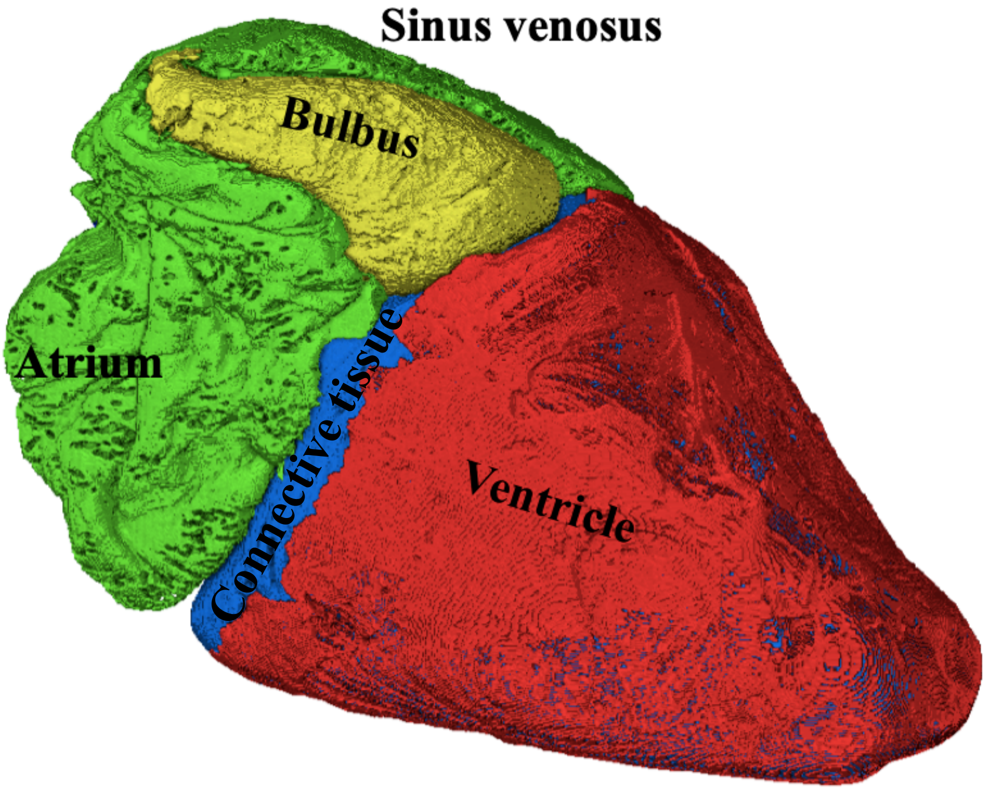

Figure 6.4: The 3D geometry segmented of the teleost fish heart. Identification of the heart four chambers including; the atrium, ventricle, sinus venosus and bulbus. These chambers can be seen clearly and they are based on inter tissue contrast in the micro-CT images. In this image, the brighter color correlated to the X-ray intensity, indicating lower intensity/higher X-rays absorption. This results from the higher accumulation of the iodine levels in the corresponding tissues.

Accordingly, the micro-CT contrast enabled the 3D geometry reconstruction of a trout heart, and the segmentation of its four chambers (tissue types) are shown in posterior and anterior views in Figure 6.5.

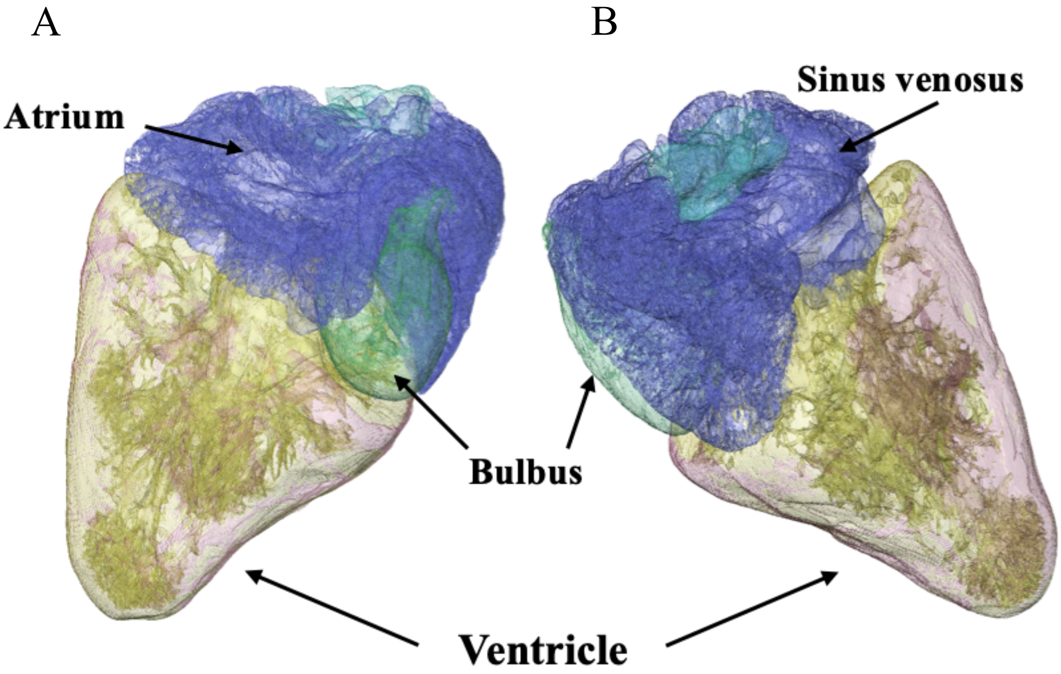

Figure 6.5: 3D geometry reconstruction from micro-CT of the teleost heart. A: Posterior view. B: Anterior view. Tissue structures in the fish heart can be seen in (A) and (B).

Micro-CT reconstructs three-dimensional geometries at micrometre resolution by using differential X-ray absorption by biological tissues. Recently, experimental studies in vivo have indicated that in micro-CT images, the iodine staining technique can enhance the contrast between cardiac myofibres and connective tissue [68]. Hence, it provides high resolution and high contrast images, allowing studies for non-destructive in-depth tissue. Moreover, this technique, coupled with a good knowledge of cardiac anatomy provides fast tracing of SA and AV nodes as well as their 3D geometry reconstruction [60].

The current study used this technique and applied it in order to reconstruct a teleost fish heart and mainly the ventricle, with an effective resolution of 0.18 mm (approximately). Figure 6.6 illustrates the 3D geometry of the teleost heart, with the segmented regions of the atrium with the sinus venosus and ventricle for the simulation studies.

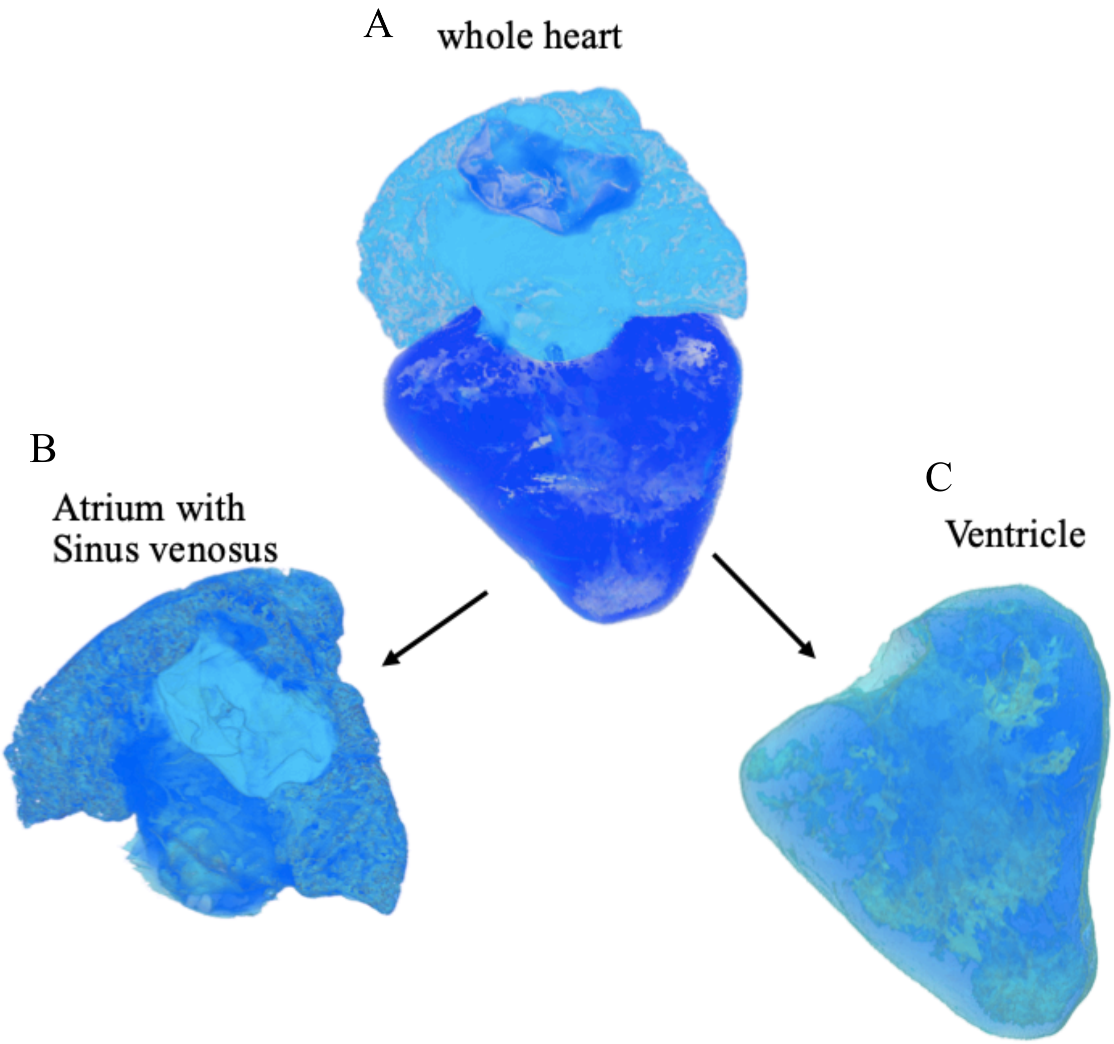

Figure 6.6: Segmentation of 3-D geometry of the fish heart (Anterior view) in (A). Identification of the atrium with sinus venosus in (B) and ventricle in (C), based on inter-tissue contrast in micro-CT images by the finite difference method (FDM) grids for cardiac simulation.

As mentioned, high resolution and high contrast images can be provided by the micro-CT with iodine staining allowing for non-destructive in-depth tissue studies [60]. This method with the knowledge of cardiac anatomy is suited for the fast tracing of the sinus venosus and atrioventricular node as well as the atrium and reconstruction of their 3D geometry.

The ventricle (which is the main object of this thesis) represents the biggest chamber of the teleost heart and varies widely between different fish species [74] depending on several features including the external shape of the ventricle, the relative mass, the coronary distribution and the histology [200] (see Chapter 2). However, these categories reflect functional rather than phylogenetic correlates. Moreover, the ventricles very often do not entirely fit into any particular category. This is true, particularly when data between various categories are crossed [74, 200]. Earlier studies showed that the different external ventricular shapes had been grouped into three major categories: tubular, sac-like, and pyramidal [85].

Teleost fish such as brown trout has the pyramidal ventricle shape (as shown in Figure 6.4 and 6.6C) which is an inverted pyramid with a base of triangular which is approximately equilateral proportions. The pyramidal ventricle is orientated so that the ventricle caudal aspect is formed by one side of the triangular pyramidal base and therefore the rostral ventricle aspect is angular (Figure 6.6 C). The pyramidal ventricle lies ventral to both bulbus arteriosus and atrium (Figure 6.4) [74, 200]. Pyramidal ventricles have several functional implications, such as, an active life style, a high output of work and a robust ventricular wall. This type of ventricle is present in the salmonid, scombrid families and the very active tuna. However, in many species, such as in several of the sparid and serranid families and in the Antarctic teleosts, the existence of a pyramidal ventricle does not associate with either a very active lifestyle or a robust ventricle [85] (see Chapter 2).

6.3.1.3 Effective Ventricle Tissue Resolution

In the current study, the architectures of the 3D ventricle tissue were reconstructed from the contrast micro-CT data at 11.7μm as a voxel resolution. However, this value of the voxel resolution is not the exact tissue resolution that can be integrated into the computational models as the numerical integration space step. In fact, there is no straightforward process that can measure the exact tissue resolution from micro-CT imaging data, which might be due to some factors that might affect the reconstructed resolution. These factors include 1) the size of the focal on the target sample, however, in general, the size varies between different experiments depending on the voltage value that has been used, 2) the distances of the sample to source and detector, and 3) the signal to noise ratio (more details can be found in [68]). As a result, a clear signal can be achieved by empirically selecting the correct voltage and current for the sample under study [68].

6.3.2 Action Potentials Propagation in the Teleost Fish Ventricular Cells

The AP model of the teleost fish ventricular cell at 18°C [157] has been discussed in detail earlier in Section 4.3.1. However, in this section, the AP morphology at 18°C was plotted, and the AP features were compared to the available experimental findings more clearly, as shown in Figure 6.7 and Figure 6.8.

The model was based at a 1-Hz stimulation rate (BCL=1000 ms), and the simulated AP was obtained and calculated after at least 30 s of continuous simulation to ensure that a steady-state solution has been reached. Figure 6.7 shows the AP for teleost fish ventricular myocytes at 18°C [157].

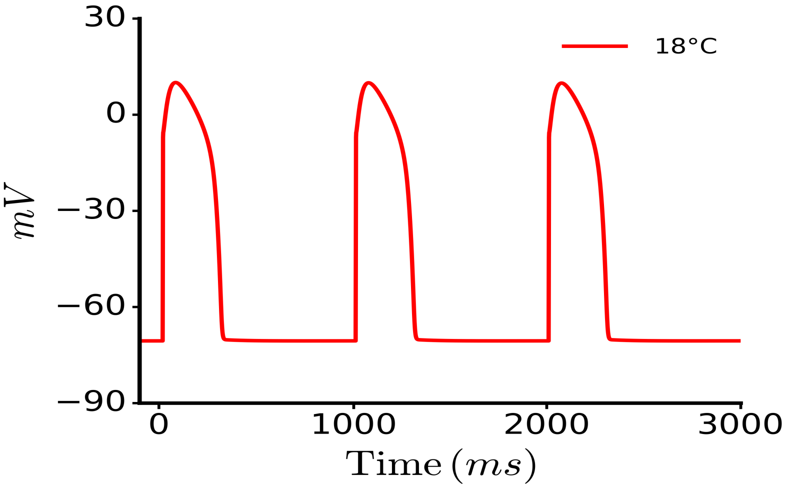

Figure 6.7. Simulated steady state AP at 1Hz (BCL=1000ms) of the teleost ventricular cells at 18°C (for 3000ms) [157].

6.3.2.1 Model Validation

Figure 6.8 shows the simulation AP characteristics of the teleost ventricular cell model at the physiological temperature of 18°C validated to the experimental records. In simulations, OS and APA were 9.5 and 84 mV, respectively, which are in agreement with experimental data [42]. The computed resting membrane potential (RMP) was -72 mV, which is the same as that of experimental recordings [42]. The simulated APD at 50% of AP repolarisation (APD_{50}) of the ventricular cell had a value of 265 ms, and the simulated APD at 90% of AP repolarisation (APD_{90}) was 308.8 ms, all of which match well with experimental findings of different teleost species including rainbow, perch, pike, burbot, roach, crucian carp from Haverinen and Vornanen [42]. Moreover, the maximum upstroke velocity (dV/dt_{max}) calculated from the model was 50 V/s, but no experimental data has been published to date for comparisons.

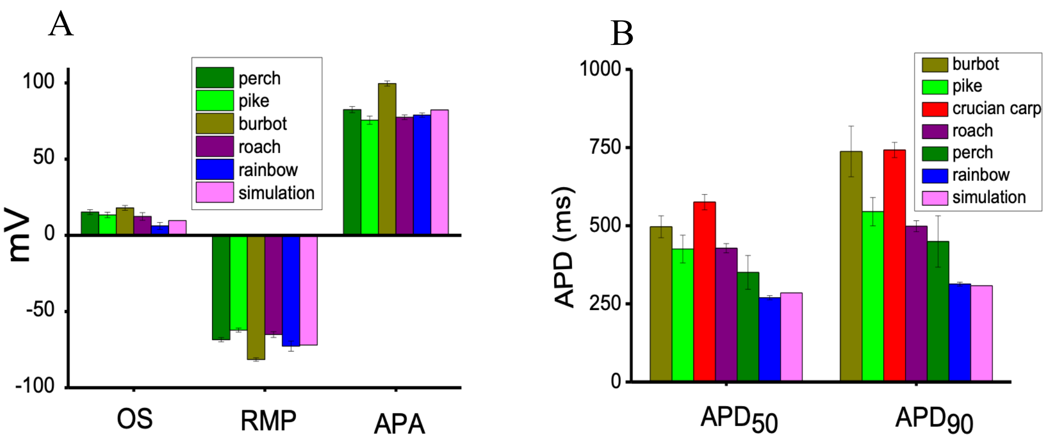

Figure 6.8. Characteristics of simulated APs compared with experimental data for teleost ventricular myocytes model. A: is shown the overshoot (OS), resting potential (RMP) and AP amplitude (APA), while APD_{50} and APD_{90} values are shown in (B). The source of simulations is from [157] and the experimental data is from Haverinen and Vornanen [42].

6.3.3 Action Potentials Propagation in the 3D Ventricle

Action potential propagation was simulated in the reconstructed teleost fish ventricle using the finite difference method (see Section 3.7.2) with 0.18 mm as a space step and a time step of 0.01ms. The simulation results were performed using the 3D anatomical geometry of the teleost ventricular (see Section 6.2.1). Activation was initiated at the top of the ventricle base then spread towards the apex at the heart bottom. The action potential propagation in the ventricle at 3 ms intervals is shown in Figure 6.9.

Figure 6.9 shows snapshots of the progression of the simulated excitation in the teleost fish ventricle from different views, where A is the anterior view, B is the posterior view, and C is a cross-section view. In the simulations, the first site activated was the upper part of the anterior ventricle close to the endocardium wall. At t = 3 ms, a site in the endocardium wall in the top of the ventricular base began to activate. At t = 6 ms, this activation site expanded to larger areas in the endo-surface, and the intramural conduction was much slower. At t = 9 ms, in the ventricle, the activation site spread towards the base and the sharp edges of the pyramidal shape of the ventricular. At t = 12 ms, the activation expanded towards the apex while the flat face of the ventricle breakthrough was about to happen. At t = 16 ms, the activation joints from the edges expanded towards the septum of the flat face and the apex. At t = 18 ms, the majority of the ventricle was activated except for the apex myocardium part. At t = 20 ms, ventricle myocardium activation was almost completed, while the wavefront just reached the posterior wall of the apex. The total excitation of the ventricle was accomplished at t = 22 ms with a conduction velocity of 0.5 m/s (calculated at 18°C in Chapter 5).

The tissue activation time is shown in Figure 6.10. It shows the time at which each cell reached 0 mV after a specific stimulus. Again, this figure shows the special conduction of the APs along with the isotropic structure of the ventricle in the absence of the fibre orientations.

Shiels et al. empirically measured the activation time in the brown trout fish (unpublished data), as shown in Figure (6.10). Shiels et al. found the ventricle activation time to be approximately 18.5 ms, while in the developed 3D model (current study), the ventricle activation time is 22 ms. This activation time is within standard deviations of the experimental results.

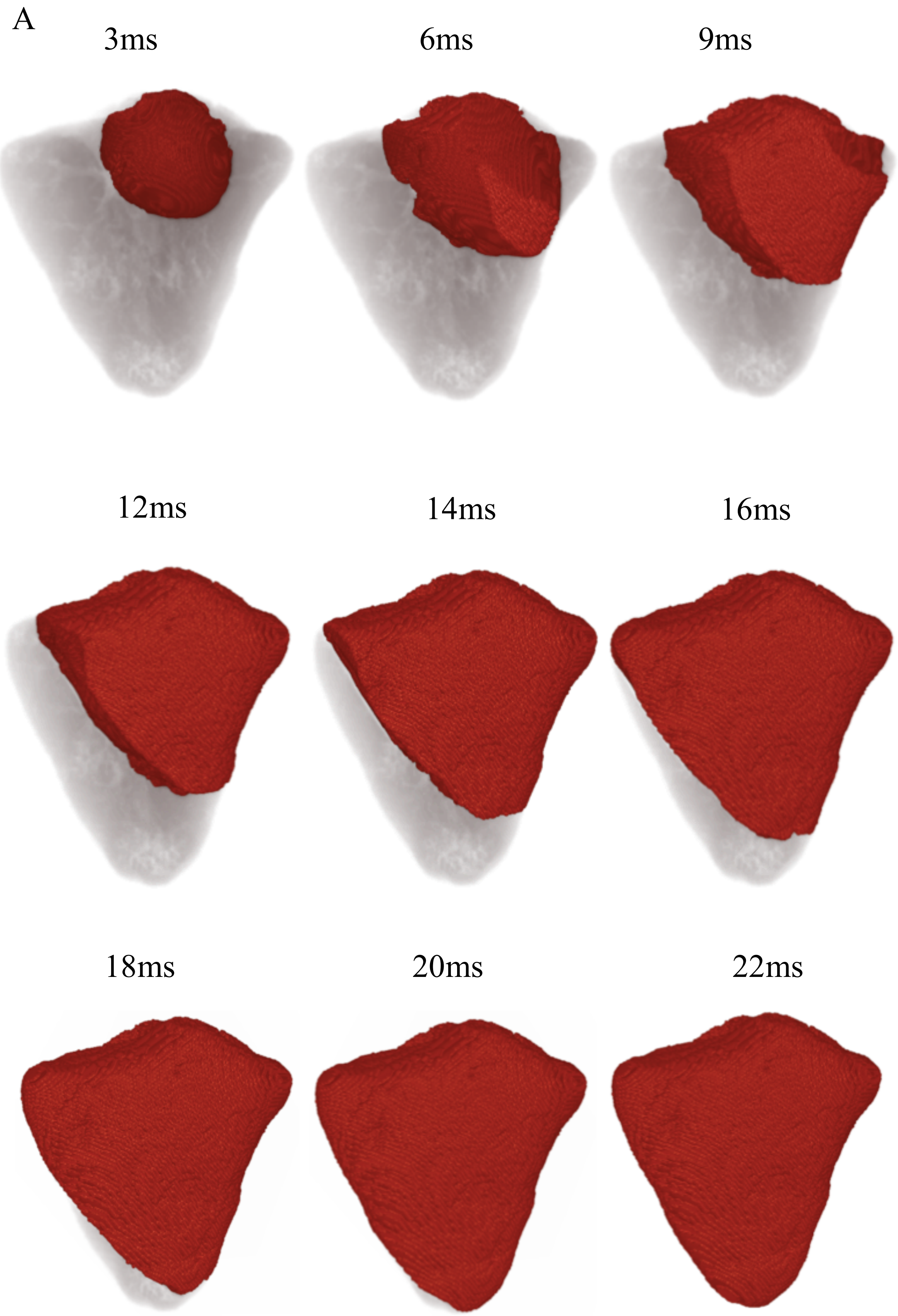
A
3ms
6ms
9ms
12ms
14ms
16ms
18ms
20ms
22ms

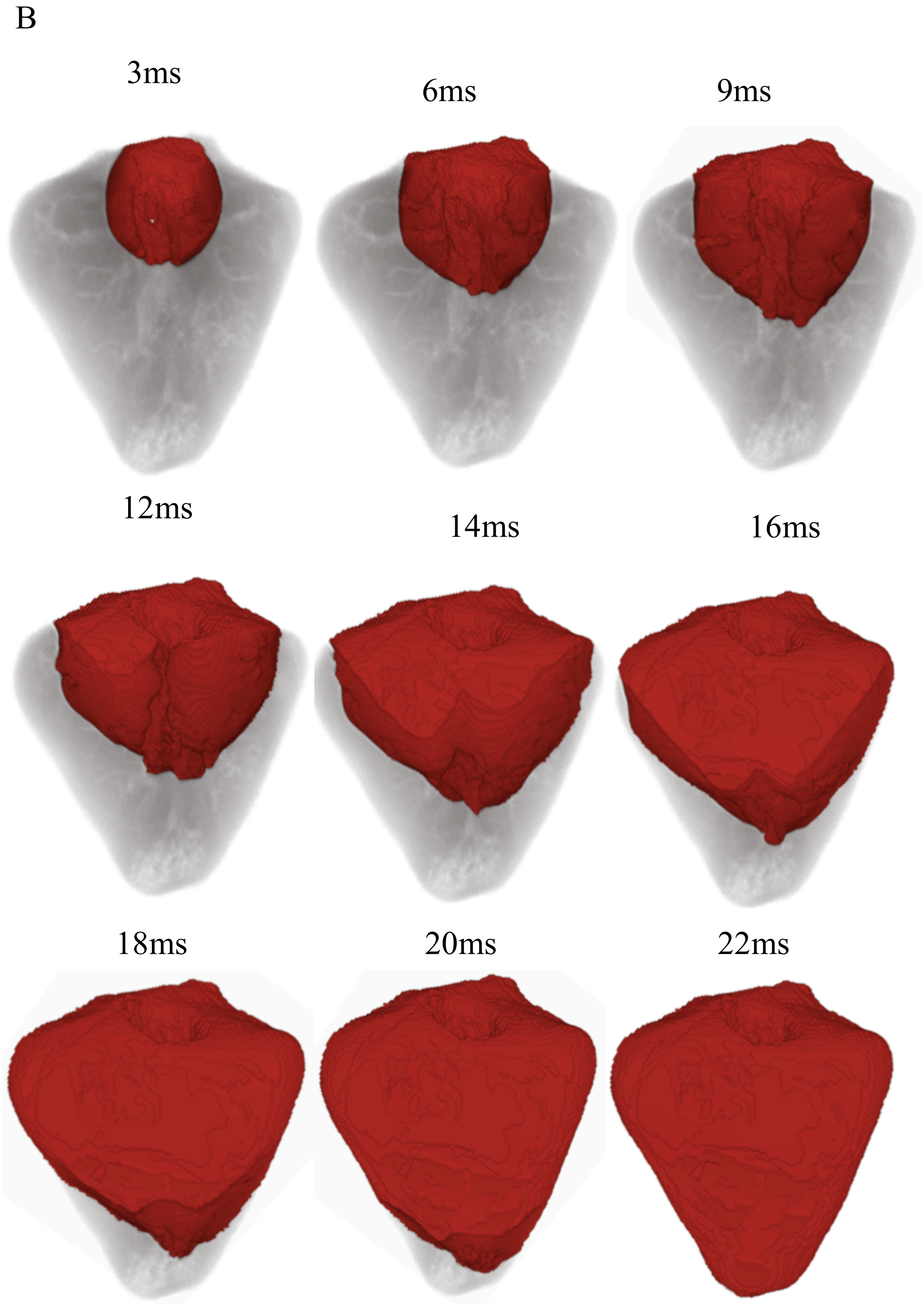
B
3ms
6ms
9ms
12ms
14ms
16ms
18ms
20ms
22ms

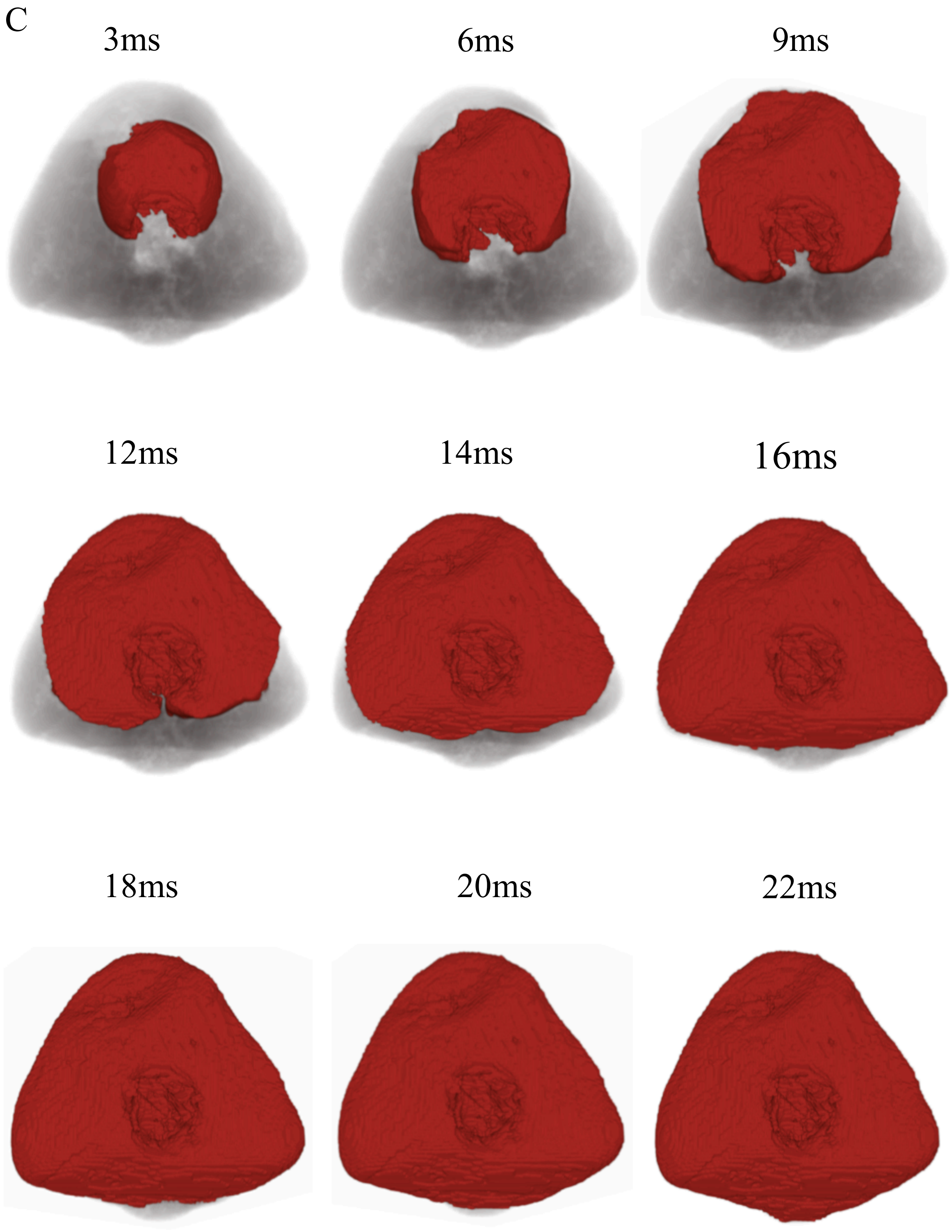

Figure 6.9: Snapshots of simulated progressive excitation in the teleost fish ventricle at 18°C. The snapshots showing ventricular excitation in anterior view (A), posterior view (B) and cross- section view (C), with red representing depolarized tissue.

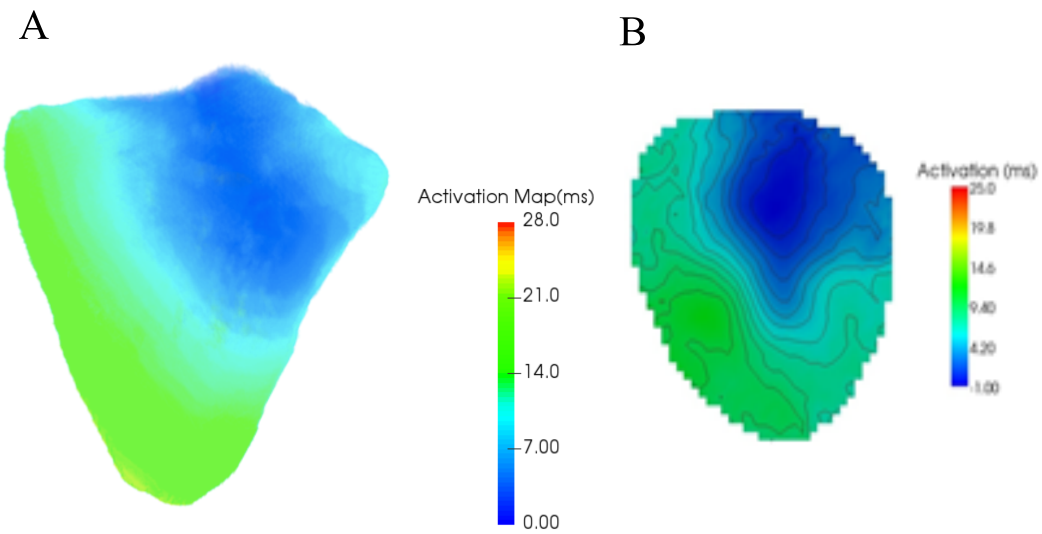

Figure 6.10: Activation time of the teleost fish ventricle as isotropic media. Times run from blue to red, as shown in the colourbar. (A) Simulated activation time in the ventricle as compared to (B) experimental observations by Shiels et al. from unpublished work

6.4 Discussion

In this chapter, a novel 3D biophysically detailed and anatomically accurate model of the teleost fish ventricle has been developed at the physiological temperature of 18°C. The 3D computational model was based on a family of single cell models previously developed in Chapter 4 and incorporated a 3D geometry of the teleost ventricle region that has been segmented from the reconstruction of the whole heart of the teleost fish using the micro-CT scan with an iodine staining technique. The developed model reproduced the electrical excitation propagation of the teleost ventricle with good agreement with the available experimental observations.

6.4.1 3D Anatomical Model of Teleost Ventricle

In order to obtain a good understanding of the spatiotemporal electrical dynamics of the teleost fish heart, a 3D anatomical model has been reconstructed (Figure 6.1) using X-ray micro-CT scan with an iodine staining technique. It has been found that staining iodine enhanced micro-CT images [60]. The high resolution and high contrast micro-CT images of the teleost heart were obtained without fibre orientation. The micro-CT images are used to 1) reconstruct 3D geometry of the teleost heart (Figure 6.3), and 2) segment the teleost heart into its main myocardial tissue chambers, including the atrium, sinus venosus, bulbus and ventricle (Figure 6.4).

The segmented 3D geometries are vital for constructing biophysically detailed computational models of the heart to obtain good knowledge in the investigations of the underlying mechanisms of cardiac arrhythmias. In this thesis, the 3D geometry of the teleost ventricle was reconstructed from micro-CT images, and its detailed 3D architecture has been implemented in a novel 3D biophysically detailed computational cardiac model of the fish heart for investigating the conduction system of different parts of the heart during temperature changes.

6.4.2 Single Cell Model of Teleost Fish Ventricular Myocytes at 18°C

A single cell electrophysiological model of teleost fish ventricular cells was developed earlier in this thesis (see Chapter 4 and Section 6.2.2.1) at the physiological temperature of 18°C and validated with the available experimental findings (Section 6.3.2).

6.4.3 3D Computational Model of Teleost Fish Ventricle at 18°C

The novel 3D ventricular model was constructed upon an anatomical geometry of the teleost ventricle as isotropic media (in the absence of the fibre orientation). Simulations showed that the activation pattern started at the upper top of the ventricle base and then spread towards the ventricle sites before reaching the bottom of the heart at the apex; this conduction pattern is shown in Figure

6.9. In the 3D teleost ventricle model, the simulation activation sequence of the tissue was 22 ms, which was within standard deviations of the experimental observations by Shiels et al. who measured the activation time in the ventricle of the brown trout fish (approximately 18.5 ms) (unpublished data), as seen in Figure 6.10.

6.5 Limitations

In addition to the limitation associated with developing a single cell model (see Section 4.6), there are some limitations associated with the present study. One of the most important limitations is the consideration of the teleost ventricle tissue as a homogenous and isotropic media. Therefore, more experimental examinations are required to provide clear information on whether the teleost ventricle wall has a homogenous or heterogeneous structure. The absence of fibre orientations might affect the accuracy of reconstruction of structural features reconstructed using micro-CT as well as the activation sequence pattern of the ventricle.

So far, there is no published study for the micro-CT reconstruction of the teleost fish heart; the only qualitative comparison we can make is the activation time sequence with data from one unpublished study. Therefore, more experimental investigations need to be done to obtain a clear understanding of the teleost heart structure.

As the limitations in the developed single cell model have been detailed earlier in this thesis (see Chapter 4), they are not reiterated here.

In the 3D model developed, simulations showed a fast propagation of the electrical excitation (from its initiations at the top of the ventricle base to the ventricle apex) in the sharp edges of the ventricle (see Figure 6.9A) while a noticeable delay can be seen in the flat side of the ventricle (see Figure 6.9B). This might be due to the trabecular and spongy structure of the inner ventricle, which can be more complicated on this side of the heart. Therefore, further experimental investigations on the teleost ventricle are necessitated to improve the model here.

6.6 Summary

In the present chapter, a micro-CT scan with sustaining iodine technique [60] has been used to reconstruct a novel 3D anatomical model of the teleost fish heart. The contrast micro-CT images of the teleost heart were then segmented into 3D geometries of the four chambers of the teleost heart (atrium, ventricle, bulbus and sinus venosus). In this thesis, we dealt with the 3D ventricle geometry only; other chambers might be our future work. A 3D biophysically computational model of the teleost ventricle at the physiological temperature of 18°C has been developed for dissecting and clarifying the electrical dynamics procedure in the teleost fish ventricle. The 3D model was developed based on our previously developed single cell model into the anatomically detailed 3D geometry of a fish ventricle. This affords a computational platform suitable for the detailed study of ventricle arrhythmias that can result from changing temperatures due to global warming.

7. Hypertension Effects on the Contractile Function of the Human Left Ventricle Using a Multi-Dimensional Electromechanics Model

Addendum Part of this Chapter has been presented in the form of a conference proceeding [240]:

> Naser H, Zhang Y, Zhang H. Modelling the Effects of Hypertension on Ventricle Cells of Human Heart. Computing in Cardiology (CinC). Singapore: IEEE; 2019. (Conference proceedings).

Cardiac arrhythmias denote to the condition which exhibits as a non-physiologically justified the heart rhythm. The irregular electrical activity of the heart can cause inefficient pumping of blood and may damage other organs and threat organisms' life [2, 7]. The abnormal heart rhythm leads to irregular contraction and hence a reduction in the cardiac output that may result in sudden death [7].

Arrhythmias can occur in different organisms such as mammals and vertebrates and it can be developed under different conditions. For example, in mammals such as human, cardiac arrhythmia can be resulted from several cardiac diseases such as hypertension (HP) with left ventricular (LV) hypertrophy that risks morbidity and sudden death [206], while in vertebrate such as fish it can be developed by the temperature changes condition in their environment as a result of the worldwide problem of global warming [30]. Although there are various types of arrhythmias can be established in different parts of the heart including atria and ventricle, the ventricle arrhythmia carries the greatest risk of sudden death which is the main cause of mortality and appears to be reasonably common in the general population with important health implications in some arrhythmia types [1].

In this sense, an investigation to the mechanisms underlining the ventricular arrhythmia (which is the objective of this thesis) in mammals including human and in vertebrate including fish and under different arrhythmia conditions by the use of electrophysiological computational models, will help to understanding the genetics of ion channel disturbances responsible for inherited cardiac arrhythmias under different conditions. This will improve the pharmacological drugs in the cardiac arrhythmia treatments and saving hundreds of thousands of lives and also highlight the effects of the remarkable changing climate on the aquatic animals including fish species.

Therefore, the current Chapter will discuss the cardiac arrhythmia in human heart that can be developed under hypertension (HP) condition and the associated LV hypertrophy. In the last three Chapters, we discussed the pervasive effects of environmental temperature on the rate of life processes in the fish heart as ectothermic animals. We showed how animal performance is affected by changing the ambient temperature with the finite thermal limits for vital body functions, including the electrical excitation that initiates and controls the rate and rhythm of the fish heart. Changes in temperature chronically or acutely; 1) alter the frequency of the heartbeat and the duration of ventricular APs, 2) induce compensatory changes in ion channel expression and function when prolonged exposure to new thermal conditions represent the direct effects of temperature on cardiac APs and heart rate.

Fish that live in variable thermal habitats are termed eurythermal. For these animals' water temperature, and thus heart temperature, may change by more than 30°C seasonally (i.e. chronic changes) or when diving vertically across thermoclines in the oceans (i.e. acute changes) [40, 152]. Indeed, acute cooling hypertrophies the fish heart, slows heart rate, and can depress cardiac contractility [33]. These effects are similar to those induced by hypertension (HP) disease on mammal's hearts. These changes in whole heart electrical and contractile function under temperature change condition for fish and under HP for mammals are determined by the remodelling in ionic conductance through the ion channels and ionic pumps in membrane of the cardiomyocytes that make up the fish and mammals heart.

Thus understanding such effects on individual ion channels, and their culmination in the cellular action potential and tissue excitation, provides insight into how such changes influence the myocyte, tissue and possibly the well-being of fish in a changing thermal environment and human in the current lifestyle.

Therefore, as HP is becoming a major public health problem in the developed world population [201], in the current Chapter, the O'Hara-Rudy (ORd) electromechanics model [55] has been modified to investigate the hypertension impact on the left human ventricle at cellular, 1D strand tissue and 2D sheet.

7.1 Introduction

Systemic hypertension (HP) represents one of the major risk factors for developing cardiac hypertrophy and heart failure (HF). The hypertensive heart disease impact remodelling by its high prevalence and complications [201]. For instance, in the US, around 30% of adults have hypertension. Moreover, 60% of these people develop cardiac hypertrophy causing a significant disease burden [201].

Previous studies [120, 202–205] have shown that cardiac hypertrophy is correlated with changed excitation-contraction (E-C) coupling and enhanced myocardial contraction, while HF is correlated with diminished contractility. These findings suggest that a direct relationship exists between the onset of hypertension and the Ca^{2+} signaling upregulation that possibly lead to hypertrophy and heart failure with protracted exposure to hypertension systemic blood [120]. However, the causative cellular and molecular mechanisms that link hypertension to HF are still unclear. Left ventricular hypertrophy that results from hypertension produces remodelling of several ion channels and also prolongs ventricles depolarisation [206]. It has been found that in rat left ventricular cells [206], hypertrophy induces changes in sodium channel current, I_{Na}, the outward transient potassium channel current, I_{to}, the sodium-calcium exchanger current, I_{NaCa}, cell size, and myofilament responses to Ca^{2+} in the cardiac cell. These changes have been incorporated in the E-C model for human the ventricular cell to simulate hypertrophy.

In the current chapter, electromechanical models of the O'Hara-Rudy (ORd) human ventricle model at cellular and tissue levels previously developed by Adeniran et al. [137] was used to investigate the hypertension effects on cardiac mechanical dynamics including contracting mechanisms and force-generating of the human ventricular myocytes. The ORd electromechanical model has been modified depending on experimental rat data in Sham (control) and hypertension conditions from Jin et al. [202]. As the myocytes mechanical contraction is triggered by the electric excitation, the electromechanical coupling (E-C) has an essential role in the trigger mechanism. The molecular mechanisms underlying the cardiomyocytes contraction are presented in this chapter.

7.2 Myofilament Model

In order to simulate the cellular mechanical properties of the cardiac myocytes, the Rice et al. [207] myocyte contraction model (RMM) was used. This model is based on the cross-bridge cycling contraction model of the cardiac muscle as explained previously in Chapter 2. RMM model has the ability to reproduce a wide range of experimental data [207] including different relationships such as the force and sarcomere length (F-SL), sarcomere length-calcium (SL-Ca) and force-calcium (F–Ca) relationships under various physiological conditions.

Biophysical processes of cell contraction such as the dynamical time course of the action potential and active force development of ventricular cardiac cells have been described by a set of ordinary differential equations.

7.3 Single Cell Electromechanical Model

The electrophysiology (EP) model linked to the myofilament mechanics (MM) model through the intracellular calcium concentration ($[Ca^{2+}]_i$) and the related calcium- handling dynamics. The $[Ca^{2+}]_i$ which produced from the EP model as dynamic output during the AP time course is used as an input to trigger the mechanics model from which the Ca^{2+} amount bound to troponin is evaluated [62, 137].

The myoplasmic Ca^{2+} concentration expression in the O'Hara & Rudy electrophysiological model is:

$$\frac{d[Ca^{2+}]_i}{dt} = \beta_{Cai} \cdot \left(-\left(I_{pCa} + I_{Cab} - 2 \cdot I_{NaCa,i}\right) \cdot \frac{A_{cap}}{2 \cdot F \cdot v_{myo}} - J_{up} \cdot \frac{v_{nsr}}{v_{myo}} + J_{diff,Ca} \cdot \frac{v_{ss}}{v_{myo}}\right) \tag{7.1}$$

Where β_{Cai} is the $[Ca^{2+}]_i$ buffer factor, Acap is capacitive area, v_{nsr} is the network SR compartment volume, v_{myo} is the myoplasmic compartment volume, v_{ss} is the subspace compartment volume, J_{up} is the entire flux of the Ca^{2+} uptake, through SERCA pump from myoplasm to the SR network, and $J_{diff,Ca}$ is the Ca^{2+}diffusion flux from the subspace to the myoplasm.

In order to couple the MM model [207] to the O'Hara & Rudy EP model [55], the change in the Ca^{2+} concentration that binds to troponin from the MM model is added to Equation 7.1 for the Ca^{2+}calculation as shown below:

$$\frac{d[Ca^{2+}]_i}{dt} = \beta_{Cai} \cdot \left(-\left(I_{pCa} + I_{Cab} - 2 \cdot I_{NaCa,i} + \frac{I_{sac}}{3}\right) \cdot \frac{A_{cap}}{2 .F.v_{myo}} - J_{up} \cdot \frac{v_{nsr}}{v_{myo}} + J_{diff,Ca} \cdot \frac{v_{ss}}{v_{myo}} - \frac{J_{Trop}}{1000}\right) \tag{7.2}$$

Here, J_{Trop} is the Ca^{2+} concentration flux bound to troponin. The stretch activated channels is produced in the model to investigate the stretch impacts on the mechanical systole under Sham and HP conditions.

By the including of all the state variables describing the MM model in the ORd electrophysiological model, and with Equation (7.2), the effectively coupled between the two models is achieved. This resulted in an electromechanical model of a human ventricular cell, basing on a differential-algebraic equations (DAE) system [62, 207].

7.3.1 Stretch-Activated Channel

In the cardiac tissue, some of ionic channels have been identified as they can be activated by cell stretch [208]. Therefore, they known as stretch-activated channels (SACs) which represents the effect of mechano-electric feedback (MEF). These channels can significantly affect some of the electrophysiological properties of the cardiac cells [208], including shortening [209] or prolongation [210] of the AP, and also alterations in the AP morphology such as premature excitation, diastolic depolarisation [211], and after-depolarisation [212]. Moreover, stretch can increase the intracellular calcium concentration, this change is linked to the contractile force in the heart. The stretch-activated channels response to mechanical stimuli by increasing the open possibility rather than conductance [213].

In accord with previous studies of Panfilov et al. [214], Lunze et al. [215] and Youm et al. [216], a stretch-activated current (I_{sac}) was integrated into the electromechanical model by the use of the following formulation:

$$I_{sac} = G_{sac} \cdot P_m \cdot (V_m - E_{sac}) \tag{7.3}$$

where V_m represents the membrane potential, G_{sac} is the maximum conductance of SACs, E_{sac} is the reversal potential of SACs and P_m is the open channel probability which is modelled as:

$$P_m = \frac{1.0}{1+e^{-\left(\frac{\varepsilon-\varepsilon_{1/2}}{k_\varepsilon}\right)}} \tag{7.4}$$

where ε is the strain (linearly dependent on the sarcomere length), $\varepsilon_{1/2}$ is the half-activation strain, and k_ε is the activation slope with a value of 0.02 based on previous studies [214] . In the electromechanical model, the reversal potential, E_{sac} was typically 1 [217, 218]. Furthermore, the channel in the electromechanical model was set to permeable equally to the three major ions, Na^+, $K^+$and Ca^{2+}.

7.4 Tissue Mechanics Model

The mechanics of cardiac tissue was modelled within the framework of nonlinear finite element method. In this method, each boundary value problem is consisted of three fundamental relations which comprise equations of motion, kinematics relations and constitutive relations [137]. The equations of motion, also known as the equilibrium relations which represent the balance notions described the essential rules of physics that govern a continuum motion. The kinematics relations define the body displacement and the strain field relationship and they govern the deformation and motion of the under examination body. A specific material behaviour and response to an applied load can be described by the constitutive relations [62]. The ventricular tissue is modelled as nearly incompressible material, anisotropic and inhomogeneous which is similar to other previous studies [62, 219, 220]. In the current study, an active strain approach was adopted as it requires no tunings of the active forces produced by single cell models in order to drive the deformations observed in the cardiac tissue.

In order to formulate the entire potential energy function for the mechanic's problem, a two-field variational principle was used. These fields include the deformation vector (u) and the hydrostatic pressure (p) [219], as follow:

$$\prod(u, p) = \prod_{int}(u, p) + \prod_{ext}(u) \tag{7.5}$$

where $\prod(u, p)$ represents the entire strain energy of the body, while the external potential energy is represented by $\prod_{ext}(u)$ which is the potential energy arising from the external loading of the body.

The deformation gradient tensor (F) maps elements configurations from the undeformed to the deformed. It is decomposed into two components; a microscopic (active) (F_o) and a macroscopic (passive) (F_e) [219]:

$$F = F_e F_o \tag{7.6}$$

Changing in tissue length owing to muscle contraction can be measured via the active component, while the tissue passive mechanical response as well as probable tension owing to external loads can be accounted via the passive component.

The active component (F_o) links to the microscopic active strain through:

$$F_o = I + \eta f \otimes f \tag{7.7}$$

where I represents the identity tensor, f denotes the unique direction of the fibres (fibre orientations) and η is the active strain field which depends on the sarcomere length of the cells and therefore it is given by:

$$\eta = (\mathrm{SL} - \mathrm{SL_O})/\mathrm{SL_O} \tag{7.8}$$

where $\mathrm{SL_O}$ refers to sarcomere length at resting state. Hence, $\eta > 0$ indicates elongation, while $\eta < 0$ indicates contraction.

Thus, the macroscopic (passive) component ($\mathrm{F_e}$) is obtained from:

$$\mathrm{F_e} = \mathrm{F}\mathrm{F_O^{-1}} \tag{7.9}$$

and the related Right Cauchy-Green strain tensor (C) that measures the squared length of infinitesimal fibres in the deformed structure, is given by:

$$\mathrm{C_e} = \mathrm{F_e^T}\mathrm{F_e} \tag{7.10}$$

while the associated Green-Lagrange strain tensor (E) which measures the length changes in a material fibre and angles between fibres pairs in a deformed solid, is obtained from:

$$\mathrm{E_e} = \frac{1}{2}(\mathrm{C_e} - 1) \tag{7.11}$$

7.5 Mechanical Feedback in the Tissue Model

Similar to previous studies [221, 222], the monodomain equations of cardiac tissue were employed for the electrophysiological model (as explained in Chapter 3) with some modifications of incorporating the Right Cauchy Green deformation tensor (C). The reason of integrating a feedback in the diffusion term is to allow the monodomain equation to consider the effect of the deforming tissue [223, 224]:

$$\mathrm{C_m}\frac{\mathrm{dV}}{\mathrm{dt}} = -(\mathrm{I_{ion}} + \mathrm{I_{stim}}) + \nabla \cdot (\mathrm{D}\mathrm{C}^{-1}\nabla \mathrm{V}) \tag{7.12}$$

where V is the transmembrane potential, C_m is the cell capacitance, I_{ion} and I_{stim} are the total ionic currents and the applied stimulus current. D is the diffusion tensor, governing the intercellular electrical coupling. As seen from Equation (7.12) the only different from the monodomain Equation (3.20) is the incorporating of the C^{-1} term which represents the inverse of the Right Cauchy-Green deformation tensor. In fact, this term suggests that the electrical wave propagates across the gap junctions and through the tissue is varied between the deformed and undeformed tissue [62, 219].

7.6 Single Cell Electromechanical Simulations

The O'Hara-Rudy (ORd) model for human ventricular cells [55] was coupled with the myofilament model [207] (as described in the previous sections) in order to obtain an electromechanical model that can describe the human heart contraction.

The ORd human ventricle electromechanics model was modified by integrating available experimental data from rat ventricular cells under Sham (the normal cell) and hypertension (HP) conditions [202]. Hypertrophy induced by the HP condition was modelled following the work of Kharche et al. [206] by integrating experimental findings of changes in several ion channels, including sodium channel current, I_{Na}, the outward transient potassium channel current, I_{to}, the sodium-calcium exchanger current, I_{NaCa}, and cell size; these changes are based on [206] changes in the myofilament responses to Ca^{2+} in the cardiac cell (based on experimental data from Jin et al. [202]).

Firstly, changes in the myofilament responses to Ca^{2+}(calcium sensitivity of L-type Ca^{2+}), EC_{50} [202] have been incorporated in Sham and HP models (Figure 7.1A). Secondly, the hypertrophy model includes changes in the down-regulated I_{to} (a decrease in conductance by 35]%), up-regulated I_{Na} (increase in conductance by 8%), up-regulated sodium-calcium exchanger current (increasing the I_{NaCa} scaling factor by 5%), cell size and cell capacitance (elevated by 30%); all these data are from [206]. These changes have been implemented in the HP model, as shown in Table 7.1.

Table 7.1: Modification to the model parameters in simulating the hypertrophy and hypertension conditions. Exp. is the experimental parameters of rat ventricular myocytes from literatures, while Sim. is the electromechanichal model parameters of human heart ventricular cells and Ref. refers to the data reference.

Substrate	**Exp.**	**Sim.**	**Ref.**
EC_{50}	Shifted to right by 34%	Shifted to right by 34%	[202]
I_{Na}	↑ 8%	↑ 8%	[225]
I_{to}	↓ 35%	↓ 35%	[204]
I_{NaCa}	↑ 5%	↑ 5%	[203]
Cell capacitance (C)	↑ 30%	↑ 30%	[205]

Both Sham and HP models were integrated using the forward Euler method with a time step of 0.05 ms in order to achieve stable solutions. By using a sequence of supra-threshold stimuli (amplitude of -80 pA/pF and time interval of 1000 ms), the electromechanical models of Sham and HP generate a successful series of action potentials (APs) and replicate transmural heterogeneity of the action potential [137, 213] throughout the ventricular wall. These models are compatible with studying re-entrant arrhythmias in human ventricular tissue at the 2D level (next sections). The Hodgkin-Huxley-type formulations for the gating variables of different ion-channels in the ORd model were incorporated using Rush and Larsen's method [146].

7.6.1 Single Cell Simulations Without Incorporation of I_{sac}

At the cellular level, we investigated the effects of hypertension on the relationship between the active force and the calcium transient $[Ca^{2+}]_i$ (Figure 7.1 A), the AP of human ventricular myocytes (Figure 7.1 B),), Ca^{2+}intracellular concentration (Figure 7.1 C), the sarcomere length (Figure 7.1 D), and the active force (Figure 7.1 E). Such effects that developed in the electromechanical ventricular single cell model were investigated with (and without) the consideration of the I_{sac} current at a stimulation frequency of 1Hz (BCL=1000 ms). The simulated results have been validated with the available experimental findings from Jin et al. [202], as shown in Figure 7.2.

Simulations show that HP produces the following: 1) relaxation phase of the normalised active force–$[\mathrm{Ca}^{2+}]_\mathrm{i}$ relationship of left ventricular (LV) cells shifted to the right by 34% for 50% of active force (EC_{50}) (Figure 7.1A), indicating a reduction in the myofilament Ca^{2+} sensitivity [226, 227, 227]; 2) prolongation of the APD_{90} by approximately 4.5% (from 207ms in Sham and increased to 216.4 ms in HP) (Figure 7.1 B); 3) an increase of the intracellular calcium concentration ($[\mathrm{Ca}^{2+}]_\mathrm{i}$) by 36% and a faster relaxation and time constant of $[\mathrm{Ca}^{2+}]_\mathrm{i}$ decay (tau) (Figure 7.1 C); 4) no obvious change in the sarcomere length, as the initial sarcomere length was 2.2 µm, and the minimum contracted sarcomere length was 2.14 µm; however, the time course of the SL decreased by 13.7% in HP than in Sham (Figure 7.1 D); 5) the contractile force (normalised active force where the force has been normalised to its maximum value) has not changed with a value of 100% while the time course of the normalised active force decreased by 12.8% in HP than in Sham (Figure 7.1E). Indeed, the unchanged amplitude of SL and the contractile force suggest that there is no change in the contraction of the cardiac myocytes under HP condition [202]. Figure 7.1F and G are the experimental findings of the SL and $[\mathrm{Ca}^{2+}]_\mathrm{i}$ for rat ventricular myocytes in Sham and HP from Jin et al. [202]. A summary of these results from the simulation with the experimental records [202] is shown in Figure 7.2A,B,C, and D while Figure 7.2E represents validated simulation results from HP model with the available experimental data.

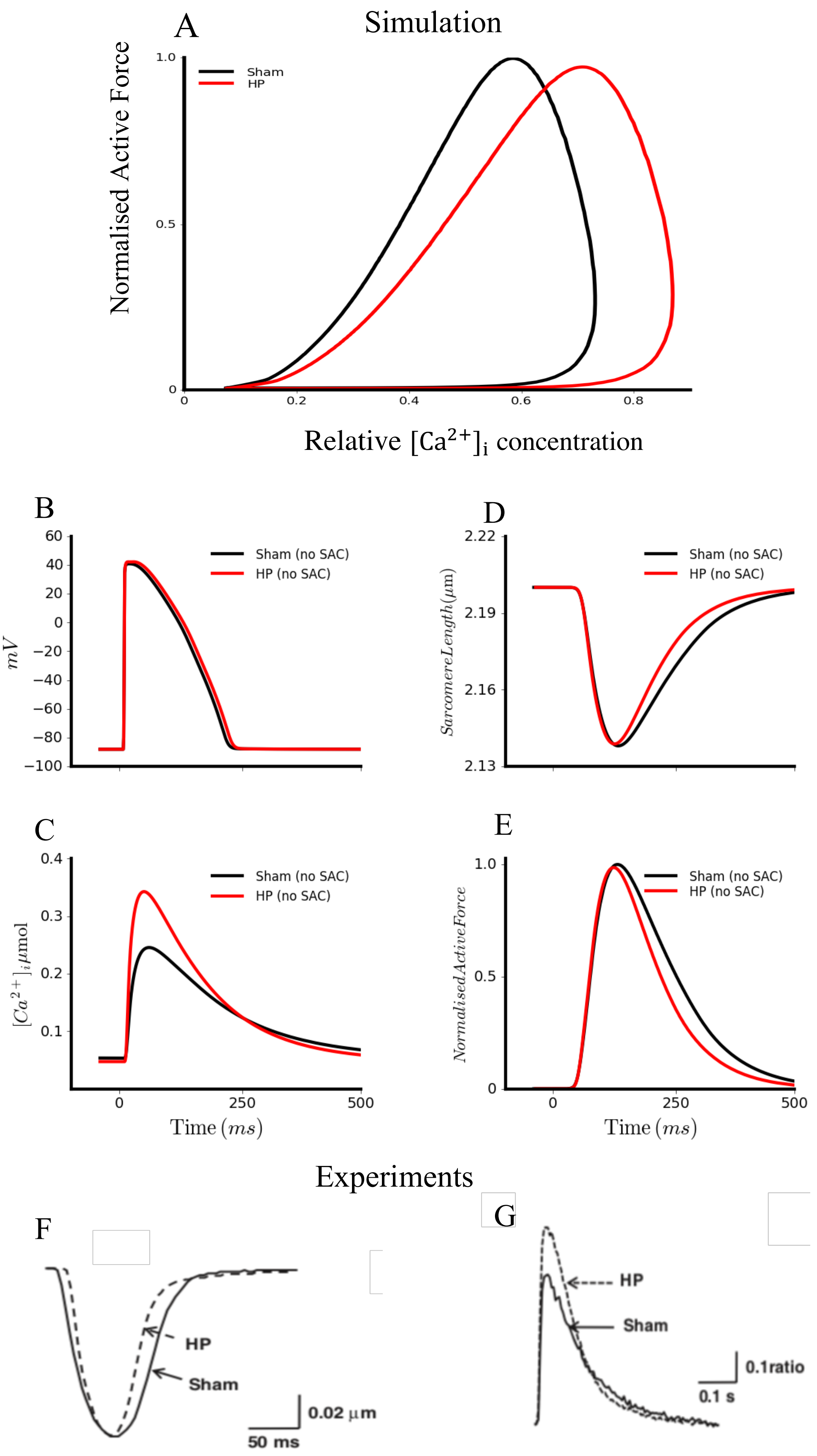

Simulation
A
Normalised Active Force
Sham
HP
1.0
0.5
0
0
0.2
0.4
0.6
0.8
Relative $[\mathrm{Ca}^{2+}]_i$ concentration
B
mV
60
40
20
0
−20
−40
−60
−80
−100
Sham (no SAC)
HP (no SAC)
D
$Sarcomere Length (\mu m)$
2.22
2.19
2.16
2.13
Sham (no SAC)
HP (no SAC)
C
$[Ca^{2+}]_i \mu mol$
0.4
0.3
0.2
0.1
Sham (no SAC)
HP (no SAC)
0
250
500
Time (ms)
E
$Normalised Active Force$
1.0
0.5
0
Sham (no SAC)
HP (no SAC)
0
250
500
Time (ms)
Experiments
F
HP
Sham
0.02 µm
50 ms
G
HP
Sham
0.1ratio
0.1 s

Figure 7.1: Single cell electromechanical effects of the HP without I_{sac}. Simulated (A) normalised active force and ($[\mathrm{Ca}^{2+}]_{\mathrm{i}}$) relationship, (B) AP, (C) calcium transient ($[\mathrm{Ca}^{2+}]_{\mathrm{i}}$), (D) sarcomere length (SL) and (E) active force, (B, C, D and E published in [240]). (F and G) the experimental time course of SL and $[\mathrm{Ca}^{2+}]_{\mathrm{i}}$, respectively, which elicited by an action potential in rat ventricular myocytes from [202]. In all figures, black line represents Sham while red represents hypertension (HP).

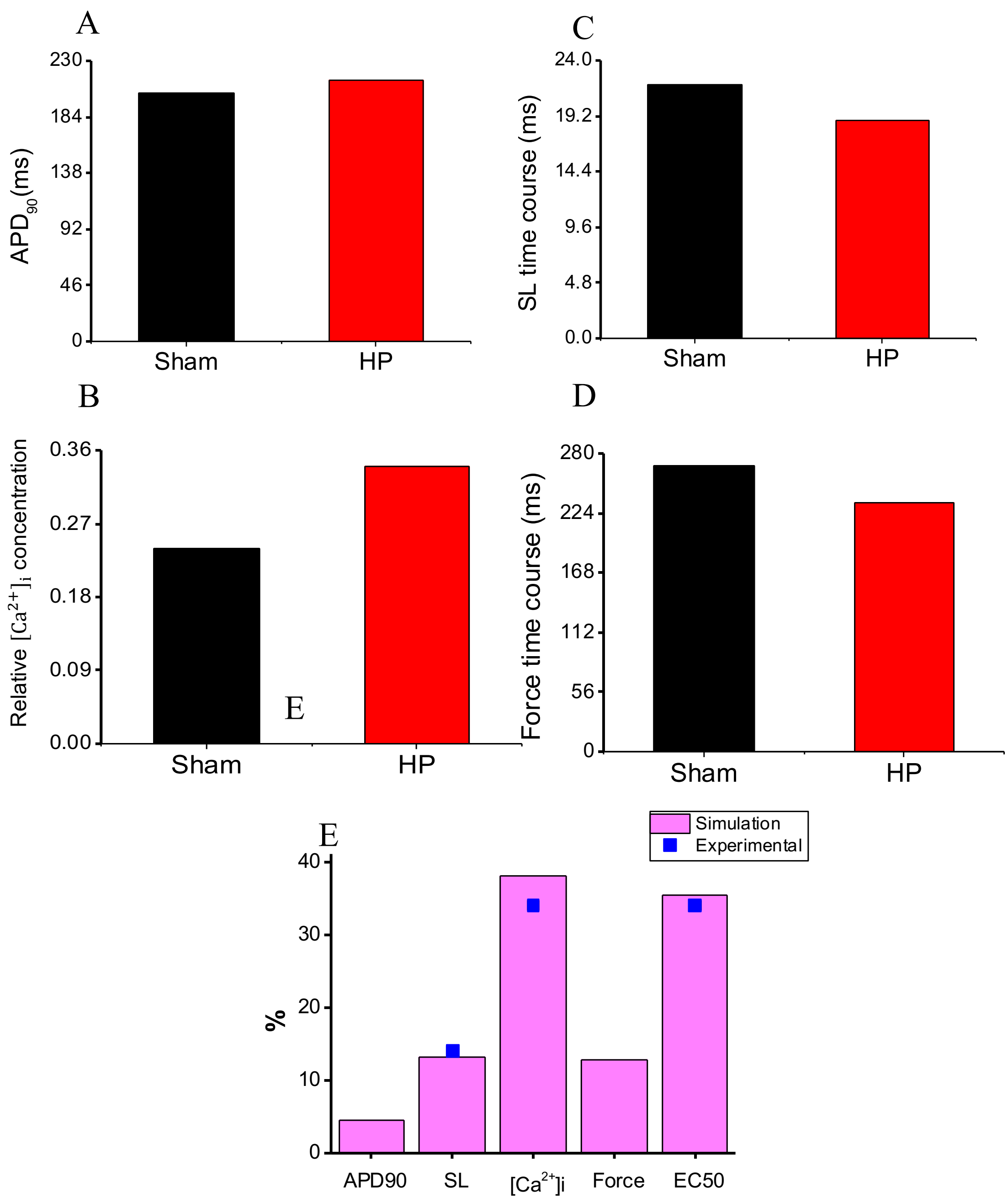

Figure 7.2: Bar plots showing the effects of HP on human left ventricular myocytes (without SAC). Simulated (A) APD_{90} under Sham and HP conditions, (B) relative changes of calcium transient ($[Ca^{2+}]_i$), (C) sarcomere length (SL), (D) active force and (E) the percentages of simulations [240] and experimental from [202]. In the simulations, SACs were not incorporated. In all figures, black columns refer to Sham, red columns refer to hypertension (HP), pink columns refer to simulations and the blue squares are the experimental data [202].

7.6.2 Single Cell Simulations with Incorporation of I_{sac}

Figure 7.3 shows the effects of hypertension on the AP, SL, calcium transient ($[\mathrm{Ca}^{2+}]_i$), and the active force developed in the electromechanical ventricular single cell model with the I_{sac} current.

Under HP condition and with consideration of I_{sac} effects, simulation results show that: APD_{90} was prolonged by approximately 5% (from 210 ms in Sham to 221.5 ms in HP) (Figure 7.3 A), $[\mathrm{Ca}^{2+}]_i$ increased by 39.1%, relaxation and time constant of $[\mathrm{Ca}^{2+}]_i$ decay (tau) were faster (Figure 7.3 B) in both Sham and HP, the minimum contracted sarcomere length was 2.09 µm while the time course of the SL decreased by 14.2% in HP than in Sham (Figure 7.3 C), there was no change in the contraction as the contractile force (normalised active force) in both Sham and HP was 100% while the time course of the normalised active force decreased by 13.6% in HP than in Sham (Figure 7.1 D). A summary of these results is shown in Figure 7.4.

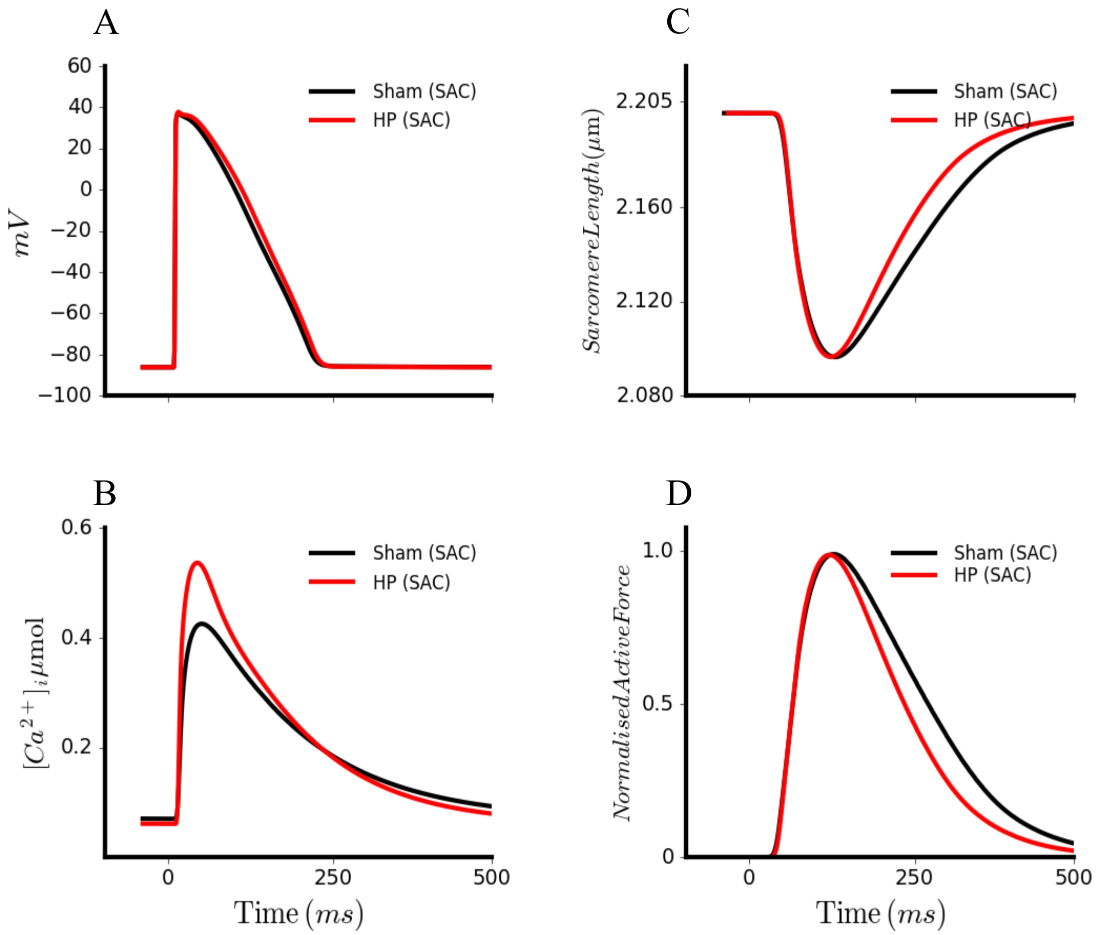

Figure 7.3: Single cell electromechanical effects of the HP with I_{sac}. Simulated (A) AP, (B) calcium transient ($[Ca^{2+}]_i$), (C) sarcomere length (SL), (D) normalised active force. In all figures, black line represents Sham, red represents hypertension (HP).

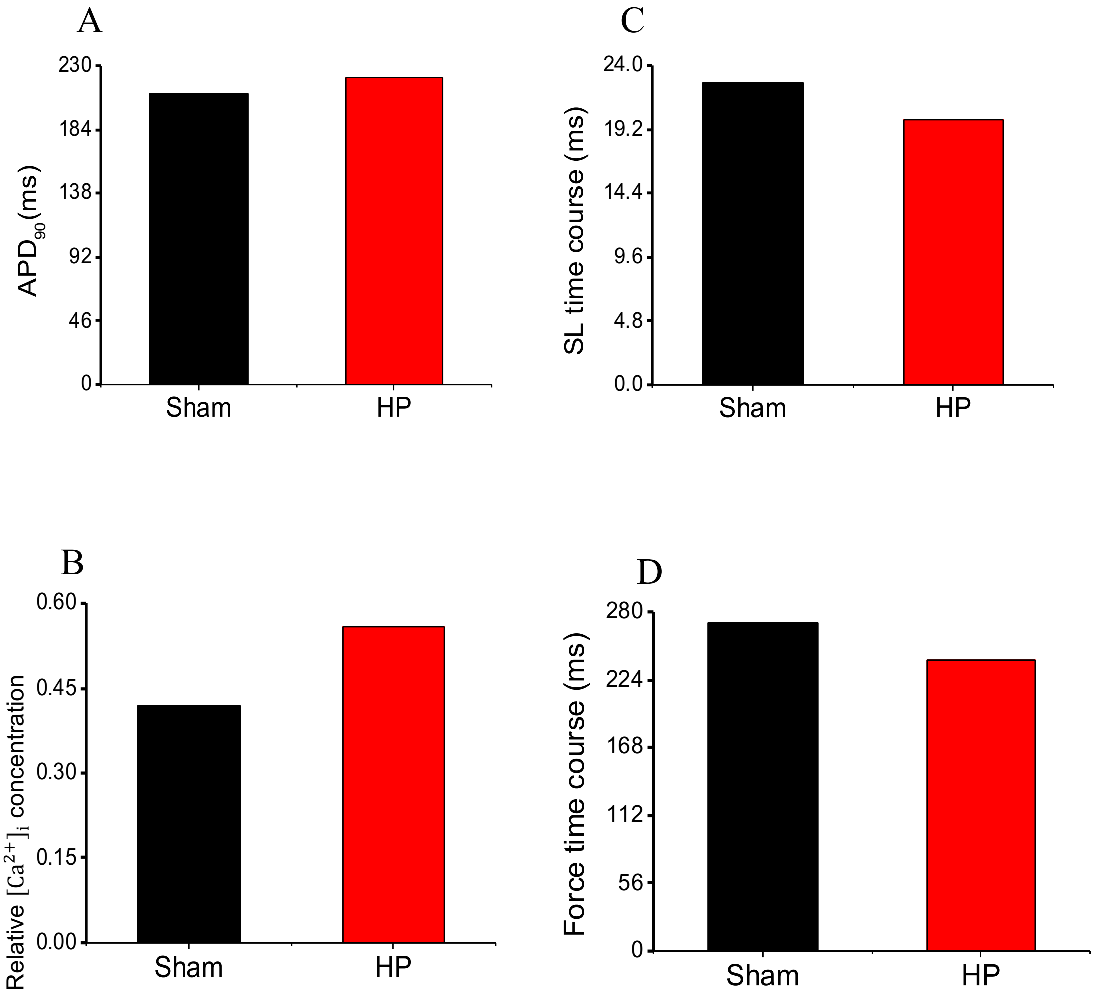

Figure 7.4: Bar plots showing the effects of HP on human ventricular myocytes (with SAC). Simulated (A) APD_{90} under Sham and HP conditions, (B) calcium transient ($[Ca^{2+}]_i$), (C) sarcomere length (SL), (D) normalised active force. In all figures, black columns represent Sham while red columns represent hypertension (HP).

7.6.3 Rate Dependent Restitution Properties of Sham and Hypertension Conditions

7.6.3.1 APD_{90} Restitution Curves (APD_{90}-R)

The APD restitution (APD-R) curve illustrates the recovery of the action potential duration (APD) as a function of the basic cycle length (BCL) (Chapter 2). The prolongation of APD_{90} by the hypertension condition was rate dependent. The APD-R curve is shown in Figure 7.5 A. The APD_{90} was bigger in HP condition than in the Sham condition through the BCLs intervals range studied. Simulation results show that the APD_{90} prolongation in the left ventricular myocytes under HP caused a leftward shift and increased maximal slopes, making APD_{90} restitution curves less flattened in HP than Sham [240] (Figure 7.5B).

7.6.3.2 ERP Restitution Curves (ERP-R)

The effective refractory period (ERP) restitution curves were plotted, as described in Chapter 2. The HP condition also prolonged ERP for LV ENDO cell type and caused a leftward shift of the ERP restitution (ERP-R) curve (Figure 7.6). Prolonging of the ERP was also rate-dependent and was bigger under HP than Sham conditions within the range of (BCL) investigated. At fast heart rates, the leftward shift of the ERP restitution curves can be seen (Figure 7.6 A). The HP condition also steepened the ERP-R curves (as in the APD-R curves), as shown by calculated the maximal ERP slopes (Figure 7.6 B). The Steepening APD-R and ERP-R curves are correlated with the increasing of the instability of re-entrant excitation waves [62]. The ERP-R curves' leftward shift under HP condition also suggests that at higher rates, the ability of the HP to reinforce electrical activity increased. Therefore, these results indicate the pro-arrhythmic nature of hypertension disease.

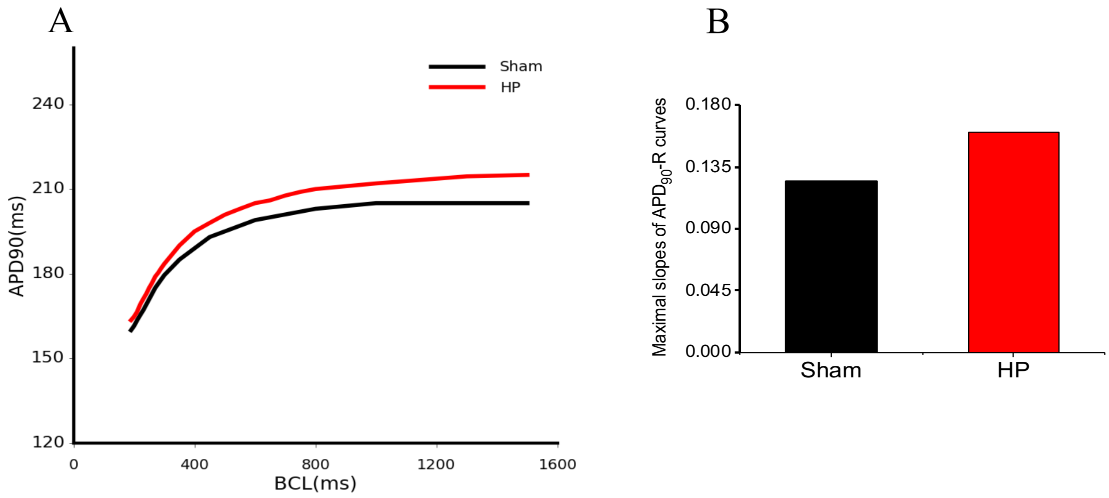

Figure 7.5: Steady-state APD_{90} rate dependence curves for Sham (black) and HP (red) electromechanical models. APD_{90} is plotted against the basic cycle length (BCL). A: Steady state APD_{90} restitution curves for Sham and HP conditions, which were plotted to examine the rate dependence of APD_{90} (ms) with BCL(ms). HP model showed greater prolongation APD_{90} (ms) than the Sham model. B: Slopes of Sham and HP APD restitution curves. An increasing in the slope of the steady state restitution curves can be seen with the increasing APD_{90} for the HP [240].

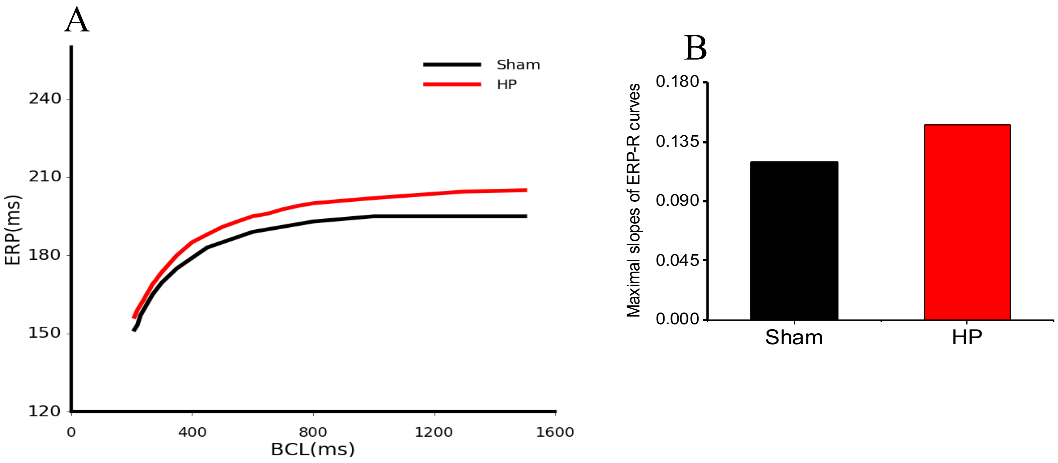

Figure 7.6: ERP restitution curves for Sham (black) and HP (red) electromechanical models. A: Steady state ERP restitution curves for Sham and HP conditions, which were plotted to examine the rate dependence of ERP(ms) with BCL(ms). HP model showed ERP increasing than Sham model. B: An increasing in the maximal slope of the ERP- R curves along with the shift of ERP-R curves towards left side for HP condition comparing to Sham condition.

7.7 Tissue Simulations

7.7.1 1D Heterogeneous Transmural Strand Model

A single fibre with 15 mm in length (close to the ordinary range of human transmural ventricle width [193, 228]) was used for the 1D mesh simulations. This single fibre consists of 100 nodes spaced 0.15 mm apart, and each node is 150 µm cylindrical cells. The strand comprises 40 epicardial cells (EPI), 35 middle cells (MCELL) and 25 endocardial cells (ENDO), suggesting 6.00, 5.25 and 3.75 mm in the EPI, MCELL and ENDO regions, respectively. Each region proportion in the strand is comparable to the proportions used in previous studies [185, 229].

In multicellular tissue models, initiation and conduction of APs were modelled by the use of the monodomain equation as described previously.

$$C_m \frac{\partial V}{\partial t} = -(I_{ion} + I_{stim}) + \nabla.(D\nabla V) \tag{7.13}$$

$C_m$is the cell capacitance per surface area unit, I_{ion}represents the sum of all membrane ionic currents and I_{stim} is the external stimulus current. 'D' is the diffusion coefficient which its value was set at 0.00152 cm^2/ms. This value gives a conduction velocity with a value of 65cm/s across the strand at 1Hz rate, which is close the conduction velocity of 70 cm/s alongside the fibre direction in the ventricular myocardium of human heart [230].

7.7.2 The Conduction Velocity and Conduction Velocity Restitution Curve

From one-quarter and three-quarter nodes along the 1D strand, the conduction velocity (CV) was computed. For each point, the activation time was defined as the time at which the dV/dt_{max} reached.

In order to calculate the conduction velocity, a series of 10 conditioning pulses was applied at 1 Hz in the 1D strand model, and the CV was measured by computing the time ΔT for the conducting wave to propagate from x–Δx to x+Δx [62]. The CV was plotted against different BCLs under investigating to obtain the CV restitution curve for Sham and HP conditions.

As a result, the CV can be calculated as:

$$CV = \frac{2\Delta x}{\Delta T} \tag{7.14}$$

7.7.3 The Tissue Excitation Threshold

The tissue excitation threshold (TET) can be defined as a minimal stimulus that can evoke an action potential propagated in cardiac tissue [62]. In the 1D strand tissue model, a standard S1-S2 protocol (previously explained in Chapter 2) was used to measure the tissue excitation threshold. S1 stimulus was applied at one end of the strand, with an amplitude of -80μA/μF and spatial size of 0.2mm for 0.5ms duration. A second premature stimulus (S2) was applied in the middle of the strand and was similar to the S1 stimulus in the special size and duration. TET was measured as the minimum amplitude of the S2 stimulus that can initiate an AP propagation along the strand.

7.7.4 The Temporal Vulnerable Window Measurement

As discussed in the previous sections, the conditioning excitation wave is initiated by supra-threshold stimuli at the ENDO end; then it propagates towards the EPI end of the 1D strand as seen in Figure 7.7 and 7.10. A refractory tail follows the propagating wave.

Applying a premature stimulus too early after the refractory tail will produce a conduction block along the strand in both directions. This is because the tissue around the premature stimulus is still excited from the previous excitation wave and have not recovered yet, as seen in Figure 7.9 Ai.

However, if the premature stimulus is applied too late after this time period, another excitation wave will develop and propagate along the strand in both directions. This is known as bi-directional conduction, as shown in Figure 7.7 Aiii, and it is due to the appropriate recovery of the tissue surrounding this stimulus site from the previous excitation wave.

There is a time period between these two extremes, identified as the vulnerable window (VW). The VW is when an applied premature stimulus results in a unidirectional conduction block. The unidirectional block is a solitary wave propagated in one direction (Figure 7.7 Aii) but not in both directions. The propagating direction is either forward or backwards, depending on the tissue region to which the premature stimulus is applied. The unidirectional conduction block induces the tissue vulnerable to re-entry [231].

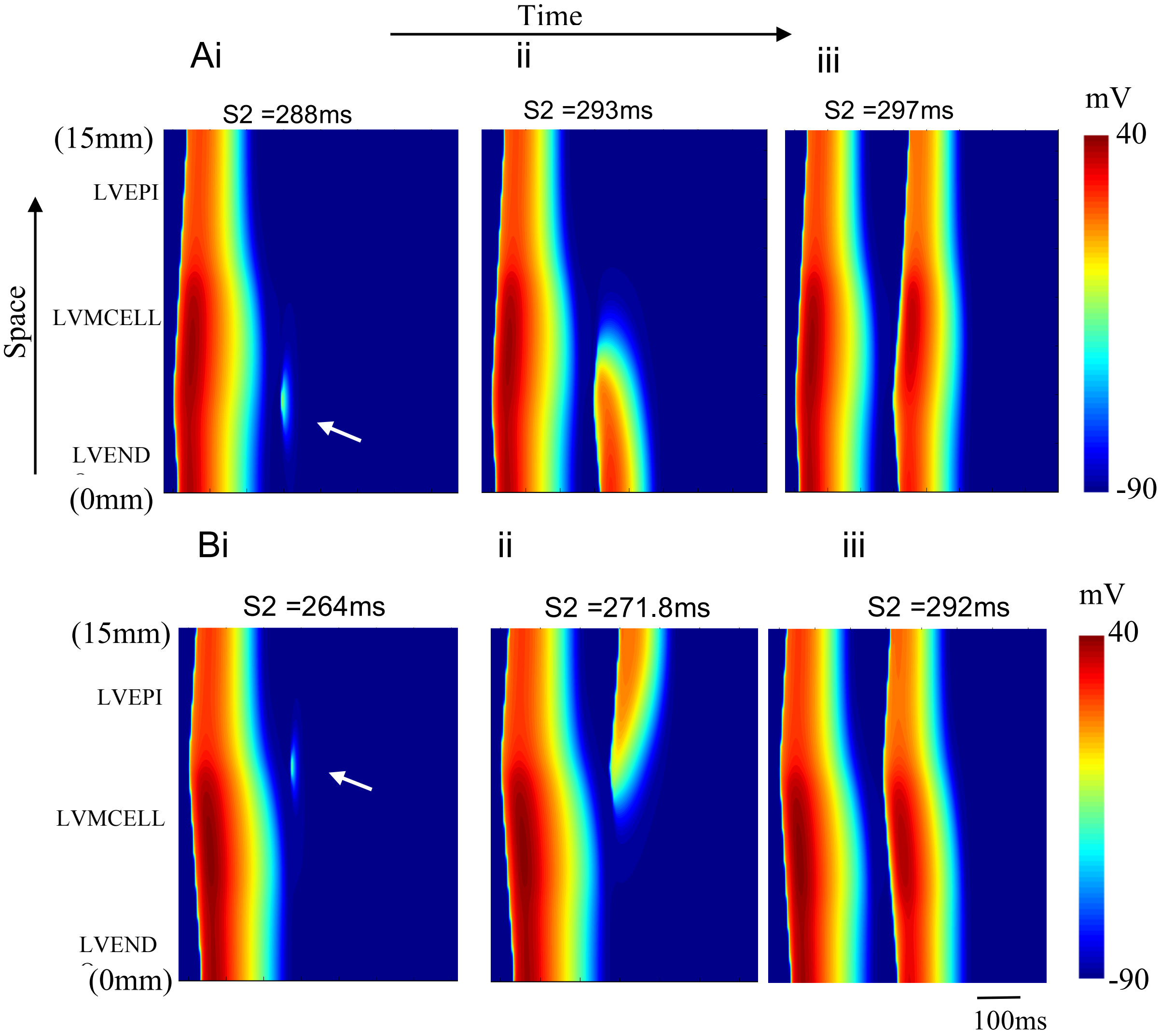

Figure 7.7: Space-time plot of excitation wave propagation in a 1D strand and tissue response to a premature stimulus (S2) at different time interval delays after an earlier conditioning wave (S1) (under hypertension condition). Space runs from the ENDO end (0 mm) to the EPI end (15 mm), vertically, while time runs from left to right, horizontally. A colour spectrum ranging from blue (-90 mV) to red +40 mV) is used to map membrane potential of the 1D strand model. (Ai,ii,iii): A premature stimulus applied at ENDO/MCELL region (showed in the Figure by arrow); (i) conduction block; (ii) unidirectional conduction; (iii) Bidirectional conduction. (Bi,ii,iii): A premature stimulus applied at MCELL/EPI region; (i) conduction block; (ii) unidirectional conduction; (iii) Bidirectional conduction.

7.8 Investigation of the Hypertension Effects on the Electrocardiogram

7.8.1 1D Strand Model of Sham and HP Simulations

The 1D transmural ventricular tissue strand model of the left ventricular (LV) wall, which was described in Section 7.9.1, was used in the simulations. It was paced at a BCL of 1000 ms. At the end of the LVENDO of the strand, a supra-threshold stimulus (amplitude: -80µA/µF, duration: 0.5 ms) was applied to evoke a conducting excitation wave which propagates towards the LVEPI end of the strand as shown in Figures 7.9 and 7.10.

7.8.2 Simulation of the ECG under Sham and HP Conditions

Pseudo ECGs were calculated for Sham and hypertension conditions (Figure 7.8C) by using the transmural ventricular tissue strand model of the left ventricular (LV). The manifestations of the Hypertension on the QT interval were simulated. The QT interval value was corrected using Bazett's formula [232].

The traces of quantified QTc of Sham and HP are shown in (Figure 7.8 C). The Sham model produced a QTc of 252 ms, while the HP model exhibited moderately prolonged QTc to a value of 265 ms. Furthermore, the T-wave duration was extended, and its amplitude was slightly elevated under hypertension conditions. A long QT interval at HP conditions is a major characteristic, observed clinically in the ECGs of the HP patients [120, 201, 233–235]. Simulations, therefore, reproduced this feature.

7.8.3 Investigating the Conduction Velocity under Hypertension Condition

The conduction velocity (CV) through the transmural strand of the human ventricular was computed under Sham and HP conditions (Figure 7.9 A). At low rates, the HP condition enhanced CV (PCL

> 570 ms; rate < 105 beats/min), while it decreased CV at higher rates. The CV increasing at low rates was owning to increased tissue excitability, as shown in Figure 7.9 B. At a heart rate of 60 beats/min with BCL=1000 ms, the calculated CV was 65 cm/s for Sham and 67 cm/s for HP conditions whereas at higher rates between 154 and 190 beats/min (315 ms < PCL < 390 ms), the calculated CV was much lower under the HP condition than Sham condition due to longer ERP under this condition compared to the Sham condition. As a result, the ventricular tissue highest rate in order to aid conduction was 188 beats/min (SI = 320 ms) in the Sham condition while it was 162 beats/min (SI = 370 ms) in the HP condition.

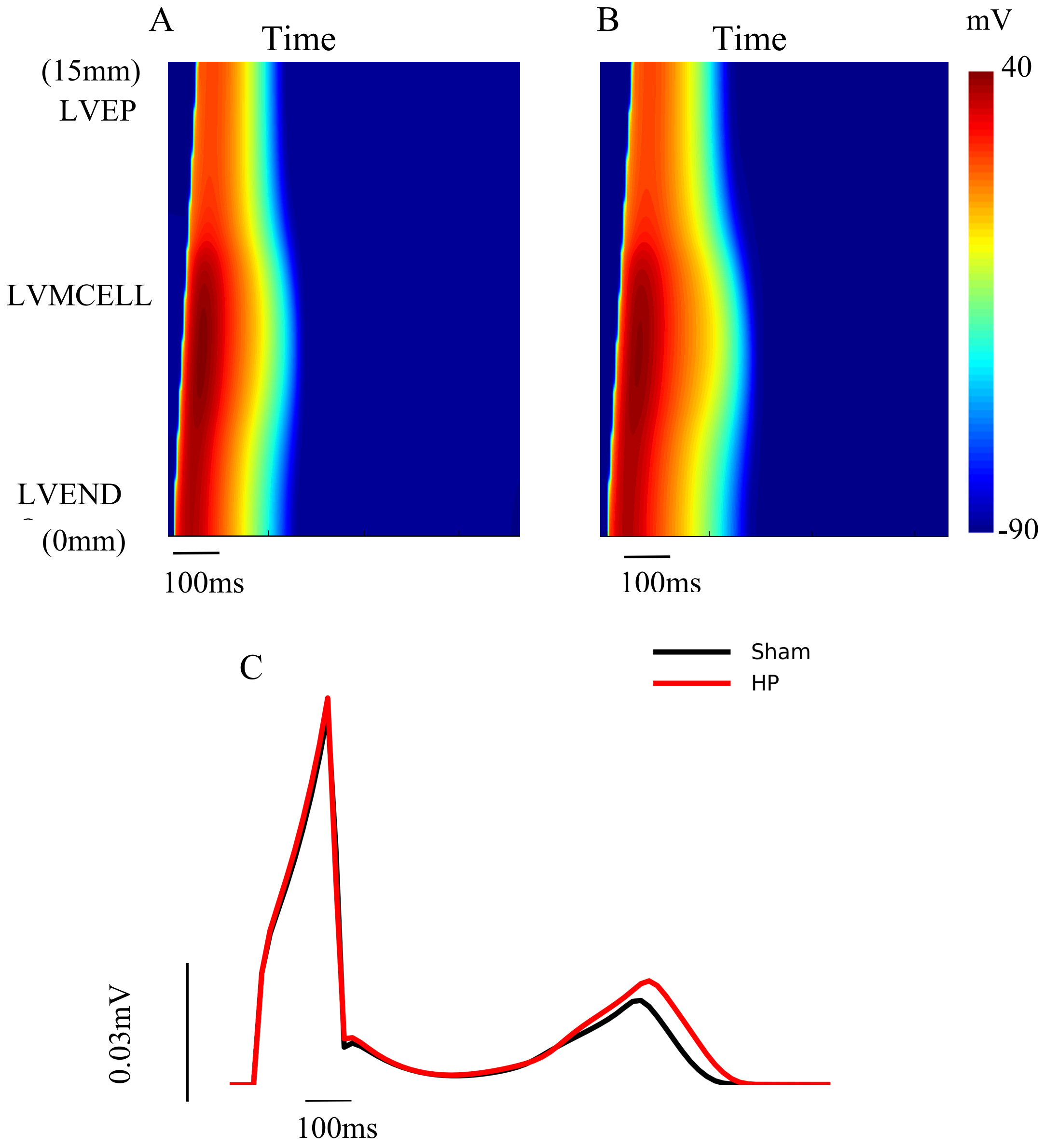

Figure 7.8: Space-time plots of excitation wave propagation and related pseudo-ECG of human ventricular wall strand. A and B: Colour mapping of membrane potential alongside the 1D strand under Sham (A) and hypertension (B) conditions. In A and B, each excitation wave was initiated by a supra- threshold stimulus that applied to the end of the LVENDO region. The excitation waves propagated LVENDO toward the LVMCELL and LVEPI regions of the strand. Time runs from left to right on each panel, horizontally. C: Pseudo-ECGs related to space-time plot of excitation wave propagation, under both Sham (black line) and HP (red line) conditions. CL = 1000ms.

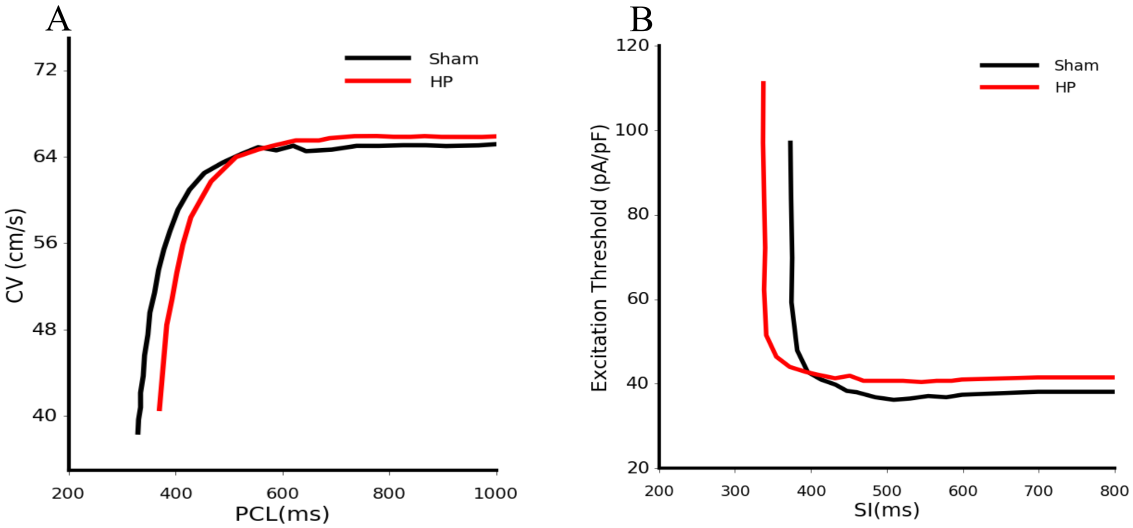

Figure 7.9: Computed conduction velocity (CV) and the Excitation threshold. A: CV restitution under Sham (black) and HP (red) conditions. B: Excitation threshold of the ventricular tissue plotted against (SIs) for the Sham and HP conditions, Note: PCL is the pacing cycle length and SIs is the stimulus intervals.

7.8.4 Effects of Hypertension on Tissue Vulnerability

A 10 S1 stimuli sequence was applied (amplitude: -80 µA/µF, duration: 0.5 ms) at one end of the 1D transmural strand and paced at 1 Hz to evoke a propagating excitation wave. After the 10th S1 stimulus and following a time delay (ΔT), a second stimulus (S2) with similar amplitude and duration to S1, was applied at the ENDO/MCELL junction (Figure 7.7 A) and the MCELL/EPI junction (Figure 7.7 B) part of the strand.

During the time window of the maximal and minimal value of ΔT (T1 and T2, respectively), the S2 stimulus induces an excitation wave propagated unidirectionally in the strand. Therefore, the tissue's temporal vulnerability can be obtained by measuring the width (T1–T2).

Figure 7.10 shows the VW width under Sham and HP conditions. It illustrates that the HP condition delayed the occurrence of the temporal VW in S2. Moreover, at the MCELL/EPI junction (Figure

7.10 A), the calculated width of the VW was much wider than the calculated width at the ENDO/MCELL junction (Figure 7.10 B). This is mainly due to more profound action potential duration (APD) heterogeneity between EPI and MCELL under Sham and HP conditions. In addition, the VW widths were slightly increased under the HP condition. Simulations showed that VW was 5 ms under the HP condition while under the Sham condition, it was 4 ms when measured at the ENDO/MCELL junction. Moreover, the VW width in HP was 7.8 ms and 5.5 ms in Sham conditions at the MCELL/EPI junction.

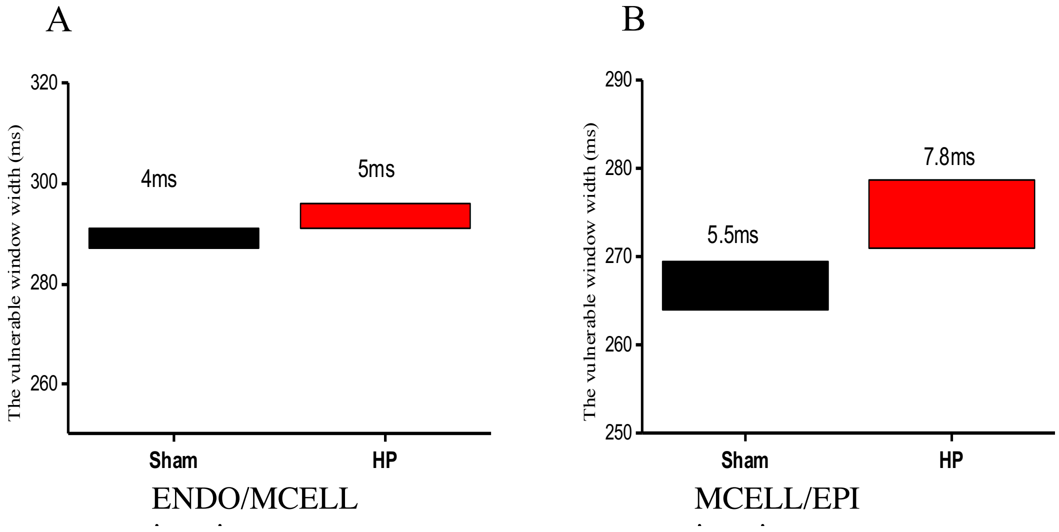

Figure 7.10: Measured width difference of vulnerable window between Sham (black) and HP (red) conditions at the ENDO/MCELL in (A) and MCELL/EPI junctions in (B), respectively.

7.9 Investigating the Arrhythmogenic Substrate in Sham and Hypertension Electromechanical Models: Idealised 2D Geometry Simulations

A simple sheet of human left ventricular tissue was used as an idealised geometry for the simulations of the electromechanically coupled 2D models of Sham and hypertension conditions, as seen in Figure 7.11 A. The tissue sheet dimensions were 27 mm in the x-direction (with 180 nodes) by 37 mm in the y-direction (with 250 nodes) for the Sham tissue model, while for the HP tissue model it was 37 mm in both x and y-directions with 250 nodes. The increasing of the sheet width in the HP models is due to the ventricle wall hypertrophy under the hypertension condition [120, 236].

The 2D tissue model was employed in the investigations of the re-entrant wave behaviour in Sham and HP conditions. It also calculated the minimal spatial length of the premature stimulus required to initiate re-entry for both Sham and HP conditions (Figure 7.11 B, C). The 2D tissue sheet had three distinct regions (ENDO, MCELL and EPI), similar to the 1D transmural strand. Also, the monodomain equation described previously was utilised to solve the excitation wave propagation problem [143, 187].

In the 2D tissue model, to evoke re-entrant waves, the S1-S2 protocol (described in Chapter 2) was used and can be illustrated as follows: A conditioning stimulus (S1) was applied at the end of the ENDO region of the 2D sheet to initiate an excitation wave that propagated from the ENDO towards the EPI region of the 2D tissue sheet for Sham and HP conditions (Figure 7.11 B, C).

Following a time delay, a second stimulus (S2) was applied during the VW of the EPI region (Sham; Figure 7.11 B and HP; Figure 7.11 C). While the MCELL region was still refractory (owning to its slower repolarisation compared to ENDO and EPI regions), the excitation wave evoked by S2 will be blocked by unrecovered MCELL. This generates unidirectional conduction towards the EPI region. This resulted in the development of spiral re-entrant excitation waves in Sham and HP conditions. For Sham and HP, the time delay between S1 and S2 was 245 ms and 205 ms, respectively. The development of the re-entrant excitation waves depends on the length of the second (premature) stimulus. Therefore, the minimal tissue substrate length required to induce re-entry was calculated as 23.5 mm for the Sham and 34 mm for the HP conditions (Figure 7.12).

The re-entrant excitation waves in the electromechanical models of Sham and HP were self-terminated. Under the Sham condition, the spiral wave self-terminated after 575 ms and within 335 ms after its initiation, while for the HP condition it was sustained longer and terminated after 990 ms and within 785 ms after its initiation (Figure 7.13). Simulations showed that there is no significant difference between the time spans of re-entrant waves in the Sham and HP conditions;

however, the life span of the re-entrant wave is still shorter for the electromechanical 2D tissue model of Sham compared to the HP model.

These simulation results indicate that greater susceptibility to ventricular arrhythmia is expected under HP condition.

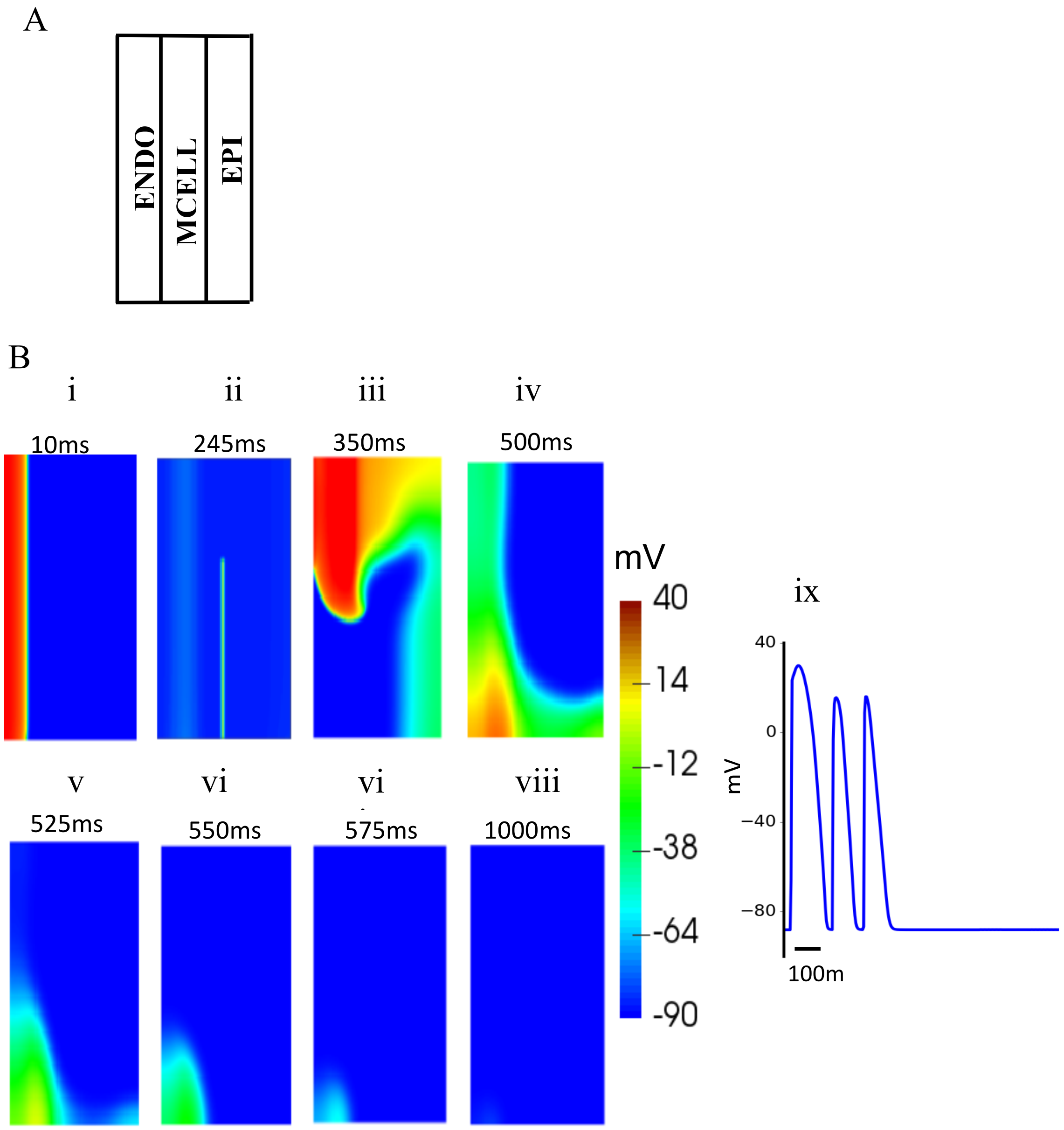

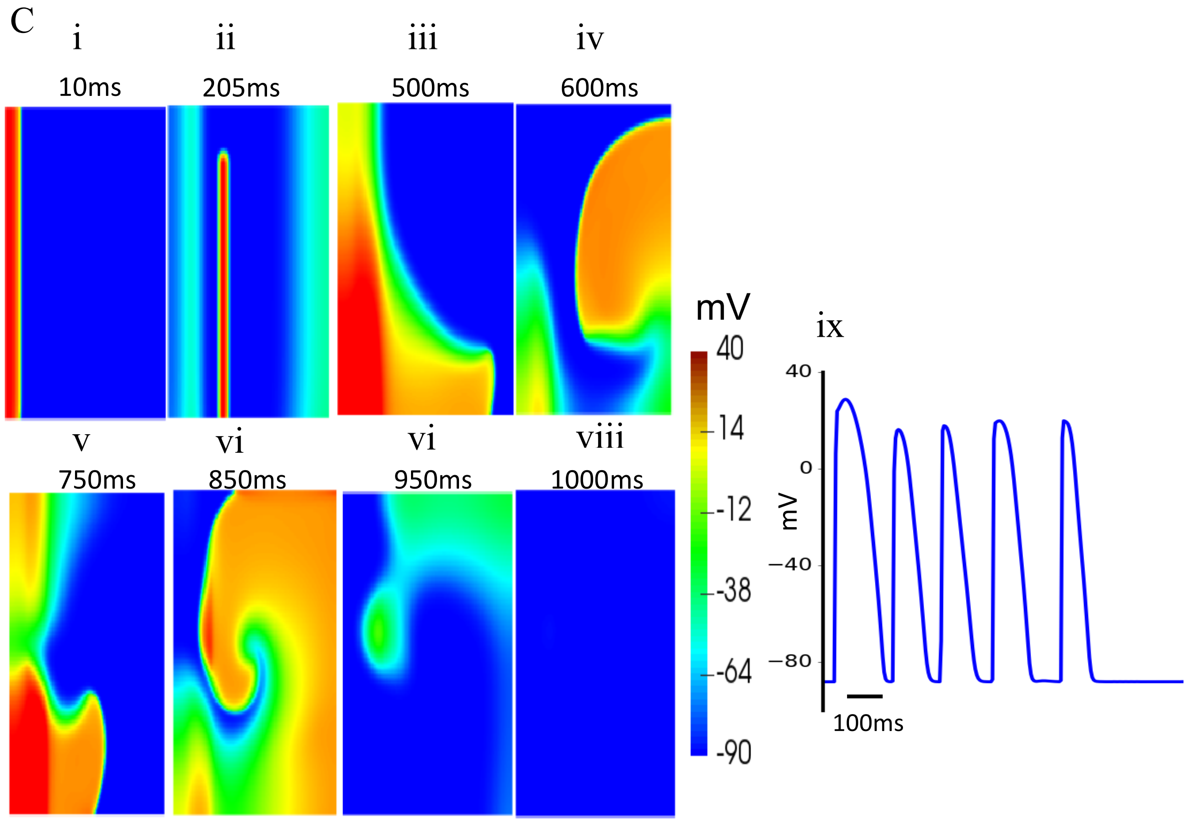

Figure 7.11: Snapshots of generation and conduction of re-entry excitation wave in a 2D idealised model of transmural LV tissue, under Sham and hypertension conditions. A: Graphic illustration of the 2D model. In B and C, i) A planar conditioning wave produced by S1 stimulus at the ENDO end region. Snapshots at 10 ms. ii) Snapshots of the S2 stimulus applied to the EPI region throughout the VW of the local tissue. iii to vii) Established a spiral wave due to S2 stimulus. viii) Snapshots of spiral wave at 1,000 ms. The spiral wave is self-terminated under Sham condition before this recording point, however it is continued for longer under HP condition. ix) Development of the AP of a cell in the epicardial region for Sham and HP conditions.

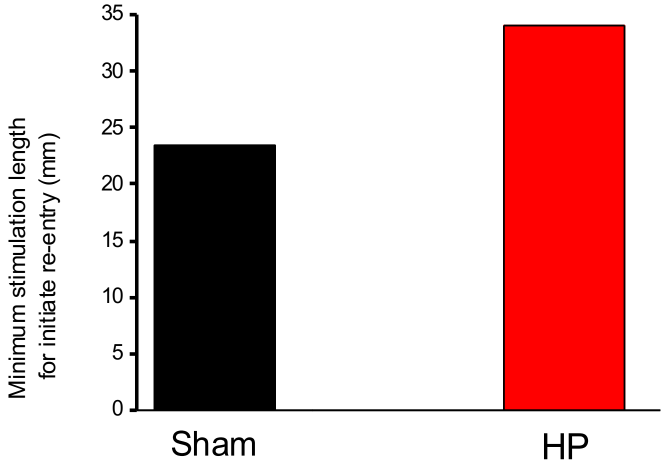

Figure 7.12: Minimal length of the premature stimulus (S2) required to induce re-entry in the 2D electromechanical tissue models for the Sham (black) and HP (red) conditions.

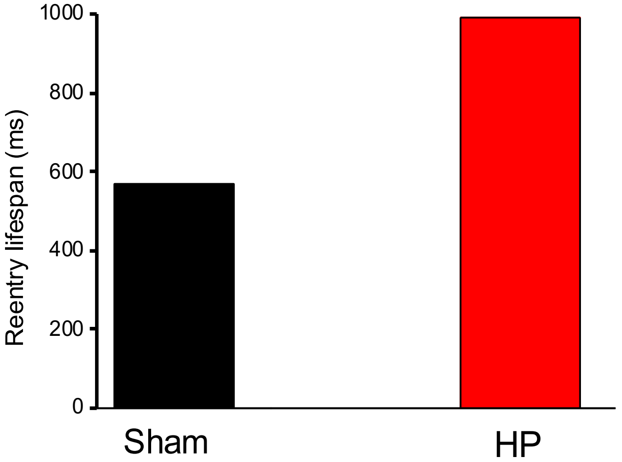

Figure 7.13: Total life span of the re-entrant spiral wave in the 2D electromechanical tissue models for the Sham (black) and HP (red) conditions, (computed from Figure 7.11B,C).

7.10 Discussion

A multi-dimensional biophysically detailed model of human left ventricle electromechanical function was used in the current chapter in order to assess the hypertension effects on the contractile function of the human left ventricle. This includes demonstrations of inotropic effects brought about by a hypertension condition at both the cellular and tissue level, and also investigations on the mechanisms underlying these effects.

7.10.1 The Electromechanical Model of the Ventricle

In this chapter, the ORd electromechanical model of human ventricular myocytes was used under Sham and hypertension (HP) conditions using experimental findings from rat ventricular cells, while the hypertrophy (induced by HP) model was modelled following the work of Kharche et al. (2005) [206]. It produced qualitatively analogous results in the relative calcium transient concentration, time course of the SL and the right shift of the calcium sensitivity development seen in rat ventricular myocytes reported in a previous experimental study [202].

A two-dimensional (2D) model of the human ventricular electromechanics was updated with the new modifications of single cell models. It was then used to study the re-entrant excitation wave under Sham and HP conditions.

7.10.2 Hypertension Effects on Human Left Ventricular Myocytes

7.10.2.1 At Single Cell Level

The active force generated from contraction is associated with the sarcomere contraction. Single cell simulations of LV without considering the effects of I_{sac} showed that hypertension produces a right shift in the relaxation phase of the normalised active force–$[\mathrm{Ca}^{2+}]_\mathrm{i}$ increasing EC_{50}value and indicating a reduction in the myofilament sensitivity to $[\mathrm{Ca}^{2+}]_\mathrm{i}$ under HP condition [202, 226, 227], a prolongation in the action potential duration at 90% of repolarisation (APD_{90}), an increase in the intracellular calcium concentration ($[\mathrm{Ca}^{2+}]_\mathrm{i}$) and a faster relaxation and time decay of $[\mathrm{Ca}^{2+}]_\mathrm{i}$.

Moreover, the sarcomere length, as well as the active (contractile) force, remained unchanged, suggesting that the HP condition might not modulate the contraction of the LV cardiac cells. However, the time course of SL and the normalised active force decreased in the HP condition which might result from the faster time constant decay of $[\mathrm{Ca}^{2+}]_\mathrm{i}$. These results were in a good agreement with experimental records from [202] shown in Figure 7.1 and Figure 7.2.

It has been found that alterations in cell stretch or cell volume induce mechanical stimuli that activated some cardiac ion channels. This represents the essential mechanism of electromechanical coupling [62, 219].

Accordingly, a non-selective cationic stretch-activated current (I_sac) was integrated into the electromechanics models. Incorporation of the I_sac current resulted in prolonged APD_{90}, increased amplitude of the intracellular $[\mathrm{Ca}^{2+}]_\mathrm{i}$, and a shortened time course of the active force and the sarcomere length under both Sham and HP conditions (Figures 7.5 and 7.6). These simulation results are comparable to those reported experimentally from [238]. In the human ventricle, the mechanical stretch-induced ventricular arrhythmias with consequent ventricular fibrillation leading to sudden cardiac death [238]. The literature reports that hypertrophic remodelling resulting from hypertension can strongly increase the risk of stretch-induced arrhythmias [239].

7.10.2.2 At 1D Tissue Strand

In the 1D strand model of left ventricular cells, the electrocardiogram (ECG) was calculated under Sham and hypertension conditions. It showed that the HP condition prolonged the QT interval compared to the Sham (Figure 7.8). The long QT syndrome (LQTS) is associated with proarrhythmic implications including the risk of ventricular fibrillation and a high risk of cardiovascular events (CVE) in hypertensive patients (associated with the left ventricular hypertrophy (LVH) under the HP condition) [236, 247].

7.10.2.3 At 2D Tissue

In the 2D tissue simulations, the hypertension condition produces early initiation for the re-entrant excitation wave due to the tissue's VW to the genesis of unidirectional conduction, which was slightly protracted and delayed in timing. This indicates increasing vulnerability to induction of arrhythmia by the HP condition. Moreover, re-entrant excitation waves were maintained longer under HP compared to Sham conditions.

7.10.3 Novelty and Relevance to Previous Studies

The present study highlights the role of the hypertension condition and related hypertrophy in modulations of ventricular contractility and represents, to the best of the author's knowledge, the first attempt to investigate such modulations using biophysically electromechanical detailed models at cellular and tissue levels. The simulations increase our understanding of the hypertension roles and relevant hypertrophy in ventricle contractility. Although some simulations on the functional role of HP in the ventricle have been performed [52, 241–243], these studies focused on the impact of the modulation of HP on electrical activities of the ventricle without considering either ventricle hypertrophy or ventricle contractile functions. Effects of HP on ventricular contraction have been investigated experimentally at the cellular level [120, 202, 227], offering a robust understanding of mechanistic insights into the inotropic effects of HP.

7.11 Limitations

Limitations of both the ORd electrophysiology model [55] and the Rice et al. [207] myofilament model have been discussed in detail previously and hence are not discussed here.

In the present study, the inotropic effects of hypertension were compared with Sham from experimental rat data. It was assumed that the hypertrophy induced by HP modulations does not mediate any changes other than alterations to some ion channel currents including $\mathrm{I_{Na}}$, $\mathrm{I_{to}}$ and $\mathrm{I_{NaCa}}$

without consideration of the possible alterations to other currents in the model. Therefore, the validity of such an assumption requires further experimental investigations.

Another limitation lies in the validations of the single cell simulations. In the absence of experimental data from human ventricular myocytes, the model was validated against multiple studies in rat ventricular cells. However, in several previous studies, such an approach in integrating and comparing data from alternative species has been adopted in many previous papers and for different parts of the heart [63, 156, 185, 198].

Mechanoelectrical feedback was included via the inclusion of I_{sac} following previous studies [137, 223, 244]. Mechanoelectrical feedback has been proposed to contribute other effects such as stretch-induced changes to the intracellular Ca^{2+} handling system and the interactions between ventricular myocytes and fibroblasts were not considered.

7.12 Summary

In the current Chapter, multi-scale computational models have been used to assess the functional impact of the hypertension condition on the cardiac mechanical dynamics and the contracting mechanisms of the left ventricular myocytes and QT interval. At the cellular level, the electromechanical model simulations demonstrated that the HP condition produced a reduction in the myofilament Ca^{2+}sensitivity and a prolongation in the APD_{90} of the left ventricular (Figure 7.1) compared to the Sham condition (control). These results were consistent with experimental findings, validating the HP model development. ECG was calculated from the 1D strand model, showing that the QTc was prolonged under the HP condition. The long QT syndrome (LQTS) is associated with proarrhythmic implications including the risk of ventricular fibrillation and a high risk of cardiovascular events (CVE) in hypertensive patients (associated with the left ventricular hypertrophy (LVH) under HP) (Figure 7.8). In the 2D tissue simulations, the re-entrant excitation wave was initiated earlier and sustained for longer under HP compared to Sham conditions, signifying the pro-arrhythmic effects of HP and providing mechanistic insights into understanding the increased risk of ventricular fibrillation in hypertensive patients.

8. Discussion and Conclusion

In this Chapter, a summary of the main findings as well as novelty and significance of the studies from this thesis will be presented. The key experimental relevance of these findings is outlined, and then the directions of the future work of this thesis are discussed.

The main contributions of this thesis are summarised as follows.

Part I of this thesis focused on investigating the effects of altering temperature that resulted from global warming on the teleost heart function as a vertebrate animal, which might lead to their sudden death and heart failure. In Chapter 4, a novel biophysically detailed single cell model for the electrical action potential of a teleost ventricular myocyte for fish adapted to a chronically cold (cold-acclimated, CA, 4°C) has been developed. The developed model was used to simulate the ion channels remodelling impact on the electrical properties of the teleost fish ventricular myocytes at thermal acclimation for fish acclimated to a chronically warm (warm-acclimated, WA, 18°C) and for the common experimental temperature of 11°C. Then effects of changing chronic temperature or changing temperature acutely were also investigated at cold and warm acclimation conditions. Chapter 5, a 1D strand tissue model of the teleost ventricle at the physiological temperature of 4°C and 18°C have been developed to elucidate the impact of increasing acute temperature on the electrical conduction in the teleost fish ventricular tissues.

Part II presented the development of a novel 3D biophysically detailed and anatomically accurate computational model for the teleost ventricle developed at the physiological temperature of 18°C. In Chapter 6, a 3D geometry of the teleost fish heart was reconstructed and segmented into the main fish heart chambers using micro-CT scan with sustaining iodine technique. Then the 3D geometry of the fish ventricle was implemented into a 3D computational model for the teleost fish at 18°C to investigate the electrical excitation propagation in teleost heart.

Part III of this thesis presented another cause of heart failure, which is relevant but in the mammal heart, arising from the hypertension (high blood pressure) disease. Chapter 7 showed a work using a multi-scale electromechanical model of the human ventricle to investigate the impact of hypertension on the left ventricle contractile function.

8.1 Novelty and Significance

The work presented in this thesis represents a significant advance in the cardiac modelling of the vertebrate and mammal's heart. First, the developed teleost fish ventricular cell model is novel and a first attempt (to the author's best knowledge) to simulate the electrical excitation in the fish heart. It consists of a novel family of models for some major ionic currents, which are remodelled by changing chronic temperature (cold and warm acclimation), allowing a detailed comparison of such models within a consistent framework of temperature changes. Also, the investigation of the effects of increasing the acute temperature on the depolarisation and repolarisation of fishes ventricular AP shed light to understand how altered temperature affected the AP characteristics at single cell level, and conduction at the 1D strand tissue level that plays an important role in generating teleost cardiac arrhythmia and hence the fish lifespan. The model of the effects of changing chronic and acute temperatures on the AP in general show strong agreement with the available experimental data from different teleost species.

Second, the 3D model of the teleost fish ventricles was developed. The anatomical model of the fish heart was reconstructed and segmented into distinctive regions by using the micro-CT scan with sustaining iodine technique. For the first time, anatomically accurate and detailed models of the teleost ventricle have been incorporated into a 3D teleost ventricle model.

Thus, the models developed in the first two parts of this thesis have been used to underpin some of the underlying mechanisms of teleost fish ventricle (as a vertebrate animal) arrhythmias when the fish ambient temperature changes. These models also provide a detailed computational platform for future investigation of fish ventricle arrhythmias which contains a greater level of physiological relevance, detail and complexity.

Third, the focus of the last part of this thesis is in multi-dimensional electromechanical computational models of human ventricle (as a mammal) in order to investigate the impacts of hypertension on the heart contractile function. The new electromechanical human LV model modified incorporates different aspects associated with high blood pressure including hypertrophy and mechanical contraction conditions model to generate a more physiologically precise model and also contains a high degree of dynamic complications than the previous models on which it is based.

The model of the effect of hypertension on the AP and Ca^{2+} is a novel approach which has not been previously investigated in a human ventricular electromechanical model. For the first time, a detailed model of LV hypertrophy has been integrated into cell models describing Endo LV region under Sham and HP conditions. Insight has been provided into the effects of HP remodelling on the Ca^{2+} transient, and the role that LV hypertrophy plays in remodelled APs.

8.2 Summary of Major Findings and Novel Contributions

The main findings in this thesis are summarised here:

8.2.1 Chapter 4: Development of a Novel Teleost Fish Ventricular Myocyte Model

Although computational cardiac models have been developed for different animal species, models for fish heart have not developed yet. In Chapter 4, a novel model of the teleost fish ventricular AP was developed at cold acclimated, at the physiological body temperature of 4°C. A novel family of mathematical formulations for the major membrane ion channel currents (including I_{Na}, I_{CaL}, I_{Kr} and I_{K1}) responsible for generating the electrical APs of teleost fish ventricular myocytes have been developed. The currents from simulations were in good fitting to the relevant experimental recordings from different teleost species. The mathematical formulations of these currents have been incorporated into the Luo and Rudy model [54], the basal framework of our model for the teleost ventricular cells. The model development was validated by its ability to reproduce the AP characteristic of the teleost ventricle at 4°C.

Recent studies [17, 42, 43, 104, 107, 154, 155] showed a wide range of remodelling in the membrane ionic currents of the ventricle cardiac myocytes in the fish heart in response to changes in the environment temperature. It has been found that these ionic currents represent one of the key factors in setting the thermal limits for the function of the fish heart [16, 42] (see Section 4.2.4). Therefore, the developed model at 4°C has been modified to investigate possible effects of changed ionic currents on fish ventricular APs during chronic temperature in cold and warm acclimation. The modifications include the kinetics and the I-V relation of the ionic currents based on experimental findings from several teleost species. The developed models at CA and WA demonstrates a strong agreement to the available experimental data, and the resultant APs replicate well the morphologies observed experimentally from different teleost species due to the big lack in the experimental data for teleost cardiac myocytes.

8.2.2 Chapter 5: Investigating the Effects of Increasing Acute Temperature on the APs and ECGs of the Teleost Ventricular Using Single Cell and 1D Strand Tissue Models at Different Temperature

8.2.2.1 Developed a 1D Strand Tissue Model

The single cell models of the teleost fish ventricular cells at the physiological temperature 4 and 18ºC developed previously, are expanded to a 1D linear strand with a length of 16.5 mm (110 nodes). In the 1D model, the strand length was similar to those used by Zhang and Hancox for human ventricular myocytes [185]. The teleost ventricle tissue assumed to be homogenous as no experimental records published yet about any heterogeneity in the fish ventricle wall. Simulations at both temperatures the ECG features from the 1D strand models for fish ventricle including QRS, QT, RT and conduction velocity were in agreement with the available experimental data from brown trout fish [17], that validated the models development.

8.2.2.2 Effects of Increasing the Acute Temperature

In Chapter 4, the thermal tolerance of the teleost fish ventricular myocytes has been investigated by the modifications of the single cell and 1D strand tissue model at 4 and 18°C. These modifications have been carried out at a range of temperature from cold of 4°C to the thermal limits of most teleost fish (salmonid species such as brown trout and rainbow trout fish) of 33°C.

The teleost ventricular models presented in this thesis have helped to highlight the underlying mechanisms of the effects of changing the ambient temperature on remodelling of one or more of the membrane ionic currents and hence the AP and ECG.

From all the modified models at various temperatures, the simulated AP and ECG properties at all temperatures studied were in a fairly close to those observed experimentally from brown trout fish [17].

The next Sections illustrate the increasing acute temperature effects on the depolarising $\boldsymbol{I_{Na}}$ and repolarising $(\boldsymbol{I_{Kr}})$ currents (see Table 5.1) and hence the AP and ECG features.

8.2.2.2.1 Effects of Increasing Acute Temperature on I_{Na} and I_{Kr} Currents

It has been found that under a rising temperature regime, the I_{Na} current function is compromised, therefore, it might be one of temperature- dependent factors that lead to contractility depression of the cardiac myocytes in the trout heart [17]. In Chapter 5, simulations showed that when the temperature rises few degrees (slightly above 21.2°C) less than the thermal limits of the trout hearts (usually between 4 to 25.5°C) [17], the I_{Na} density decreased inducing a reduction in the upstroke velocity of the AP and slowing the conduction velocity in the ventricle tissue.

Further to this, while the I_{Na} current density decreased, the I_{Kr} density still increased with raising temperature. This results in an imbalance between repolarizing and depolarizing currents which prevents reaching the threshold potential (that needs to evoke AP) leading the cardiac myocyte to become electrically unexcitable. Hence, this can cause, i.e. AP fails leading to heart failure [17, 119, 190].

8.2.2.2.2 Effects of Increasing Acute Temperature on AP

In cellular level simulations, the simulated characteristics of AP at the range of temperature between 4 to 31°C replicate those observed experimentally [17] (Figure 5.3A). Simulation results showed an increase in the APA and the $\mathrm{dV/dt_{max}}$ when the temperature rises from 4 to 17°C, and above that the APA levelled off while the dV/dt_{max} decreased in an inverted V shaped that have a peak at approximately 16°C and minimum values at 4 and 33°C.

In addition, a fast reduction in AP duration was linked to increase in temperature [42, 245], however, at higher temperatures reduction in $\mathrm{APD_{90}}$ becomes slower [17] (Figure 5.3C). The APD shortening with a rise in temperature indicates augmented total repolarizing current. Shortening of AP plateau is necessary for cardiac function making room for diastolic filling of the heart when cardiac cycles are abbreviated. This might fasten the fish heart rate which might cause a sudden cardiac failure and animal over heated death [17]. These simulation results showed close agreements to the experimental recordings [42, 104].

8.2.2.2.3 Effects of Increase in Acute Temperature on ECG

In the 1D strand tissue model, the simulated ECG features at different temperatures (Figure 5.2C) from cold of 4°C up to the thermal limitation of 31°C were fairly close to the available experimental findings [17]. Simulations showed a sudden increase in QRS complex duration at high temperatures, above 24°C, indicating a depression in the rate of AP propagation over the heart when temperature increases [17].

The 1D model also calculated the RT interval which increased linearly from 4 to 18°C, and above that the RT interval slightly declined (Figure 5.4B). Temperature dependencies of RT interval suggest that systolic/diastolic duration remains constant fairly under acute temperature changes. Additionally, the simulated QT interval also showed a linear change with temperature (Figure 5.4C).

Furthermore, the calculated conduction velocity (CV) is also affected by changing temperature, which is increased by 24% from 4 to 17°C and above that it slowed down by approximately 60%, (Figure 5.4D). Simulations showed that although fish as ectothermic animals can adapt a wide range of change in their ambient temperature, it still has a limit upper thermal tolerance. When the temperature exceeded it, cardiac failure leading to their sudden death can occur. This can be an interesting topic for further research in the molecular mechanism to investigate which factors (such as which amino acid sequences), or ion channel domains are involved in the ectothermic heat sensitivity. Such information will be increasingly valuable given predicted changes in global temperatures.

8.2.3 Chapter 6: Developing a Novel Three-Dimensional Model of the Teleost Fish Ventricle

8.2.3.1 3D Anatomical Model of Teleost Ventricle

In Chapter 6, a 3D anatomical geometry for the teleost brown fish heart has been reconstructed and segmented into several distinctive regions including the atrium, bulbus, ventricle and sinus venosus (Figure 6.4). This has been done by using micro-computed tomography (micro-CT) with iodine staining [60]. Recently, micro-CT scan has been used widely to create high-resolution 3-D tissue images from different animals species [60, 68, 192, 246]. It has been found that higher resolution images can be obtained from micro-CT scan by staining with iodine (Section 6.2.1.2).

The segmented 3D geometries are essential for constructing biophysically detailed computational models of the heart to obtain a good understanding of the underlying mechanisms of arrhythmias. In this thesis, the 3D geometry of the teleost ventricle was reconstructed from micro-CT images, and its detailed 3D architecture has been implemented in a novel 3D biophysically detailed computational cardiac model of the fish heart for exploring the conduction system of different parts of the heart during temperature changes.

8.2.3.2 3D Computational Model of Teleost Fish Ventricle at 18°C

This Chapter focuses on the development of a novel 3D biophysically detailed computational model that anatomically accurate for the teleost fish ventricle at the physiological temperature 18°C. A single cell mathematical AP model of the teleost ventricular cells that developed early in this thesis at 18°C (see Chapter 4 and Section 6.2.2.1) was used along with the anatomically detailed reconstruction of the teleost ventricle region as homogenous, isotropic tissue media (in the absence of the fibre orientations).

Action potential propagation was then initiated in this 3D reconstruction using the single cell model (at 18°C) developed in Chapter 4. The APs propagate through the tissue with the excitation wave propagating from the upper top of the ventricle base and then spreading towards the ventricle sites before reaching the bottom of the heart at the apex. This conduction pattern is shown in Figure 6.9. The activation time of the tissue was 22 ms, within standard deviations of the experimental observations by Shiels et al. that measured activation sequence in the ventricle of the brown trout fish (approximately 18.5 ms) [unpublished data], as seen in Figure 6.10.

8.2.3.3 A Computational Platform for Studying Ventricle Arrhythmias

The combination of single cell AP model of the ventricle myocytes at specific temperature, combined with the realistic 3D reconstruction of a teleost ventricle provide a powerful platform for the study of ventricle arrhythmias that induced by changing the teleost fish ambient temperature.

As shown with the study of changing chronic and acute temperature in Chapter 4 and 5, respectively, the mechanisms underlying cardiac arrhythmias can be complex. As the effects of altered environment temperature can modulate individual ion channels leading to a higher vulnerability to irregular heart rhythms or conduction patterns. It could be very difficult to reproduce this phenomenon without the using of the detailed cell models for computer simulations as these can have effects on both current magnitudes, and current kinetics.

Moreover, physiologically detailed models of the APs, accurate and detailed tissue reconstructions are required for experimentally relevant simulations. It is especially true in the ventricle, where the anatomy is complex with very trabecular structures.

The platform presented in most work done in this thesis contains both detailed electrophysiological models at different temperature, those models are specific to the teleost fish, in addition to a detailed anatomically accurate reconstruction of the teleost ventricle. This platform is therefore well suited for the study of ventricle arrhythmias under global warming condition.

8.2.4 Chapter 7: Hypertension Effects on the Contractile Function of the Human Left Ventricle Using a Multi-Dimensional Electromechanics Model

8.2.4.1 Hypertension Effects on Human Left Ventricular

8.2.4.1.1 At Single Cell Level

In the present Chapter, the using of ORd electromechanical model of human ventricular cells under Sham (control) and hypertension (HP) conditions based on experimental data from rat ventricular cells from Jin et al. [202]. The LV hypertrophy (induced by HP) model was modelled following the work of Kharche et al. [206]. The electromechanical model combined hypertrophy model was used to investigate the effects of HP on the LV of human heart.

Single cell simulations of the human LV showed that under HP condition: A) without I_{sac} effects; 1) the EC_{50} value increased due to a right shift in the relaxation phase of the normalised active force–$[\mathrm{Ca}^{2+}]_\mathrm{i}$ relation curve indicating a reduction in the myofilament sensitivity to $[\mathrm{Ca}^{2+}]_\mathrm{i}$ [202, 226, 227], 2) APD_{90} was prolonged, 3) $[\mathrm{Ca}^{2+}]_\mathrm{i}$ was increased while the relaxation and the time decay of $[\mathrm{Ca}^{2+}]_\mathrm{i}$ were faster, 4) the SL as well as the active (contractile) force unchanged, suggesting that HP condition might not modulate the contraction of the LV cardiac cells, however, the time course of SL and the normalised active force decreased in the HP condition which might be resulted from the faster time constant decay of $[\mathrm{Ca}^{2+}]_\mathrm{i}$. These simulations showed qualitatively analogous results which were in a good agreement to the relative experimental data from rat ventricular myocytes reported in [202] (Figure 7.3 and 7.4). B) with $\mathrm{I_{sac}}$ effects; 1) a moderate prolongation in the $\mathrm{APD_{90}}$, 2) increased amplitude of the intracellular $[\mathrm{Ca^{2+}}]_\mathrm{i}$, 3) shortened the time course of the sarcomere length and the active force under both Sham and HP conditions (Figures 7.5 and 7.6). These effects are similar to those reported experimentally from [238].

It has been found that in human ventricle, the mechanical stretch induced ventricular arrhythmias with consequent ventricular fibrillation leading to sudden cardiac death. This indicates that the hypertrophic remodeling which results from hypertension can strongly increase the risk for stretch induced arrhythmias [238].

8.2.4.1.2 At 1D Tissue Strand

QT interval of the electrocardiogram (ECG) was calculated under Sham and hypertension conditions using the 1D strand model of LV cells. Simulations showed that QT prolonged under HP condition compared to the Sham condition (Figure 7.10). In hypertensive patients, it has been found that the long QT syndrome (LQTS) is associated with proarrhythmic implications including the risk of ventricular fibrillation and a high risk of cardiovascular events (CVE). This is associated with the left ventricular hypertrophy (LVH) under HP condition [236, 247].

8.2.4.1.2 At 2D Tissue

The two-dimensional (2D) ventricular electromechanics model was updated with the new modifications of the single cell electromechanics models under Sham and HP conditions. Then it used to study the re-entrant excitation wave under these conditions.

In the 2D tissue simulations, HP condition induced an early initiation of the re-entrant excitation wave due to the tissue's VW to the genesis of unidirectional conduction was slightly protracted and delayed in timing. This resulted in the formation of spiral re-entrant excitation wave in both Sham and HP conditions, which self-terminated under the Sham condition but was sustained longer for the HP condition. Thus these simulations suggest that in the HP condition, there is a greater susceptibility to ventricular arrhythmia.

8.2.4.2 Novelty and Relevance to Previous Studies

The study in the present Chapter highlights the role of hypertension condition and related hypertrophy in modulations of ventricular contractility of human heart. It also represents to the best of the author's knowledge, the first attempt to investigate such modulations using biophysically electromechanics detailed models at cellular and tissue levels. Simulation results help to increase our understanding on the hypertension roles and relevant hypertrophy in hypertensive patients.

The functional role of HP condition in human ventricles have been performed in some previous studies [52, 241–243], however, these studies focused on the modulations impact of HP on the electrical activities of the ventricle without considering either ventricle hypertrophy or ventricle contractile functions. Therefore, the current study investigates the effects of HP condition on the human left ventricular contraction using a model that includes both the electromechanics features and hypertrophy properties. Simulation results offered a well understanding of mechanistic insights into the inotropic effects of HP condition on LV which are in a fair close to those observed experimentally [120, 202, 227].

8.3 Future Work

The work presented in this thesis poses some interesting research questions for future investigations. The most fundamental ones are discussed here:

In Chapter 4, although the single cell models were based on electrophysiology experiment records of teleost ventricles for the main ionic currents, other currents, such as I_{NaCa}, I_{CaT} and $I_{Ks,}$ need to be experimentally examined to assess whether or not they exist in the teleost heart; then, the possible effects of changing temperatures on such currents and how they can regulate the AP morphology need to be investigated. This would provide comprehensive information regarding the individual ionic currents underlying the AP for teleost ventricular cells. Additionally, the concentrations of intracellular and extracellular ions might differ at changing temperatures or from once species to another; this would affect the relative currents and thus the cell membrane stability. Therefore, it is crucial to take the potential variation of the ionic concentrations under different temperatures for future investigations.

Furthermore, in the developed models, the description of the Ca^{2+} handling mechanism in the SR is adapted from an existing quantitative model of the mammal ventricular cell resulting in a higher Ca^{2+} transient amplitude. Therefore, developing a good model for the Ca^{2+} transient based on experimental electrophysiology data of fish ventricle can solve this and then be used to investigate the mechanical contraction function of the teleost ventricular at different temperatures.

In Chapter 5, for the 1D strand tissue model, the ventricular tissue was considered as a homogeneous tissue. This was similar to Chapter 6, where, for developing the 3D model, the ventricular tissue was considered isotropic media (in the absence of the fibre orientation). Both 1D and 3D models did not consider the potential heterogeneity of the ventricle tissue, which may play a vital role in the propagation of the electrical excitation wave and therefore warrants further investigations.

At present, there are insufficient experimental data for all teleost fish ventricular properties at different temperatures. However, simulation results of the present thesis form a basis for further research by experimentalists and mathematical modellers, out of which, over the next few years, a clearer picture will emerge.

The simulation in Chapter 7 assumed that the hypertrophy induced by the HP condition modulated alterations to some ion channel currents including I_{Na}, I_{to} and I_{NaCa} without consideration of the probable alterations to other currents in the model.

Mechanoelectrical feedback has been proposed in the contribution of other effects such as changes in the intracellular Ca^{2+} handling system which were induced by stretch and the ventricular cells interactions while fibroblasts were not taking in the consideration. Therefore, to validate such assumptions, it warrants further investigations.

8.4 Closing Words

The work presented in this thesis has provided novel teleost fish ventricular cell models at thermal acclimation and thermal tolerance of the fish heart. These models have been used to investigate possible effects of changes in the ambient chronic and acute temperature in the fish environment on the function of their heart. In the light of the worldwide problem of changing climate and global warming, computational modelling is expected to play an unparalleled role in investigating the underlying mechanisms of rising the water temperature on the cardiac function of the fish heart, which may threat the fish species population as well as their lives. The teleost cardiac models carried out at single cell, 1D tissue strand and 3D tissue whole organ levels, which represents to the best of the author's knowledge, the first attempt to develop such models for the fish heart.

This thesis also includes a work for investigating the mechanisms of hypertension condition and associated left ventricle (LV) hypertrophy in modulations of ventricular contractility of human heart. It is the first to use biophysically electromechanics detailed models at cellular and tissue levels for such investigations. Simulation results help to advance understanding of the hypertension roles and relevant hypertrophy in hypertensive patients.

In summary, the work presented in this thesis represents a significant advance in the cardiac modelling of the vertebrate and mammal's heart.

9. Appendix

9.1 Teleost Fish Single Cell Model Equations

This section includes all of the equations used in the single cell models at cold and warm acclimation. Here, equations for all models at 11°C CA, 11°C WA and 18°C are shown below:

9.1.1 Total Ionic Membrane Current

$$I_{ion,tot} = I_{Na} + I_{CaL} + I_{Kr} + I_{K1} + I_{Cab} + I_{Nab} + \tag{9.1}$$

$$I_{Kp} + I_{pCa} + I_{K(ATP)} + I_{NaCa} + I_{NaK}$$

9.1.2 Ion Concentrations

$$\frac{d[Na]_i}{dt} = \frac{-3I_{NaK} - 3I_{NaCa} - I_{Nab} - I_{Na}}{FV_i} \tag{9.2}$$

$$\frac{d[K]_i}{dt} = \frac{2I_{NaK} - I_{K1} - I_{to} - I_{Kur} - I_{Kr} - I_{Ks} - I_{stim}}{FV_i} \tag{9.3}$$

$$\frac{d[Ca]_i}{dt} = \frac{2I_{NaCa} - I_{pCa} - I_{CaL} - I_{Cab}}{2FV_i} + \frac{V_{up}\left(I_{upleak} - I_{up}\right) + (V_{rel} I_{rel})}{V_i} - [Trpn]_{max} \frac{d[Ca]_{Trpn}}{dt} -$$

$$[Cmdn]_{max} \frac{d[Ca]_{Cmdn}}{dt} \tag{9.4}$$

$$\frac{d[Ca]_{up}}{dt} = I_{up} - I_{upleak} - I_{tr} \frac{V_{rel}}{V_{up}} \tag{9.5}$$

$$\frac{d[Ca]_{rel}}{dt} = I_{tr} - I_{rel} - 31.0 \frac{d[Ca]_{Csqn}}{dt} \tag{9.6}$$

9.1.3 Equilibrium Potentials

$$E_{Na} = \left(\frac{\mathrm{RT}}{\mathrm{F}}\right).\log\frac{[\mathrm{Na}^{+}]_{\mathrm{i}}}{[\mathrm{Na}^{+}]_{\mathrm{o}}} \tag{9.7}$$

$$E_K = \left(\frac{\mathrm{RT}}{\mathrm{F}}\right).\log\frac{[\mathrm{K}^+]_\mathrm{i}}{[\mathrm{K}^+]_\mathrm{o}} \tag{9.8}$$

$$E_{Ca} = \left(\frac{\mathrm{RT}}{\mathrm{F}}\right).\log\frac{[\mathrm{Ca}^{2+}]_\mathrm{i}}{[\mathrm{Ca}^{2+}]_\mathrm{o}} \tag{9.9}$$

9.1.4 Fast Na^+ Current, I_{Na}

$$I_{Na} = g_{Na}\,.m^3.h.(v - E_{Na}) \tag{9.10}$$

$$\alpha_\mathrm{m} = \begin{cases} \frac{0.32(\mathrm{v}+57.13)}{1-\exp(-0.1(\mathrm{v}+57.13))} & For\ 4°\mathrm{C} \\ \frac{0.32(\mathrm{v}+65.13)}{1-\exp(-0.1(\mathrm{v}+65.13))} & For\ 11°\mathrm{C}\ CA \\ \frac{0.32(\mathrm{v}+60.13)}{1-\exp(-0.1(\mathrm{v}+60.13))} & For\ 11°\mathrm{C}\ WA \\ \frac{0.32(\mathrm{v}+60.13)}{1-\exp(-0.1(\mathrm{v}+60.13))} & For\ 18°\mathrm{C} \end{cases} \tag{9.11}$$

$$\beta_\mathrm{m} = \begin{cases} 0.08\exp\left(\frac{(\mathrm{v}+6)}{-11}\right) & For\ 4°\mathrm{C} \\ 0.14\exp\left(\frac{(v+15)}{-11}\right) & For\ 11°\mathrm{C}\ CA \\ 0.085\exp\left(\frac{(v+5)}{-11}\right) & For\ 11°\mathrm{C}\ WA \\ 0.08\exp((v+6)/-11) & For\ 18°\mathrm{C} \end{cases} \tag{9.12}$$

$$m_\infty = \frac{\alpha_m}{(\alpha_m+\beta_m)} \tag{9.13}$$

$$\tau_m = \frac{1}{(\alpha_m+\beta_m)} \tag{9.14}$$

$$\frac{dm}{dt} = \frac{m_\infty - m}{\tau_m} \tag{9.15}$$

$$\alpha_h = \begin{cases} 0.0 & For\ \ V\ \ >= -40\ mV \\ 0.135\ exp((V+90)/-6.8) & For\ \ \mathrm{V}\ < \ -40\ \mathrm{mV} \end{cases} \tag{9.16}$$

$$\beta_h = \begin{cases} \frac{0.8}{0.12(1+\exp((V+30.66)/-11))} & For\ \ V\ \geq -40\ mV \\ 3.56\exp(0.08V) + 3.1\times10^5\exp(0.35V) & For\ \ \mathrm{V}\ <\ -40\ \mathrm{mV} \end{cases} \tag{9.17}$$

$$h_\infty = \frac{\alpha_h}{(\alpha_h+\beta_h)} \tag{9.18}$$

$$\tau_h = \frac{1}{(\alpha_h+\beta_h)} \tag{9.19}$$

$$\frac{dh}{dt} = \frac{h_\infty - h}{\tau_h} \tag{9.20}$$

9.1.5 L-Type Ca^{2+} Current, I_{CaL}

$$I_{CaL} = g_{CaL}.d.f.f_{Ca}.(V-65) \tag{9.21}$$

$$d_\infty = \begin{cases} \frac{0.9}{1+\exp\left(\frac{V+10}{-6}\right)} & For\ 4\text{°C} \\ \frac{1}{1+\exp\left(\frac{V+15}{-9}\right)} & For\ 11\text{°C}\ CA \\ \frac{1}{1+\exp\left(\frac{V+15}{-6}\right)} & For\ 11\text{°C}\ WA \\ \frac{0.67}{1+\exp\left(\frac{V+15}{-6}\right)} & For\ 18\text{°C} \end{cases} \tag{9.22}$$

$$\tau_d = \begin{cases} \frac{1-0.16\,exp\ \left(\frac{(V+10)}{-6.24}\right)}{0.035(v+10)[(0.16\exp((V+10)/-6.24))+(1+\exp\ (v+10)/-6.24)]} & For\ 4\text{°C} \\ \frac{1-0.16\,exp\ \left(\frac{(V+15)}{-6.24}\right)}{0.035(v+15)[(0.16\exp((V+15)/-6.24))+(1+\exp\ (v+15)/-6.24)]} & For\ other\ models \end{cases} \tag{9.23}$$

$$E_{Ca} = 65\ \mathrm{mV}$$

$$\frac{dd}{dt} = \frac{d_\infty - d}{\tau_d} \tag{9.24}$$

$$f_\infty = \frac{1}{1+\exp((V+20.6)/6.2)} \tag{9.25}$$

$$\tau_{f,slow} = \begin{cases} 600\{1+0.1.exp[-0.0007(V-9)^2]\}^{-1} & For\ 4\text{°C} \\ 700\{1+0.1.exp[-0.0007(V-9)^2]\}^{-1} & For\ 18\text{°C} \end{cases} \tag{9.26}$$

$$\tau_{f,fast} = \begin{cases} 300\{1 + 0.1.exp[-0.0007(v-4)^2]\}^{-1} \;\; For\ 4℃ \\ 400\{1 + 0.1.exp[-0.0007(v-4)^2]\}^{-1} \;\; For\ 18℃ \end{cases} \tag{9.27}$$

$$\frac{df_{fast}}{dt} = \frac{f_\infty - f_{fast}}{\tau_{f,fast}} \tag{9.28}$$

$$\frac{df_{slow}}{dt} = \frac{f_\infty - f_{slow}}{\tau_{f,slow}} \tag{9.29}$$

$$f_{ca} = 0.29 + 0.8\left[1 + exp\left(\frac{[Ca^{2+}]_i - 0.12}{0.6}\right)\right]^{-1} \tag{9.30}$$

$$\tau_f = \begin{cases} 500\{1 + 0.1.exp[-0.0007(v-9)^2]\}^{-1} \;\; For\ 11℃\ CA \\ 600\{1 + 0.1.exp[-0.0007(v-9)^2]\}^{-1} \; For\ 11℃\ WA \end{cases} \tag{9.31}$$

$$A_{f,fast} = 0.64,\ A_{f,slow} = 1 - A_{f,fast} \;\; \text{at } 4℃ \tag{9.32}$$

$$A_{f,fast} = 0.44,\ A_{f,slow} = 1 - A_{f,fast} \;\; \text{at } 18℃ \tag{9.33}$$

$$f = A_{f,fast} \cdot f_{fast} + A_{f,slow} \cdot f_{slow} \tag{9.34}$$

$$\frac{df}{dt} = \frac{f_\infty - f}{\tau_f} \tag{9.35}$$

9.1.6 Rapid Delayed Rectifier K^+ Current, I_{Kr}

$$r = \begin{cases} \dfrac{1}{1+exp\left(\frac{v+15}{22.4}\right)} & For\ 4℃ \\ \dfrac{1}{1+exp\left(\frac{v-63.4}{176.3}\right)} & For\ 11℃\ CA\ and\ WA \\ \dfrac{1}{1+exp((v-63.01)/178.3)} & For\ 18℃ \end{cases} \tag{9.36}$$

$$xr_\infty = \begin{cases} \dfrac{1}{1+exp\left(\frac{v+16.1}{-9.5}\right)} & For\ 4℃ \\ \dfrac{1}{1+exp((v+9.7)/-16.3)} & For\ other\ models \end{cases} \tag{9.37}$$

$$\alpha_r = \begin{cases} \frac{0.3\times10^{-5}(v+13.1)}{1-exp\left(\frac{v+5.0}{-3.3}\right)} \quad For\ 4℃ \\ \frac{1.05\times10^{-5}(v-2.45)}{1-exp\left(\frac{v-2.45}{-0.8}\right)} \quad For\ 11℃\ CA\ and\ WA \\ \frac{1.02\times10^{-5}(v-2.4)}{1-exp((v-2.45)/-0.7)} \quad For\ 18℃ \end{cases} \tag{9.38}$$

$$\beta_r = \begin{cases} \frac{7.4\times10^{-5}(v-328)}{exp\left(\frac{v-328}{5.1}\right)-1} \quad For\ 4℃ \\ \frac{7.4\times10^{-5}(v+4.8)}{exp\left(\frac{v+4.8}{35.3}\right)-1} \quad For\ other\ model \end{cases} \tag{9.39}$$

$$\tau_{xr} = \frac{1}{\alpha_r+\beta_r} \tag{9.40}$$

$$\frac{dxr}{dt} = \frac{xr_{\infty}-xr}{\tau_{xr}} \tag{9.41}$$

9.1.7 Inwardly Rectifying K$^+$ Current, I_{K1}

$$I_{K1} = g_{K1}.K.(v-E_K) \tag{9.42}$$

$$\alpha_K = \begin{cases} \frac{1}{1+exp\left(0.014(v-E_K+7.21)\right)} \quad For\ 4℃\ and\ 11℃\ CA \\ \frac{1}{1+exp\left(0.014(v-E_K+25.21)\right)} \quad for\ 11℃\ WA\ and\ 18℃ \end{cases} \tag{9.43}$$

$$\beta_K = \begin{cases} \frac{0.4\ exp\left(0.07(v-E_K+0.57)\right)+exp\left(0.06(v-E_K+584.31)\right)}{1+exp\left(-0.5(v-E_K+4.35)\right)} \quad For\ 4℃ \\ \frac{0.5\ exp\left(0.07(v-E_K+0.57)\right)+exp\left(0.058(v-E_K+584.31)\right)}{1+exp\left(-0.5(v-E_K+4.35)\right)} \quad For\ 11℃\ CA \\ \frac{0.4\ exp\left(0.075(v-E_K+5.0)\right)+exp\left(0.058(v-E_K+584.31)\right)}{1+exp\left(-0.5(v-E_K+4.35)\right)} \quad For\ 11℃\ WA \\ \frac{0.39\ exp\left(0.075(v-E_K+4.97)\right)+exp\left(0.06(v-E_K+584.31)\right)}{1+exp\left(-0.5(v-E_K+4.35)\right)} \quad For\ 18℃ \end{cases} \tag{9.44}$$

$$K = \frac{\alpha_K}{\alpha_K+\beta_K} \tag{9.45}$$

9.1.8 Plateau K$^+$ Current, $\boldsymbol{I_{Kp}}$

$$I_{Kp} = g_{Kp}.K_p.\left(V - E_{Kp}\right) \tag{9.46}$$

$$E_{Kp} = E_{K1}$$

$$K_p = 1/\{1 + exp[(7.488 - V)/5.98]\} \tag{9.47}$$

9.1.9 Na$^+$/Ca$^+$ Exchanger Current, $\boldsymbol{I_{NaCa}}$

$$I_{NaCa} = K_{NaCa}.\frac{1}{K_{m,Na}^3 + [Na^+]_o^3}.\frac{1}{K_{m,Ca} + [Ca^{2+}]_o}.\frac{1}{1 + K_{sat}.exp\left[(\eta - 1).V.\frac{F}{RT}\right]}$$
$$.\left\{exp\left(\eta.V.\frac{F}{RT}\right)[Na^+]_i^3.[Ca^{2+}]_o - exp\left[(\eta - 1).V.\frac{F}{RT}\right][Na^+]_o^3.[Ca^{2+}]_i\right\} \tag{9.48}$$

9.1.10 Na$^+$/K$^+$ Pump Current, $\boldsymbol{I_{NaK}}$

$$I_{NaK} = \bar{I}_{NaK}.f_{NaK}.\frac{1}{1+\left(K_{m,Nai}/[Na^+]_i\right)^{1.5}}.\frac{[K^+]_o}{[K^+]_o+K_{m,Ko}} \tag{9.49}$$

$$f_{NaK} = \frac{1}{1+0.1245.exp\left(-0.1.\frac{VF}{RT}\right)+0.0365.\sigma.exp\left(-\frac{VF}{RT}\right)} \tag{9.50}$$

$$\sigma = \frac{1}{7}.\left[exp\left(\frac{[Na^+]_o}{67.3}\right) - 1\right] \tag{9.51}$$

σ: is the $[Na^+]_o$-dependence factor of f_{NaK}

9.1.11 Background $\boldsymbol{Na^+}$ and $\boldsymbol{Ca^{2+}}$ Currents, $\boldsymbol{I_{bNa}}$ and $\boldsymbol{I_{bCa}}$

$$I_{bNa} = g_{b,Na}(V - E_{Na}) \tag{9.52}$$

$$I_{bCa} = g_{b,Ca}(V - E_{Ca}) \tag{9.53}$$

9.1.12 Intracellular Ca^{2+} Dynamics

$$I_{pCa} = \bar{I}_{p(Ca)} . \frac{[Ca^{2+}]_i}{K_{m,p(Ca)} + [Ca^{2+}]_i} \tag{9.54}$$

$$I_{up} = \bar{I}_{up} . [Ca^{2+}]_i / \left([Ca^{2+}]_i + K_{m,up}\right) \tag{9.55}$$

$$\mathrm{I}_{\mathrm{upleak}} = \mathrm{K}_{\mathrm{leak}} . [Ca^{2+}]_{NSR} \tag{9.56}$$

$$\mathrm{K}_{\mathrm{leak}} = \bar{\mathrm{I}}_{\mathrm{up}} / \overline{[\mathrm{Ca}^{2+}]}_{NSR} \tag{9.57}$$

$$\mathrm{I}_{\mathrm{tr}} = \left([\mathrm{Ca}^{2+}]_{\mathrm{NSR}} - [\mathrm{Ca}^{2+}]_{\mathrm{JSR}}\right) / \tau_{\mathrm{tr}} \tag{9.58}$$

$$\mathrm{I}_{\mathrm{rel}} = \mathrm{G}_{\mathrm{rel}} . \left([\mathrm{Ca}^{2+}]_{\mathrm{JSR}} - [\mathrm{Ca}^{2+}]_{\mathrm{i}}\right) \tag{9.59}$$

$$\mathrm{G}_{\mathrm{rel}} = \bar{\mathrm{G}}_{\mathrm{rel}} . \frac{\Delta[\mathrm{Ca}^{2+}]_{\mathrm{i,2}} - \Delta[\mathrm{Ca}^{2+}]_{\mathrm{i,th}}}{\mathrm{K}_{\mathrm{m,rel}} + \Delta[\mathrm{Ca}^{2+}]_{\mathrm{i,2}} - \Delta[\mathrm{Ca}^{2+}]_{\mathrm{i,th}}} . (1 - \exp[-\mathrm{t}/\tau_{\mathrm{on}}]) . \exp[-\mathrm{t}/\tau_{\mathrm{off}}] \tag{9.60}$$

9.1.13 Ca^{2+} Buffers in the Myoplasm

$$\text{Buffered [TRPN]} = \overline{[\mathrm{TRPN}]} . \left\{[\mathrm{Ca}^{2+}]_{\mathrm{i}} / \left([\mathrm{Ca}^{2+}]_{\mathrm{i}} + \mathrm{K}_{\mathrm{m,TRPN}}\right)\right\} \tag{9.61}$$

$$\text{Buffered } [CMDN] = \overline{[CMDN]} . \left\{[Ca^{2+}]_i / \left([Ca^{2+}]_i + K_{m,CMDN}\right)\right\} \tag{9.62}$$

$$\text{Buffered[CSQN]} = [\overline{\mathrm{CSQN}}] . \left\{[\mathrm{Ca}^{2+}]_{\mathrm{JSR}} / \left([\mathrm{Ca}^{2+}]_{\mathrm{JSR}} + \mathrm{K}_{\mathrm{m,CSQN}}\right)\right\} \tag{9.63}$$

9.2 Models Constants

Table 9.1: The constants parameters of all models at cold and warm acclimation.

Model parameter	**Value**	**Definition**
$\mathrm{K_{m,Ca}}$	0.0006 mM	Half-saturation concentration of Ca^{2+} channel
$\mathrm{K_{atp}}$	0.250 mM	Half-maximal saturation point of ATP-sensitive K current
$\mathrm{I_{NaCa}^{max}}$	1.0 $\mathrm{pA/pF}$	Maximum Na^{+}/Ca^{2+}exchange current
$\mathrm{K_{NaCa}}$	0.00025 $\mathrm{pA/pF}$	Scaling factor of Na^{+}/Ca^{2+}exchange
$\mathrm{K_{m,Na}}$	1.0 mM	Na^{+} half-saturation constant for Na^{+}/Ca^{2+}exchange
$\mathrm{K_{m,Ca}}$	1.0 mM	Ca^{+} half-saturation constant for Na^{+}/Ca^{2+}exchange
$\mathrm{K_{sat}}$	1.0	Na^{+}/Ca^{2+}exchange saturation factor at very negative potentials
$\mathrm{I_{NaK}^{max}}$	2.25 $\mathrm{pA/pF}$	Maximum Na^{+}/K^{+} pump current
$\mathrm{K_{m,Nai}}$	10 mM	Na^{+} half-saturation constant for pump current
$\mathrm{K_{m,Ko}}$	1.5 mM	K^{+} half-saturation constant for Na^{+}/K^{+}exchange current
$\mathrm{I_{pCa}^{max}}$	1.15 $\mathrm{pA/pF}$	Maximum Ca^{2+} pump current
$\mathrm{K_{m,p(Ca)}}$	0.5 mM	Ca^{2+} half-saturation constant for Ca^{2+} pump
$[\overline{\mathrm{TRPN}}]$	70 µM	Maximum Troponin, Ca^{2+} buffer in the myoplasm
$\overline{[\mathrm{CMDN}]}$	50 µM	Maximum Calmodulin, Ca^{2+} buffer in the myoplasm
$\mathrm{K_{m,TRPN}}$	0.5 µM	Half-saturation concentration of Troponin
$\mathrm{K_{m,CMDN}}$	2.38 µM	Half-saturation concentration of CMDN
$\Delta[\mathrm{Ca^{2+}}]_{\mathrm{i,th}}$	0.18 µM	Threshold for external triggering of Ca^{2+} release from JSR
$\mathrm{K_{m,rel}}$	0.08 µM	Half-saturation concentration of Ca^{2+} release from JSR to myoplasm
τ_{on}	2 ms	Time constants of activating (on) Ca^{2+} release from JSR
τ_{off}	2 ms	Time constants of deactivating (off) Ca^{2+} release from JSR
$[\overline{\mathrm{CSQN}}]$	10 mM	Threshold of Ca^{2+}-bound [CSQN] for internal triggering of Ca^{2+} release from JSR under Ca^{2+}-overload conditions

$K_{m,CSQN}$	0.8 mM	Half-saturation concentration of $CSQN$
$K_{m,up}$	0.92 μM	Half-saturation concentration of Ca^{2+} fluxes from the cytosol to the network sarcoplasmic reticulum (SR)
$\bar{I}_{up}$	0.005 μM	Ca^{2+} fluxes from the cytosol to the network sarcoplasmic reticulum (SR)
$\overline{[Ca^{2+}]}_{NSR}$	15 mM	Maximum translocation of Ca^{2+} ions from NSR to JSR
τ_{tr}	180 ms	Ca^{2+} flux from the network SR (NSR) to junctional SR (JSR)

References

[1] Arts T, Reneman RS, Veenstra PC. A model of the mechanics of the left ventricle. *Annals of Biomedical Engineering* 1979; **7**: 299–318.

[2] Dyer LA, Kirby ML. The role of secondary heart field in cardiac development. *Dev Biol* 2009; **336**: 137–144.

[3] Qu Z, Hu G, Garfinkel A, et al. Nonlinear and stochastic dynamics in the heart. *Physics Reports* 2014; **543**: 61–162.

[4] Stephenson A, Adams JW, Vaccarezza M. The vertebrate heart: an evolutionary perspective. *J Anat* 2017; **231**: 787–797.

[5] Onai T. The evolutionary origin of chordate segmentation: revisiting the enterocoel theory. *Theory Biosci* 2018; **137**: 1–16.

[6] Zhang Z-Q. Animal biodiversity: An update of classification and diversity in 2013. In: Zhang, Z.-Q. (Ed.) Animal Biodiversity: An outline of higher-level classification and survey of Taxonomic Richness (Addenda 2013). *Zootaxa* 2013; **3703**: 5–11.

[7] Katz AM. Physiology of the heart, en. Fifth. Lippincott Williams & Wilkins, 2010.

[8] Huxley AF, Niedergerke R. Structural changes in muscle during contraction: Interference microscopy of living muscle fibres. *Nature* 1954; **173**: 971–973.

[9] Noble D. A modification of the Hodgkin-Huxley equations applicable to Purkinje fibre action and pacemaker potentials. *The Journal of Physiology* 1962; **160**: 317–352.

[10] Huxley H, Hanson J. Changes in the cross-striations of muscle during contraction and stretch and their structural interpretation. *Nature* 1954; **173**: 973–976.

[11] Farrell AP. Environment, antecedents and climate change: lessons from the study of temperature physiology and river migration of salmonids. *Journal of Experimental Biology* 2009; **212**: 3771–3780.

[12] Gulzar, A. & Mehmood, M. & Ganie, S. & Showqi, I. A Brief review on global warming and climate change: consequences and mitigation strategies. *International Journal of Advance Research in Science and Engineering* 2018; **07**: 2146–2156.

[13] Williams SE, Bolitho EE, Fox S. Climate change in Australian tropical rainforests: an impending environmental catastrophe. *Proceedings of the Royal Society of London Series B: Biological Sciences* 2003; **270**: 1887–1892.

[14] Aho E, Vornanen M. Contractile properties of thermally acclimated trout heart. *The Journal of Experimental Biology* 1999; **202**: 2663–2677.

[15] Hassinen M, Paajanen V, Haverinen J, et al. Cloning and expression of cardiac $K_{ir}2.1$ and $K_{ir}2.2$ channels in thermally acclimated rainbow trout. *American Journal of Physiology-Regulatory, Integrative and Comparative Physiology* 2007; **292**: R2328–R2339.

[16] Portner HO, Knust R. Climate change affects marine fishes through the Oxygen limitation of thermal tolerance. *Science* 2007; **315**: 95–97.

[17] Vornanen M, Haverinen J, Egginton S. Acute heat tolerance of cardiac excitation in the brown trout (Salmo trutta fario). *Journal of Experimental Biology* 2014; **217**: 299–309.

[18] Deutsch CA, Tewksbury JJ, Huey RB, et al. Impacts of climate warming on terrestrial ectotherms across latitude. *Proceedings of the National Academy of Sciences* 2008; **105**: 6668–6672.

[19] Bolis CL, Piccolella M, Dalla Valle AZ, et al. Fish as model in pharmacological and biological research. *Pharmacological Research* 2001; **44**: 265–280.

[20] Haverinen J, Vornanen M. Temperature acclimation modifies sinoatrial pacemaker mechanism of the rainbow trout heart. *American Journal of Physiology-Regulatory, Integrative and Comparative Physiology* 2007; **292**: R1023–R1032.

[21] Nguyen KDT, Morley SA, Lai C-H, et al. Upper temperature limits of tropical marine ectotherms: global warming implications. *PLoS ONE* 2011; **6**: e29340.

[22] Luís S, Vauclair C-M, Lima ML. Raising awareness of climate change causes? cross-national evidence for the normalization of societal risk perception of climate change. *Environmental Science & Policy* 2018; **80**: 74–81.

[23] Tylianakis JM, Didham RK, Bascompte J, et al. Global change and species interactions in terrestrial ecosystems. *Ecology Letters* 2008; **11**: 1351–1363.

[24] Parry ML, Rosenzweig C, Iglesias A, et al. Effects of climate change on global food production under SRES emissions and socio-economic scenarios. *Global Environmental Change* 2004; **14**: 53–67.

[25] Lejeusne C, Chevaldonné P, Pergent-Martini C, et al. Climate change effects on a miniature ocean: the highly diverse, highly impacted Mediterranean Sea. *Trends in Ecology & Evolution* 2010; **25**: 250–260.

[26] Bale JS, Masters GJ, Hodkinson ID, et al. Herbivory in global climate change research: direct effects of rising temperature on insect herbivores. *Global Change Biology* 2002; **8**: 1–16.

[27] Kheshgi HS, Jain AK. Projecting future climate change: Implications of carbon cyclemodel intercomparisons. *Global Biogeochemical Cycles* 2003; **17**: 1047. DOI: 10.1029/2001gb001842.

[28] SVS: Global temperature anomalies from 1880 to 2018, https://svs.gsfc.nasa.gov/cgi-bin/details.cgi?aid=4626. (Accessed 14 August 2019).

[29] https://data.giss.nasa.gov/gistemp/graphs/ (Accessed 17 July 2019).

[30] Vornanen M. The temperature dependence of electrical excitability in fish hearts. *The Journal of Experimental Biology* 2016; **219**: 1941–1952.

[31] Ekström A. Thermal tolerance in teleost fish: importance of cardiac oxygen supply, ATP production and autonomic control. Department of biological and environmental sciences, Faculty of Science, University of Gothenburg, 2017.

[32] Somero GN. The physiology of climate change: how potentials for acclimatization and genetic adaptation will determine 'winners' and 'losers'. *Journal of Experimental Biology* 2010; **213**: 912–920.

[33] Keen AN, Klaiman JM, Shiels HA, et al. Temperature-induced cardiac remodelling in fish. *The Journal of Experimental Biology* 2017; **220**: 147–160.

[34] https://www.thoughtco.com/cartilaginous-fishes-129756 (Accessed 17 July 2019).

[35] http://abacus.bates.edu/acad/depts/biobook/Pal02pix.htm (Accessed 17 July 2019).

[36] https://sites.google.com/site/animalbiologyspring2011/home/lobe-finned-fish-coelacanth (Accessed 17 July 2019).

[37] http://www.seawater.no/fauna/chordata/Actinopterygii.html (Accessed 17 July 2019).

[38] http://ourmarinespecies.com/c-tuna/tuna-fish/ (Accessed 17 July 2019).

[39] Coyne MD, Kim CS, Cameron JS, et al. Effects of temperature and calcium availability on ventricular myocardium from rainbow trout. *American Journal of Physiology-Regulatory, Integrative and Comparative Physiology* 2000; **278**: R1535–R1544.

[40] Brette F, Luxan G, Cros C, et al. Characterization of isolated ventricular myocytes from adult zebrafish (Danio rerio). *Biochemical and Biophysical Research Communications* 2008; **374**: 143–146.

[41] Hassinen M, Laulaja S, Paajanen V, et al. Thermal adaptation of the crucian carp (*Carassius carassius*) cardiac delayed rectifier current, I_{Ks}, by homomeric assembly of $K_v7.1$ subunits without MinK. *American Journal of Physiology-Regulatory, Integrative and Comparative Physiology* 2011; **301**: R255–R265.

[42] Haverinen J, Vornanen M. Responses of action potential and K^+ currents to temperature acclimation in fish hearts: phylogeny or thermal preferences? *Physiological and Biochemical Zoology* 2009; **82**: 468–482.

[43] Haverinen J, Vornanen M. Temperature acclimation modifies Na^+ current in fish cardiac myocytes. *Journal of Experimental Biology* 2004; **207**: 2823–2833.

[44] Shiels HA, Vornanen M, Farrell AP. Temperature and I_{Ca} in trout heart. *The Journal of*

Experimental Biology 2000; **203**: 2771–2780.

[45] Keen JE, Vianzon D-M, Farrell AP, et al. Effect of temperature and temperature acclimation on the ryanodine sensitivity of the trout myocardium. *Journal of Comparative Physiology B* 1994; **164**: 438–443.

[46] Shiels HA, Galli GLJ. The sarcoplasmic reticulum and the evolution of the vertebrate heart. *Physiology* 2014; **29**: 456–469.

[47] Hodgkin AL, Huxley AF. A quantitative description of membrane current and its application to conduction and excitation in nerve. *The Journal of Physiology* 1952; **117**: 500–544.

[48] Pandit SV, Clark RB, Giles WR, et al. A mathematical model of action potential heterogeneity in adult rat left ventricular myocytes. *Biophysical Journal* 2001; **81**: 3029–3051.

[49] Winslow RL, Scollan DF, Holmes A, et al. Electrophysiological modeling of cardiac ventricular function: from cell to organ. *Annual Review of Biomedical Engineering* 2000; **2**: 119–155.

[50] Butters TD, Aslanidi OV, Zhao J, et al. A novel computational sheep atria model for the study of atrial fibrillation. *Interface Focus* 2013; **3**: 20120067–20120067.

[51] Ramirez RJ, Nattel S, Courtemanche M. Mathematical analysis of canine atrial action potentials: rate, regional factors, and electrical remodeling. *American Journal of Physiology-Heart and Circulatory Physiology* 2000; **279**: H1767–H1785.

[52] Kharche S, Yu J, Lei M, et al. A mathematical model of action potentials of mouse sinoatrial node cells with molecular bases. *American Journal of Physiology-Heart and Circulatory Physiology* 2011; **301**: H945–H963.

[53] Bondarenko VE, Szigeti GP, Bett GCL, et al. Computer model of action potential of mouse ventricular myocytes. *American Journal of Physiology-Heart and Circulatory Physiology* 2004; **287**: H1378–H1403.

[54] Luo CH, Rudy Y. A dynamic model of the cardiac ventricular action potential. I. Simulations of ionic currents and concentration changes. *Circulation Research* 1994; **74**: 1071–1096.

[55] O'Hara T, Virág L, Varró A, et al. Simulation of the undiseased human cardiac ventricular action potential: model formulation and experimental validation. *PLoS Computational Biology* 2011; **7**: e1002061.

[56] Faber GM, Rudy Y. Action potential and contractility changes in $[\mathrm{Na}^+]_i$ overloaded cardiac myocytes: A simulation study. *Biophysical Journal* 2000; **78**: 2392–2404.

[57] Pandit SV, Giles WR, Demir SS. A mathematical model of the electrophysiological alterations in rat ventricular myocytes in Type-I diabetes. *Biophysical Journal* 2003; **84**: 832–841.

[58] Benson AP, Bernus O, Dierckx H, et al. Construction and validation of anisotropic and orthotropic ventricular geometries for quantitative predictive cardiac electrophysiology. *Interface Focus* 2011; **1**: 101–116.

[59] Benson AP, Aslanidi OV, Zhang H, et al. The canine virtual ventricular wall: A platform for dissecting pharmacological effects on propagation and arrhythmogenesis. *Progress in Biophysics and Molecular Biology* 2008; **96**: 187–208.

[60] Aslanidi OV, Nikolaidou T, Jichao Zhao, et al. Application of micro-computed tomography with iodine staining to cardiac imaging, segmentation, and computational model development. *IEEE Transactions on Medical Imaging* 2013; **32**: 8–17.

[61] Cooper D, Turinsky A, Sensen C, et al. Effect of voxel size on 3D micro-CT analysis of cortical bone porosity. *Calcified Tissue International* 2007; **80**: 211–219.

[62] Adeniran I. Modelling the short QT syndrome gene Mutations. *Springer International Publishing* 2014. DOI: 10.1007/978-3-319-07200-5.

[63] Colman MA. Mechanisms of Atrial Arrhythmias. *Springer International Publishing* 2014. DOI: 10.1007/978-3-319-01643-6.

[64] Zhao J, Kharche S, Hansen B, et al. Optimization of catheter ablation of atrial fibrillation: insights gained from clinically-derived computer models. *International Journal of Molecular Sciences* 2015; **16**: 10834–10854.

[65] Davies MR, Wang K, Mirams GR, et al. Recent developments in using mechanistic cardiac modelling for drug safety evaluation. *Drug Discovery Today* 2016; **21**: 924–938.

[66] Clayton RH, Bernus O, Cherry EM, et al. Models of cardiac tissue electrophysiology: Progress, challenges and open questions. *Progress in Biophysics and Molecular Biology* 2011; **104**: 22–48.

[67] Scharm M. Improving reproducibility and reuse of modelling results in the life sciences. The University of Rostock, 2018.

[68] Aslanidi OV, Colman MA, Varela M, et al. Heterogeneous and anisotropic integrative model of pulmonary veins: computational study of arrhythmogenic substrate for atrial fibrillation. *Interface Focus* 2013; **3**: 20120069–20120069.

[69] Vornanen M, Hassinen M. Zebrafish heart as a model for human cardiac electrophysiology. *Channels* 2016; **10**: 101–110.

[70] Bakkers J. Zebrafish as a model to study cardiac development and human cardiac disease. *Cardiovascular Research* 2011; **91**: 279–288.

[71] Dhillon SS, Dóró É, Magyary I, et al. Optimisation of embryonic and larval ECG measurement in zebrafish for quantifying the effect of QT prolonging drugs. *PLoS ONE* 2013; **8**: e60552.

[72] Grunow B, Mohamet L, Shiels HA. Generating an in vitro 3D cell culture model from zebrafish larvae for heart research. *Journal of Experimental Biology* 2015; **218**: 1116–1121.

[73] Nemtsas P, Wettwer E, Christ T, et al. Adult zebrafish heart as a model for human heart? an electrophysiological study. *Journal of Molecular and Cellular Cardiology* 2010; **48**: 161–171.

[74] Icardo JM. The teleost heart: A morphological approach. In: Sedmera D, Wang T (eds) Ontogeny and phylogeny of the vertebrate heart. *Springer New York* 2012: 35–53.

[75] Icardo JM. Conus arteriosus of the teleost heart: dismissed, but not missed. *The Anatomical Record Part A: Discoveries in Molecular, Cellular, and Evolutionary Biology* 2006; **288A**: 900–908.

[76] Santer RM, Cobb JLS. The fine structure of the heart of the teleost. *Z.Zellforsch* 1972; **131**: 1-14. https://doi.org/10.1007/BF00307196.

[77] Vornanen, M. Electrical excitability of the fish heart and its autonomic regulation. In: Gamperl, A.K., Gillis, T.E., Farrell, A.P., Brauner, C.J. (Eds.), The cardiovascular system: morphology, control and function. *Fish Physiology* 2017; **36A**: 99–153.

[78] Santer RM, Walker MG, Emerson L, et al. On the morphology of the heart ventricle in marine teleost fish (teleostei). *Comparative Biochemistry and Physiology Part A: Physiology* 1983; **76**: 453–457.

[79] Shih J, Fraser SE. Characterizing the zebrafish organizer: microsurgical analysis at the early-shield stage. Development 1996; **122**: 1313-1322.

[80] Tota B. Myoarchitecture and vascularization of the elasmobranch heart ventricle. *Journal of Experimental Zoology* 1989; **252**: 122–135.

[81] Icardo JM, Colvee E. The atrioventricular region of the teleost heart. A distinct heart segment. *The Anatomical Record: Advances in Integrative Anatomy and Evolutionary Biology* 2011; **294**: 236–242.

[82] Moorman AF, Christoffels VM. Cardiac chamber formation: development, genes, evolution. Physiol Rev 2003; **83**:1223–1267.

[83] Sedmera D, Reckova M, deAlmeida A, et al. Functional and morphological evidence for a ventricular conduction system in zebrafish and *Xenopus* hearts. *American Journal of Physiology-Heart and Circulatory Physiology* 2003; **284**: H1152–H1160.

[84] Hu N, Sedmera D, Yost HJ, et al. Structure and function of the developing zebrafish heart. *The Anatomical Record* 2000; **260**: 148–157.

[85] Sanchez-Quintana D, Garcia-Martinez V, Climent V, et al. Morphological analysis of the fish heart ventricle: myocardial and connective tissue architecture in teleost species. *Annals of Anatomy - Anatomischer Anzeiger* 1995; **177**: 267–274.

[86] Tota B, Cimini V, Salvatore G, et al. Comparative study of the arterial and lacunary systems of the ventricular myocardium of elasmobranch and teleost fishes. *American Journal of Anatomy* 1983; **167**: 15–32.

[87] Sedmera D, Wang T (eds). Ontogeny and phylogeny of the vertebrate heart. *Springer New York* 2012. DOI 10.1007/978-1-4614-3387-3.

[88] Farrell AP, Farrell ND, Jourdan H, Cox GK. A Perspective on the Evolution of the Coronary Circulation in Fishes and the Transition to Terrestrial Life. In: Sedmera D., Wang T. (eds) Ontogeny and Phylogeny of the Vertebrate Heart. *Springer New York* 2012: 75–102.

[89] Munshi JSD, Olson KR, Roy PK, et al. Scanning electron microscopy of the heart of the climbing perch. *Journal of Fish Biology* 2001; **59**: 1170–1180.

[90] Gamperl AK. Cardiac plasticity in fishes: environmental influences and intraspecific differences. *Journal of Experimental Biology* 2004; **207**: 2539–2550.

[91] Farrell AP, Gamperl AK, Hicks JMT, et al. Maximum cardiac performance of rainbow trout (oncorhynchus mykiss) at temperatures approaching their upper lethal limit. *The Journal of Experimental Biology* 1995; **199**: 663–672.

[92] Grimes AC, Kirby ML. The outflow tract of the heart in fishes: anatomy, genes and evolution. *Journal of Fish Biology* 2009; **74**: 983–1036.

[93] Icardo JM, Brunelli E, Perrotta I, et al. Ventricle and outflow tract of the African lungfish protopterus dolloi. *Journal of Morphology* 2005; **265**: 43–51.

[94] Montgomery J, Clements K. Disaptation and recovery in the evolution of Antarctic fishes. *Trends in Ecology & Evolution* 2000; **15**: 267–271.

[95] Icardo JM, Colvee E, Cerra MC, et al. The bulbus arteriosus of stenothermal and temperate teleosts: a morphological approach. *Journal of Fish Biology* 2000; **57**: 121–135.

[96] Icardo JM. Bulbus arteriosus of the antarctic teleosts. II. The red-blooded Trematomus bernacchii. *Anat Rec* 1999; **256**:116-26.

[97] Icardo JM, Schib JL, Ojeda JL, et al. The conus valves of the adult gilthead seabream (Sparus auratus). *J. Anat.* 2003; **202**: 537–550.

[98] Sandblom E. The venous circulation in teleost fish: responses to exercise, temperature and hypoxia. Göteborg: Göteborg University, Department of Zoology/Zoophysiology, 2007.

[99] Lai NC, Graham JB, Dalton N, et al. Echocardiographic and Hemodynamic Determinations of the Ventricular Filling Pattern in Some Teleost Fishes. *Physiological Zoology* 1998; **71**: 157–167.

[100] http://www.cardio-research.com/heart-anatomy-on-different-vertebrates (Accessed 17 July 2019).

[101] Nilsson S, Sundin L. Gill Blood Flow Control. *Comparative Biochemistry and Physiology Part A: Molecular & Integrative Physiology* 1998; **119**: 137–147.

[102] Brown H, Difrancesco D. Voltage-clamp investigations of membrane currents underlying pace-maker activity in rabbit sino-atrial node. *The Journal of Physiology* 1980; **308**: 331–351.

[103] Zhang H, Holden AV, Kodama I, et al. Mathematical models of action potentials in the periphery and center of the rabbit sinoatrial node. *American Journal of Physiology-Heart and Circulatory Physiology* 2000; **279**: H397–H421.

[104] Haverinen J, Vornanen M. Significance of Na^+ current in the excitability of atrial and ventricular myocardium of the fish heart. *Journal of Experimental Biology* 2006; **209**: 549–557.

[105] Arreola J, Dirksen RT, Shieh RC, et al. Ca^{2+} current and Ca^{2+} transients under action potential clamp in guinea pig ventricular myocytes. *American Journal of Physiology-Cell Physiology* 1991; **261**: C393–C397.

[106] Shiels HA, Paajanen V and Vornanen M. Sarcolemmal ion currents and sarcoplasmic reticulum Ca^{2+} content in ventricular myocytes from the cold stenothermic fish, the burbot (Lota lota). *Journal of Experimental Biology* 2006; **209**: 3091–3100.

[107] Vornanen M. L-type Ca^{2+} current in fish cardiac myocytes: Effects of thermal acclimation and β-adrenergic stimulation. *The Journal of Experimental Biology* 1998; **201**: 533–547.

[108] Maltsev VA, Vinogradova TM, Lakatta EG. The emergence of a general theory of the initiation and strength of the heartbeat. *Journal of Pharmacological Sciences* 2006; **100**: 338–369.

[109] Graham MS, Farrell AP. The effect of temperature acclimation and adrenaline on the performance of a perfused trout heart. *Physiological Zoology* 1989; **62**: 38–61.

[110] Thonhboon L, Senarat S, Kettratad J, et al. Heart histology of the four chambers in the Spotted scat, Scatophagus argus, during the juvenile stage. Suranaree Journal of Science & Technology 2016; **23**: 429-433.

[111] Shiels HA, Vornanen M, Farrell AP. Effects of temperature on intracellular $[Ca^{2+}]_i$ in trout atrial myocytes. The Journal of Experimental Biology 2002; **205**: 3641–3650.

[112] Whittaker DG. Pathophysiology and pharmacology of short QT syndrome gene mutations in the human atria: Insights from multi-scale computational modelling. The University of Manchester, 2018.

[113] Grandi E, Pasqualini FS, Bers DM. A novel computational model of the human ventricular action potential and Ca^{2+} transient. *Journal of Molecular and Cellular Cardiology* 2010; **48**: 112–121.

[114] Walker CA, Spinale FG. The structure and function of the cardiac myocyte: A review of fundamental concepts. *The Journal of Thoracic and Cardiovascular Surgery* 1999; **118**: 375–382.

[115] https://en.wikipedia.org/w/index.php?title=File:Cell membrane detailed diagram edit2.svg&oldid+531777839 (Accessed 17 July 2019).

[116] Brown H. and Kozlowski R. Physiology and Pharmacology of the Heart, (Paperback), 1997.

[117] http://www.j-circ.or.jp/english/sessions/reports/64th-ss/nerbonne-l1.htm (Accessed 17 July 2019).

[118] Haverinen J, Abramochkin DV, Kamkin A, et al. Maximum heart rate in brown trout (*Salmo trutta fario*) is not limited by firing rate of pacemaker cells. *American Journal of Physiology-Regulatory, Integrative and Comparative Physiology* 2017; **312**: R165–R171.

[119] Huxley AF. Ion movements during nerve activity. *Annals of the New York Academy of Sciences* 1959; **81**: 221–246.

[120] Chen-Izu Y, Chen L, Bányász T, et al. Hypertension-induced remodeling of cardiac excitation-contraction coupling in ventricular myocytes occurs prior to hypertrophy development. *American Journal of Physiology-Heart and Circulatory Physiology* 2007; **293**: H3301–H3310.

[121] Moreno C, Macías Á, Prieto Á, et al. Effects of n−3 Polyunsaturated Fatty Acids on cardiac ion channels. *Frontiers in Physiology* 2012; 3. DOI: 10.3389/fphys.2012.00245.

[122] Bers DM. Cardiac excitation–contraction coupling. *Nature* 2002; **415**: 198-205.

[123] Vornanen M. Na^+/Ca^{2+} Exchange current in ventricular myocytes of fish heart: contribution to sarcolemmal Ca^{2+} influx . *The Journal of Experimental Biology* 1999; **202**:1763–1775.

[124] Shiels HA, Di Maio A, Thompson S, et al. Warm fish with cold hearts: thermal plasticity of excitation–contraction coupling in bluefin tuna. *Proc R Soc B* 2011; **278**: 18–27.

[125] Zhang H, Holden AV, Noble D, et al. Analysis of the chronotropic effect of Acetylcholine on sinoatrial node cells. *Journal of Cardiovascular Electrophysiology* 2002; **13**: 465–474.

[126] Landis EN, Keane DT. X-ray microtomography. *Materials Characterization* 2010; **61**: 1305–1316.

[127] Du Plessis A, Broeckhoven C, Guelpa A, et al. Laboratory x-ray micro-computed tomography: a user guideline for biological samples. *GigaScience* 2017; **6**. DOI: 10.1093/gigascience/gix027.

[128] Broeckhoven C, Diedericks G, Hui C, et al. Enemy at the gates: rapid defensive trait diversification in an adaptive radiation of lizards: brief communication. *Evolution* 2016; **70**: 2647–2656.

[129] O'Connor PM, Sertich JJW, Stevens NJ, et al. The evolution of mammal-like crocodyliforms in the Cretaceous Period of Gondwana. *Nature* 2010; **466**: 748–751.

[130] Faulwetter S, Vasileiadou A, Kouratoras M, et al. Micro-computed tomography: introducing new dimensions to taxonomy. *ZooKeys* 2013; **263**: 1–45.

[131] Cnudde V, Boone MN. High-resolution X-ray computed tomography in geosciences: a review of the current technology and applications. *Earth-Science Reviews* 2013; **123**: 1–17.

[132] Boerckel JD, Mason DE, McDermott AM, et al. Microcomputed tomography: approaches and applications in bioengineering. *Stem Cell Research & Therapy* 2014; **5**: 144.

[133] Gordon AM, Regnier M, Homsher E. Skeletal and cardiac muscle contractile activation: tropomyosin "Rocks and Rolls". *Physiology* 2001; **16**: 49–55.

[134] Fukuda N, Terui T, Ohtsuki I, et al. Titin and Troponin: central players in the Frank-Starling mechanism of the heart. *Current Cardiology Reviews* 2009; **5**: 119–124.

[135] Linke WA, Hamdani N. Gigantic business: Titin properties and function through thick and thin. *Circulation Research* 2014; **114**: 1052–1068.

[136] Rodríguez JE, McCudden CR, Willis MS. Familial hypertrophic cardiomyopathy: basic concepts and future molecular diagnostics. *Clinical Biochemistry* 2009; **42**: 755–765.

[137] Adeniran I, Hancox JC, Zhang H. Effect of cardiac ventricular mechanical contraction on the characteristics of the ECG: A simulation study. *Journal of Biomedical Science and Engineering* 2013; **06**: 47–60.

[138] Leong IUS, Skinner JR, Shelling AN, et al. Zebrafish as a model for long QT syndrome: the evidence and the means of manipulating zebrafish gene expression. *Acta Physiologica* 2010. DOI: 10.1111/j.1748-1716.2010.02111.x.

[139] https://opentextbc.ca/anatomyandphysiology/chapter/19-2-cardiac-muscle-and-electrical-activity/ (Accessed 14 August 2019).

[140] Popp lulia M, Seemann G, Dössel O. A simulation study of the reaction of human heart to biphasic electrical shocks. *BMC Cardiovascular Disorders* 2004; **4**. DOI: 10.1186/1471-2261-4-9.

[141] Bittihn P. Complex structure and dynamics of the heart. Cham: Springer International Publishing 2015. https://doi.org/10.1007/978-3-319-12232-8.

[142] Rudy Y, Silva JR. Computational biology in the study of cardiac ion channels and cell electrophysiology. *Quarterly Reviews of Biophysics* 2006; **39**: 57.

[143] Clayton RH, Bernus O, Cherry EM, et al. Models of cardiac tissue electrophysiology: Progress, challenges and open questions. *Progress in Biophysics and Molecular Biology*

2011; **104**: 22–48.

[144] Rudy Y. From genome to physiome: integrative models of cardiac excitation. *Annals of Biomedical Engineering* 2000; **28**: 945–950.

[145] Sano T, Takayama N, Shimamoto T. Directional difference of conduction velocity in the cardiac ventricular syncytium studied by microelectrodes. *Circulation Research* 1959; **7**: 262–267.

[146] Rush S, Larsen H. A Practical Algorithm for Solving Dynamic Membrane Equations. *IEEE Transactions on Biomedical Engineering* 1978; **BME-25**: 389–392.

[147] Dormand JR, Prince PJ. A family of embedded Runge-Kutta formulae. *Journal of Computational and Applied Mathematics* 1980; **6**: 19–26.

[148] Cohen SD, Hindmarsh AC, Dubois PF. CVODE, a stiff/nonstiff ODE solver in C. *Computing in Physics* 1996; **10**: 138.

[149] Clayton RH, Panfilov AV. A guide to modelling cardiac electrical activity in anatomically detailed ventricles. *Progress in Biophysics and Molecular Biology* 2008; **96**: 19–43.

[150] Iserles A. *A first course in the numerical analysis of differential equations*. Cambridge ; New York: Cambridge University Press, 1996.

[151] Luo CH, Rudy Y. A model of the ventricular cardiac action potential. Depolarization, repolarization, and their interaction. *Circulation Research* 1991; **68**: 1501–1526.

[152] Bernal D, Brill RW, Dickson KA, et al. Sharing the water column: physiological mechanisms underlying species-specific habitat use in tunas. *Reviews in Fish Biology and Fisheries* 2017; **27**: 843–880.

[153] Hassinen M, Paajanen V, Vornanen M. A novel inwardly rectifying K^+ channel, Kir2.5, is upregulated under chronic cold stress in fish cardiac myocytes. *Journal of Experimental Biology* 2008; **211**: 2162–2171.

[154] Galli GLJ, Lipnick MS, Block BA. Effect of thermal acclimation on action potentials and sarcolemmal K^+ channels from Pacific bluefin tuna cardiomyocytes. *American Journal of Physiology-Regulatory, Integrative and Comparative Physiology* 2009; **297**: R502–R509.

[155] Haverinen J, Egginton S, Vornanen M. Electrical excitation of the heart in a basal vertebrate, the European River Lamprey (*Lampetra fluviatilis*). *Physiological and Biochemical Zoology* 2014; **87**: 817–828.

[156] Courtemanche M, Ramirez RJ, Nattel S. Ionic mechanisms underlying human atrial action potential properties: insights from a mathematical model. *American Journal of Physiology-Heart and Circulatory Physiology* 1998; **275**: H301–H321.

[157] Naser H, Whittaker D, Shiels H and Boyett M and Zhang H. A Novel Model of Electrical

Action Potentials of Teleost Fish Ventricular Myocytes. Computing in Cardiology Conference (CinC), Maastricht, Netherland: *IEEE*; 2018. DOI: 10.22489/CinC.2018.032.

[158] KléBer AG, Rudy Y. Basic mechanisms of cardiac impulse propagation and associated arrhythmias. *Physiological Reviews* 2004; **84**: 431–488.

[159] Schram G. Differential distribution of cardiac ion channel expression as a basis for regional specialization in electrical function. *Circulation Research* 2002; **90**: 939–950.

[160] Fozzard H. Cardiac sodium and calcium channels: a history of excitatory currents. *Cardiovascular Research* 2002; **55**: 1–8.

[161] Leblanc N, Hume. Sodium current-induced release of calcium from cardiac sarcoplasmic reticulum. *Science* 1990; **248**: 372–376.

[162] Maier SKG, Westenbroek RE, Schenkman KA, et al. An unexpected role for brain-type sodium channels in coupling of cell surface depolarization to contraction in the heart. *Proceedings of the National Academy of Sciences* 2002; **99**: 4073–4078.

[163] Haverinen J, Hassinen M, Vornanen M. Fish cardiac sodium channels are tetrodotoxin sensitive. *Acta Physiologica* 2007; **191**: 197–204.

[164] Callewaert G. Excitation-contraction coupling in mammalian cardiac cells. *Cardiovascular Research* 1992; **26**: 923–932.

[165] Fabiato A. Calcium-induced release of calcium from the cardiac sarcoplasmic reticulum. *Am J Physiol* 1983; **245**: C1–C14.

[166] Shiels HA, Galli GLJ, Block BA. Cardiac function in an endothermic fish: cellular mechanisms for overcoming acute thermal challenges during diving. *Proceedings of the Royal Society B: Biological Sciences* 2014; **282**: 20141989–20141989.

[167] Reuter H. Properties of Two Inward Membrane Currents in the Heart. *Annual Review of Physiology* 1979; **41**: 413–424.

[168] Hassinen M, Paajanen V, Haverinen J, et al. Cloning and expression of cardiac $K_{ir}2.1$ and $K_{ir}2.2$ channels in thermally acclimated rainbow trout. *American Journal of Physiology-Regulatory, Integrative and Comparative Physiology* 2007; **292**: R2328–R2339.

[169] Driedzic WR, Bailey JR, Sephton DH. Cardiac adaptations to low temperature in non-polar teleost fish. *The Journal of Experimental Zoology* 1996; **275**: 186–195.

[170] Hibino H, Terzic A, Inanobe A, et al. Chapter 14 regulation of ion channels by membrane proteins. C*urrent Topics in Membranes* 1999; **46**: 243-272.

[171] Keen JE, Vianzon D-M, Farrell AP, et al. Thermal acclimation alters both adrenergic sensitivity and adrenoceptor density in cardiac tissue of rainbow trout. *The Journal of Experimental Biology* 1993; **181**: 27–47.

[172] Aho E, Vornanen M. Ca^{2+}-ATPase activity and Ca^{2+} uptake by sarcoplasmic reticulum in fish heart: effects of thermal acclimation. *The Journal of Experimental Biology* 1998; **201**: 525–532.

[173] Vornanen M, Ryökkynen A, Nurmi A. Temperature-dependent expression of sarcolemmal K^{+} currents in rainbow trout atrial and ventricular myocytes. *American Journal of Physiology-Regulatory, Integrative and Comparative Physiology* 2002; **282**: R1191–R1199.

[174] Barry DM, Nerbonne JM. Myocardial Potassium Channels: electrophysiological and molecular diversity. *Annual Reviews Physiology* 1996; **58**: 363–394.

[175] Boutilier RG. Mechanisms of metabolic defense against hypoxia in hibernating frogs. *Respiration Physiology* 2001; **128**: 365–377.

[176] Crawshaw LI. Low-temperature dormancy in fish. *American Journal of Physiology-Regulatory, Integrative and Comparative Physiology* 1984; **246**: R479–R486.

[177] Jackson DC. Living without oxygen: lessons from the freshwater turtle. *Comparative Biochemistry and Physiology Part A: Molecular & Integrative Physiology* 2000; **125**: 299–315.

[178] Lutz PL, Nilsson GE. Contrasting strategies for anoxic brain survival–glycolysis up or down. *The Journal of Experimental Biology* 1997; **200**: 411–419.

[179] Vornanen M, Shepherd N, Isenberg G. Tension-voltage relations of single myocytes reflect Ca release triggered by Na/Ca exchange at 35 degrees C but not 23 degrees C. *American Journal of Physiology-Cell Physiology* 1994; **267**: C623–C632.

[180] Eaton DC. Ionic channels of excitable membranes. Bertil Hille. Sunderland, Ma: Sinauer Associates, 1984. *Journal of Neuroscience Research* 1985; **13**: 599–600.

[181] Allen DG, Kurihara S. The effects of muscle length on intracellular calcium transients in mammalian cardiac muscle. *The Journal of Physiology* 1982; **327**: 79–94.

[182] Rose WC, Balke CW, Wier WG, et al. Macroscopic and unitary properties of physiological ion flux through L-type Ca^{2+} channels in guinea-pig heart cells. *The Journal of Physiology* 1992; **456**: 267–284.

[183] Lagerspetz KY. Temperature effects on different organization levels in animals. *Symposia of the Society for Experimental Biology* 1987; **41**: 429–449.

[184] Seebacher F, Davison W, Lowe CJ, et al. A falsification of the thermal specialization paradigm: compensation for elevated temperatures in Antarctic fishes. *Biology Letters* 2005; **1**: 151–154.

[185] Zhang H, Hancox JC. In silico study of action potential and QT interval shortening due to loss of inactivation of the cardiac rapid delayed rectifier potassium current. *Biochemical and Biophysical Research Communications* 2004; **322**: 693–699.

[186] Gima K. Ionic current basis of electrocardiographic waveforms: a model study. *Circulation Research* 2002; **90**: 889–896.

[187] Clayton RH, Holden AV. Dynamics and interaction of filaments in a computational model of re-entrant ventricular fibrillation. *Physics in Medicine and Biology* 2002; **47**: 1777–1792.

[188] Zheng H, Liu W, Anderson LY, et al. Lipid-dependent gating of a voltage-gated potassium channel. *Nature Communications*; 2011. DOI: 10.1038/ncomms1254.

[189] Widmark J, Sundstrom G, Ocampo Daza D, et al. Differential evolution of voltage-gated sodium channels in tetrapods and teleost fishes. *Molecular Biology and Evolution* 2011; **28**: 859–871.

[190] Rosenthal JJC, Bezanilla F. Action potentials from tropical and temperate squid axons. T*he Journal of Experimental Biology* 2002; **205**: 1819–1830.

[191] Aguado-Sierra J, Krishnamurthy A, Villongco C, et al. Patient-specific modeling of dyssynchronous heart failure: A case study. *Progress in Biophysics and Molecular Biology* 2011; **107**: 147–155.

[192] Beighley PE, Thomas PJ, Jorgensen SM, et al. 3D Architecture of myocardial microcirculation in intact rat heart: a study with micro-CT. In: Sideman S, Beyar R (eds) Analytical and quantitative cardiology. *Advances in Experimental Medicine and Biology* 1997; **430**:165–175.

[193] Drouin E, Charpentier F, Gauthier C, et al. Electrophysiologic characteristics of cells spanning the left ventricular wall of human heart: Evidence for presence of M cells. *Journal of the American College of Cardiology* 1995; **26**: 185–192.

[194] Franz MR, Burkhoff D, Yue DT, et al. Mechanically induced action potential changes and arrhythmia in isolated and in situ canine hearts. *Cardiovascular Research* 1989; **23**: 213–223.

[195] Stephenson RS, Boyett MR, Hart G, et al. Contrast enhanced micro-computed tomography resolves the 3-dimensional morphology of the cardiac conduction system in mammalian hearts. *PLoS ONE* 2012; **7**: e35299.

[196] Lecker DN, Kumari S, Khan A. Iodine binding capacity and iodine binding energy of glycogen. *Journal of Polymer Science Part A: Polymer Chemistry* 1997; **35**: 1409–1412.

[197] Barta E, Adam D, Salant E, et al. 3-D ventricular myocardial electrical excitation: A minimal orthogonal pathways model. *Annals of Biomedical Engineering* 1987; **15**: 443–456.

[198] Ni H, Adeniran I, Zhang H. In-silico investigations of the functional impact of KCNA5 mutations on atrial mechanical dynamics. *Journal of Molecular and Cellular Cardiology* 2017; **111**: 86–95.

[199] Whittaker DG, Ni H, Benson AP, et al. Computational Analysis of the Mode of Action of

Disopyramide and Quinidine on hERG-Linked Short QT Syndrome in Human Ventricles. *Frontiers in Physiology* 2017; **8**. DOI: 10.3389/fphys.2017.00759.

[200] Wirkner CS. The circulatory system in Malacostraca-evaluating character evolution on the basis of differing phylogenetic hypotheses. *Arthropod Systematics and Phylogeny* 2009; **67**:57–70.

[201] Yildirir A. Hypertension and arrhythmia: blood pressure control and beyond. *Europace* 2002; **4**: 175–182.

[202] Jin CZ, Jang JH, Kim HJ, et al. Myofilament Ca^{2+} desensitization mediates positive lusitropic effect of neuronal nitric oxide synthase in left ventricular myocytes from murine hypertensive heart. *Journal of Molecular and Cellular Cardiology* 2013; **60**: 107–115.

[203] Gómez AM, Schwaller B, Porzig H, et al. Increased exchange current but normal Ca^{2+}transport via Na^{+}-Ca^{2+} exchange during cardiac hypertrophy after myocardial infarction. *Circulation Research* 2002; **91**: 323–330.

[204] Li Q, Keung EC. Effects of myocardial hypertrophy on transient outward current. *American Journal of Physiology-Heart and Circulatory Physiology* 1994; **266**: H1738–H1745.

[205] Yokoshiki H, Kohya T, Tomita F, et al. Restoration of action potential duration and transient outward current by regression of left ventricular hypertrophy. *Journal of Molecular and Cellular Cardiology* 1997; **29**: 1331–1339.

[206] Kharche S., Zhang H., Clayton RC., and Holden A.V. Hypertrophy in rat virtual left ventricular cells and tissue. In Pritchard, D., & Reeve, J. (Eds). *Euro-Par '98 parallel processing: 4th International Euro-Par Conference Southampton*, UK, September 1-4, 1998; **1470** proceedings.

[207] Rice JJ, Wang F, Bers DM, et al. Approximate model of cooperative activation and crossbridge cycling in cardiac muscle using ordinary differential equations. *Biophysical Journal* 2008; **95**: 2368–2390.

[208] Hansen DE, Craig CS, Hondeghem LM. Stretch-induced arrhythmias in the isolated canine ventricle. Evidence for the importance of mechanoelectrical feedback. *Circulation* 1990; **81**:1094–1105.

[209] Suleymanian M, Clemo H, Cohen N, et al. Stretch-activated channel blockers modulate cell volume in cardiac ventricular myocytes. *Journal of Molecular and Cellular Cardiology* 1995; **27**: 721–728.

[210] Reiter MJ. Effects of mechano-electrical feedback: potential arrhythmogenic influence in patients with congestive heart failure. *Cardiovascular Research* 1996; **8**.

[211] Tavi P, Han C, Weckström M. Mechanisms of stretch-induced changes in $[Ca^{2+}]_i$in rat atrial myocytes: role of increased troponin C affinity and stretch-activated ion channels. *Circulation Research* 1998; **83**: 1165–1177.

[212] Franz MR, Cima R, Wang D, et al. Electrophysiological effects of myocardial stretch and mechanical determinants of stretch-activated arrhythmias. *Circulation* 1992; **86**: 968-78.

[213] Lab MJ. Mechanically dependent changes in action potentials recorded from the intact frog ventricle. *Circulation Research* 1978; **42**: 519–528.

[214] Adeniran I, Hancox JC, Zhang H. In silico investigation of the short QT syndrome, using human ventricle models incorporating electromechanical coupling. *Frontiers in Physiology* 2013; **4**. DOI: 10.3389/fphys.2013.00166.

[215] Panfilov AV, Keldermann RH, Nash MP. Self-organized pacemakers in a coupled reaction-diffusion-mechanics system. *Physical Review Letters* 2005; **95**: 258104.

[216] World Congress on Medical Physics and Biomedical Engineering, Dössel O, Schlegel WC, et al. (eds). *World Congress on Medical Physics and Biomedical Engineering: 7 - 12 September, 2009, Munich, Germany; [WC 2009; 11th international congress of the IUPESM]. **8**: Micro- and nanosystems in medicine, active implants, biosensors*. Berlin: Springer, 2009.

[217] Youm JB, Han J, Kim N, et al. Role of Stretch-activated channels in the heart: action potential and Ca^{2+} transients. In: Kamkin A, Kiseleva I (eds) Mechanosensitivity in cells and tissues. Moscow: Academia 2005. http://www.ncbi.nlm.nih.gov/books/NBK7490/.

[218] Trayanova N, Li W, Eason J, et al. Effect of stretch-activated channels on defibrillation efficacy. *Heart Rhythm* 2004; **1**: 67–77.

[219] Kohl P, Hunter P, Noble D. Stretch-induced changes in heart rate and rhythm: clinical observations, experiments and mathematical models. *Progress in Biophysics and Molecular Biology* 1999; **71**: 91–138.

[220] Adeniran I, MacIver DH, Garratt CJ, et al. Effects of persistent atrial fibrillation-induced electrical remodeling on atrial electro-mechanics – insights from a 3D model of the human atria. *PLOS ONE* 2015; **10**: e0142397.

[221] Niederer SA, Smith NP. An improved numerical method for strong coupling of excitation and contraction models in the heart. *Progress in Biophysics and Molecular Biology* 2008; **96**: 90–111.

[222] Keener J, Sneyd J. Mathematical physiology I: cellular physiology. *New York, NY: Springer* 2009.

[223] Potse M, Dube B, Richer J, et al. A comparison of monodomain and bidomain reaction-diffusion models for action potential propagation in the human heart. *IEEE Transactions on Biomedical Engineering* 2006; **53**: 2425–2435.

[224] Nash MP, Panfilov AV. Electromechanical model of excitable tissue to study reentrant cardiac arrhythmias. *Progress in Biophysics and Molecular Biology* 2004; **85**: 501–522.

[225] Whiteley JP, Bishop MJ, Gavaghan DJ. Soft tissue modelling of cardiac fibres for use in coupled mechano-electric simulations. *Bulletin of Mathematical Biology* 2007; **69**: 2199–2225.

[226] Alvarez JL, Aimond F, Lorente P, et al. Late post-myocardial infarction induces a tetrodotoxin-resistant Na^+ current in rat cardiomyocytes. *Journal of Molecular and Cellular Cardiology* 2000; **32**: 1169–1179.

[227] Chung J-H, Biesiadecki BJ, Ziolo MT, et al. Myofilament calcium sensitivity: role in regulation of in vivo cardiac contraction and relaxation. *Front Physiol* 2016; **7**. DOI: 10.3389/fphys.2016.00562.

[228] Jin CL, Yin MZ, Paeng JC, et al. Neuronal nitric oxide synthase modulation of intracellular Ca^{2+} handling overrides fatty acid potentiation of cardiac inotropy in hypertensive rats. *Pflügers Archiv - European Journal of Physiology* 2017; **469**: 1359–1371.

[229] Yan G-X, Shimizu W, Antzelevitch C. Characteristics and distribution of m cells in arterially perfused canine left ventricular wedge preparations. *Circulation* 1998; **98**: 1921–1927.

[230] Weiss D, Seemann G, Sachse F, et al. Modelling of short QT syndrome in a heterogeneous model of the human ventricular wall. *Europace* 2005; **7**: S105–S117.

[231] Taggart P, Sutton PM, Opthof T, et al. Inhomogeneous transmural conduction during early ischaemia in patients with coronary artery disease. *Journal of Molecular and Cellular Cardiology* 2000; **32**: 621–630.

[232] Braess D. Finite Elements: Theory, Fast Solvers, and Applications in Elasticity Theory. *Cambridge: Cambridge University Press* 2007. DOI: 10.1017/CBO9780511618635.

[233] Johnson JN, Ackerman MJ. QTc: how long is too long?. *British Journal of Sports Medicine* 2009; **43**: 657–662.

[234] Hardy MEL, Pervolaraki E, Bernus O, et al. Dynamic action potential restitution contributes to mechanical restitution in right ventricular myocytes from pulmonary hypertensive rats. *Frontiers in Physiology* 2018; **9**. DOI: 10.3389/fphys.2018.00205.

[235] Salles GF, Cardoso CRL, Leocadio SM, et al. Recent ventricular repolarization markers in resistant hypertension: are they different from the traditional qt interval?. *American Journal of Hypertension* 2008; **21**: 47–53.

[236] Schillaci G, Pirro M, Pasqualini L, et al. Prognostic significance of isolated, non-specific left ventricular repolarization abnormalities in hypertension. *Journal of Hypertension* 2004; **22**: 407–414.

[237] Gosse P, Jan E, Coulon P, et al. ECG detection of left ventricular hypertrophy: the simpler, the better?. *Journal of Hypertension* 2012; **30**: 990–996.

[238] KamkinA. Stretch-activated currents in ventricular myocytes: amplitude and arrhythmogenic

effects increase with hypertrophy. *Cardiovascular Research* 2000; **48**: 409–420.

[239] Pye MP, Cobbe SM. Mechanisms of ventricular arrhythmias in cardiac failure and hypertrophy. *Cardiovascular Research*1992; **26**: 740–750.

[240] Naser H, Zhang Y, Zhang H. Modelling the Effects of Hypertension on Ventricle Cells of Human Heart. Computing in Cardiology (CinC). Singapore: *IEEE*; 2019. (Conference proceedings).

[241] Coulshed DS, Cowan JC, Drinkhill MJ, et al. The effects of ventricular end-diastolic and systolic pressures on action potential and duration in anaesthetized dogs. *The Journal of Physiology* 1992; **457**: 75–91.

[242] Davidson K, Jonas BS, Dixon KE, et al. Do depression symptoms predict early hypertension incidence in young adults in the cardia study?. *Archives of internal medicine* 2000; **160**: 1495–1500.

[243] Turner MJ, van Schalkwyk JM. Blood pressure variability causes spurious identification of hypertension in clinical studies: a computer simulation study. *American Journal of Hypertension* 2008; **21**: 85–91.

[244] Weise LD, Panfilov AV. A discrete electromechanical model for human cardiac tissue: effects of stretch-activated currents and stretch conditions on restitution properties and spiral wave dynamics. *PLoS ONE* 2013; **8**: e59317.

[245] Talo A, Tirri R. Temperature acclimation of the perch (Perc fluviatilis L.): Changes in duration of cardiac action potential. *Journal of Thermal Biology* 1991; **16**: 89–92.

[246] Degenhardt K, Wright AC, Horng D, et al. Rapid 3D phenotyping of cardiovascular development in mouse embryos by micro-CT with iodine staining. *Circulation: Cardiovascular Imaging* 2010; **3**: 314–322.

[247] Schwartz PJ, Crotti L, Insolia R. Long-QT syndrome: from genetics to management. *Circulation: Arrhythmia and Electrophysiology* 2012; **5**: 868–877.